**Western Australian School of Mines: Minerals, Energy and Chemical Engineering**

# Preparation of Carbon-Based Materials for Water Remediation

**Wenjie Tian**

**This thesis is presented for the Degree of**
**Doctor of Philosophy**
**of**
**Curtin University**

**May 2018**

# Declaration

To the best of my knowledge and belief this thesis contains no material previously published by any other person except where due acknowledgment has been made. This thesis contains no material which has been accepted for the award of any other degree or diploma in any university.

Signature: Wenjie Tian (Wenjie Tian)

Date: 09/05/2018

## Acknowledgement

First and foremost, I would like to express my sincerest thanks and appreciation to my principal supervisor, Prof. Shaobin Wang, for his professional, inspiring and instructive guidance in planning and advancing my research work. The distinguished achievement that Prof. Wang has gained leads us forward positively in the field of research. Every time when I feel confused or lost, he is always patient to offer wise and valuable suggestions that help me overcome difficulties in my life and study.

In the same way, I would also like to express my great thanks towards my co-supervisor, Prof. Hongqi Sun, for his inspiring encouragement, continual support and constructive suggestions in designing research plans throughout my study. Special thanks are given for his innovative guidance in problem solving and useful feedbacks in paper writing.

Also, many thanks to Prof. Shaomin Liu, who is the chairperson of this thesis committee, for his kind encouragement and instructive suggestions on my work.

This work was conducted under the financial support from CRC for Contamination Assessment and Remediation of the Environment (CRC CARE). Great thanks go to CRC CARE.

I would also like to extend my thanks to the lab technician team of Curtin University for their assistance in preparing chemicals and training equipment. Special thanks are given to Roshanak and Anja for their constant help and understanding during the process of conducting experiments in the lab.

Last but not least, I want to give my sincere thanks to my friends and fellow students, Xiaoguang, Xiaochen, Guanliang, KJ, Chi, Ping, Stacey, Zana, Hussein, Li, Lihong, Chen, Qi, Yazi, Heng, Xiaojie, Ruofei, Zhengxin, Qiaoran, Spark, Sharon, Qiang, Hong, Xinyuan, Yu and Lei. Thanks for their supports, assistance and company, which have enriched my life and encouraged me to continue my study.

The deepest love is given to my family for their continual trust and unconditional support all the time and thank you, my beloved spouse Huayang, for understanding, helping and encouraging me so much throughout this period.

# Abstract

The scarcity of clean water has been a worldwide issue. Water pollution by non-biodegradable organic pollutants caused by human activities has further boosted the pressure on clean water supply. To effectively address this pressing situation, novel materials and techniques for water remediation have been extensively studied in the last few decades. Recently, carbon-based materials, for example, graphene, carbon nanotube, nanodiamond, and porous carbon, have become attractive candidates owing to their unique physical and chemical properties, high stability and environmental friendliness. Among them, special attention has been paid to porous carbons because of their large specific surface areas (SSA), abundant porosities, tuneable surface chemistry and low cost. These attributes offer them enormous advantages to effectively remove organic pollutants in wastewater by direct physical adsorption or by efficient catalytic degradation, known as advanced oxidation processes (AOPs).

Driven by the desire of lower cost, higher efficiency, and green synthesis with minimal environmental impact, this study innovatively develops several large-surface-area, porous carbons with controllable features (for example, N or N, S doping, cobalt modification), using sustainable and inexpensive glucose or flour as the carbon precursors. Structural control is sophisticatedly conducted at different experimental parameters (for instance, various synthesis temperatures or precursor ratios) and the derived samples were carefully characterized, to deliver the optimum craft for the high-performance sample. The resulting porous-carbon-based nanoarchitectures with three-dimensional (3D) and interconnected frameworks can not only serve as excellent adsorbents for organics in wastewater but also work efficiently in AOPs for catalyzing potassium persulfate (PS) or peroxymonosulfate (PMS) to produce strongly oxidizing radicals for complete removal of pollutants. Despite that these porous carbons are designed for water remediation, they are also examined for other applications including $CO_2$ uptake, supercapacitors and oxygen reduction reaction (ORR), demonstrating the fascinating features of the resultant samples.

# Publications

**1. W. Tian**, H. Zhang, H. Sun*, A. Suvorova, M. Saunders, M. Tade, S.B. Wang*. Heteroatom (N or N-S)-doping induced layered and honeycomb microstructures of porous carbons for $CO_2$ capture and energy applications. *Adv. Funct. Mater.* 2016, 26 (47): 8651–8661.

**2**. **W. Tian**, H. Zhang, X. Duan, H. Sun*, M. Tade, H. Ang, S. Wang*, Nitrogen-and sulfur-codoped hierarchically porous carbon for adsorptive and oxidative removal of pharmaceutical contaminants. *ACS Appl. Mater. Inter.* 2016, 8(11): 7184–7193.

**3. W. Tian**, H. Zhang, Z. Qian, T. Ouyang, H. Sun*, J. Qin, M.O. Tadé, S. Wang*, Bread-making synthesis of hierarchically Co@C nanoarchitecture in heteroatom doped porous carbons for oxidative degradation of emerging contaminants, *Appl. Catal. B: Environ.* 2018, 225: 76–83.

**4. W. Tian**, H. Zhang, H. Sun*, M. Tade, S. Wang*, Template-free synthesis of N-doped carbon with pillared-layered pores as bifunctional materials for supercapacitor and environmental applications. *Carbon* 2017, 118: 98–105.

**5. W. Tian**, H. Zhang, H. Sun*, M. Tade, S. Wang*, One-step synthesis of flour-derived functional nanocarbons with hierarchical pores for versatile environmental applications, *Chem. Eng. J.* 2018, 347 : 432–439.

**6.** H. Zhang, **W. Tian**, Y. Li, H. Sun*, M. Tade, S. Wang*, Heterostructured $WO_3$@$CoWO_4$ bilayer nanosheets for enhanced visible-light photo, electro and photoelectro-chemical oxidation of water, *J. Mater. Chem. A* 2018, 6: 6265.

**7.** H. Zhang, **W. Tian**, Z. Qian, T. Ouyang, M. Saunders, J. Qin, S. Wang*, M.O. Tadé, H. Sun*, Co@C/CoOx coupled with N-doped layer-structured carbons for excellent $CO_2$ capture and oxygen reduction reaction, *Carbon* 2018, 133: 306–315.

**8.** H. Zhang, **W. Tian**, L. Zhou, H. Sun*, M. Tade, S. Wang*, Monodisperse $Co_3O_4$ quantum dots on porous carbon nitride nanosheets for enhanced visible-light-driven water oxidation. *Appl. Catal. B: Environ.* 2017, 223: 2–9.

**9.** H. Zhang, **W. Tian**, X. Guo, L. Zhou, H. Sun*, M. Tade, S. Wang*, Flower-like cobalt hydroxide/oxide on graphitic carbon nitride for visible-light-driven water oxidation. *ACS Appl. Mater. Inter.* 2016, 8 (51), 35203–35212.

**10.** X. Ma, Y. Zhao, **W. Tian**, H. Chen, Y. Wu, X. Liu*, A novel Al matrix composite reinforced by nano-$AlN_p$ network. *Sci. Rep.* 2016, 6: 34919.

**11.** Y. Liu, H. Zhang, J. Ke, J. Zhang, **W. Tian**, X. Xu, X. Duan, H. Sun*, M. Tade, S. Wang*, 0D ($MoS_2$)/2D (g-$C_3N_4$) heterojunctions in Z-scheme for enhanced photocatalytic and electrochemical hydrogen evolution. *Appl. Catal. B: Environ.* 2018, 228: 64–74.

**12.** P. Liang, Q. Wang, J. Kang, **W. Tian**, H. Sun, S. Wang*, Dual-metal zeolitic imidazolate frameworks and their derived nanoporous carbons for multiple environmental and electrochemical applications. *Chem. Eng. J.* 2018, 351: 641–649.

## Manuscripts in Preparation

W. Tian, H. Zhang, H. Sun, S. Wang, Recent advances in the preparation of porous carbon nanostructures

## International Academic Conference

**7. 2013** Participated in RACI CENTENARY CONGRESS 2017, Melbourne, Australia (presentation type: Chemeca: Poster)

# Contents

# Chapter 1 Introduction

## 1.1 Background

Clean water scarcity has become a pervasive global issue, exerting a worldwide impact on human society.[1] Although that most of the Earth's surface is covered by water, approximately 97% of water reserve is sea water, which is unsuitable for direct drinking needs. About 3% remains as freshwater, of which 79% is stored in polar ice caps or glaciers, while merely 21% is useable for human stored in groundwater (20%) or approachable surface water (1%).[2] In the last few decades, the ever-increasing population and non-stopping industrialization put more demands on the dwindling clean water. It has been pointed out that approximately 80% of the population all over the globe is in the face of water security menace.[3] In addition, freshwater resources are becoming increasingly scarce because of water contamination arising from anthropogenic activities, such as discharges from domestic, agricultural and industrial effluents. Water pollution can arise from heavy metals, dyes, oil spills, and organic compounds. Especially, dumping of wastewater which contains non-biodegradable persistent organic pollutants (POPs) into the environment, has posed great threats to the well-being of wildlife and human health.[4, 5] The majority of POPs are toxic, and they can disrupt endocrine of humans, aquatic life and animals even at low concentrations.[6] Prompt actions are required to mitigate the impact of water pollution around the world.

To date, a variety of water purification techniques have been proposed, including ion exchange, adsorption/seperation, electrolysis, photocatalytic degradation, membrane filtration, and advanced oxidation processes (AOPs).[7, 8] Among these methods, direct adsorption is the most economical and facile method to conduct, but it has its limitations due to the existence of adsorption-desorption equilibrium, and it tends to be difficult to capture pollutants with an ultralow concentration. It is worth noting that advanced oxidation processes (AOPs) have attracted tremendous research interests because of the powerful ability for complete removal of organics.[9, 10] Specifically, strong oxidizing species such as hydroxyl radicals ($^{\bullet}OH$), singlet oxygen ($^1O_2$) and sulfate radicals ($SO_4^{\bullet-}$) are generated in AOPs.[9] These radicals can work selectively or nonselectively to oxidize most organic pollutants and decompose them into nontoxic compounds, water and carbon dioxide.[11] Conventional Fenton reactions produce $^{\bullet}OH$ radicals by activating hydrogen peroxide ($H_2O_2$). By contrast, $^{\bullet}OH$, $^1O_2$, and $SO_4^{\bullet-}$ can be produced simultaneously via the chemical activation of oxidants like peroxymonosulfate

($HSO_5^-$, PMS) or potassium persulfate ($S_2O_8^{2-}$, PS), allowing the process to be much more stable, efficient as well as non-selective.[12-14]

PS or PMS could be successfully activated by different routes, for instance, light irradiation,[15] heating,[16] and chemical catalysis.[17] Extensive studies have shown that chemical catalysis can be the most efficient. Multifarious metal ions like $Fe^{2+}$, $Co^{2+}$, $Ni^{2+}$, $Mn^{2+}$, $Ce^{3+}$, and $Ru^{3+}$ have been reported for PMS activation.[18] Unfortunately, the leaching of these metal ions in water tends to be toxic and hazardous, causing potential second pollution to the ecosystem if handled improperly.[19] On account of this, heterogeneous catalysts are particularly desirable. For instance, alternative metal oxides ($MnO_2$, $Co_3O_4$, and $Fe_3O_4$, etc.) and carbon-based materials have been developed for PMS activation in AOPs recently.[15, 16, 20-26] Special attention has been given to functionalized green carbon-based samples such as graphene, carbon nanotubes, and porous carbon, which exhibit not only superior efficiencies in activating PMS but also avoid secondary contamination.[14, 19, 27, 28] Note that the synthesis processes of graphene or carbon nanotubes are generally involved with high cost multi-steps, and harsh treatment, porous carbon materials are more appealing as they can be readily prepared by scalable, economical and facile approaches. The fascinating properties of porous carbons in terms of large specific surface areas (SSAs), high stability, and desirable environmental benignity,[29, 30] make them ideal adsorbents for POPs. For catalysis, as pristine carbons have limited activity, surface modifications are widely employed to tailor the carbon structure by the introduction of heteroatoms (for example, B, N, S, P) or metal species (like Co, Fe), endowing them with enhanced catalytic abilities.[31-33] Apart from water treatment issues, functional porous carbons with excellent electrical conductivity, good chemical stability are also highly attractive in $CO_2$ (one of the major green-house gases causing global warming) capture, supercapacitors and oxygen reaction reduction.[34-36]

## 1.2 Research Objectives

This research aims to develop novel methods to synthesize several kinds of porous-carbon-based nanoarchitectures with large surface areas and excellent properties under the assistance of N, or N, S doping, and metal catalysis. The as-prepared products were used for removal of several common POPs by adsorption and AOPs. In addition, the different mechanisms in AOPs were elaborately studied by investigating the main radical species. Finally, the performance of

the synthesized samples was also evaluated in $CO_2$ uptake, supercapacitors and ORR where applicable.

The specific objectives are as follows：

1) Develop sustainable, scalable, cost-effective, easily-handled strategies to synthesize hierarchically porous carbons.
2) Employ different carbon sources with the characteristics of environmental friendliness, great abundance, low value, easy access and rapid regeneration, together with other precursors to synthesize several porous carbons with different functional features.
3) Tune the synthesis crafts to derive optimum porous carbons with large SSAs, abundant porosity, and well-defined surface chemistry.
4) Investigate the adsorptive and catalytic ability of the derived porous carbon samples on several representative organics in wastewater.
5) Illustrate the mechanism of AOPs in different systems.
6) Extend the applications of the resulting carbons to $CO_2$ uptake and energy-related aspects to maximize their values.

## 1.3 Thesis Organisation

This thesis is composed of eight chapters, including introduction, literature review, results and discussions (five chapters), main conclusions with some perspectives for future studies.

***Chapter 1***: Introduction

This chapter summarizes current issues with clean water scarcity and water pollution. The promising solutions via adsorption or AOPs using porous carbons are proposed to address the contamination of POPs in wastewater. Also, research objectives and thesis organization are included in this chapter.

***Chapter 2***: Literature Review

This chapter outlines the recent advances in synthesizing porous carbons to obtain an overall concept of controlling porosities and chemical structures of porous carbons at different scales

in detail. This will provide valuable instructions on synthesizing porous carbons with desired physical or chemical structural features for water and wastewater treatment.

***Chapter 3***: Template-Free Synthesis of N-doped Carbon with Pillared-Layered Pores as Bifunctional Materials for Supercapacitor and Environmental Applications *(Adapted from Carbon* 2017, 118: 98–105)

This chapter describes the preparation of cross-linked, N-doped, pillared-layered porous carbons via a template-free pyrolysis process at 600 - 800 °C, which have multiple functional applications in sulfachloropyridazine (SCP) removal in wastewater and supercapacitors.

***Chapter 4***: Nitrogen- and Sulfur-Codoped Hierarchically Porous Carbon for Adsorptive and Oxidative Removal of Pharmaceutical Contaminants *(Adapted from ACS Appl. Mater. Inter.* 2016, 8(11): 7184–7193)

This chapter reports the successful synthesis of N, S co-doped hierarchically porous carbons with large surface areas through direct pyrolysis of a mixture containing glucose, thiourea and sodium bicarbonate. The resulting products show high adsorption capacities on SCP and work effectively in PS activation for efficient oxidative degradation of SCP.

***Chapter 5***: Heteroatom (N or N-S)-Doping Induced Layered and Honeycomb Microstructures of Porous Carbons for $CO_2$ Capture and Energy Applications *(Adapted from Adv. Funct. Mater.* 2016, 26 (47): 8651–866)

In this chapter, two microstructured porous carbons, namely N-doped layered carbon and N, S co-doped honeycomb carbon were prepared by pyrolysis of mixed glucose, sodium bicarbonate, and urea or thiourea. The mechanism of different pore shapes formation is analysed. In addition, $CO_2$ capture and ORR properties are evaluated on the resultant N or N, S codoped carbons.

***Chapter 6***: One-Step Synthesis of Flour-Derived Functional Nanocarbons with Hierarchical Pores for Versatile Environmental Applications *(Adapted from Chem. Eng. J.* 2018, 347 : 432–439)

This chapter presents the synthesis of flour-derived N-doped porous carbon with super high surface areas. The porous structure can be tuned by adjusting precursor varieties and pyrolysis tempratures. The final products show superior $CO_2$ storage capacities, efficient degradation of

*p*-hydroxybenzoic acid (HBA) in PMS-activated AOPs. In a mixed solution of phenol and HBA, selective adsorption on HBA is observed, while both of them can be effectively degraded by AOPs.

***Chapter 7***: Bread-Making Synthesis of Hierarchical Co@C Nanoarchitecture in Heteroatom Doped Porous Carbons for Oxidative Degradation of Emerging Contaminants *(Adapted from Appl. Catal. B: Environ.* 2018, 225: 76–83)

This chapter presents a direct pyrolysis route for uniform assembly of Co@C core-shell nanoparticles with N and S doping into porous carbon frameworks, employing wheat flour, cysteine, sodium bicarbonate, and cobalt nitrate as precursors. The resulting products are highly efficient catalysts for the oxidative decomposition of HBA and phenol.

***Chapter 8***: Conclusions and Perspectives

This chapter provides a summary of the above research results and presents some perspectives for future research.

## References

[1] M.A. Shannon, P.W. Bohn, M. Elimelech, J.G. Georgiadis, B.J. Marinas, A.M. Mayes, Science and Technology for Water Purification in the Coming Decades, Nature, 452 (2008) 301.

[2] U. Tahir, A. Yasmin, U.H. Khan, Phytoremediation: Potential Flora for Synthetic Dyestuff Metabolism, Journal of King Saud University - Science, 28 (2016) 119.

[3] R.P. Schwarzenbach, B.I. Escher, K. Fenner, T.B. Hofstetter, C.A. Johnson, U. von Gunten, B. Wehrli, The Challenge of Micropollutants in Aquatic Systems, Science, 313 (2006) 1072.

[4] X. Qu, J. Brame, Q. Li, P.J.J. Alvarez, Nanotechnology for a Safe and Sustainable Water Supply: Enabling Integrated Water Treatment and Reuse, Accounts of Chemical Research, 46 (2013) 834.

[5] A.B. Bhuiyan, M.B. Mokhtar, M.E. Toriman, M.B. Gasim, G.C. Ta, R. Elfithri, M.R. Razman, The Environmental Risk and Water Pollution: A Review from the River Basins around the World, American-Eurasian Journal of Sustainable Agriculture, 7 (2013) 126.

[6] X. Gao, F. Zhou, C.-T.A. Chen, Pollution Status of the Bohai Sea: An Overview of the Environmental Quality Assessment Related Trace Metals, Environment International, 62 (2014) 12.

[7] C.A. Martínez-Huitle, E. Brillas, Decontamination of Wastewaters Containing Synthetic Organic Dyes by Electrochemical Methods: A General Review, Applied Catalysis B: Environmental, 87 (2009) 105.
[8] I. Koyuncu, O.A. Arikan, M.R. Wiesner, C. Rice, Removal of Hormones and Antibiotics by Nanofiltration Membranes, Journal of Membrane Science, 309 (2008) 94.
[9] K.E. O'Shea, D.D. Dionysiou, Advanced Oxidation Processes for Water Treatment, Journal of Physical Chemistry Letters, 3 (2012) 2112.
[10] P.D. Hu, M.C. Long, Cobalt-Catalyzed Sulfate Radical-Based Advanced Oxidation: A Review on Heterogeneous Catalysts and Applications, Applied Catalysis B-Environmental, 181 (2016) 103.
[11] W.H. Glaze, J.-W. Kang, D.H. Chapin, The Chemistry of Water Treatment Processes Involving Ozone, Hydrogen Peroxide and Ultraviolet Radiation, Ozone: Science & Engineering, 9 (1987) 335.
[12] P. Liang, C. Zhang, X. Duan, H. Sun, S. Liu, M.O. Tade, S. Wang, An Insight into Metal Organic Framework Derived N-Doped Graphene for the Oxidative Degradation of Persistent Contaminants: Formation Mechanism and Generation of Singlet Oxygen from Peroxymonosulfate, Environmental Science: Nano, 4 (2017) 315.
[13] E. Saputra, S. Muhammad, H. Sun, H.-M. Ang, M.O. Tadé, S. Wang, Shape-Controlled Activation of Peroxymonosulfate by Single Crystal A-$Mn_2O_3$ for Catalytic Phenol Degradation in Aqueous Solution, Applied Catalysis B: Environmental, 154–155 (2014) 246.
[14] H.Q. Sun, S.Z. Liu, G.L. Zhou, H.M. Ang, M.O. Tade, S.B. Wang, Reduced Graphene Oxide for Catalytic Oxidation of Aqueous Organic Pollutants, ACS Applied Materials & Interfaces, 4 (2012) 5466.
[15] T.K. Lau, W. Chu, N.J.D. Graham, The Aqueous Degradation of Butylated Hydroxyanisole by Uv/$S_2O_8^{2-}$: Study of Reaction Mechanisms Via Dimerization and Mineralization, Environmental Science & Technology, 41 (2007) 613.
[16] R.H. Waldemer, P.G. Tratnyek, R.L. Johnson, J.T. Nurmi, Oxidation of Chlorinated Ethenes by Heat-Activated Persulfate: Kinetics and Products, Environmental Science & Technology, 41 (2007) 1010.
[17] Y.C. Lee, S.L. Lo, J. Kuo, C.P. Huang, Promoted Degradation of Perfluorooctanic Acid by Persulfate When Adding Activated Carbon, Journal of Hazardous Materials, 261 (2013) 463.
[18] G.P. Anipsitakis, D.D. Dionysiou, Radical Generation by the Interaction of Transition Metals with Common Oxidants, Environmental Science & Technology, 38 (2004) 3705.

[19] X.B. Wang, Y.L. Qin, L.H. Zhu, H.Q. Tang, Nitrogen-Doped Reduced Graphene Oxide as a Bifunctional Material for Removing Bisphenols: Synergistic Effect between Adsorption and Catalysis, Environmental Science & Technology, 49 (2015) 6855.

[20] J.C. Yan, M. Lei, L.H. Zhu, M.N. Anjum, J. Zou, H.Q. Tang, Degradation of Sulfamonomethoxine with $Fe_3O_4$ Magnetic Nanoparticles as Heterogeneous Activator of Persulfate, Journal of Hazardous Materials, 186 (2011) 1398.

[21] S. Indrawirawan, H. Sun, X. Duan, S. Wang, Nanocarbons in Different Structural Dimensions (0-3D) for Phenol Adsorption and Metal-Free Catalytic Oxidation, Applied Catalysis B: Environmental, 179 (2015) 352.

[22] S. Indrawirawan, H. Sun, X. Duan, S. Wang, Low Temperature Combustion Synthesis of Nitrogen-Doped Graphene for Metal-Free Catalytic Oxidation, Journal of Materials Chemistry A, 3 (2015) 3432.

[23] G. Li, Y. Lu, C. Lu, M. Zhu, C. Zhai, Y. Du, P. Yang, Efficient Catalytic Ozonation of Bisphenol-a over Reduced Graphene Oxide Modified Sea Urchin-Like α-$MnO_2$ Architectures, Journal of Hazardous Materials, 294 (2015) 201.

[24] L. Duan, X. Zhou, S. Liu, P. Shi, W. Yao, 3D-Hierarchically Structured $Co_3O_4$/Graphene Hydrogel for Catalytic Oxidation of Orange II Solutions by Activation of Peroxymonosulfate, Journal of the Taiwan Institute of Chemical Engineers, 76 (2017) 101.

[25] G. Li, K. Li, A. Liu, P. Yang, Y. Du, M. Zhu, 3D Flower-Like B-$MnO_2$/Reduced Graphene Oxide Nanocomposites for Catalytic Ozonation of Dichloroacetic Acid, 7 (2017) 43643.

[26] Y. Liu, X. Liu, Y. Zhao, D.D. Dionysiou, Aligned A-Feooh Nanorods Anchored on a Graphene Oxide-Carbon Nanotubes Aerogel Can Serve as an Effective Fenton-Like Oxidation Catalyst, Applied Catalysis B: Environmental, 213 (2017) 74.

[27] H.Q. Sun, Y.X. Wang, S.Z. Liu, L. Ge, L. Wang, Z.H. Zhu, S.B. Wang, Facile Synthesis of Nitrogen Doped Reduced Graphene Oxide as a Superior Metal-Free Catalyst for Oxidation, Chemical Communications, 49 (2013) 9914.

[28] X.G. Duan, H.Q. Sun, Y.X. Wang, J. Kang, S.B. Wang, N-Doping-Induced Nonradical Reaction on Single-Walled Carbon Nanotubes for Catalytic Phenol Oxidation, ACS Catalysis, 5 (2015) 553.

[29] W.J. Tian, H.Y. Zhang, X.G. Duan, H.Q. Sun, M.O. Tade, H.M. Ang, S.B. Wang, Nitrogen- and Sulfur-Codoped Hierarchically Porous Carbon for Adsorptive and Oxidative Removal of Pharmaceutical Contaminants, ACS Applied Materials & Interfaces, 8 (2016) 7184.

[30] C.Z. Zhu, H. Li, S.F. Fu, D. Du, Y.H. Lin, Highly Efficient Nonprecious Metal Catalysts Towards Oxygen Reduction Reaction Based on Three-Dimensional Porous Carbon Nanostructures, Chemical Society Reviews, 45 (2016) 517.
[31] W. Xia, R.Q. Zou, L. An, D.G. Xia, S.J. Guo, A Metal-Organic Framework Route to in Situ Encapsulation of Co@$Co_3O_4$@C Core@Bishell Nanoparticles into a Highly Ordered Porous Carbon Matrix for Oxygen Reduction, Energy & Environmental Science, 8 (2015) 568.
[32] D.H. Deng, L. Yu, X.Q. Chen, G.X. Wang, L. Jin, X.L. Pan, J. Deng, G.Q. Sun, X.H. Bao, Iron Encapsulated within Pod-Like Carbon Nanotubes for Oxygen Reduction Reaction, Angewandte Chemie-International Edition, 52 (2013) 371.
[33] J. Liang, Y. Jiao, M. Jaroniec, S.Z. Qiao, Sulfur and Nitrogen Dual-Doped Mesoporous Graphene Electrocatalyst for Oxygen Reduction with Synergistically Enhanced Performance, Angewandte Chemie-International Edition, 51 (2012) 11496.
[34] S. Dutta, A. Bhaumik, K.C.W. Wu, Hierarchically Porous Carbon Derived from Polymers and Biomass: Effect of Interconnected Pores on Energy Applications, Energy & Environmental Science, 7 (2014) 3574.
[35] J. Lee, J. Kim, T. Hyeon, Recent Progress in the Synthesis of Porous Carbon Materials, Advanced Materials, 18 (2006) 2073.
[36] D.C. Wu, Z.H. Li, M.J. Zhong, T. Kowalewski, K. Matyjaszewski, Templated Synthesis of Nitrogen- Enriched Nanoporous Carbon Materials from Porogenic Organic Precursors Prepared by Atrp, Angewandte Chemie-International Edition, 53 (2014) 3957.

# Chapter 2 Literature Review

Over the past decade, continued development has been rapidly made in the synthesis of porous carbon nanoarchitectures ranging in pore sizes and structures. These porous carbon materials have wide applicability in various fields such as water remediation, gas or molecule separation, biomedicine, catalysis and energy conversion and storage. In this review, the most up to date strategies for structural control and functionalization of porous carbon are summarized, in terms of different porous structure, namely microporous, mesoporous, macroporous and hierarchically porous carbons with disordered or ordered, amorphous or graphitic structure. Although these porous carbons are not all designed for water remediation, the advanced properties of these materials provide promising design opportunities and make them potentially applicable in this area.

## 2.1 Introduction

Porous carbon materials have always drawn intensive scientific interests due to their outstanding properties such as large specific surface area (SSA) and pore volume, tuneable surface functionality and pore size distribution, endowing them with great potentials for various applications, including water purification processes,[1, 2] gas adsorption and separation,[3] active material loading,[4] energy conversion and storage,[5, 6] $CO_2$ electroreduction,[7] and so forth. Based on their average sizes, pores are classified into micropores if the internal diameter is less than 2 nm, mesopores if it is between 2 and 50 nm, and macropores if it is larger than 50 nm by the International Union of Pure and Applied Chemistry (IUPAC).

As illustrated in Chapter 1, our research will focus on developing novel functional carbons for water remediation by adsorption and AOPs. Therefore, a brief introduction will be first given on the requirement of water treatment, and then the various methods for synthesizing porous carbons will be elaborated and compared.

### *2.1.1 Water Treatment*

In recent years, there is growing concern over freshwater shortage and the presence of contaminants in waste water.[8] Reutilization of wastewater is increasingly being viewed

as the major long-term strategy for saving limited freshwater resources. In addition, it serves to safeguard the aquatic environment which is threatened by persistent contaminants in wastewater.[9] The presence of emerging organic contaminants is of particular concern regarding the health of both human and the environment. Pharmaceuticals, fuel additives, plasticisers, flame-retardants, and other domestic, industrial or agricultural organic pollutants have been detected in elevated concentrations in surface and ground water. Even at low concentrations (for example, in the range of ng $L^{-1}$), these persistent organic pollutants (POPs) could bring about adverse health and ecological impacts.[10] Extensive investigations have been conducted focusing on developing effective water treatment methods for efficient removal or degradation of existing pollutants. Among currently available techniques, direct adsorption is most facile to conduct while AOPs are most efficient in terms of complete degradation. It is important to understand how to improve the performance of porous carbon in adsorption and AOPs, so that a general strategy in designing these samples can be achieved. Specifically, adsorption and AOPs will mainly depend on the following attributes of porous carbons.

***Pore size distribution.*** SSA and porosity will directly affect the adsorption performance of porous carbon. More importantly, the accessibility of organic molecules toward the inner adsorbent surface that is related to pore size plays a critical role. Under the suitable experimental condition, micropores can be accessed by small molecules like phenol, while mesopores can be accessed by natural organic matter, and macropores can be accessed by large species such as bacteria. It is also suggested that pore sizes in a range close to the molecular size of the target pollutant determine the final adsorption capacity.[11] As a result, the suitability of given porous carbons in particular applications is determined by their present pore dimension ratios. For small molecular-weight organic contaminants, most of the adsorption tends to occur in micropores, contributed by the enhanced adsorption potential of pore walls and the diffusion through the micropores is the rate controlling step.[12] A well-defined meso- and macro- porosity is desired to fasten adsorption kinetics for larger molecules.

Practically, the performance of AOPs will also depend on the high SSA (to enable the exposure of active sites) and accessibility of compounds (organic pollutants or PMS/PS involved in AOPs) to the active sites on the carbon media (so suitable pore size range is required).

***Carbon surface chemistry.*** Despite that accessible high SSA and suitable porosity have been considered as important parameters defining the adsorption ability of porous carbons, it is increasingly realized that surface chemistry brought by heteroatoms (e.g. N, S, O) can also have a direct impact in the adsorptive behavior.[13] The surface functionalities of carbon can bond molecules by various forces. i) The adsorption could proceed by non-electrostatic physical forces of the van der Waals kind, π-π interaction and hydrogen bonding. For example, it is reported that the interaction between $sp^2$-C in carbon materials with delocalized π-bond of the target aromatic organic compounds is an important driving force for adsorption.[14, 15] ii) Adsorption could be driven by electrostatic interactions, which are of great importance for charged molecules. In this case, modifying chemical nature (e.g. acidity or charge) of activated carbon or the solvent will consequently affect the adsorbent-adsorbate interactions as well as the corresponding adsorptive properties.[14]

Suitable surface chemistry of porous carbon is also highly desired for efficient AOPs because pristine carbons were generally poor in catalysis, which can be improved by heteroatom (e.g. N, S, B, P) doping.[16, 17]. For instance, density functional theory (DFT) calculations indicate that when N is doped into carbon skeletons, charge transfer can be induced from C to adjacent N atoms, creating positively charged C that is capable of enhancing the catalytic capability of the carbon.[17-20] In some cases, N, S codoping shows better performance than solely atom doping because of a synergistic effect.[17, 21-23]

To sum up, rational and precise control over pore size, surface area, and surface chemistry is required to obtain excellent adsorbents and catalysts for efficient water remediation.

### *2.1.2 Synthetic Methods of Porous Carbon Materials*

There have been various approaches to synthesize porous carbon nanostructures, and Table 2.1 presents a comparison of some particular advantages and disadvantages of representative methods. These methods can be classified as hard-templating, soft-templating, and template-free routes such as chemical and physical activation, salt melt

synthesis. Apart from the difference in sizes, pores can be formed in various shapes, such as closed or open, cylindrical (featured by plane walls), or slit-shaped. Also, the whole porous structure can be an ordered or a disordered network with amorphous or graphitic walls according to the protocols. In principle, it is possible to design porous carbons with selected morphology, size, porosity, crystallinity, and chemical composition by utilizing, modifying or combining these methods.

**Table 2.1** A comparison of synthesis methods for porous carbon nanostructures.

| Methods | Basic steps | Advantages | Disadvantages | References |
|---|---|---|---|---|
| Hard-templating method | Preformed Templates+ Precursor filling and conversion+ Template removal | ▪ Easy to control and highly applicable<br>▪ Highly crystalline product<br>▪ High quality product<br>▪ Ordered structure | ▪ Multistep and time consuming<br>▪ High cost<br>▪ Corrosive for template removal | [7] [24] [25] [26] [27] [28] [29] [30] [31] [32] [33] [34] [35] |
| *In-situ* templating method | Phase separation + *In-situ* templates | ▪ Simple and easy to operate<br>▪ Low cost | ▪ Low quality<br>▪ Hard to acquire order structures | [36] [37] [38] [39] [40] |
| Soft-templating method | Co-assembly +Surfactants+ Template removal | ▪ Controllable structures and pore sizes<br>▪ High quality product<br>▪ Easily handled<br>▪ Scalable | ▪ Surfactant-directed<br>▪ Relatively low crystallinity<br>▪ Sensitive to the reaction conditions | [7, 41] [42] [43] [44] |
| Multiple-templating method | Multiple templates+ Precursor infiltration and conversion+ Template removal | ▪ Hierarchically porous structure | ▪ Requires multiple templates<br>▪ High cost<br>▪ Multiple steps and time consuming | [45] [46] [47] [48] [49] [50] |
| Self-templating method | Pyrolysis of zeolites, MOFs, cross-linked polymers, etc. | ▪ Unique and flexible structure<br>▪ Hierarchical pores structure with high-density active sites | ▪ Synthesis of MOF or zeolites requires high cost<br>▪ Multi-step | [51] [52] [53] [54] [55] [56] [57] [58] [37] [59] [60] [61] [62] [63] [64] [65] [66] [67] [68] |
| Activation | Using physical or chemical activating agents | ▪ Simple synthesis<br>▪ Hierarchically porous structure<br>▪ Scalable | ▪ Hard to acquire ordered nanostructures | [3] [69] [70] [71] [72] [73] [74] [75] [76] [77] [78] [79] [80] [81] [82] [83] [84] [85] [86] |
| Salt melt synthesis | Employs molten inorganic salts as the medium | ▪ Hierarchically porous structure<br>▪ Facile steps<br>▪ Scalable | ▪ Hard to acquire ordered nanostructures | [38] [39] [87] [88] |

**Hard-templating method.** Nanocasting, adopting hard templates is regarded as the most effective approach to create ordered porous structures. Many kinds of rigid structures can be adopted as hard templates including fibres, films, powders, silica, colloidal particles and biological materials. Typically, there are four steps in hard-templating route: 1) synthesize preformed hard templates and a precursor solution where the precursors are closely cross-linked; 2) fill or coat the hard templates with precursors. This can be completed by infiltrating the precursors in the voids of the porous hard templates, which leads to the final 3D porous structure (Figure 2.1a). In addition, if spherical solids are used as hard templates and soaked in the precursor solution, a coating process happens and results in hollow spheres ultimately (Figure 2.1b). Hard templates with various structures and morphologies result in different porous carbon structures. It is noted that the wetness of precursors on the template surface is highly important and there are several ways to fill or coat substrates into templates, including melt infusion, solvent evaporation impregnation, chemical vapor deposition, and the incipient wetness method;[46] 3) chemical or thermal treatments to transform the precursors into solid carbon phases; and 4) remove the sacrificial template by HF or NaOH etching.

Heteroatoms precursors can be introduced with hard templates, and thus porous carbon nanostructures with appropriate heteroatom doping can be fabricated and optimized after carbonation for enhanced properties in many applications such as water remediation, fuel cells, supercapacitor, and $CO_2$ capture.[6] Although the hard-templating method is universally applicable as the choice for acquiring negative replicas of various templates, it has its limitations due to the complex and tedious process, and the use of hazardous chemicals for template removal seems time-consuming and harmful to the environment.[5, 89]

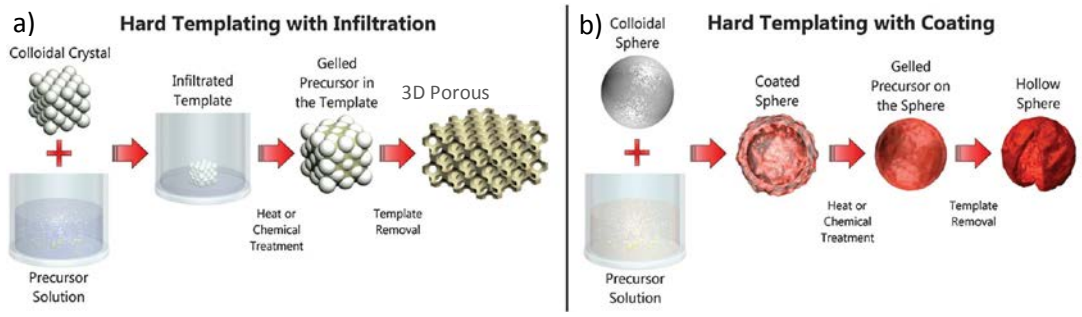


**Figure 2.1** Schemes detailing the hard-templating process. Left: An example of hard templating conducted using an infiltration process. Right: An example of hard templating

conducted via a coating process.[90] Copyright 2013, the Royal Society of Chemistry 2013.

***In-situ* templating method.** Instead of always being prepared beforehand, it is pointed that hard templates can be *in-situ* generated via phase separation (for example, ice crystals formed by freeze-drying) from chemical species in the precursor solutions during the chemical or thermal treatments,[90] as shown in Figure 2.2. For in situ templates, the infiltration and coating steps can be avoided. However, pores produced by these *in-situ* templates are usually irregular or randomly distributed. Therefore, rational control of the templates is required for preparing high-quality porous carbon materials.

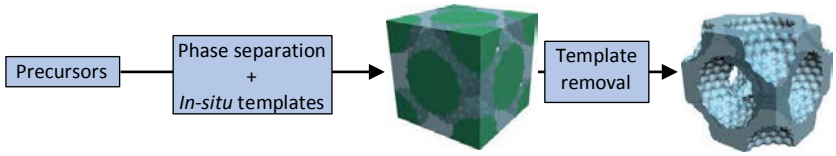


**Figure 2.2** The *in-situ*-templating methods for synthesizing porous materials.[5] Copyright 2016, Macmillan Publishers Limited.

**Soft-templating method.** Soft-templating strategy which was initiated by the pioneering works of the Dai group,[91, 92] Zhao group,[93, 94] and Nishiyama group,[95] does not involve the synthesis and removal of hard templates. The soft-templating route adopts thermally decomposable surfactants like amphiphilic block copolymers, which are co-assembled with carbon precursors and solvent molecules (such as water, ethanol) into cylindrical or spherical micelles at elevated concentration or temperature (Figure 2.3). Three major categories of anionic, cationic, and non-ionic surfactants can be utilized for soft-templating.[90] Typically, ionic surfactants generate micropore or small mesopores (2 ~ 4 nm), while non-ionics result in mesopores ranging in size from several to over 10 nm.[96] Ionic surfactants interact with precursors and solvent molecules mainly by electrostatic interactions, while the self-assembly with non-ionic surfactants proceeds primarily by van der Waals force and hydrogen bonding interactions. The assembly between surfactant molecules and guest species to develop micelles and/or a liquid crystalline phase is critical, which can be realised by a hydrothermal process, cooperative assembly, or evaporation-induced self-assembly (EISA) process.[97, 98] Among these assembly strategies, EISA provides a more versatile process for large-scale production.[43] Further chemical or thermal treatment helps remove the surfactant templates and residual

solvent and carbonize the material. Ordered mesostructured carbon materials with open networks, tailorable morphologies and surface properties can be thus produced.

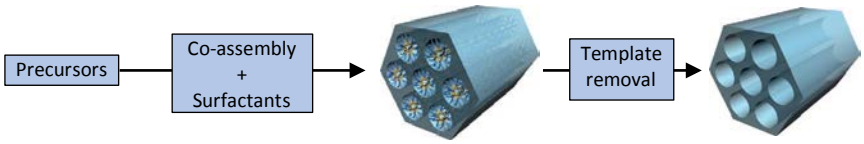


**Figure 2.3** The soft-templating methods for synthesizing porous materials.[5] Copyright 2016, Macmillan Publishers Limited.

**Multiple-templating method.** Combining hard- and soft-templating approaches can induce dramatic changes in the template mesostructure and generate structural hierarchy with the ordered network (Figure 2.4), which are particularly useful in some applications such as supercapacitors and batteries.

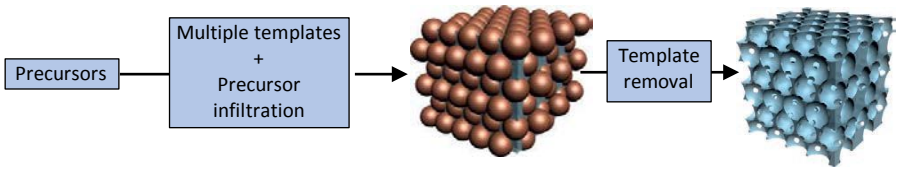


**Figure 2.4** The multiple-templating methods for synthesizing porous materials.[5] Copyright 2016, Macmillan Publishers Limited.

**Self-templating method.** This route typically utilizes the direct carbonization of porous materials such as zeolites, metal organic frameworks (MOFs), covalent organic frameworks (COFs) and porous organic polymers to prepare highly porous carbon. The intriguing structural features[99] of these porous solids permit their use in fabricating high-quality porous carbons. The pore structure and surface functionality of the final carbon can also be optimized by introducing additional sources of carbons or heteroatoms into the porous channels. The graphitic degree of porous-solid-derived carbon is closely related with the involved metal species and carbon precursors. Carbon materials, typically with abundant porosities, unique structural and compositional features in nanometer or micrometer scale can be created, bringing unique and improved properties that are unexpected in their counterparts obtained by conventional routes.[100]

**Activation method.** Activation methods include physical activation, chemical activation and a combination of them. Physical activation can be achieved by reactions with gaseous etchants like $CO_2$, $NH_3$ or $H_2O$.[70, 101, 102] During chemical activation, carbon precursors are impregnated with activating agents such as KOH, $ZnCl_2$, $Na_2CO_3$, $K_2CO_3$,

$NaHCO_3$, NaOH, $H_3PO_4$ and $H_2SO_4$.[103-106] It is considered as a well-established approach to synthesize highly porous carbon structures with super high specific surface areas (for instance, over 3000 $m^2 g^{-1}$). In addition, renewable, inexpensive biomass or bio-waste are highly preferred to be adopted as precursors for activation. The formation of porous structures can be realized after carbonization of the precursors first, followed by an activation process. It is also common to introduce activating agents into carbon precursors and make activation and carbonation happen simultaneously. Chemical activation has the merits of simple operation, high yield and cheap as well as flexible activating agents. Although porous carbon with a hierarchical structure and high SSA can be easily acquired by this method, it is hard to acquire ordered nanostructures by this method.

**Salt melt synthesis.** Salt melt synthesis (SMS) usually adopts different types of salts, and the operation temperature should be higher than the melting point of the salts. Molten salts may act as hard templates in the carbonization process. Some highly active molten salts may serve as activating agents to react with carbon framework and generate pores. This method has the advantages of easy isolation of the product as the salts are water soluble. Besides, many of the salts are not harmful and can be easily recycled.[107] Hierarchically porous carbon can be generated. However, similar to the activation method, pores generated from SMS are generally randomly distributed and disordered.

### *2.1.3 Main Content of This Review*

In this review, the most up to date strategies for structural control and functionalization of porous carbons are summarized, in terms of different porous structures, namely microporous, mesoporous, macroporous and hierarchically porous carbons with disordered or ordered, amorphous or graphitic structure, which will have a direct influence on the performance of adsorption and AOPs (as described in 2.1.1). The main methods for deriving favorable structural parameters in porous carbons are systematically summarized, and some outstanding examples in each type are selected and discussed in detail, since going over every accessed approach is beyond the scope of this work.

On the other hand, there are increasing evidence indicating that global warming (that mainly arises from $CO_2$ emission by fossil fuel combustion and geological activities) will

aggravate the situation of freshwater shortage in the future, as more frequent and serious droughts will be expected across many areas of the world. Impressively, efficient $CO_2$ capture and storage technique can mitigate the impact of global warming, while deploying clean energy resources (e.g. $H_2$) will also help in reducing $CO_2$ emission. In this regard, although this review focus on the controllable synthesis of porous carbon, their multifunctional applications are also included where appropriate in $CO_2$ uptake and energy conversion and storage technologies related with batteries, oxygen reduction reaction (ORR), hydrogen evolution reaction (HER), oxygen evolution reaction (OER), $CO_2$ electroreduction, and supercapacitors. These applications will help alleviate water shortage indirectly. In many cases, the activities of porous carbons in different applications are potentially related. The outlined advanced properties of these materials will provide various perspectives and promising opportunities to design adsorbents and catalysts in water treatment.

## 2.2 Microporous Carbon Nanostructures

### *2.2.1 Disordered Microporous Carbons*

Microporous carbons, also known as molecular sieving carbons, have been used in various fields including organic adsorption, gas separation, supercapacitor electrodes, and batteries. Representative synthesis approaches for microporous carbons include, but not limited to pyrolysis of porous solid precursors and chemical activation.

The microporous structure can generally be retained in the derived carbon from pyrolysis of porous solids (for example, porous cross-linked polymers). Recently, microporous polymer networks have been discovered as precursors to generate microporous carbons. For instance, Wang et al.[108] described the design of conjugated microporous polycarbazole networks by oxidation with $FeCl_3$ in nitromethane/chloroform mixtures, which acted as novel carbon precursors. By a direct pyrolysis method, the derived N-doped microcarbons exhibited a large surface area (1280 $m^2\ g^{-1}$), with a large micropore volume (1.64 $cm^3\ g^{-1}$) and ultramicropore sizes in the range of 0.7 - 1 nm. These carbons displayed reversible and efficient $CO_2$ uptake (can store 20.4 wt.% at 1 bar, 273 K), and a high electrochemical capacity (558 F $g^{-1}$ in 6 M KOH) with a fast charge/discharge rate and excellent cycle stability. Besides, rational design of hollow microporous carbon

spheres was reported,[109] in which pyrrole-aniline copolymer and Triton X-100 were selected as the carbon source and soft template, respectively. Ammonium persulfate (APS) was also added to promote oxidative polymerization of the precursors. As a result, abundant micropores (1 - 2 nm in diameters) were generated after carbonization removal of Triton X-100 tails. Hollow core formed due to the difference in hydrophobicity between pyrrole and aniline monomers. It was described that an onion-like microporous carbon could be prepared by direct carbonization of the diamond-like porous aromatic framework (PAN-1)[61] that possessed a high surface area of 3800 $m^2$ $g^{-1}$ and microporous texture with pore size centred at 1.26 nm.[110] The derived carbon sample showed a curved graphitic structure with a specific surface area of 1084 $m^2$ $g^{-1}$ and micropores peaked at 0.5 and 1.2 - 1.3 nm, demonstrating an excellent performance when it was used as an electrode material for supercapacitors.

Zeolites with a uniform pore wall thickness generally < 1 nm have been employed as inorganic templates to generate microporous carbons. For instance, pyrolysis of ZIF-8 filled with furfuryl alcohol (as a second carbon source) generated microporous carbon (90 - 95% microporosity) after template etching.[66] Besides, direct carbonization of ZIF-8 (a framework by coordination of $Zn^{2+}$ with 2-methylimidazolate) can produce microporous carbon. N-doped microporous carbon with a specific surface area of 1135.1 $m^2$ $g^{-1}$ and narrow pore sizes (< 1 nm) centring at about 0.5 nm was reported, by direct pyrolysis of ZIF-8.[56] Carbonization temperature and heating rate have significant effects on the textural properties of the samples, and as a result, some mesopores were sometimes produced. In another study,[67] ZIF-8 derived carbons showed a narrow pore size distribution peaked at 1.1 nm, accompanied by some mesopores (with sizes of 2.0 - 3.0 nm). The micropores contributed up to 89% of the total surface area.

Gong et al.[60] described the preparation of N-doped microporous carbon fibres where N was only deposited on the surface of microporous carbon fibres, utilizing a poly(ionic liquid) for N coating and mild activation for micropores via a self-templating mechanism.[111] The optimum sample delivered a surface area of 1476.3 $m^2$ $g^{-1}$ and pore volume of 0.58 $cm^3$ $g^{-1}$ with a pore size ranging from 0.6 to 2.2 nm, indicating the dominance of micropores. A carbon/carbon heterojunction was produced in the as-prepared sample, which favours the interaction of carbon fibre with $CO_2$ promoted by

electronic effects. A super high $CO_2$ adsorption capacity (6.9 mmol $g^{-1}$) at 273 K and 1 bar with an excellent $CO_2/N_2$ selectivity of 44 were observed on the final sample.

Although KOH activation is widely used to prepare activated carbon, hierarchically porous structures with both micro- and meso- porosities were obtained in most cases.[73-75] In fact, the porous nature of final activated carbon is closely related with the type of carbon sources. For instance, Blankenship et al. presented cellulose acetate-derived oxygen-rich microporous carbons by KOH activation.[79] A hydrothermal treatment was conducted on cellulose acetate first, followed by KOH activation in flowing $N_2$. The derived carbon exhibited a high surface area (3800 $m^2$ $g^{-1}$) and a large pore volume (1.8 $cm^3$ $g^{-1}$) that were mainly contributed (> 90%) by micropores. The micropores were composed of ultramicropores (0.6 - 0.7 nm), small micropores (0.85 nm) and certain medium-sized micropores centred at 1.2 nm, endowing them with exceptional hydrogen ($H_2$) storage capacities. The carbons stored up to 1.2 wt% (total) and 0.8 wt% (excess) $H_2$ at 30 bar and room temperature. Similarly, in Ref.[80], layered microporous carbons were synthesized from coal tar and melamine by in-situ KOH activation. The final carbon sample exhibited a specific surface area up to 1865 $m^2$ $g^{-1}$ with most of the pore diameters below 2 nm. The abundance of pores in size range of 0.6 - 1 nm contributed drastically to the high specific capacitance in supercapacitor test. Balahmar et al. discovered that the mechanochemical treatment of KOH and hydrochar biomass prior to thermal treatment enhanced the activation effect.[3] By decreasing the voids and maximizing the interactions between carbon source and KOH after compressing treatment, enhanced surface areas and pore volumes were obtained on the activated carbons. The final carbon possessed enhanced porosity dominated by ultramicropores (0.58 - 0.65 nm), resulting in a drastic increase for $CO_2$ capture capacity at low pressures (up to 5.8 mmol $g^{-1}$ at 25 °C and 1 bar). Zhou et al. proposed that the difference in metal species of alkali salts (MOH, M ion varied from $Li^+$, $Na^+$, $K^+$, $Rb^+$ to $Cs^+$) would result in adjustable ultramicropore diameters.[81] The ultramicropore diameters could be subtly adjusted in the range of 0.60 - 0.76 nm due to the various alkali ion sizes and different activating strength.

### *2.2.2 Microporous Carbons with Ordered Graphitic Walls*

Due to possibly combining the unique features of graphene with a porous structure, 3D graphene structure with regular nanopores has attracted great research interests.[112] Note

that large surface areas, unique pore channels and excellent electronic conductivity can be achieved in such structures. To prepare microporous carbons not only with uniform pore arrays but also with graphitic pore walls, rigid inorganic templates such as zeolites are generally used. Zeolites are crystalline microporous aluminosilicate materials with well-defined pore networks and a wall thickness of less than 1 nm.[33] Since nanocasting of zeolites was presented by Kyotani and coworkers,[113] various well-defined 3D ordered graphitic channels have been duplicated into microporous carbon materials. Chemical vapor deposition (CVD) is widely used for zeolite nanocasting, through which carbon atoms can be introduced and deposited along the walls of the microporous zeolite channels.

Recently, Ryoo group studied in detail for the synthesis of microporous graphene-like carbons by carbonization of ethylene or acetylene gas in zeolite templates at 600 °C, followed by a further thermal treatment at 850 °C and template etching.[34] It was discovered that lanthanum (La) ions laid in zeolite pores could bring down the carbonization temperature and increase the deposition rate of ethylene or acetylene gas, permitting carbon deposition inside the zeolite template with pore diameters less than 1 nm. This catalysis also applies to yttrium (Y) and calcium (Ca). As such, well-ordered carbon can be reproduced, corresponding to various zeolite pore sizes and morphologies. Attributed to this effect, a microporous structure with high thermal stability can be derived, and the graphene-like structure was verified by selected-area electron-diffraction (SAED) pattern showing graphene (100) and (110) reflections (Figure 2.5). In essence, the graphene-like structure is built by hexagonal atomic C rings deposited along curved zeolite pore walls, and the degree of imperfections depends on the synthesis parameters. The LaY-templated graphene-like microporous carbon displayed a two-order-higher electrical conductivity than amorphous mesoporous carbon.

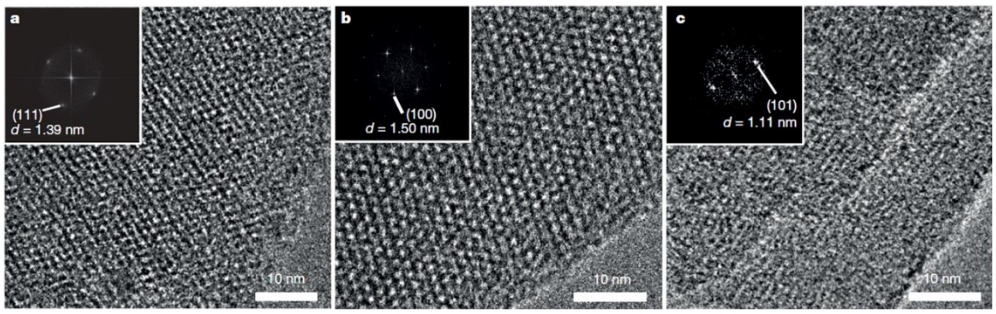


**Figure 2.5** Structures of 3D graphene-like microporous carbons. a-c) Transmission electron microscopy (TEM) images and Fourier diffractograms (insets) of carbon

generated using a template of $La^{3+}$-ion-exchanged zeolites.[34] Copyright 2016, Macmillan Publishers Limited.

Following this work, Sazama et al. reported 3D microporous graphene-like carbons (denoted as β- and Y-carbon) by nanocasting of beta (*BEA) and faujasite (FAU) zeolite templates, with propylene as a carbon source for CVD.[33] Resembling the ordered channels of the zeolites, single-atom graphene layers assembled a 3D porous system with similar specific surface areas of 2454 and 2443 $m^2\ g^{-1}$ for β- and Y-carbon. Y-carbon replicated the channel system of zeolite to a high level with a total pore volume of 1.35 $cm^3\ g^{-1}$, predominantly arising from micropores (1.25 $cm^3\ g^{-1}$). By contrast, considerable mesopores generated in β-carbon, which might result from the sectional collapse of carbon framework. The resulting β- and Y-carbon served as effective catalysts for the hydrogenation of alkenes, and cycloalkenes, accompanied by intramolecular catalytic realignment. Similarly, Kovalenko and coworkers synthesized a highly graphitic microporous carbon utilizing the $Na^+$-exchanged zeolite Y (zeolite NaY) as templates and furfuryl alcohol and propylene as carbon sources by CVD method.[57] The product was further heat treated at 900 °C and freed by HF etching. According to previous research, the thermal treatment after the CVD process boosts a long-range ordering arrangement of carbon inside the zeolite.[114] It is noted that a high specific surface area and pore-to-pore regularity can be achieved by optimizing CVD time to reduce carbon deposition on the external surface of zeolite and maximize carbon deposition inside the template. The optimum sample delivered an ordered porous structure with a micropore volume of 1.40 mL $g^{-1}$, SSA of > 3500 $m^2\ g^{-1}$ and uniform pore sizes of around 1.2 nm. The ordered structure which corresponds to graphitic carbon was confirmed by X-ray powder diffraction (XRD) tests. When used as a cathode for ionic liquid based aluminum batteries (ABs), the derived microporous carbon exhibited high volumetric (30 Wh $L^{-1}$) as well as gravimetric energy storage capacities (up to 64 Wh $kg^{-1}$).

Apart from zeolites, microporous graphitic carbon can be derived using mesoporous silica spheres as the templates and precursors.[32] Cetylpyridinium bromide aligned inside the mesopores of silica template acted as the only carbon source, which resulted in N-doped microporous carbon nanospheres with graphitic nature and uniform pore sizes of 0.62 - 0.72 nm after carbonization and silica removal (Figure 2.6).

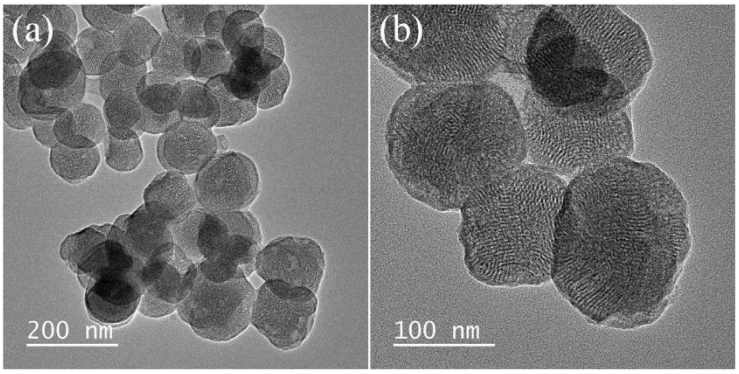


**Figure 2.6** TEM images of different magnifications.[32] Copyright 2015, Elsevier Ltd.

## 2.3 Mesoporous Carbon Nanostructures

Over the last few decades, tremendous progress has been made in developing advanced mesoporous carbons, which are appealing materials in many important applications including adsorption for large molecules, energy conversion and storage devices, catalyst supports, sensors, and biomedicine.

### *2.3.1 Mesoporous Carbons with Irregular Porous Structure*

Mesoporous carbon can be fabricated by an in-situ templating method with the assistance of freeze-drying.[36] Briefly, the mesoporous expanded gel of alginic acid was first prepared, followed by freeze drying for solvent removal and subsequent pyrolysis at 800 °C. The key step to obtain mesoporous structure was the addition of tert-butyl alcohol and water to obtain eutectic mixture during gelatinization before freeze drying. Heating rate in the pyrolysis process played a vital role in determining the final mesopore volume. The derived mesoporous carbon was used as carbon additives to improve the conductivity of $Li_4Ti_5O_{12}$ nanoparticles, and the mesopores provide channels for the electrolyte to access the active material, leading to high performances as the negative Li-ion battery electrode.

$ZnCl_2$ is an excellent activating agent to produce mesopores and $Zn^{2+}$ is normally reduced to Zn by C during pyrolysis. Zn can either be removed by etching or by volatilization at higher temperatures. Singh et al. reported a single-step activation of biomass arundo donax by solid $ZnCl_2$ to synthesize mesoporous biocarbons.[69] The micro and mesoporous structure can be simply adjusted via tuning $ZnCl_2$ to biomass ratio while the

mesoporosity increased dramatically with a higher $ZnCl_2$ amount. Under the optimized carbonization temperature (500 °C) and precursor configuration, almost 100% mesoporosity with pore width centering at 3.5 nm can be developed, accompanied by a super high SSA of 3298 $m^2 g^{-1}$ and a large pore volume of 1.9 $cm^3 g^{-1}$. In addition, $ZnCl_2$ can be combined with hard templates ($SiO_2$, nanocellulose fillers, or filter pap) to produce mesoporous carbons.[47] Polyacrylonitrile (PAN) is an ideal precursor for carbon materials as it delivers a high N content and has a high degree of graphitization. However, PAN is relatively insoluble, which limits its application in hard templating approaches where filtration of dissolved precursors is needed. Matyjaszewski and coworkers synthesized N-doped porous carbons by pyrolysis of $ZnCl_2/SiO_2$/PAN, revealing that $ZnCl_2$ can not only act as a porogen but also promote the cosolubilization of PAN within $SiO_2$ suspension since $Zn^{2+}$ as a divalent cation can serve as an ionic cross-linker for PAN.[47] Under the synergistic effect of $ZnCl_2$ activation (that produced mesopores centred at 2.3 nm) and $SiO_2$ templating (that generated mesopores peaked at 10.2 and 12.5 nm), a high mesopore volume was produced that accounted for 84 - 90% of the total surface area (up to 1776 $m^2 g^{-1}$).

MOF materials with a high density of Zn cations can be used as self-templates to produce mesoporous carbon. For instance, N-doped hierarchically mesoporous carbon structure with a bimodal pore size distribution was obtained by the pyrolysis of nonporous $[Zn_2(TPT)(BDC)_2]\cdot H_2O$ (SCUT-11).[51] Also, N-doped mesoporous carbon was prepared from pyrolyzing the mixture of oxygen-abundant Zn-MOF-74 and melamine.[52] Compared to previously low-oxygen-containing MOF-derived nanocarbons, adopting Zn-MOF-74 as a precursor and template possessed its superiority in producing larger mesopores. This can be attributed to the high oxygen content in Zn-MOF-74, which would boost the release of gaseous products ($H_2O$ and $CO_2$) during calcination, creating mesopores with large pore sizes (9.3 - 12.7 nm). Suitable N-doping and large mesopores made the derived carbon nanomaterial a high-performance ORR electrocatalyst that is comparable to or better than Pt/C in pH-universal media. It is noted that mesoporous carbons with large pore sizes (> 10 nm) are acquisitive in particular fields. They can ensure a fast mass transport in catalysis and serve as excellent supports for metallic nanoparticles or large-sized guest molecules (protein, gene, dye and RNA). To meet these demands, Wei et al. summarized the tailored synthesis of large-pore ordered mesoporous materials via the soft-templating method in detail.[43]

*2.3.2 Ordered Mesoporous Carbons*

Ordered meso-structure can be well-formed by soft-templates like Pluronic F127 and hard-templates like mesoporous silica materials. The dimension and porous structure of the mesoporous silica materials could be readily controlled by adjusting the experimental parameters, such as the chain length of surfactants, and the ratio of surfactants to the silica precursor. Hexagonally ordered mesoporous silica SBA-15 is widely used as hard templates to prepare ordered mesoporous carbons.

Since the development of the organic-organic self-assembly strategy, it is generally restricted to the wet processing. For instance, F127 was self-assembled with carbon precursors (o-aminophenol and hexamine) in aqueous solution by evaporation-induced self-assembly (EISA) process. Followed by a one-step pyrolysis process, N-doped carbon spheres can be prepared, with ordered mesopores centering at about 5.0 nm that were created by the thermal removal of F127.[41] Different from the wet processing, Zhang et al.[42] reported a solid-state mechanochemical assembly route without any solvents. Using a vibrating ball miller, biomss-derived tannin were ground together with F127 and transition metal acetates, forming a cross-linked network in a homogeneous gel-like mixture. Both F127 and metal salts are important for the successful self-assembly. This route has several advantages. The mechanochemical process proceeds in solid condition, enabling the assembly time shorter than that in the solution route. In addition, the solid-state assembly allows for using insoluble precursors, especially inexpensive biomasses to replace toxic organic precursors, making the method more versatile. Solvent waste can be avoided, making the process more environmentally friendly. Uniform, ordered and adjustable mesopores (4 - 10 nm) with cylindrical structures were created in the final carbons after carbonization. Nickel nanoparticles (5.4 nm) could be introduced, confined and dispersed to the cylindrical carbon nanochannels, which exhibited good thermal stability and exceptional performance in the selective hydrogenation of bulky molecules (2 nm).

As described before, heteroatoms play a vital role in modifying the properties of pristine carbon. Qiang et al. presented an example of incorporating high concentrations of various heteroatoms (up to 26 at.% N, 15 at.% B, 7 at.% P, or 4 at.% S) into an ordered mesoporous

carbon.[45] A combined soft-hard templating method was adopted using cross-linked mesoporous resol-silica as the starting material, followed by melt infiltration of suitable dopants and subsequent carbonation process. Pluronic F127 served as the soft-template for ordered mesopores, while silica nanoparticles transformed from tetraethyl orthosilicate (TEOS) can reinforce the nanostructure to prevent the collapse or distortion of the ordered mesostructure during pyrolysis.

The difference in the morphologies of templates results in pores of various shapes. Interestingly, Song et al. suggested that pore channel configuration has an impact on the catalytic behavior of mesoporous carbon.[7] N-doped mesoporous carbon (c-NC) was synthesized using self-assembled resol (the carbon source), dicyandiamide (the nitrogen source) and F127. Ordered cylindrical pore channels with pore diameter centering at 5.1 nm were produced in c-NC (a1, a2 in Figure 2.7B). For comparison, N-doped carbon with an inverse mesoporous morphology (i-NC, as described by the models in Figure 2.7A) was fabricated using SBA-15 as the hard template and quinoline-polymerized pitch as the precursor. i-NC possessed similar pore parameters (b1, b2 in Figure 2.7B) with c-NC, with pore width peaked at 3.3 nm after template removal. As described in Figure 2.7A, c-NC and i-NC with different structure configurations displayed various electrocatalytic activities in $CO_2$ electroreduction. c-NC with cylindrical channel structures containing pyridinic/pyrrolic N sites exhibited its superiority in selectively facilitating CO* dimerization and ethanol generation.

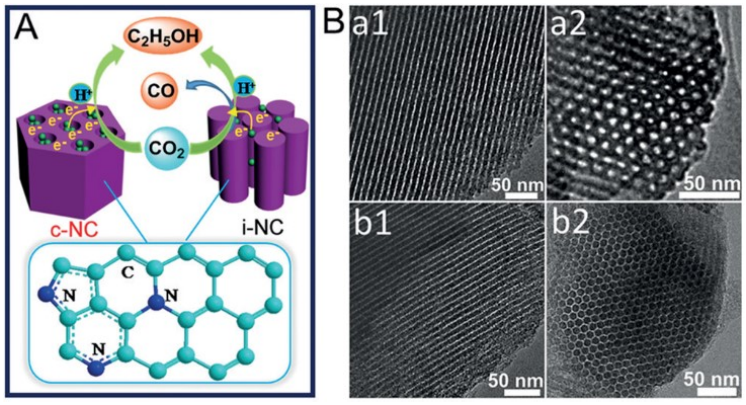


**Figure 2.7** A) Illustration of c-NC and i-NC for $CO_2$ electroreduction. B) TEM images of (a1, a2) c-NC and (b1, b2) i-NC viewed along (a1, b1) [110] and (a2, b2) [100] directions.[7] Copyright 2017, Wiley-VCH Verlag GmbH & Co.

*2.3.3 Mesoporous Carbons with Graphitic Pore Walls*

As illustrated before, the interaction between $sp^2$-C and delocalized π-bond of aromatic organic compounds is one kind of driving force for adsorption.[14, 15] On account of this, a high-surface area mesoporous carbon with a higher graphitic degree might be beneficial to achieve enhanced adsorption capability. This high level of graphitization in mesoporous carbon products also makes them attractive for some electrochemical applications due to its stability and excellent electrical conductivity. Actually, the graphitic degree of the derived carbon is closely related with the involved transition metal species and carbon precursors.

Knossalla et al. provided a detailed description of the synthesis of mesoporous graphitic hollow spheres.[46] These mesoporous graphitic spheres were prepared in a combination of various templating strategies and heat treatment. Basically, using the soft-templating method, porous core-shell silica template was prepared and acted as a scaffold for the following nanocasting. Divinylbenzene as the carbon source and iron as the graphitization catalyst were penetrated into the pores of silicas. During the carbonization, iron catalyzed the formation of graphitic domains in the final samples. After removing silica and iron, graphitic porous hollow spheres were finally received (Figure 2.8). The graphitization can be verified via XRD and TEM. Without a transition metal catalyst, disordered amorphous carbon will be formed in the resulting hollow spheres.

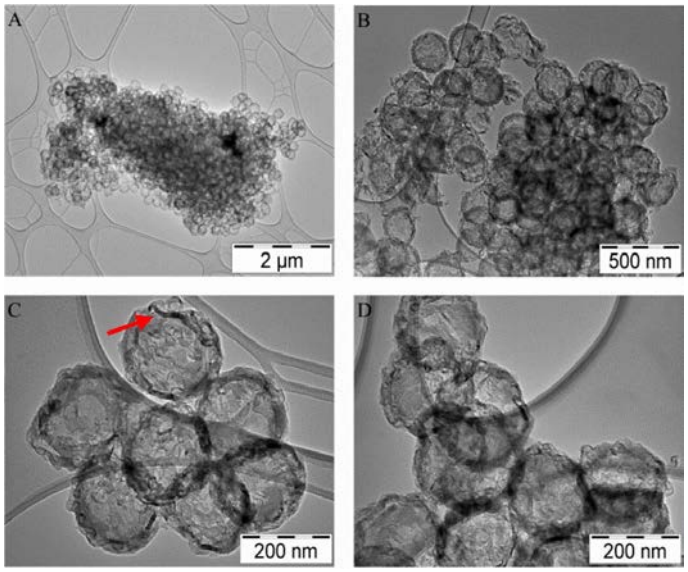


**Figure 2.8** Collection of micrographs with of the HGS (red arrows pointing at the characteristic features of the graphitic domains, which can be detected by TEM).[46] Copyright 2017, American Chemical Society.

Benzigar et al. proposed a new method to prepare mesoporous structure with crystalline $C_{60}$ walls, by using mesoporous silica SBA-15 as the inorganic template, and 1-chloronaphthalene as the solvent wherein $C_{60}$ is highly solubilized and can fill in the pores of SBA-15.[24] It is known that the poor solubility of $C_{60}$ in most solvents makes it difficult to create ordered pores by nanocasting since it is hard for $C_{60}$ to fill in the voids of the inorganic templates. Remarkably, this solvent promotes the formation of crystalline fullerene framework by boosting the polymerization via cross-linking of $C_{60}$. After carbonization and etching the silica template, the derived $C_{60}$ exhibits well-ordered, and rod-shaped mesoporous structure with crystalline $C_{60}$ walls.

## 2.4 Macroporous Carbon Nanostructures

Macroporous carbon materials can be prepared by templating and template-assisted freeze drying methods. Submicrometer-sized spherical polymers or silica particles have been employed as templates to prepare macroporous carbon materials. By tuning the particle diameter of the spherical particles, the pore size of the resultant macroporous carbon materials could be adjusted accordingly.

Gueon et al. synthesized macroporous carbon spheres using polymer spheres (PS with an even diameter of 700 nm) as the soft templates.[44] In brief, PS and carbon nanotubes (CNTs) were dispersed in deionized (DI) water to form a suspension, which was sprayed at 140 °C using a spray dryer. Followed by a heat-treatment of the mixture at 500 °C under the inert condition, the PS template was removed, and macropores in hundreds of nanometers were produced. It was also reported that using 100 nm-sized polystyrene nanobeads as a template and polyvinylpyrrolidone as a carbon source, macroporous carbon microspheres (with macropore size of 50 - 90 nm) were achieved by one-pot spray pyrolysis.[26] Yin et al. reported a unique technique by combining electrospinning with a hard templating method.[25] Briefly, silica spheres were dispersed into a polymer shell of polyacrylonitrile in dimethylformamide (DMF) solution. Then, the as-prepared solution was electrospun to generate precursor textile, followed by pre-oxidation, carbonization and de-templating using hydrofluoric acid. Hollow carbon fibers composed of macroscopic carbon spheres (180 nm in diameter) were thus achieved.

In addition, 3D macroporous carbon materials can be obtained using a salt melt method combined with freeze-drying. As reported, interconnected 3D macroporous architecture composed of cubic NaCl crystals surrounded by $C_6H_8O_7$–$SnCl_2$–$NH_2$-$CSNH_2$ complexes were prepared, assisted by a freeze-drying process. After carbonation and removal of NaCl template, macropores of 1 - 3 μm are produced.[38] Wang et al. also reported the synthesis of macroporous carbon using NaCl and freeze-drying, which formed Fe/polyvinylpyrrolidone-enclosed NaCl crystallites.[39] The melting point of NaCl is around 800 °C. Carbonization of the precursors below 800 °C produces macropores after removing NaCl templates. If the temperature is higher than 800 °C, the melting of NaCl crystallites can create mesopores.

Macroporous carbons can also be derived from direct pyrolysis of some biomass materials. For instance, interconnected macroporous carbon tube structure was synthesized by freeze drying and followed carbonization of eggplant under $N_2$.[37]

Xu et al. demonstrated the formation of few-layer ordered macroporous carbons using multiple templates.[48] In brief, harnessing polymethylmethacrylate (PMMA) microspheres with a diameter of 220 nm, a self-assembled organic cubic-opal template was prepared. This template was then filled by nickel nitrate (for graphene formation catalysis), F-127 (a surfactant), $Al(NO_3)_3$•$9H_2O$ (provide cations for gelation), dicyandiamide (a nitrogen source) and ethyl silicate (TEOS, the source of silicon) to form a multiple organic-inorganic template, followed by a gelation process. The organic template was decomposed by a calcination course up to 1000 ºC, followed by a CVD process under a gas flow of $CH_4$ at 1000 ºC and N doping could be realized by adding an $NH_3$ flow during the CVD. The inorganic substance was removed by acid etching finally. By adjusting TEOS amount, the macropore shapes evolved from circular, square to honeycomb network structures (Figure 2.9). Ordered macropores of about 170 nm were obtained with few-layer graphene pore walls formed by Ni catalysis. The ordered macroporous carbon has a large accessible surface area to the electrolyte, which plays a critical role for capacitor performance at high current densities. To elevate the specific surface area of macroporous carbon, micro- and meso- pores can be integrated to ordered macropore walls.

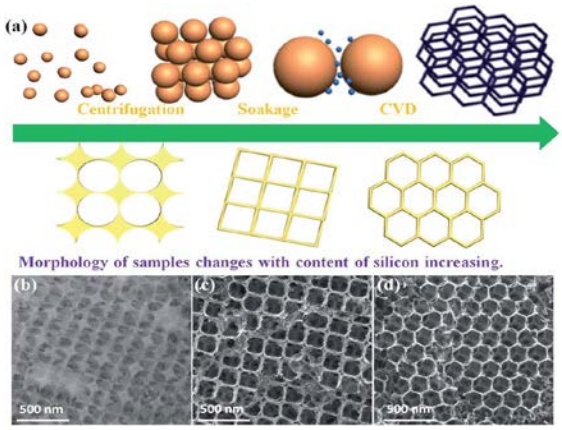


**Figure 2.9** (a) Schematic diagram of the preparation of few-layer ordered macroporous carbon. (b-d) Scanning electron microscopy (SEM) images of the samples. (b) Ordered circular network structure of FOMC-0, (c) ordered square network structure of FOMC-1 and (d) ordered honeycomb network structure of the FOMC-2 sample.[48] Copyright 2017, The Royal Society of Chemistry.

## 2.5 Hierarchically Porous Carbon Nanostructures

3D hierarchical porous carbon materials contain pores of different scales from micro-, meso- to macro-pores, which are of critical importance to gain optimal performance and properties in versatile applications. This is because such porous nanostructures integrate high SSAs with unique functionalities and appropriate channels, allowing for fast diffusion and better contact of any substances (e.g. liquid organic or gas adsorbates, electrolytes etc.) to the entire surface.[115] High microporosity ensuring a high SSA can provide the exposure of abundant active sites while rich meso/macropores are favorable for substance transport. This is expected in various applications such as pollutant adsorption in wastewater, catalytic POP degradation in AOPs, gas capture, ORR and supercapacitors.[76]

### *2.5.1 MOF-Derived Porous Carbons*

Over the past decades, MOFs (including ZIFs) as typical inorganic-organic crystalline hybrids coordinated with metal ions, have emerged as interesting self-templates and carbon precursors to create functional nanoporous carbons.[64, 116] In a general process, MOFs are pyrolyzed in an inert atmosphere, followed by acid-etching (this step can be avoided if the metal species are vaporized).[53, 117] Extra precursors (for example,

polyvinyl pyrrolidone or furfuryl alcohol) might also be incorporated to the pore channels in MOF or ZIF thereby optimizing the structure and functionality of resulting carbon.[58, 118, 119] The moderate thermal stability of MOFs makes it possible to obtain derived structures in a tuneable manner. Typically, highly porous and/or hollow/or framework-like carbons with high surface areas can be acquired due to the high porosity of MOFs, template removal and pyrolysis of organic moieties create abundant cavities. For instance, the specific surface area of the resultant carbon from nanocasting of ZIF-8 with furfuryl alcohol can reach a super high value (3405 $m^2 g^{-1}$), which showed excellent hydrogen sorption capacities.[119] In addition, Yang et al.[53] prepared hierarchically porous carbons by a facile heat adjustment of highly crystalline MOFs without any other carbon source. The MOF-derived carbon materials exhibited an exceptional porosity with a high ultramicroporosity (< 0.8 nm, up to 0.63 $cm^3 g^{-1}$), large surface area (up to 3174 $m^2 g^{-1}$), and super high total pore volume (up to 4 $cm^3 g^{-1}$), which synergistically contributed to the unique $H_2$ storage capacities at low and high pressures.

The diversities in structures, morphologies and properties of parental MOFs, together with the different conversion methods, determine the qualities of the resulting porous carbon materials. Unique morphologies and structures can be obtained in the final functional carbon in the micrometer/nanometer scale, which has been a key incentive for developing MOF-based synthetic strategies. Recently, it was indicated that direct carbonization of a rod-like MOF precursor (MOF-74-Rod) created carbon nanorods, which were transformed into graphene nanoribbons by a subsequent KOH treatment (Figure 2.10A).[64] The derived carbon nanorods and graphene nanoribbons exhibited surface areas of 1559 and 1492 $m^2 g^{-1}$, respectively. The graphene nanoribbons (electrical conductivity = 4.93 S $cm^{-1}$) delivered a better conductivity and electrochemical capacitive properties than the nanorods (electrical conductivity = 3.47 S $cm^{-1}$).

The graphitic degree of carbon is closely related with the metal species in MOF precursors.[65, 120] Yamauchi and coworkers presented hybrid particles with an N-doped amorphous C core and a highly graphitic C shell, by thermal treatment (at 800 °C) of core-shell ZIF-8@ZIF-67 particles that were constructed by two isostructural MOFs (Figure 2.10B, C).[65] This work verified the simultaneous generation of graphitic carbon with the catalytic assistance of transition metals (Co contained in ZIF-67) and N-doping from N-containing imidazole linkers (ZIF-8). The hybrid carbon materials exhibited a well-

developed hierarchically structure with interconnected micro/mesopores and surface area up to 1276 $m^2$ $g^{-1}$. Electrochemical tests suggested that the unique nanoarchitecture integrated the advanced properties of both carbon forms, with specific capacitance up to 270 F $g^{-1}$ obtained at 2 A $g^{-1}$ as supercapacitors electrode in a three-electrode system.

Similarly, Liu et al.[55] described double-shelled nanocages (Figure 2.10D) with inner shells of N-doped microporous carbon and outer shells of Co-N-doped graphitic carbon as a bifunctional electrocatalyst for ORR and OER. There were inner cavities within the carbon shells. The nanocages were synthesized by the controlled pyrolysis of core-shell metal-organic framework, which consisted of core-shell ZIF-8 (with Zn coordination) @ZIF-67 (with Co coordination) particles. The ZIF-8-derived inner amorphous shells were generated by the decomposition of ZIF-8 to ZnO/carbon composite and subsequent reduction and vaporization of Zn with the temperature rise. The ZIF-67-obtained outer shells possessed relatively loose graphitic carbon embedded with short carbon nanotubes (CNTs) formed by the catalytic effect of Co.

Liu et al.[54] reported the synthesis of uniform hollow carbon nanocubes (HMCNCs) with inner mesoporous walls and outer microporous shells by pyrolysis of silica-coated ZIF-8 nanocubes. Interestingly, the different thicknesses of coated mesoporous $SiO_2$ on ZIF-8 resulted in different structures. In brief, direct pyrolysis of ZIF-8 nanocubes generated dominant microporous carbon. Carbonization of ZIF-8 with a thick $SiO_2$ layer produced HMCNCs with a hollow cavity after silica removal, while a thin layer of $SiO_2$ on ZIF-8 resulted in mesoporous carbon nanotubes (SMCNCs) with concave faces and no hollow cavity (Figure 2.10E). The SSAs and pore volumes of HMCNCs and SMCNCs were tested to be 1085 $m^2$ $g^{-1}$ and 3.77 $cm^3$ $g^{-1}$, 1141 $m^2$ $g^{-1}$ and 1.92 $cm^3$ $g^{-1}$, respectively. The pore size of HMCNCs peaked at 24.6 nm, while a broader pore size distribution centring at 12.5 nm was observed for SMCNCs. The unique structure of HMCNCs endowed it with better properties than SMCNCs to accommodate selenium sulfide ($SeS_2$) guests, showing an outstanding rate capability and excellent cyclic stability in Li-ion battery applications.

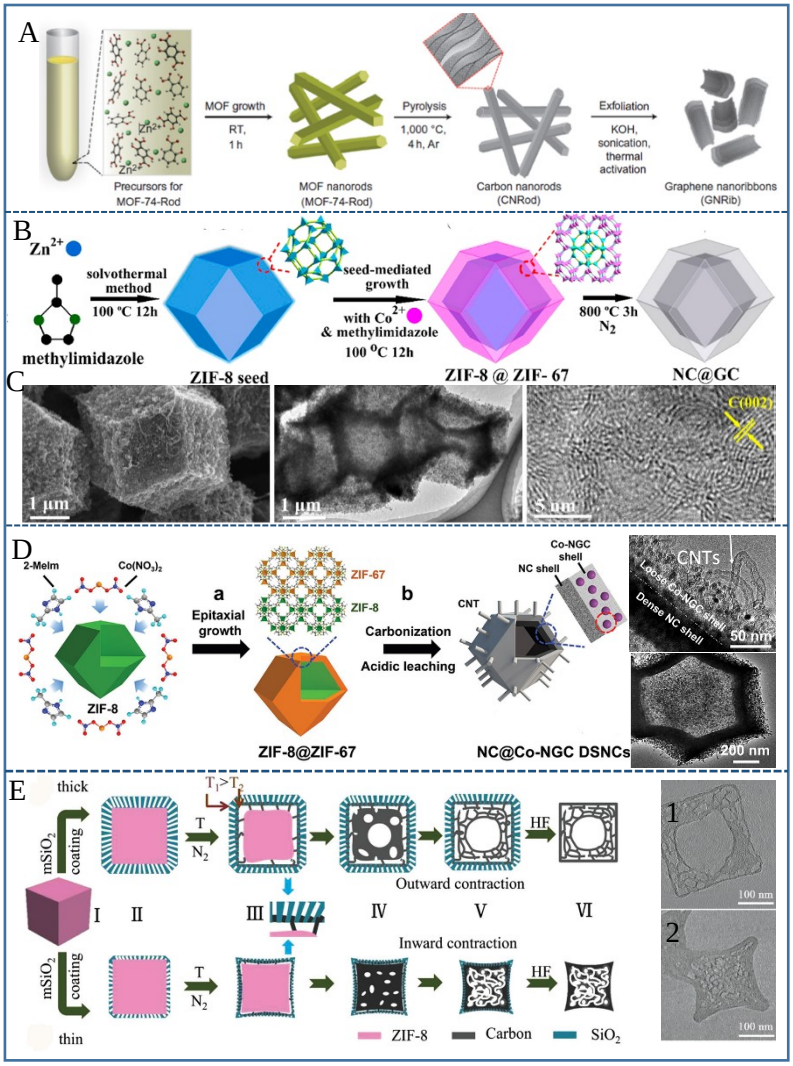


**Figure 2.10** A) Schematic synthesis of MOF-74-Rod, carbon nanorods and graphene nanoribbons.[64] Copyright 2016, Macmillan Publishers Limited. B) Synthetic scheme for the preparation of core-shell ZIF-8@ZIF-67 crystals and the hybrid nanocages (NC@GC); and C) SEM, TEM and HRTEM images of the NC@GC.[65] Copyright 2015, American Chemical Society. D) Schematic illustration of the synthesis of NC@Co-NGC DSNCs.[55] E) Schematic illustration of the fabrication of 1 hollow mesoporous carbon nanocubes (HMCNCs) and 2 mesoporous carbon nanocubes (SMCNCs).[54] D, E) Copyright 2017, WILEY-VCH Verlag GmbH & Co.

Although MOFs act as a critical platform for developing advanced functional porous carbon materials, this method is multi-step, costly and difficult for large-scale production. Regardlessly, it remains an area of intense research interest. This is because novel properties and features can be brought to MOF-derived carbon materials and this strategy has tremendous advantages in compositional and structural controls of the resulting

carbons.[121] Specifically, the MOF-based route is efficient and unique to produce porous and/or hollow nanostructures/microstructures with tightly coupled carbon/metal moieties. From a practical viewpoint, it would be more appealing to simplify the procedures and design low-cost MOFs, which can serve as self-templates to derive functional carbons easily.

### *2.5.2 3D Hierarchical Porous Carbon Nanospheres*

By virtue of low densities, unique nanoporous shapes and large interior void space fractions, hollow carbon nanospheres ranging in diameters from nano- to micro- metres, have attracted much scientific and technological research attention. Designing a well-established porous structure in hollow carbon spheres plays a key role for their potential applications in adsorption and separation systems, nanoreactors, catalyst supports, and electrodes for supercapacitors and batteries.[63]

Figure 2.11 shows the synthesis of hierarchical, hollow, nanoporous carbon spheres by the surface-coating hard-templating method. Different shaped porous carbon nanospheres can be designed, by controlling the structure of hard templates. Based on Figure 2.11a, Zhang et al. [28] developed double-shell pomegranate-like hollow carbon microspheres utilizing double templates. In brief, calcium carbonate@silica ($CaCO_3$@$SiO_2$) microspheres were prepared in a controlled manner, followed by acetylene deposition, calcination and removal of $CaCO_3$ and $SiO_2$ templates. N-doped double carbon-shell structure was obtained with integrated outer carbon layers containing inner interconnected hollow carbon nanospheres (Figure 2.11b). These features endow the samples with enhanced electrochemical properties in Li-ion batteries.

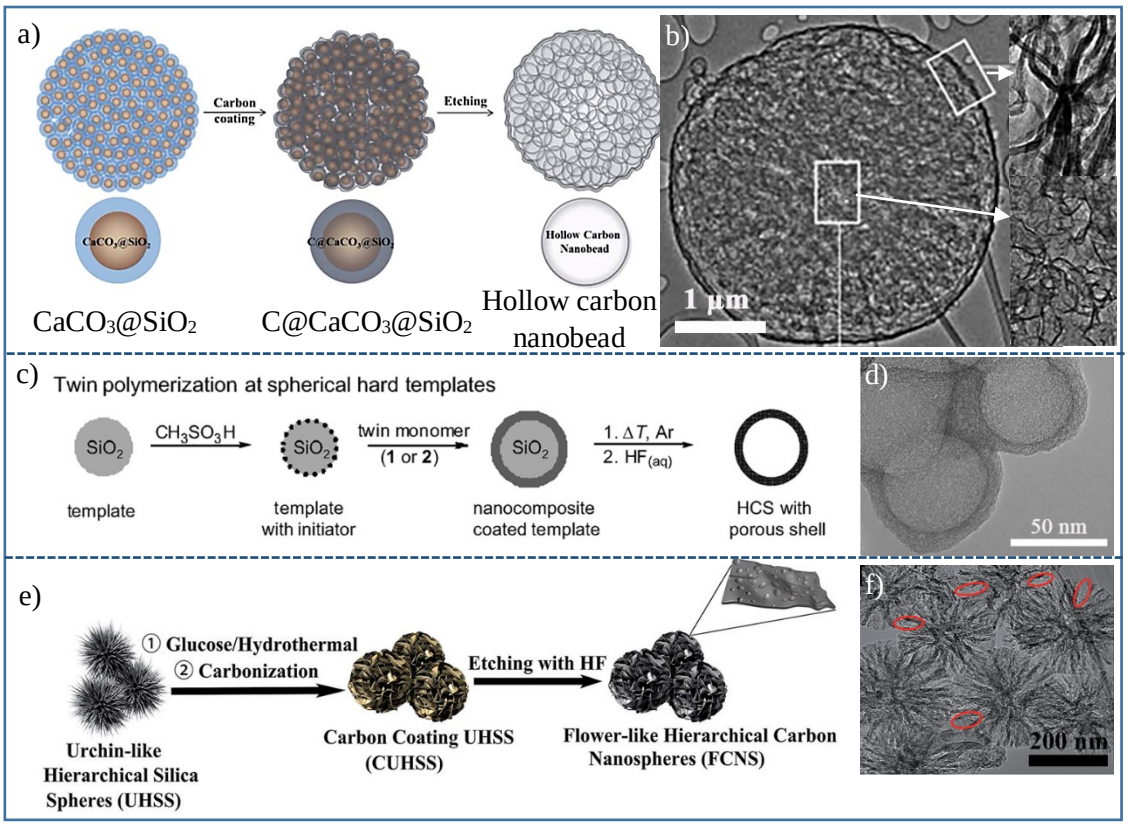


**Figure 2.11** Hollow carbon spheres obtained by surface coating hard-templating method. a) Schematic synthesis and b) TEM images of double-shell pomegranate-like porous carbon microspheres.[28] c) Schematic synthesis and d) TEM image of hollow carbon spheres.[31] Copyright 2013, Wiley-VCH Verlag GmbH & Co. KGaA, Weinheim. e) Schematic synthesis and f) TEM image of flower-like hierarchical carbon nanospheres.[35] Copyright 2017, The Royal Society of Chemistry 2017.

Bottger-Hiller et al.[31] described the synthesis of size-adjustable hollow carbon spheres (HCSs) with controllable meso- or miro- porous shells by template-assisted twin polymerization. 2, 2'-Spirobi [4H-1, 3, 2-benzodioxasiline] (denoted as monomer 1) and tetrafurfuryloxysilane (named as monomer 2) were employed as carbon precursors. Methanesulfonic acid served as a surface catalyst, which can be adsorbed on $SiO_2$ particles (the hard templates). As presented in Figure 2.11c, spherical $SiO_2$ particles were encircled by methanesulfonic acid and twin monomer (1 or 2). After carbonization of the hybrid materials, microporous shells are produced in HCSs when using twin monomer 1, while mainly mesoporous shells when 2 was used. On the other hand, template removal generated the inner hollow pores, thus the diameters of which can be precisely controlled by adjusting the sizes of $SiO_2$. The morphology, pore texture and shell thickness of the final HCSs can be tuned by changing the monomer/template ratio. The final HCSs (Figure

2.11d) possessed SSAs of 690 - 1370 $m^2$ $g^{-1}$ and pore volumes of 0.49 - 2.33 $cm^3$ $g^{-1}$. Selected HCSs were employed for $H_2$ storage, and HCSs melted with sulphur as $C/S_8$ hybrid materials were tested in lithium-sulfur batteries, where a capacity of 850 mAh $g^{-1}$ was achieved.

As shown in Figure 2.11e, homogeneous N-doped flower-like carbon hollow nanospheres were designed using urchin-like silica spheres as the hard templates.[35] The 3D urchin-like silica spheres were first prepared and modified through surface grafting of the aminopropyltrimethoxysilane template, which was then coated with glucose by a hydrothermal treatment. After subsequent carbonization and the removal of the silicon, the relevant flower-like carbon nanospheres were produced successfully (Figure 2.11f). By introduction of an $NH_3$ flow during carbonation, N doping was realized on the final product, which exhibited a large pore volume (2.33 $cm^3$ $g^{-1}$) and SSA (1223 $m^2$ $g^{-1}$) for sulphur accommodation for lithium/sulphur battery cathodes, showing an excellent cycling stability and rate capability of 829 mA h $g^{-1}$ at 5C.

Apart from tuning the structure of templates, it is suggested that slight adjustment in carbon precursors can produce various features in the resulting hollow carbons.[30] Using $SiO_2$ nanospheres as the hard template and polydopamine as the carbon source, the derived porous carbon displayed a uniform hollow spherical structure with a smooth surface. By contrast, the use of N-enriched dopamine analogue as a carbon source resulted in defect-rich porous carbon with a large SSA, numerous meso/micropores in carbon sphere shells and rich pyridinic N. The derived carbon can act as a superb bifunctional metal-free catalyst for both OER and HER in alkaline electrolyte.

Recently, self-templating methods received much attention to synthesize carbon spheres with unique structure from pyrolysis of controlled organic polymers (Figure 2.12). According to Figure 2.12a, Wu and co-workers developed a simple self-templating strategy by carbonization of polyaniline-co-polypyrrole hollow spheres.[63] When the carbonization time was extended from 3 to 20 h or the heating rate was increased from 2 to 10 °C $min^{-1}$, the surface area was elevated drastically. Hollow carbon spheres with optimum nanoporous structure showed a superior SSA of 3022 $m^2$ $g^{-1}$, abundant micropores and small mesopores (with the size peaked at 2.5 nm). Accompanying single hollow core of about 26 nm, a uniform outer size as small as 69 nm was acquired (Figure

2.12b). This is highly desirable noting that it is generally hard to synthesize carbon spheres below the size of 100 nm, a diameter that is required to produce many valued nanoscale effects. The derived sample exhibited an excellent electrical conductivity of 3.5 S $cm^{-1}$, larger than that of commercial activated carbons (0.6 S $cm^{-1}$ or 1.07 S $cm^{-1}$), and plenty of other nanocarbons.[122-124] For applications, the sample not only performed very well in adsorption of environmentally concerned organic vapours (methanol and toluene), but also served as well-defined cathode host materials for lithium-sulfur (Li-S) batteries and electrodes for supercapacitors. In addition, Xu et al.[68] presented the synthesis of carbon superstructures with polyimides (PIs) as the crucial polymer precursor, as shown in Figure 2.12a. The assembly of PI can be readily regulated by changing polymerization conditions, generating various hierarchical superstructures. Due to their excellent thermal stability, these PI hierarchical structures can be maintained while transforming into N-doped porous carbon by pyrolysis and $NH_3$ activation. 3D hierarchical crystalized carbon frameworks with flower-like, disk-like, and lantern-shaped morphologies were prepared, constructed by graphitic 2D nanosheets (i-iii in Figure 2.12). By using different monomers to prepare PI, the building block of the flower-like carbon sphere changed from nanosheets to nanobelts (iv in Figure 2.12), induced by different polymer-polymer and polymer-solvent interactions. The derived flower-like carbon architecture exhibited a high specific surface area (1375 $m^2$ $g^{-1}$), excellent catalytic activity for ORR, outstanding capacitive and cyclic performance as an electrode material for supercapacitors.

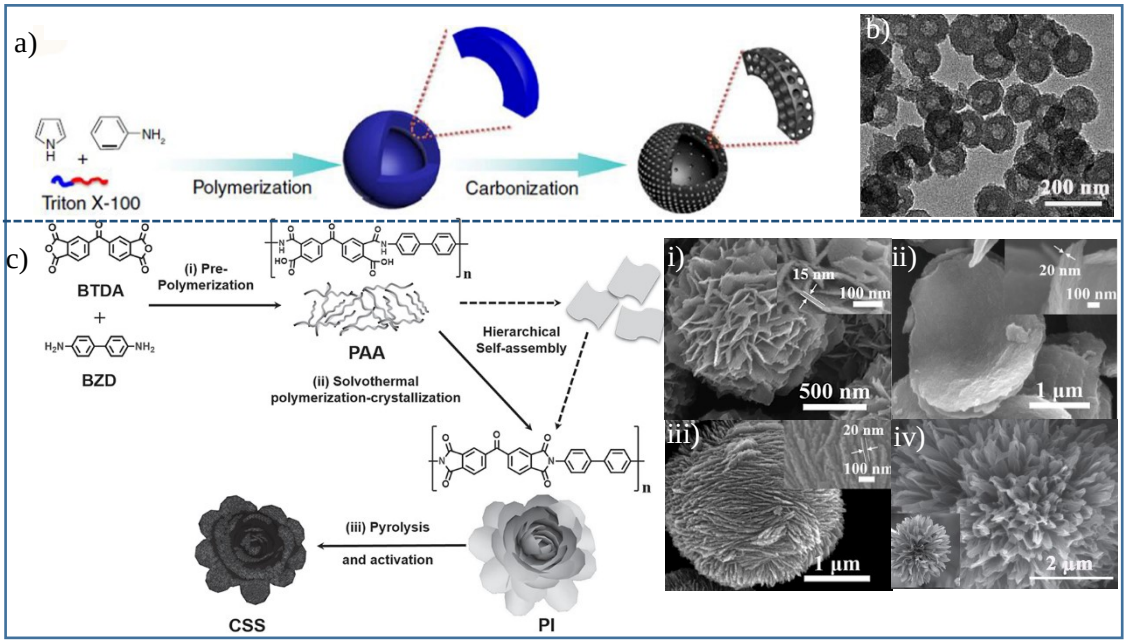


**Figure 2.12** Hierarchical porous carbon nanospheres derived by the self-templating approach. a) Schematic synthesis and b) TEM image of the hollow carbon spheres.[63]

Copyright 2015, Macmillan Publishers Limited. c) Schematic synthesis and SEM images of PI-derived hierarchical structured carbon spheres with i) nanosheet-built-flower-like, ii) disk-like, iii) lantern-shaped and iv) nanobelt-constructed-flower-like morphologies.[68] Copyright 2016, WILEY-VCH Verlag GmbH & Co.

### *2.5.3 Hierarchically Porous Carbons with Ordered Structures*

Porous carbons with ordered hierarchical structures are generally prepared via multiple templating routes. As reported by Guo et al.,[49] ordered macroporous silica frameworks were first prepared, using polystyrene spheres as the soft template and silica alkoxide as the precursor. F127 and resol were then filled into the voids of the macroporous silica, followed by heat treatment of the mixture. Ordered interconnected carbon spheres (about 200 nm in diameter) were produced after silica template removal. The carbon spheres possessed a mesoporous structure (8 nm mesopores with 3 nm wall thickness), while the voids between these carbon spheres formed 60 nm macropores (Figure 2.13). The ordered mesopores can boost effective $Li^+$ diffusion and electron transfer, while the macropores can provide channels for $O_2$ diffusion in rechargeable Li-$O_2$ batteries.

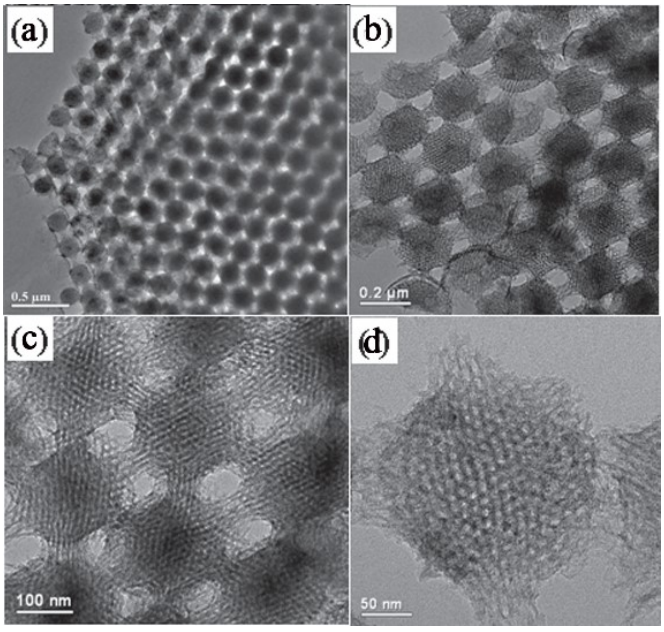


**Figure 2.13** TEM images of the as-prepared porous carbon samples with different magnifications.[49] Copyright 2013, WILEY-VCH Verlag GmbH & Co.

*2.5.4 Hierarchically Porous Carbons with Graphitic Walls*

Hierarchical porous carbons with graphitic walls can either be transformed from high-graphitizing precursors such as pitch, polyacrylonitrile (PAN),[50] or be generated by transition metal (e.g., Co, Fe, Ni) catalysis. Estevez et al. described a strategy to engineer hierarchical graphitic porous carbon using PAN by multiple templates of ice and colloidal silica.[50] The use of ice templating was very critical for the highly porous structure, which not only enabled macropore formation but also allowed for the heavy loading of the silica template to the PAN precursor. The final carbon displayed competing textural features including a large SSA (> 2500 $m^2$ $g^{-1}$) and super high pore volume (> 11 $cm^3$ $g^{-1}$, with mesopore volume up to 7.53 $cm^3$ $g^{-1}$), making it applicable for oil adsorption and supercapacitors.

Histidine, as one kind of amino acid, is also a precursor that can produce carbon of a high graphitization degree. Using this chemical, N-doped ordered macroporous frameworks with ultrathin micro/mesoporous graphene-like pore walls were constructed by a surface coating hard-templating method (Figure 2.14).[27] Histidine possesses a strong binding affinity with silica. Benefited from this, the opal that is composed of packed silica spheres was uniformly coated by thin histidine molecule layers. After subsequent carbonization and template removal, graphene-like ultrathin carbon layers (2.8 nm thick) were achieved with hierarchically porous structures.

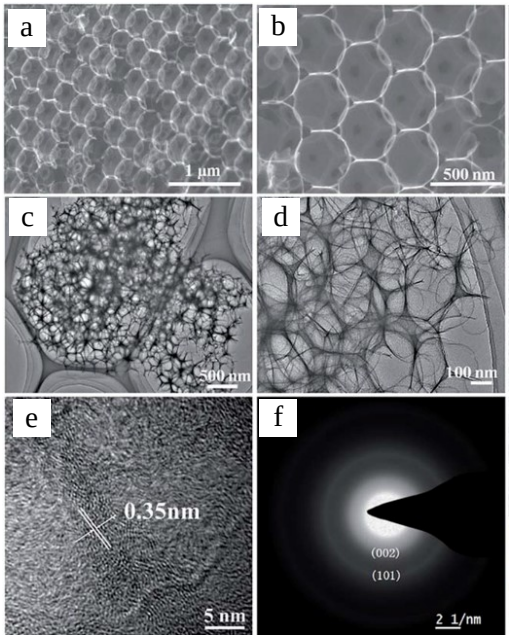

**Figure 2.14** a, b) SEM; c, d) TEM; e) HRTEM and f) selected area electron diffraction (SAED) pattern of the representative N-doped porous carbon sample.[27] Copyright 2017, The Royal Society of Chemistry.

Gong et al. developed a biomass-derived three-dimensional porous graphitic carbon from a single-step route.[72] Bamboo char served as the carbon source, while potassium ferrate ($K_2FeO_4$) was used as activating agent (K) and catalyst (Fe species) for graphitization. Carbonization of the original bamboo char resulted in a hollow elongated morphology with few pores on its surface. When $K_2FeO_4$ was introduced, the original hollow structure was retained in the as-prepared sample, accompanied by large SSA (1732 $m^2$ $g^{-1}$), graphitic walls, and abundant porosities.

### *2.5.5 Biomass and Biowaste-Derived Hierarchically Porous Carbons*

Disordered 3D hierarchically porous carbons can be easily synthesized by various methods, including, but not limited to templating, molten salt, physical or chemical activation approaches. Special attention was given to biomass and biowaste-derived hierarchical porous carbons. Biomass or biowaste derived from agricultural or forest crops and residues, marine wastes, industrial wastes and domestic wastes, which are economical, ecofriendly and renewable, have been employed as carbon sources to develop scalable porous carbon materials. Until now, carbonaceous materials have been demonstrated to be produced from a wide variety of precursors including lignin, corncob, willow leaves, ginkgo leaves, corn starch, sweet potato, cornstalk, bacterial cellulose, peanut shells, willow catkins, banana skins, pinecone hull, cherry stones, ox horns, sea shells, bamboo chopsticks, and sea shells. Several critical strategies have been developed for creating porous nanostructures with modified surface functionalities.

KOH activation has been most widely used to convert biomass or biowaste into hierarchically porous carbons. Balahmar et al. demonstrated the conversion of various biomass materials such as sawdust, seaweed, or paeonia lactiflora to activated carbons with high yields by direct KOH activation processes.[75] Activated carbon with primarily small micropore sizes (0.5 - 0.7 nm) was synthesized that favored postcombustion $CO_2$ capture (4.6 mmol $g^{-1}$ at 25 °C, 1 bar). In addition, activated carbon containing high-proportioned large micropores (1 - 2 nm) and small mesopore (2 - 3 nm) can be developed

for excellent precombustion $CO_2$ uptake at higher pressures (up to 22 mmol $g^{-1}$ at 25 °C, 20 bar). Similarly, to satisfy the different needs for low pressure $CO_2$ uptake (that requires small micropores) and high pressure $CO_2$ capture (that demands high surface area), various activated carbons have been prepared from other biomass materials such as Jujun grass, Camellia japonica,[83] pine core shells[84] by KOH activation.

Biomass of willow catkin was also successfully converted into interconnected carbon nanosheets by KOH activation, followed by effective N and S co-doping (with thiourea as the doping agent).[86] The final sample exhibited an SSA of 1533 $m^2$ $g^{-1}$ and excellent rate performance with a high specific capacitance of 298 F $g^{-1}$ at 0.5 A $g^{-1}$ while 233 F $g^{-1}$ at 50 A $g^{-1}$ in a three-electrode supercapacitor test. Rehman et al. reported a unique porous nanoarchitecture of vertically aligned carbon nanosheets by direct carbonization of agar/KOH.[82] The resulted porous carbon had an SSA of 1750 $m^2$ $g^{-1}$ and interconnected microporous carbon nanosheets with 3D channels of macrovoids and mesopores that allowed enough sulfur loading for enhanced performance in Lithium-Sulfur Batteries (LSBs). Huang et al. reported chitosan-derived hierarchically porous carbon with an ultrahigh SSA of 3532 $m^2$ $g^{-1}$ by combining hydrothermal treatment with KOH activation.[74] The addition of acetic acid during hydrothermal carbonization was critical in helping construct a conducive environment that would benefit the subsequent KOH activation. A high capacitance (455 F $g^{-1}$ at 0.5 A $g^{-1}$) with excellent cycling stability (99% capacity retention over 20000 cycles) was achieved in the final carbon when used as a supercapacitor electrode in 6 M KOH and a three-electrode system. Nitrogen-doped activated carbons were obtained from corncobs through a one-step KOH activation under $N_2$ flow with $NH_3$ introduced for another activating agent and N doping.[85] The obtained samples displayed high SSAs up to 2900 $m^2$ $g^{-1}$ with an N content of up to 4 wt.%.

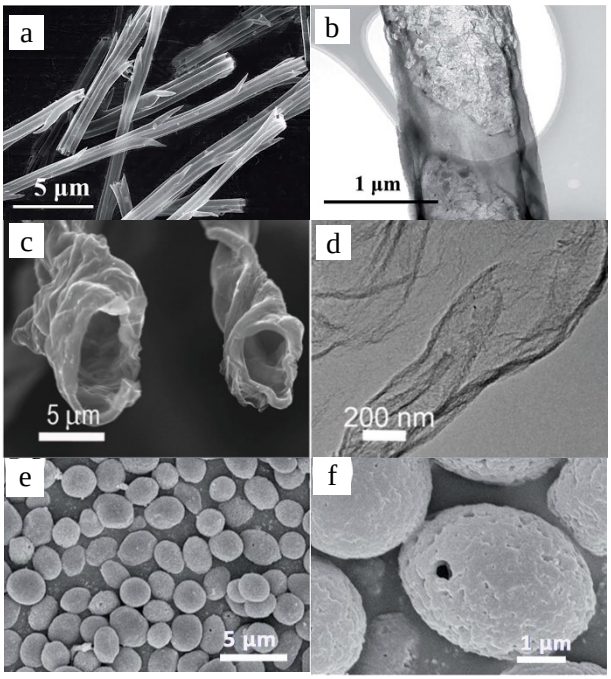


**Figure 2.15** Morphologies of biomass-derived carbon. a) SEM and b) TEM images of hollow bundled structure derived from dandelion fluff (B/N-PCTB).[73] Copyright 2017, The Royal Society of Chemistry. c) SEM and d) TEM images of cotton-derived N-doped porous carbon microtubes.[78] e, f) SEM images of N-doped hollow porous carbon microspheres derived from pre-cultivated yeast cells.[62] Copyright 2016, The Royal Society of Chemistry 2016.

In some cases, special morphologies can be inherited from the porous structure of natural sources, as presented in Figure 2.15. Interestingly, direct carbonization of dandelion fluff resulted in a hollow bundled structure with thin-walls (PCTB).[73] Each carbon microbundle consists of several hollow and thin-wall carbon nanotubes. After KOH activation and B, N co-doping, the bundled tube structure can be retained in the as-prepared carbon with numerous micropores and mesopores on the walls (B/N-PCTB, Figure 2.15a, b). Owing to the impressive open hollow channels, low tortuosity, and abundant porosity, the optimized sample delivered a specific capacitance of 355 F $g^{-1}$ at 1 A $g^{-1}$ in a three-electrode system of supercapacitor tests. In addition, Li et al. synthesized a flexible N-doped 3D porous carbon microtube sponge by direct pyrolysis of cotton under $NH_3$ atmosphere.[78] The hollow core of micron-scale (2 - 5 µm) was inherited from macrostructure of cotton (Figure 2.15c, d). The inner part of the tubular structure consisted of a combined meso/micropore volume of 1.34 $cm^3$ $g^{-1}$, arising from $NH_3$ etching during pyrolysis. The derived unique carbon materials with a high surface area (2358 $m^2$ $g^{-1}$),

well-graphitized texture and high density of pyridinic and quaternary N, demonstrated excellent activities for both ORR and OER. Yeast, which is self-duplicable, cost-effective and N-rich, can be used for synthesizing porous carbon microspheres by heat treatment of the cultivated yeast cells (Figure 2.15e, f).[62] The self-templating-derived sample contained abundant micropores centering at 0.8 and 1.4 nm and mesopores (2 - 13 nm) and served as an excellent carbon host to load sulfur, forming a cathode material for Li-S batteries. The micropores and small mesopores can strongly enhance the contact of carbon with sulfur while large mesopores favor ion transport and electrolyte diffusion.

There are also extensive studies on other activating methods. The molten salt method was reported in Ref. [88] by employing the eutectic mixture of LiCl/KCl (with a melting point of 353 °C) as the inert chloride salts, and glucose as the carbon source. Reactive salts including $LiNO_3$ or $Na_2S_2O_3$ were added for N or S doping, which can increase the SSAs of the final carbons greatly. Highly porous heteroatom-doped carbons can be produced from the cooperative effect of the inert chloride and reactive salts. SSAs reached the maxima (up to 3250 $m^2\ g^{-1}$) at about 800 or 900 °C. Graglia et al. illustrated a salt melting strategy to prepare N-doped micro-, meso-, and macroporous functional carbons with a high SSA of 1589 $m^2\ g^{-1}$, employing lignin as a precursor. Lignin was extracted from beech wood and functionalized by aromatic nitration.[87] Then, it was ionothermally carbonized with a eutectic salt melts of $KCl/ZnCl_2$ to synthesize N-doped functional carbon as an excellent electrocatalyst for ORR, with a half-wave potential of 0.85 V (vs RHE) and 4 $e^-$ selectivity in 0.1 M KOH. In Ref.[76], different chemical agents (KOH, $H_3PO_4$, or $ZnCl_2$) were applied for the activation of cinnamon sticks. All the as-prepared carbons displayed an irregular shape, amorphous structure with disordered hierarchically porous structure. Sample CDC-1 (by KOH activation) possessed open porous structure and high surface area (3405 $m^2\ g^{-1}$), with both micropores and mesopores (3 to 4 nm). Sample CDC-2 (by $ZnCl_2$ activation) had a surface area of 2440 $m^2\ g^{-1}$ with micropores and large mesopores found over a wider size range. CDC-3 (by $H_3PO_4$ activation) had a surface area of 1810 $m^2\ g^{-1}$, a narrow pore-size distribution and almost no pores larger than 3 nm. The activation effect on pore size distribution also depends on the sources of biomass or biowaste. Ref. [77] described the synthesis of N and O dual-doped functional carbons from activation of poplar catkins by $ZnCl_2$. The optimized final carbon displayed a surface area of 1462.5 $m^2\ g^{-1}$, a pore volume of 1.31 $cm^3\ g^{-1}$ and meso-/micropores structure with its pore size centering at around 3.6 nm.[77]

It is noted that some bio-wastes can generate porous carbons in some cases by a direct pyrolysis process without additional activation or templating agents. As presented in Ref. [59], direct carbonization of sodium lignosulfonate, an industrial by-product of lignocelluloses, can result in a hierarchically porous carbon. The as-prepared carbon sample showed a moderate specific surface area (903 $m^2$ $g^{-1}$) with narrow micropores (pore size < 2 nm) and meso-/macro-pores (2 - 7 nm and 20 - 100 nm). The porous structure was generated by the activation by inorganic salts (NaCl, KCl, $Na_2SO_4$ and $Na_2CO_3$) derived from SLS.

## 2.6 Conclusions and Outlook

In conclusion, the chapter compiles and reviews some newly developed strategies mainly via templating and activation, for the controllable synthesis of functional carbons ranging in pore sizes from micro-, meso-, macro- to hierarchically porous structure. The outstanding features of porous carbons have led them to be widely applied in various fields, including water remediation, $CO_2$ capture, $H_2$ storage, electrodes or electrode hosts for fuel cells, batteries, and supercapacitors. This review is expected to provide us with a better understanding on the various approaches to obtain porous carbon with large SSAs, desirable porous textures, suitable graphitization degree, satisfying surface chemistry, which are potentially applicable in the treatment of different organic molecules in waste water. Porous carbons with various pore sizes, controllable ordered or disordered structures have been synthesized by different types of designed hard, soft, multiple or self templates. Compared to most templating routes, activation generally resulted in disordered, hierarchical, porous structures, but it possesses its advantages of scalability and simplicity, and it is able to produce porous carbons with super high SSAs.

For future research of porous carbons, it is highly critical to more precisely relate the structure features of functional porous carbons with specific application fields and make it more facile to realize different structure design requirements. For applying the porous carbons in water remediation, the first challenge is to produce high-surface-area porous carbons with tailored porosities and surface chemistry through cost-effective, reproducible, and scalable methods. Furthermore, it is essential to reduce the cost of production to the greatest extent, by exploring precursors which are renewable, low-cost

and readily available. Last but not least, a fundamental problem associated with using nanomaterials for environmental applications is large volume of waste streams generated during the preparation process, which are difficult to treat with through conventional and economical technologies, such as bioprocesses. This challenge has to be addressed in the future research or to apply life cycle analysis.

Based on this review, this thesis aims to adopt cost-effective raw materials and develop green, scalable, and easily-handled approaches that produce few wastes to synthesize hierarchically porous carbons with high surface areas and suitable surface chemistry for environmental and some other related applications.

## References

[1] W. Libbrecht, A. Verberckmoes, J.W. Thybaut, P. Van der Voort, J. De Clercq, Soft Templated Mesoporous Carbons: Tuning the Porosity for the Adsorption of Large Organic Pollutants, Carbon, 116 (2017) 528.

[2] W.J. Tian, H.Y. Zhang, Z. Qian, T.H. Ouyang, H.Q. Sun, J.Y. Qin, M.O. Tade, S.B. Wang, Bread-Making Synthesis of Hierarchically Co@C Nanoarchitecture in Heteroatom Doped Porous Carbons for Oxidative Degradation of Emerging Contaminants, Applied Catalysis B-Environmental, 225 (2018) 76.

[3] N. Balahmar, A.C. Mitchell, R. Mokaya, Generalized Mechanochemical Synthesis of Biomass-Derived Sustainable Carbons for High Performance $CO_2$ Storage, Advanced Energy Materials, 5 (2015) 1500867.

[4] H. Liu, X.X. Liu, W. Li, X. Guo, Y. Wang, G.X. Wang, D.Y. Zhao, Porous Carbon Composites for Next Generation Rechargeable Lithium Batteries, Advanced Energy Materials, 7 (2017) 1700283.

[5] W. Li, J. Liu, D.Y. Zhao, Mesoporous Materials for Energy Conversion and Storage Devices, Nature Reviews Materials, 1 (2016) 16023.

[6] C.Z. Zhu, H. Li, S.F. Fu, D. Du, Y.H. Lin, Highly Efficient Nonprecious Metal Catalysts Towards Oxygen Reduction Reaction Based on Three-Dimensional Porous Carbon Nanostructures, Chemical Society Reviews, 45 (2016) 517.

[7] Y.F. Song, W. Chen, C.C. Zhao, S.G. Li, W. Wei, Y.H. Sun, Metal-Free Nitrogen-Doped Mesoporous Carbon for Electroreduction of $CO_2$ to Ethanol, Angewandte Chemie-International Edition, 56 (2017) 10840.

[8] S.J. Tesh, T.B. Scott, Nano-Composites for Water Remediation: A Review, Advanced Materials, 26 (2014) 6056.
[9] M. Haidar, A. Dirany, I. Sires, N. Oturan, M.A. Oturan, Electrochemical Degradation of the Antibiotic Sulfachloropyridazine by Hydroxyl Radicals Generated at a Bdd Anode, Chemosphere, 91 (2013) 1304.
[10] F.C. Cabello, Heavy Use of Prophylactic Antibiotics in Aquaculture: A Growing Problem for Human and Animal Health and for the Environment, Environmental Microbiology, 8 (2006) 1137.
[11] A. Rossner, S.A. Snyder, D.R.U. Knappe, Removal of Emerging Contaminants of Concern by Alternative Adsorbents, Water Research, 43 (2009) 3787.
[12] L.R. Radovic, C. Moreno-Castilla, J. Rivera-Utrilla, Carbon Materials as Adsorbents in Aqueous Solutions, Chemistry and Physics of Carbon, 27, 27 (2001) 227.
[13] M. Valix, W.H. Cheung, K. Zhang, Role of Heteroatoms in Activated Carbon for Removal of Hexavalent Chromium from Wastewaters, Journal of Hazardous Materials, 135 (2006) 395.
[14] G.X. Zhao, L. Jiang, Y.D. He, J.X. Li, H.L. Dong, X.K. Wang, W.P. Hu, Sulfonated Graphene for Persistent Aromatic Pollutant Management, Advanced Materials, 23 (2011) 3959.
[15] L.L. Ji, W. Chen, L. Duan, D.Q. Zhu, Mechanisms for Strong Adsorption of Tetracycline to Carbon Nanotubes: A Comparative Study Using Activated Carbon and Graphite as Adsorbents, Environmental Science & Technology, 43 (2009) 2322.
[16] X.B. Wang, Y.L. Qin, L.H. Zhu, H.Q. Tang, Nitrogen-Doped Reduced Graphene Oxide as a Bifunctional Material for Removing Bisphenols: Synergistic Effect between Adsorption and Catalysis, Environmental Science & Technology, 49 (2015) 6855.
[17] J. Liang, Y. Jiao, M. Jaroniec, S.Z. Qiao, Sulfur and Nitrogen Dual-Doped Mesoporous Graphene Electrocatalyst for Oxygen Reduction with Synergistically Enhanced Performance, Angewandte Chemie-International Edition, 51 (2012) 11496.
[18] J.T. Zhang, Z.H. Xia, L.M. Dai, Carbon-Based Electrocatalysts for Advanced Energy Conversion and Storage, Science Advances, 1 (2015) e1500564.
[19] H. Zhang, W. Tian, Z. Qian, T. Ouyang, M. Saunders, J. Qin, S. Wang, M.O. Tadé, H. Sun, Co@C/CoOx Coupled with N-Doped Layer-Structured Carbons for Excellent $CO_2$ Capture and Oxygen Reduction Reaction, Carbon, 133 (2018) 306.
[20] W. Tian, H. Zhang, Z. Qian, T. Ouyang, H. Sun, J. Qin, M.O. Tadé, S. Wang, Bread-Making Synthesis of Hierarchically Co@C Nanoarchitecture in Heteroatom Doped

Porous Carbons for Oxidative Degradation of Emerging Contaminants, Applied Catalysis B: Environmental, 225 (2018) 76.
[21] X.G. Duan, K. O'Donnell, H.Q. Sun, Y.X. Wang, S.B. Wang, Sulfur and Nitrogen Co-Doped Graphene for Metal-Free Catalytic Oxidation Reactions, Small, 11 (2015) 3036.
[22] Y. Zheng, Y. Jiao, L. Ge, M. Jaroniec, S.Z. Qiao, Two-Step Boron and Nitrogen Doping in Graphene for Enhanced Synergistic Catalysis, Angewandte Chemie-International Edition, 52 (2013) 3110.
[23] Z.S. Wu, A. Winter, L. Chen, Y. Sun, A. Turchanin, X.L. Feng, K. Mullen, Three-Dimensional Nitrogen and Boron Co-Doped Graphene for High-Performance All-Solid-State Supercapacitors, Advanced Materials, 24 (2012) 5130.
[24] M.R. Benzigar, S. Joseph, H. Ilbeygi, D.H. Park, S. Sarkar, G. Chandra, S. Umapathy, S. Srinivasan, S.N. Talapaneni, A. Vinu, Highly Crystalline Mesoporous $C_{60}$ with Ordered Pores: A Class of Nanomaterials for Energy Applications, Angewandte Chemie International Edition, 57 (2018) 569.
[25] Y.B. Yin, J.J. Xu, Q.C. Liu, X.B. Zhang, Macroporous Interconnected Hollow Carbon Nanofibers Inspired by Golden-Toad Eggs toward a Binder-Free, High-Rate, and Flexible Electrode, Advanced Materials, 28 (2016) 7494.
[26] S.H. Choi, Y.C. Kang, Polystyrene-Templated Aerosol Synthesis of $MoS_2$–Amorphous Carbon Composite with Open Macropores as Battery Electrode, Chemsuschem, 8 (2015) 2260.
[27] Y. Yao, Z. Chen, A. Zhang, J. Zhu, X. Wei, J. Guo, W.D. Wu, X.D. Chen, Z. Wu, Surface-Coating Synthesis of Nitrogen-Doped Inverse Opal Carbon Materials with Ultrathin Micro/Mesoporous Graphene-Like Walls for Oxygen Reduction and Supercapacitors, Journal of Materials Chemistry A, 5 (2017) 25237.
[28] L. Zhang, Y.H. Dou, H.P. Guo, B.W. Zhang, X.X. Liu, M. Wan, W.J. Li, X.L. Hu, S.X. Dou, Y.H. Huang, H.K. Liu, A Facile Way to Fabricate Double-Shell Pomegranate-Like Porous Carbon Microspheres for High-Performance Li-Ion Batteries, Journal of Materials Chemistry A, 5 (2017) 12073.
[29] S. Li, C. Cheng, X. Zhao, J. Schmidt, A. Thomas, Active Salt/Silica-Templated 2D Mesoporous Feco-Nx-Carbon as Bifunctional Oxygen Electrodes for Zinc-Air Batteries, Angewandte Chemie International Edition, 57 (2018) 1856.
[30] Z. Zhang, Z. Yi, J. Wang, X. Tian, P. Xu, G. Shi, S. Wang, Nitrogen-Enriched Polydopamine Analogue-Derived Defect-Rich Porous Carbon as a Bifunctional Metal-

Free Electrocatalyst for Highly Efficient Overall Water Splitting, Journal of Materials Chemistry A, 5 (2017) 17064.
[31] F. Bottger-Hiller, P. Kempe, G. Cox, A. Panchenko, N. Janssen, A. Petzold, T. Thurn-Albrecht, L. Borchardt, M. Rose, S. Kaskel, C. Georgi, H. Lang, S. Spange, Twin Polymerization at Spherical Hard Templates: An Approach to Size-Adjustable Carbon Hollow Spheres with Micro- or Mesoporous Shells, Angewandte Chemie-International Edition, 52 (2013) 6088.
[32] S.E. Bae, K.J. Kim, I.H. Choi, S. Huh, Preparation of N-Doped Microporous Carbon Nanospheres by Direct Carbonization of as-Prepared Mesoporous Silica Nanospheres Containing Cetylpyridinium Bromide Template, Carbon, 99 (2016) 8.
[33] P. Sazama, J. Pastvova, C. Rizescu, A. Tirsoaga, V.I. Parvulescu, H. Garcia, L. Kobera, J. Seidel, J. Rathousky, P. Klein, I. Jirka, J. Moravkova, V. Blechta, Catalytic Properties of 3D Graphene-Like Microporous Carbons Synthesized in a Zeolite Template, ACS Catalysis, 8 (2018) 1779.
[34] K. Kim, T. Lee, Y. Kwon, Y. Seo, J. Song, J.K. Park, H. Lee, J.Y. Park, H. Ihee, S.J. Cho, R. Ryoo, Lanthanum-Catalysed Synthesis of Microporous 3D Graphene-Like Carbons in a Zeolite Template, Nature, 535 (2016) 131.
[35] D.Y. Guo, X.A. Chen, H.F. Wei, M.L. Liu, F. Ding, Z. Yang, K.Q. Yang, S. Wang, X.J. Xu, S.M. Huang, Controllable Synthesis of Highly Uniform Flower-Like Hierarchical Carbon Nanospheres and Their Application in High Performance Lithium-Sulfur Batteries, Journal of Materials Chemistry A, 5 (2017) 6245.
[36] S. Kim, A.M. Escamilla-Perez, M. De bruyn, J.G. Alauzun, N. Louvain, N. Brun, D. Macquarrie, L. Stievano, B. Boury, L. Monconduit, P.H. Mutin, Sustainable Polysaccharide-Derived Mesoporous Carbons (Starbon) as Additives in Lithium-Ion Batteries Negative Electrodes, Journal of Materials Chemistry A, 5 (2017) 24380.
[37] Y. Qu, G. Zan, J. Wang, Q. Wu, Preparation of Eggplant-Derived Macroporous Carbon Tubes and Composites of Edmct/Co(OH)$(Co_3)_{0.5}$ Nano-Cone-Arrays for High-Performance Supercapacitors, Journal of Materials Chemistry A, 4 (2016) 4296.
[38] X. Hu, J. Chen, G. Zeng, J. Jia, P. Cai, G. Chai, Z. Wen, Robust 3D Macroporous Structures with Sns Nanoparticles Decorating Nitrogen-Doped Carbon Nanosheet Networks for High Performance Sodium-Ion Batteries, Journal of Materials Chemistry A, 5 (2017) 23460.

[39] W. Wang, W. Chen, P. Miao, J. Luo, Z. Wei, S. Chen, Nacl Crystallites as Dual-Functional and Water-Removable Templates to Synthesize a Three-Dimensional Graphene-Like Macroporous Fe-N-C Catalyst, ACS Catalysis, 7 (2017) 6144.
[40] H.J. Yoon, N.R. Kim, H.J. Jin, Y.S. Yun, Macroporous Catalytic Carbon Nanotemplates for Sodium Metal Anodes, Advanced Energy Materials, 8 (2018) 1701261.
[41] J.G. Wang, H.Z. Liu, H.H. Sun, W. Hua, H.W. Wang, X.R. Liu, B.Q. Wei, One-Pot Synthesis of Nitrogen-Doped Ordered Mesoporous Carbon Spheres for High-Rate and Long-Cycle Life Supercapacitors, Carbon, 127 (2018) 85.
[42] P.F. Zhang, L. Wang, S.Z. Yang, J.A. Schott, X.F. Liu, S.M. Mahurin, C.L. Huang, Y. Zhang, P.F. Fulvio, M.F. Chisholm, S. Dai, Solid-State Synthesis of Ordered Mesoporous Carbon Catalysts Via a Mechanochemical Assembly through Coordination Cross-Linking, Nature Communications, 8 (2017).
[43] J. Wei, Z.K. Sun, W. Luo, Y.H. Li, A.A. Elzatahry, A.M. Al-Enizi, Y.H. Deng, D.Y. Zhao, New Insight into the Synthesis of Large-Pore Ordered Mesoporous Materials, Journal of the American Chemical Society, 139 (2017) 1706.
[44] D. Gueon, J.T. Hwang, S.B. Yang, E. Cho, K. Sohn, D.-K. Yang, J.H. Moon, Spherical Macroporous Carbon Nanotube Particles with Ultrahigh Sulfur Loading for Lithium-Sulfur Battery Cathodes, ACS Nano, 12 (2018) 226.
[45] Z. Qang, Y.F. Xia, X.H. Xia, B.D. Vogt, Generalized Synthesis of a Family of Highly Heteroatom-Doped Ordered Mesoporous Carbons, Chemistry of Materials, 29 (2017) 10178.
[46] J. Knossalla, D. Jalalpoor, F. Schuth, Hands-on Guide to the Synthesis of Mesoporous Hollow Graphitic Spheres and Core-Shell Materials, Chemistry of Materials, 29 (2017) 7062.
[47] J.A. Zhang, Y. Song, M. Kopec, J. Lee, Z.Y. Wang, S.Y. Liu, J.J. Yan, R. Yuan, T. Kowalewski, M.R. Bockstaller, K. Matyjaszewski, Facile Aqueous Route to Nitrogen-Doped Mesoporous Carbons, Journal of the American Chemical Society, 139 (2017) 12931.
[48] F. Xu, P. Sun, M. Qian, T.Q. Lin, F.Q. Huang, Variable Texture Few-Layer Ordered Macroporous Carbon for High-Performance Electrochemical Capacitors, Journal of Materials Chemistry A, 5 (2017) 25171.
[49] Z. Guo, D. Zhou, X. Dong, Z. Qiu, Y. Wang, Y. Xia, Ordered Hierarchical Mesoporous/Macroporous Carbon: A High-Performance Catalyst for Rechargeable Li–O2 Batteries, Advanced Materials, 25 (2013) 5668.

[50] L. Estevez, V. Prabhakaran, A.L. Garcia, Y. Shin, J.H. Tao, A.M. Schwarz, J. Darsell, P. Bhattacharya, V. Shutthanandan, J.G. Zhang, Hierarchically Porous Graphitic Carbon with Simultaneously High Surface Area and Colossal Pore Volume Engineered Via Ice Templating, ACS Nano, 11 (2017) 11047.
[51] A.-D. Tan, Y.-F. Wang, Z.-Y. Fu, P. Tsiakaras, Z.-X. Liang, Highly Effective Oxygen Reduction Reaction Electrocatalysis: Nitrogen-Doped Hierarchically Mesoporous Carbon Derived from Interpenetrated Nonporous Metal-Organic Frameworks, Applied Catalysis B: Environmental, 218 (2017) 260.
[52] L. Ye, G.L. Chai, Z.H. Wen, Zn-MOF-74 Derived N-Doped Mesoporous Carbon as Ph-Universal Electrocatalyst for Oxygen Reduction Reaction, Advanced Functional Materials, 27 (2017) 1606190.
[53] S.J. Yang, T. Kim, J.H. Im, Y.S. Kim, K. Lee, H. Jung, C.R. Park, MOF-Derived Hierarchically Porous Carbon with Exceptional Porosity and Hydrogen Storage Capacity, Chemistry of Materials, 24 (2012) 464.
[54] C. Liu, X.D. Huang, J. Wang, H. Song, Y.N. Yang, Y. Liu, J.S. Li, L.J. Wang, C.Z. Yu, Hollow Mesoporous Carbon Nanocubes: Rigid-Interface-Induced Outward Contraction of Metal-Organic Frameworks, Advanced Functional Materials, 28 (2018) 1705253.
[55] S. Liu, Z. Wang, S. Zhou, F. Yu, M. Yu, C.Y. Chiang, W. Zhou, J. Zhao, J. Qiu, Metal–Organic-Framework-Derived Hybrid Carbon Nanocages as a Bifunctional Electrocatalyst for Oxygen Reduction and Evolution, Advanced Materials, 29 (2017) 1700874.
[56] W.H. Li, S.H. Hu, X.Y. Luo, Z.L. Li, X.Z. Sun, M.S. Li, F.F. Liu, Y. Yu, Confined Amorphous Red Phosphorus in MOF-Derived N-Doped Microporous Carbon as a Superior Anode for Sodium-Ion Battery, Advanced Materials, 29 (2017) 1605820.
[57] N.P. Stadie, S.T. Wang, K.V. Kraychyk, M.V. Kovalenko, Zeolite-Templated Carbon as an Ordered Microporous Electrode for Aluminum Batteries, ACS Nano, 11 (2017) 1911.
[58] Q.X. Lai, Y.X. Zhao, Y.Y. Liang, J.P. He, J.H. Chen, In Situ Confinement Pyrolysis Transformation of ZIF-8 to Nitrogen-Enriched Meso-Microporous Carbon Frameworks for Oxygen Reduction, Advanced Functional Materials, 26 (2016) 8334.
[59] J. Pang, W.F. Zhang, J.L. Zhang, G.P. Cao, M.F. Han, Y.S. Yang, Facile and Sustainable Synthesis of Sodium Lignosulfonate Derived Hierarchical Porous Carbons for

Supercapacitors with High Volumetric Energy Densities, Green Chemistry, 19 (2017) 3916.
[60] J. Gong, M. Antonietti, J.Y. Yuan, Poly(Ionic Liquid)-Derived Carbon with Site-Specific N-Doping and Biphasic Heterojunction for Enhanced $CO_2$ Capture and Sensing, Angewandte Chemie-International Edition, 56 (2017) 7557.
[61] M. Shaibani, S.J.D. Smith, P.C. Banerjee, K. Konstas, A. Zafari, D.E. Lobo, M. Nazari, A.F. Hollenkamp, M.R. Hill, M. Majumder, Framework-Mediated Synthesis of Highly Microporous Onion-Like Carbon: Energy Enhancement in Supercapacitors without Compromising Power, Journal of Materials Chemistry A, 5 (2017) 2519.
[62] Y.P. Xie, L. Fang, H.W. Cheng, C.J. Hu, H.B. Zhao, J.Q. Xu, J.H. Fang, X.G. Lu, J.J. Zhang, Biological Cell Derived N-Doped Hollow Porous Carbon Microspheres for Lithium-Sulfur Batteries, Journal of Materials Chemistry A, 4 (2016) 15612.
[63] F. Xu, Z.W. Tang, S.Q. Huang, L.Y. Chen, Y.R. Liang, W.C. Mai, H. Zhong, R.W. Fu, D.C. Wu, Facile Synthesis of Ultrahigh-Surface-Area Hollow Carbon Nanospheres for Enhanced Adsorption and Energy Storage, Nature Communications, 6 (2015), 7221.
[64] P. Pachfule, D. Shinde, M. Majumder, Q. Xu, Fabrication of Carbon Nanorods and Graphene Nanoribbons from a Metal-Organic Framework, Nature Chemistry, 8 (2016) 718.
[65] J. Tang, R.R. Salunkhe, J. Liu, N.L. Torad, M. Imura, S. Furukawa, Y. Yamauchi, Thermal Conversion of Core-Shell Metal-Organic Frameworks: A New Method for Selectively Functionalized Nanoporous Hybrid Carbon, Journal of the American Chemical Society, 137 (2015) 1572.
[66] A. Almasoudi, R. Mokaya, Preparation and Hydrogen Storage Capacity of Templated and Activated Carbons Nanocast from Commercially Available Zeolitic Imidazolate Framework, Journal of Materials Chemistry, 22 (2012) 146.
[67] F. Bai, Y. Xia, B. Chen, H. Su, Y. Zhu, Preparation and Carbon Dioxide Uptake Capacity of N-Doped Porous Carbon Materials Derived from Direct Carbonization of Zeolitic Imidazolate Framework, Carbon, 79 (2014) 213.
[68] Z.X. Xu, X.D. Zhuang, C.Q. Yang, J. Cao, Z.Q. Yao, Y.P. Tang, J.Z. Jiang, D.Q. Wu, X.L. Feng, Nitrogen-Doped Porous Carbon Superstructures Derived from Hierarchical Assembly of Polyimide Nanosheets, Advanced Materials, 28 (2016) 1981.
[69] G. Singh, K.S. Lakhi, I.Y. Kim, S. Kim, P. Srivastava, R. Naidu, A. Vinu, Highly Efficient Method for the Synthesis of Activated Mesoporous Biocarbons with Extremely

High Surface Area for High-Pressure $CO_2$ Adsorption, ACS Applied Materials & Interfaces, 9 (2017) 29782.
[70] Z.Y. Xing, Y.T. Qi, Z.Q. Tian, J. Xu, Y.F. Yuan, C. Bommier, J. Lu, W. Tong, D.E. Jiang, X.L. Ji, Identify the Removable Substructure in Carbon Activation, Chemistry of Materials, 29 (2017) 7288.
[71] L. Qie, W.M. Chen, H.H. Xu, X.Q. Xiong, Y. Jiang, F. Zou, X.L. Hu, Y. Xin, Z.L. Zhang, Y.H. Huang, Synthesis of Functionalized 3D Hierarchical Porous Carbon for High-Performance Supercapacitors, Energy & Environmental Science, 6 (2013) 2497.
[72] Y.N. Gong, D.L. Li, C.Z. Luo, Q. Fu, C.X. Pan, Highly Porous Graphitic Biomass Carbon as Advanced Electrode Materials for Supercapacitors, Green Chemistry, 19 (2017) 4132.
[73] J. Zhao, Y.J. Li, G.L. Wang, T. Wei, Z. Liu, K. Cheng, K. Ye, K. Zhu, D.X. Cao, Z.J. Fan, Enabling High-Volumetric-Energy-Density Supercapacitors: Designing Open, Low-Tortuosity Heteroatom-Doped Porous Carbon-Tube Bundle Electrodes, Journal of Materials Chemistry A, 5 (2017) 23085.
[74] J. Huang, Y. Liang, H. Hu, S. Liu, Y. Cai, H. Dong, M. Zheng, Y. Xiao, Y. Liu, Ultrahigh-Surface-Area Hierarchical Porous Carbon from Chitosan: Acetic Acid Mediated Efficient Synthesis and Its Application in Superior Supercapacitors, Journal of Materials Chemistry A, 5 (2017) 24775.
[75] N. Balahmar, A.S. Al-Jumialy, R. Mokaya, Biomass to Porous Carbon in One Step: Directly Activated Biomass for High Performance $CO_2$ Storage, Journal of Materials Chemistry A, 5 (2017) 12330.
[76] R. Thangavel, K. Kaliyappan, H.V. Ramasamy, X.L. Sun, Y.S. Lee, Engineering the Pores of Biomass-Derived Carbon: Insights for Achieving Ultrahigh Stability at High Power in High-Energy Supercapacitors, Chemsuschem, 10 (2017) 2805.
[77] S.Y. Gao, X.G. Li, L.Y. Li, X.J. Wei, A Versatile Biomass Derived Carbon Material for Oxygen Reduction Reaction, Supercapacitors and Oil/Water Separation, Nano Energy, 33 (2017) 334.
[78] J.C. Li, P.X. Hou, S.Y. Zhao, C. Liu, D.M. Tang, M. Cheng, F. Zhang, H.M. Cheng, A 3D Bi-Functional Porous N-Doped Carbon Microtube Sponge Electrocatalyst for Oxygen Reduction and Oxygen Evolution Reactions, Energy & Environmental Science, 9 (2016) 3079.

[79] T.S. Blankenship, T.S. Blankenship, N. Balahmar, R. Mokaya, Oxygen-Rich Microporous Carbons with Exceptional Hydrogen Storage Capacity, Nature Communications, 8 (2017).
[80] X.Y. Xie, X.J. He, X.L. Shao, S.A. Dong, N. Xiao, J.S. Qiu, Synthesis of Layered Microporous Carbons from Coal Tar by Directing, Space-Confinement and Self-Sacrificed Template Strategy for Supercapacitors, Electrochimica Acta, 246 (2017) 634.
[81] J. Zhou, Z.H. Li, W. Xing, H.L. Shen, X. Bi, T.T. Zhu, Z.P. Qiu, S.P. Zhuo, A New Approach to Tuning Carbon Ultramicropore Size at Sub-Angstrom Level for Maximizing Specific Capacitance and $CO_2$ Uptake, Advanced Functional Materials, 26 (2016) 7955.
[82] S. Rehman, X.X. Gu, K. Khan, N. Mahmood, W.L. Yang, X.X. Huang, S.J. Guo, Y.L. Hou, 3D Vertically Aligned and Interconnected Porous Carbon Nanosheets as Sulfur Immobilizers for High Performance Lithium-Sulfur Batteries, Advanced Energy Materials, 6 (2016) 1502518.
[83] H.M. Coromina, D.A. Walsh, R. Mokaya, Biomass-Derived Activated Carbon with Simultaneously Enhanced $CO_2$ Uptake for Both Pre and Post Combustion Capture Applications, Journal of Materials Chemistry A, 4 (2016) 280.
[84] K.M. Li, S.C. Tian, J.G. Jiang, J.M. Wang, X.J. Chen, F. Yan, Pine Cone Shell-Based Activated Carbon Used for $CO_2$ Adsorption, Journal of Materials Chemistry A, 4 (2016) 5223.
[85] B. Li, F. Dai, Q.F. Xiao, L. Yang, J.M. Shen, C.M. Zhang, M. Cai, Nitrogen-Doped Activated Carbon for a High Energy Hybrid Supercapacitor, Energy & Environmental Science, 9 (2016) 102.
[86] Y.J. Li, G.L. Wang, T. Wei, Z.J. Fan, P. Yan, Nitrogen and Sulfur Co-Doped Porous Carbon Nanosheets Derived from Willow Catkin for Supercapacitors, Nano Energy, 19 (2016) 165.
[87] M. Graglia, J. Pampel, T. Hantke, T.P. Fellinger, D. Esposito, Nitro Lignin-Derived Nitrogen-Doped Carbon as an Efficient and Sustainable Electrocatalyst for Oxygen Reduction, ACS Nano, 10 (2016) 4364.
[88] X.F. Liu, M. Antonietti, Moderating Black Powder Chemistry for the Synthesis of Doped and Highly Porous Graphene Nanoplatelets and Their Use in Electrocatalysis, Advanced Materials, 25 (2013) 6284.
[89] J. Liu, N.P. Wickramaratne, S.Z. Qiao, M. Jaroniec, Molecular-Based Design and Emerging Applications of Nanoporous Carbon Spheres, Nature Materials, 14 (2015) 763.

[90] N.D. Petkovich, A. Stein, Controlling Macro- and Mesostructures with Hierarchical Porosity through Combined Hard and Soft Templating, Chemical Society Reviews, 42 (2013) 3721.
[91] C. Liang, Z. Li, S. Dai, Mesoporous Carbon Materials: Synthesis and Modification, Angewandte Chemie International Edition, 47 (2008) 3696.
[92] C.D. Liang, K.L. Hong, G.A. Guiochon, J.W. Mays, S. Dai, Synthesis of a Large-Scale Highly Ordered Porous Carbon Film by Self-Assembly of Block Copolymers, Angewandte Chemie-International Edition, 43 (2004) 5785.
[93] Y. Meng, D. Gu, F.Q. Zhang, Y.F. Shi, H.F. Yang, Z. Li, C.Z. Yu, B. Tu, D.Y. Zhao, Ordered Mesoporous Polymers and Homologous Carbon Frameworks: Amphiphilic Surfactant Templating and Direct Transformation, Angewandte Chemie-International Edition, 44 (2005) 7053.
[94] Y. Wan, Y.F. Shi, D.Y. Zhao, Supramolecular Aggregates as Templates: Ordered Mesoporous Polymers and Carbons, Chemistry of Materials, 20 (2008) 932.
[95] S. Tanaka, N. Nishiyama, Y. Egashira, K. Ueyama, Synthesis of Ordered Mesoporous Carbons with Channel Structure from an Organic-Organic Nanocomposite, Chemical Communications, (2005) 2125.
[96] G.J.d.A.A. Soler-Illia, C. Sanchez, B. Lebeau, J. Patarin, Chemical Strategies to Design Textured Materials: From Microporous and Mesoporous Oxides to Nanonetworks and Hierarchical Structures, Chemical Reviews, 102 (2002) 4093.
[97] G.J.A.A. Soler-Illia, O. Azzaroni, Multifunctional Hybrids by Combining Ordered Mesoporous Materials and Macromolecular Building Blocks, Chemical Society Reviews, 40 (2011) 1107.
[98] P. Innocenzi, L. Malfatti, T. Kidchob, P. Falcaro, Order-Disorder in Self-Assembled Mesostructured Silica Films: A Concepts Review, Chemistry of Materials, 21 (2009) 2555.
[99] A.G. Slater, A.I. Cooper, Function-Led Design of New Porous Materials, Science, 348 (2015) aaa8075.
[100] H. Bin Wu, X.W. Lou, Metal-Organic Frameworks and Their Derived Materials for Electrochemical Energy Storage and Conversion: Promises and Challenges, Science Advances, 3 (2017).
[101] V. Etacheri, D. Sharon, A. Garsuch, M. Afri, A.A. Frimer, D. Aurbach, Hierarchical Activated Carbon Microfiber (Acm) Electrodes for Rechargeable Li-$O_2$ Batteries, Journal of Materials Chemistry A, 1 (2013) 5021.

[102] Y.-J. Heo, S.-J. Park, A Role of Steam Activation on $CO_2$ Capture and Separation of Narrow Microporous Carbons Produced from Cellulose Fibers, Energy, 91 (2015) 142.
[103] J. Hayashi, A. Kazehaya, K. Muroyama, A.P. Watkinson, Preparation of Activated Carbon from Lignin by Chemical Activation, Carbon, 38 (2000) 1873.
[104] S. Ucar, M. Erdem, T. Tay, S. Karagoz, Removal of Lead (II) and Nickel (II) Ions from Aqueous Solution Using Activated Carbon Prepared from Rapeseed Oil Cake by $Na_2CO_3$ Activation, Clean Technologies and Environmental Policy, 17 (2015) 747.
[105] L.M. Yue, Q.Z. Xia, L.W. Wang, L.L. Wang, H. DaCosta, J. Yang, X. Hu, $CO_2$ Adsorption at Nitrogen-Doped Carbons Prepared by K2co3 Activation of Urea-Modified Coconut Shell, Journal of Colloid and Interface Science, 511 (2018) 259.
[106] W.J. Tian, H.Y. Zhang, X.G. Duan, H.Q. Sun, M.O. Tade, H.M. Ang, S.B. Wang, Nitrogen- and Sulfur-Codoped Hierarchically Porous Carbon for Adsorptive and Oxidative Removal of Pharmaceutical Contaminants, ACS Applied Materials & Interfaces, 8 (2016) 7184.
[107] X.F. Liu, N. Fechler, M. Antonietti, Salt Melt Synthesis of Ceramics, Semiconductors and Carbon Nanostructures, Chemical Society Reviews, 42 (2013) 8237.
[108] H.G. Wang, Z.H. Cheng, Y.Z. Liao, J.H. Li, J. Weber, A. Thomas, C.F.J. Faul, Conjugated Microporous Polycarbazole Networks as Precursors for Nitrogen-Enriched Microporous Carbons for $CO_2$ Storage and Electrochemical Capacitors, Chemistry of Materials, 29 (2017) 4885.
[109] S.S. Yao, J. Cui, J.Q. Huang, J.Q. Huang, W.G. Chong, L. Qin, Y.W. Mai, J.K. Kim, Rational Assembly of Hollow Microporous Carbon Spheres as P Hosts for Long-Life Sodium-Ion Batteries, Advanced Energy Materials, 8 (2018).
[110] T. Ben, H. Ren, S.Q. Ma, D.P. Cao, J.H. Lan, X.F. Jing, W.C. Wang, J. Xu, F. Deng, J.M. Simmons, S.L. Qiu, G.S. Zhu, Targeted Synthesis of a Porous Aromatic Framework with High Stability and Exceptionally High Surface Area, Angewandte Chemie-International Edition, 48 (2009) 9457.
[111] J.S. Lee, X. Wang, H. Luo, G.A. Baker, S. Dai, Facile Ionothermal Synthesis of Microporous and Mesoporous Carbons from Task Specific Ionic Liquids, Journal of the American Chemical Society, 131 (2009) 4596.
[112] S. Han, D.Q. Wu, S. Li, F. Zhang, X.L. Feng, Porous Graphene Materials for Advanced Electrochemical Energy Storage and Conversion Devices, Advanced Materials, 26 (2014) 849.

[113] T. Kyotani, T. Nagai, S. Inoue, A. Tomita, Formation of New Type of Porous Carbon by Carbonization in Zeolite Nanochannels, Chemistry of Materials, 9 (1997) 609.
[114] Z. Ma, T. Kyotani, Z. Liu, O. Terasaki, A. Tomita, Very High Surface Area Microporous Carbon with a Three-Dimensional Nano-Array Structure: Synthesis and Its Molecular Structure, Chemistry of Materials, 13 (2001) 4413.
[115] S. Dutta, A. Bhaumik, K.C.W. Wu, Hierarchically Porous Carbon Derived from Polymers and Biomass: Effect of Interconnected Pores on Energy Applications, Energy & Environmental Science, 7 (2014) 3574.
[116] W. Chaikittisilp, K. Ariga, Y. Yamauchi, A New Family of Carbon Materials: Synthesis of MOF-Derived Nanoporous Carbons and Their Promising Applications, Journal of Materials Chemistry A, 1 (2013) 14.
[117] F.C. Zheng, Y. Yang, Q.W. Chen, High Lithium Anodic Performance of Highly Nitrogen-Doped Porous Carbon Prepared from a Metal-Organic Framework, Nature Communications, 5 (2014).
[118] B. Liu, H. Shioyama, T. Akita, Q. Xu, Metal-Organic Framework as a Template for Porous Carbon Synthesis, Journal of the American Chemical Society, 130 (2008) 5390.
[119] H.-L. Jiang, B. Liu, Y.-Q. Lan, K. Kuratani, T. Akita, H. Shioyama, F. Zong, Q. Xu, From Metal–Organic Framework to Nanoporous Carbon: Toward a Very High Surface Area and Hydrogen Uptake, Journal of the American Chemical Society, 133 (2011) 11854.
[120] S. Gadipelli, T. Zhao, S.A. Shevlin, Z. Guo, Switching Effective Oxygen Reduction and Evolution Performance by Controlled Graphitization of a Cobalt-Nitrogen-Carbon Framework System, Energy & Environmental Science, 9 (2016) 1661.
[121] H.B. Wu, X.W. Lou, Metal-Organic Frameworks and Their Derived Materials for Electrochemical Energy Storage and Conversion: Promises and Challenges, Science Advances, 3 (2017) eaap9252.
[122] E. Raymundo-Pinero, F. Leroux, F. Beguin, A High-Performance Carbon for Supercapacitors Obtained by Carbonization of a Seaweed Biopolymer, Advanced Materials, 18 (2006) 1877.
[123] M.D. Stoller, S.J. Park, Y.W. Zhu, J.H. An, R.S. Ruoff, Graphene-Based Ultracapacitors, Nano Letters, 8 (2008) 3498.
[124] Z. Li, L. Zhang, B.S. Amirkhiz, X.H. Tan, Z.W. Xu, H.L. Wang, B.C. Olsen, C.M.B. Holt, D. Mitlin, Carbonized Chicken Eggshell Membranes with 3D Architectures as High-Performance Electrode Materials for Supercapacitors, Advanced Energy Materials, 2 (2012) 431.

*Every reasonable effort has been made to acknowledge the owners of copyright material. I would be pleased to hear from any copyright owner who has been omitted or incorrectly acknowledged.*

# Chapter 3. Template-Free Synthesis of N-doped Carbon with Pillared-Layered Pores as Bifunctional Materials for Supercapacitor and Environmental Applications


## Abstract

*Using glucose, sodium bicarbonate and urea as the precursors, cross-linked, N-doped, pillared-layered porous carbons (NCs) were prepared via a one-pot, template-free pyrolysis process at 600 (NC600), 700 (NC700) and 800 °C (NC800), which have bifunctional applications in supercapacitors and environmental remediation. NC700 displayed a high surface area (2118 $m^2$ $g^{-1}$) and a specific capacitance of 305 F $g^{-1}$ at 0.2 A $g^{-1}$ in a two-electrode setup. The maximum energy density of NC700 was 20.4 W h/kg at a power density of 139 W $kg^{-1}$, and 89.1% capacitance was retained after 10000 cycles of charge-discharge at 5 A $g^{-1}$. For water remediation, NC800 displayed high adsorption capacities towards flame retardant tetrabromobisphenol A (TBBPA, 372 mg $g^{-1}$) and antibiotic sulfachloropyridazine (SCP, 288 mg $g^{-1}$) in solutions, while NC700 showed the most efficient SCP oxidation removal. These results demonstrate the versatile applications of low-cost and green carbon materials as electrodes in energy storage devices, metal-free adsorbents as well as catalysts for high efficient removal of emerging contaminants in aqueous solution.*


## 3.1 Introduction

Recently, the development of renewable energy resources to alleviate environmental issues from the over-depletion of fossil fuels has accelerated intensive research efforts on technologies such as electrical energy storage devices.[1, 2] As the promising devices in this community, electrical double layer capacitors, also known as supercapacitors, have drawn enormous attention due to the capability to deliver high power density with long cycling life.[3, 4] Supercapacitors play a pivotal role in clean-energy device systems, ranging from lighting on roads, electrical motors in hybrid electric vehicles, lasers, and portable electronics, to name a few.[1, 5, 6] Because of their low cost, high specific surface areas and well-developed porous structure, porous activated carbons have been considered

as first candidate electrode materials for supercapacitors.[7] Direct pyrolysis to synthesize porous carbons without any further activation process represents the most promising method for large-scale production.[8] Until now, such reports are rather limited. For coping with commercial market guidance, the search is still on to exploit high-surface-area porous carbon materials with a facile synthesis method.[9]

Apart from energy, environment issue is another serious challenge that humanity will face with the development of human society. It is noted that severe threat has been posed to the planet Earth and mankind by fresh water contamination.[10] Emerging water contaminants such as SCP antibiotics used in human medicine and aquaculture, or TBBPA, a commercial flame retardant in plastics and electronics, have induced a highly toxic effect on aquatic life and human health.[10] Hopefully, porous carbons bring in new prospects as metal-free materials for the management of these pollutants in effluents. On the one hand, high-surface-area porous carbons can remove the target pollutants by physical adsorption. On the other hand, they can be applied in AOPs by activation of some peroxides such as persulfate ($S_2O_8^{2-}$, PS) for complete removal of these organics.[12] Glaze in 1987 proposed that AOPs are tied to the production of hydroxyl radicals, which bring out the oxidation of organic compounds.[13] Since the 1990s, various reactive oxygen species including sulfate radical, superoxide anion radical, hydrogen peroxide, and singlet oxygen have been proposed.[14] The mechanisms of different AOPs were also studied in terms of the radical species.

This study found that sodium bicarbonate is an excellent in-situ porogen for the synthesis of porous carbon and the critical influence of synthesis temperature on the physicochemical property and microstructure of these porous carbons was explored. In this chapter, NCs are studied at varying synthesis temperatures of 600, 700 and 800 ºC. The process is one-step, time-saving, and mild without harsh treatments such as KOH activation, which is extensively used in the activation process of carbon materials,[15-17] or HF washing for multistep hard-template routes.[18] The synthesized pillared-layered porous carbons were proved to be well-defined bifunctional materials in supercapacitors and water remediation.

## 3.2 Experimental Details

### *3.2.1 Sample Preparation*

Briefly, glucose (1.8 g), sodium bicarbonate (1.8 g), and urea (1.8 g) were dissolved in 60 mL deionized water to form a transparent aqueous solution, which was then put in an oven without stirring and heated at 100 °C for 24 h until dried. Subsequently, the remained mixture was annealed at 600, 700 and 800 °C, respectively, for 2 h in a tubular furnace under a nitrogen atmosphere with a heating rate of 5 °C $min^{-1}$. Finally, to remove residual inorganic salts, the obtained carbon materials were washed with water as well as ethanol, and then, dried at 80 °C. The collected samples were denoted as NC600, NC700 and NC800, respectively.

### *3.2.2 Material Characterizations*

The morphologies of all the samples were revealed by scanning electron microscopy (SEM, FEI Verios XHR 460) and transmission electron microscopy (TEM, JEOL 2100). High angle annular dark field scanning TEM (HAADF-STEM) images and energy-dispersive X-ray spectroscopy (EDX) elemental mapping were obtained by FEI Titan G2 80-200 TEM/STEM. X-ray photoelectron spectroscopy (XPS) was conducted on a Kratos Axis Ultra DLD system under ultra-high vacuum (UHV) conditions. Kratos Vision and Casa XPS software were adopted to process the obtained XPS spectra, and all spectra were calibrated based on a primary C 1s component at 284.6 eV. Raman spectroscopy was characterized on WITec alpha 300RA+. The Brunauer-Emmett-Teller (BET) specific surface area and the pore size distribution of the samples were determined by $N_2$ adsorption/desorption at –196 °C using a Micromertics Tristar 3000. The samples were degassed in vacuum at 110 °C overnight before the test. Electron paramagnetic resonance (EPR) was performed on a Bruker EMS-plus instrument to detect the free radicals, with 5, 5-dimethyl-1-pyrroline N-oxide (DMPO) as a spin-trapping agent and the quantitative information was analyzed by Xeon software (Bruker).

### *3.2.3 Electrochemical Measurements*

In a typical electrochemical measurement, 2 mg carbon powder was dispersed in a mixture of 500 µL isopropanol and 25 µL of Nafion® 117 solution by ultra-sonication. To prepare

the working electrode, 10 µL of the dispersion (containing 36 µg of catalyst) was deposited on a glassy carbon electrode (5.0 mm in diameter) and dried under air. Electrochemical measurements were performed on a Gamry electrochemical workstation (Reference 3000) in 6 M NaOH solution using a standard three-electrode configuration with Ag/AgCl (4 M KCl) as the reference electrode and a Pt wire as the counter electrode. The electrochemical performance comparison of the samples was evaluated by electrochemical impedance spectroscopy (EIS) tests from 10 mHz to 100 KHz.

As an alternative approach to analyze the supercapacitor frequency behaviour, the real and imaginary parts of the capacitance were analysed using the EIS data based on the following equations:

$$Z(\omega) = \frac{1}{j\omega C(\omega)} \qquad (3.1)$$

$$C(\omega) = C'(\omega) - jC''(\omega) \qquad (3.2)$$

$$C'^{(\omega)} = \frac{-Z''(\omega)}{\omega|Z(\omega)|^2} \qquad (3.3)$$

$$C''^{(\omega)} = \frac{Z''(\omega)}{\omega|Z(\omega)|^2} \qquad (3.4)$$

Where $C'(\omega)$ and $C''(\omega)$ represent the real and imaginary parts of the accessible capacitance, respectively.

Two-electrode system tests were carried out using two nearly identical (symmetric by size and weight) electrodes assembled with a separator between them. The working electrode consists of NC700, acetylene black and polytetrafluoroethylene in a weight ratio of 80:10:10. The area of the electrodes is about 1 × 1 $cm^2$ with a mass loading of 2.8 - 3.6 mg. Nickel foam was used as the current collector. Cyclic voltammetry (CV), Galvanostatic charge-discharge tests (GCD), EIS and cycling stability tests of the device were carried out in 6 M NaOH solution. The specific capacitance of a single electrode ($C_s$, F $g^{-1}$) was calculated from the GCD discharge curve based on:

$$C_S = \frac{4I \cdot \Delta t}{m \cdot \Delta V} \qquad (3.5)$$

Where *m* (mg) is the total mass loading of the active materials on both electrodes; ΔV (V) refers to the discharge voltage range excluding the IR drop.[19] The energy density (E, W h $kg^{-1}$) and powder density (P, W $kg^{-1}$) was calculated based on:

$$E = \frac{1}{8} C_S \cdot (\Delta V)^2 \cdot \frac{1}{3.6} \qquad (3.6)$$

$$P = \frac{E}{\Delta t} \times 3600 \qquad (3.7)$$

*3.2.4 Environmental Applications*

Adsorptive experiments were performed by dispersing 10 mg the carbon samples in 200 mL TBBPA solution (20 mg $L^{-1}$) at 25 ºC with constant stirring. The concentration of TBBPA at different time intervals were acquired by measuring the UV-Vis adsorption spectra collected on a Cary 100 UV-Visible Spectrophotometer.

Adsorptive experiments on SCP solutions (20 mg $L^{-1}$, pH 7) were also performed by similar procedures. At different time intervals, the solution was taken, filtered and then tested by using an ultra-high performance liquid chromatography (UHPLC) to determine the SCP concentration.

For SCP oxidative tests at 25 ºC, 10 mg carbon sample and 0.35 g potassium persulfate were added together into 200 mL SCP solutions to initiate the reaction. At certain time intervals, 1.0 mL of solution was withdrawn, filtered and quenched instantly by mixing with 0.5 mL of sodium nitrite solution (0.1 M). Each experiment was repeated at least three times, and the results were reproducible.

## 3.3 Results and Discussion

*3.3.1 Characterization of NCs*

Figures 3.1-3.3 display that NC600, NC700 and NC800 present 3D porous structure, with open pores distributed continuously along the pillared pore channels. It is known that blocked pore texture in conventional activated carbons greatly restricts the pore accessibility of electrolyte ions,[15] while carbon materials with open pore networks are desirable for supercapacitors. Such nano-architecture can not only shorten diffusion pathways to accelerate ion transport, but also provide a continuous electron pathway for

electrical contact.[20] Long, curved graphite ribbons are clearly observed in the HRTEM images of all samples, indicating the amorphous nature with the existence of $sp^2$-bonded C that is especially favourable to electrical conductivity.[21]

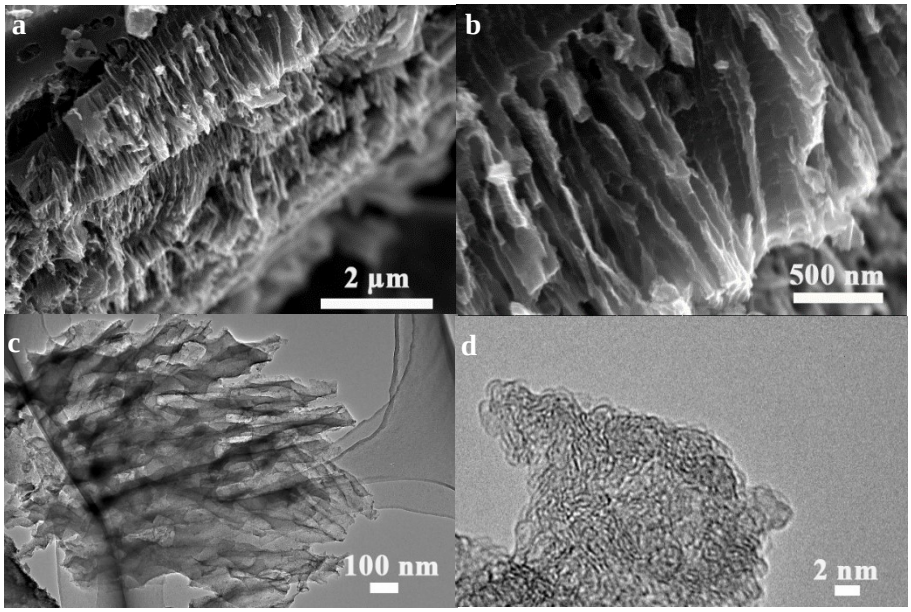


**Figure 3.1** a, b) SEM, c) TEM and d) HRTEM images of NC600.

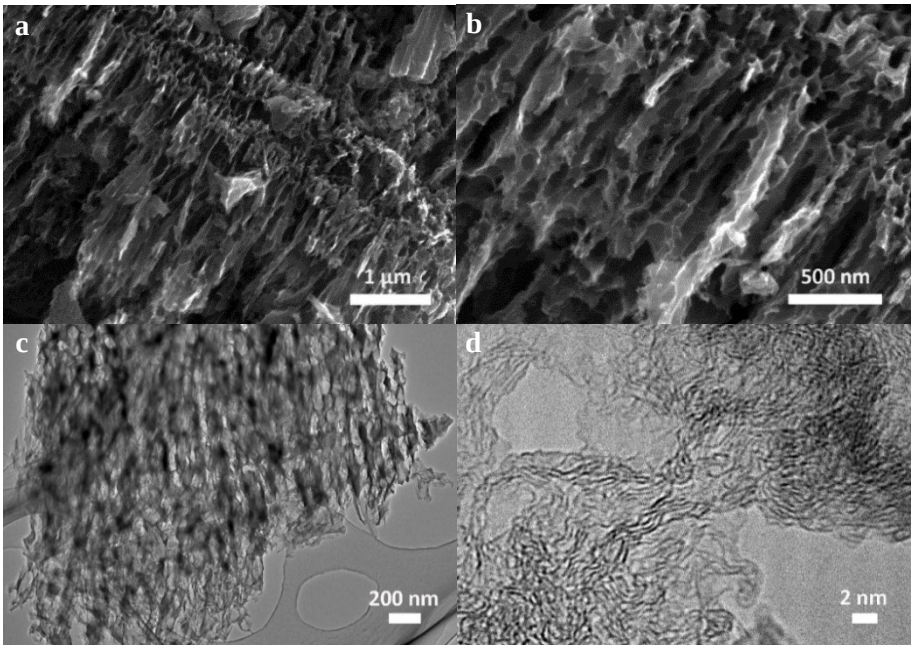


**Figure 3.2** a, b) SEM, c) TEM and d) HRTEM micrographs of NC700.

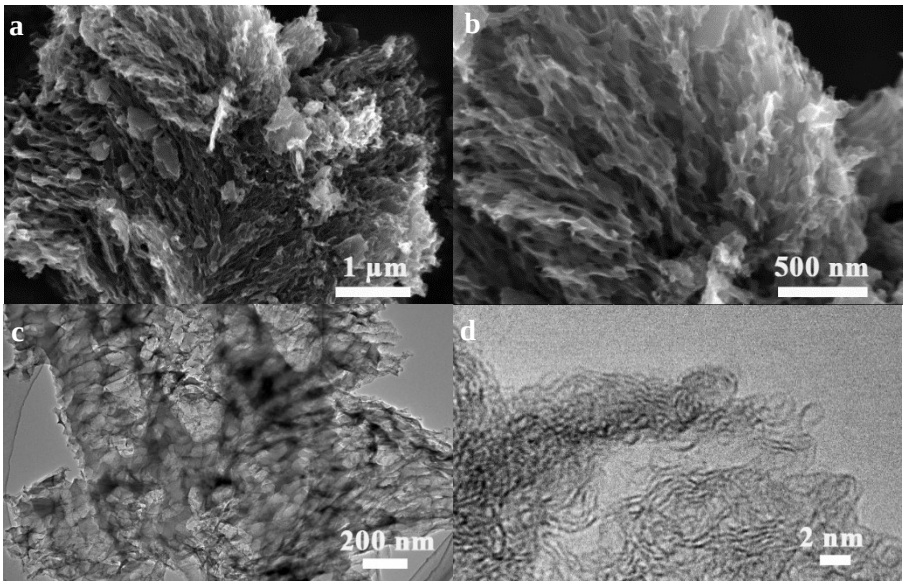


**Figure 3.3** a, b) SEM, c) TEM and d) HRTEM images of NC800.

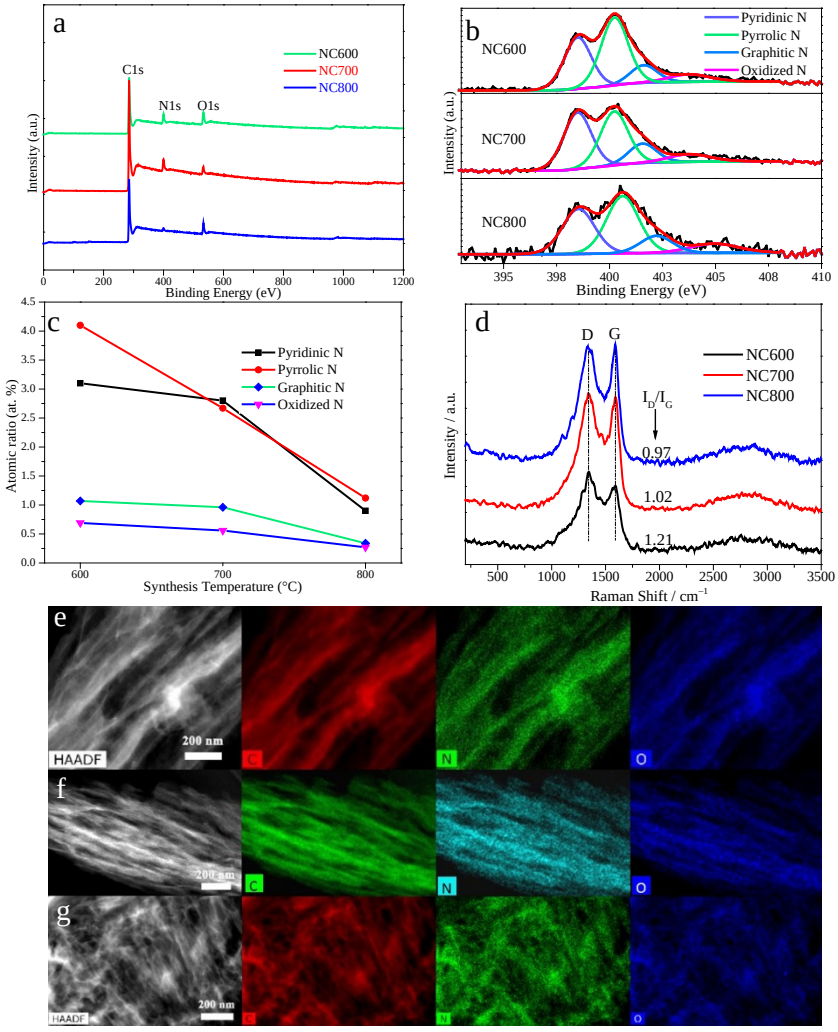


**Figure 3.4** a) XPS survey, b) high resolution N 1s survey, c) the evolution of different N species versus synthesis temperature and d) Raman spectra. HAADF-STEM and corresponding EDX elemental mapping images of e) NC 600, f) NC700 and g) NC800.

The surface chemical states of NCs were probed by XPS analysis and summarized in Figure 3.4 and Table 3.1. Nitrogen content decreased from 9.0 at.% for NC600, 7.0 at.% for NC700 to 2.6 at.% in NC800. Oxygen content showed a similar trend, descending from 8.1 at.%, 3.0 at.% to 2.2 at.%, correspondingly, possibly due to the instability and decomposition of some functional groups at higher temperatures. The elemental mapping tests indicated that C, N and O elements distributed uniformly along the pore frameworks of NCs (Figure 3.4e-f). N 1s spectra (Figure 3.4b) were fitted into four individual peaks located at around 398, 400, 401 and 404 eV, in accordance with pyridinic-, pyrrolic-, graphitic- and oxidized-N, respectively.[11, 22, 23] Figure 3.4c illustrates that, with the increase of the temperature, pyridinic-N and pyrrolic-N contents declined greatly while graphitic- and oxidized-N were more thermally stable. Raman spectra (Figure 3.4d) show the decrease in $I_D/I_G$ ratios from NC600 to NC800, suggesting a more ordered, graphitic crystalline structure and fewer defects with the rise of synthesis temperatures.

**Table 3.1** Physical and chemical properties of NC600, NC700 and NC800.

| Samples | $S_{BET}$ [a)] / $m^2\,g^{-1}$ | $V_t$ [b)] / $cm^3\,g^{-1}$ | $V_{mic}$ [c)] / $cm^3\,g^{-1}$ | C / at.% | N / at.% | O / at.% |
|---|---|---|---|---|---|---|
| NC600 | 1227.2 | 0.77 | 0.42 | 82.9 | 9.0 | 8.1 |
| NC700 | 2118.3 | 1.25 | 0.40 | 90.0 | 7.0 | 3.0 |
| NC800 | 1392.2 | 0.84 | 0.29 | 95.2 | 2.6 | 2.2 |

[a)] Specific BET surface area.
[b)] Total pore volume calculated at $P/P_0 = 0.99$.
[c)] Micropore volume obtained by the t-plot method.

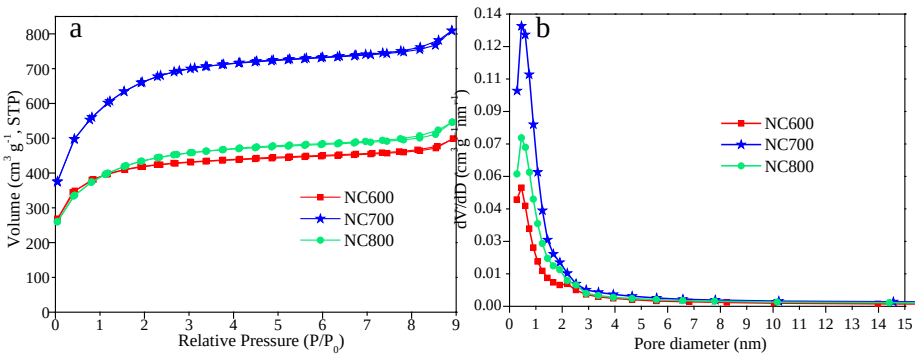


**Figure 3.5** a) $N_2$ sorption isotherms and b) BJH pore size distribution.

$N_2$ sorption isotherms of NCs were provided in Figure 3.5, which proved the excellent porogen role of sodium bicarbonate. Notably, NCs displayed well-defined plateaus in the

low-pressure range, illustrating the presence of abundant micropores. A narrow pore size distribution is observed in NCs (Figure 3.5b), with the majority of pores below 3.0 nm, while minority large mesopores also distributed continuously over a wider range. It is noting that narrow pore size distribution is profitable to achieve a higher capacitance in supercapacitors.[5] The textural properties of NCs were compared in Table 3.1. The total pore volume ($V_t$) of the samples increased first and then declined with elevated synthesis temperatures. Both $V_t$ and BET surface area ($S_{BET}$) reached the maximum in NC700. With increasing synthesis temperatures, micropore volumes did not change much from 600 to 700 °C but decreased obviously at 800 °C, while mesopore volume maximized at 700 °C. It is thus projected that 600 °C might be too low for optimal activation by $NaHCO_3/Na_2CO_3$, whereas pores will collapse at higher temperatures (800 °C). Therefore, 700 °C is the supreme activation temperature for synthesizing porous carbons with excellent textural properties in this system. Remarkably, all the samples possessed large $S_{BET}$ in the range between 1227.2 and 2118.3 $m^2 g^{-1}$, which are critical for supercapacitor and organic contaminant adsorption applications.

### *3.3.2 Electrochemical Properties of NCs*

Electrochemical performances of NCs were first evaluated by EIS measurement in a typical three-electrode setup in 6 M NaOH. Nyquist plots were obtained from EIS tests (Figure 3.6a) to understand the electrochemical performance. There were no semicircles (inset image) in the high frequency region of NCs, suggesting the low charge transfer resistance, excellent electrical conductivity and fast ion diffusion during charge/discharge operation.[24] The steep slopes of NC700 and NC800 in the low frequency region, indicated their near-ideal capacitive response,[25] better than NC600. The real and imaginary parts of the capacitance as a function of the frequency are presented in Figure 3.6b and c. From the peak frequency in the evolution curve of C″, a relaxation time constant ($\tau_0 = 1/2\pi f$) was obtained,[26] which is defined as the minimum time to discharge its storage energy with an efficiency higher than 50%.[24, 25] NC600, NC700, and NC800 exhibited operating frequencies of 5.5, 15.9 and 23.6 Hz, respectively. NC700 showed a small $\tau_0$ (0.01s) (similar to NC800 while lower than NC600), with much higher areal capacitance than NC600 and NC800, suggesting that it can deliver high power rapidly with a larger energy capacity.[24] It is also reported that a large specific surface area is conducive to acquire a high capacitance, promising for excellent energy performance.[3,

4] Based on the above EIS analysis, NC700 with the highest $S_{BET}$ is the first-candidate electrode material among NCs for supercapacitors.

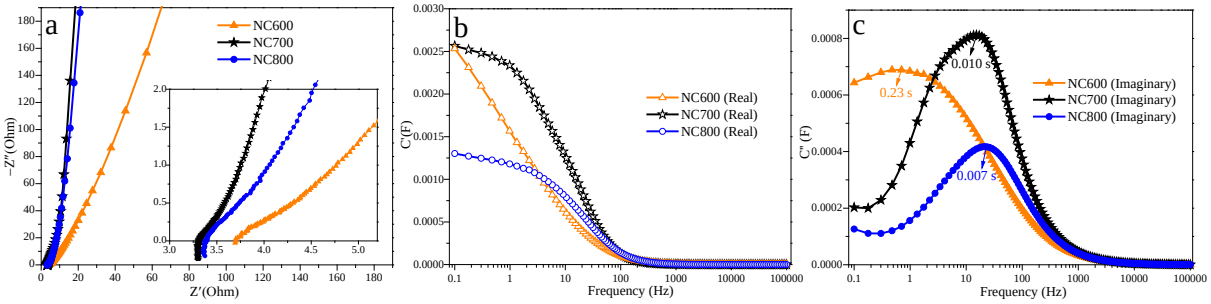


**Figure 3.6** EIS characterization of NCs in 6 M NaOH. a) Nyquist plots, b) the real, and c) imaginary part of capacitance versus frequency.

### *3.3.3 Supercapacitor Measurement of NC700 in a Two-Electrode Setup*

Utilizing NC700, a symmetric supercapacitor was assembled and tested in 6 M NaOH. The inset image of CV curves in Figure 3.7a exhibits that there was no obvious increase of anodic current even at an operating window of 0 - 1.4 V, which is much higher than typical symmetric supercapacitors in an aqueous system (in general ≤ 1.0 V).[27] The rectangular nature of CV curves illustrated the double-layer formation at electrode/electrolyte interface with no obvious redox reaction and a well-defined current response. GCD curves (Figure 3.7b) were triangular in nature, further confirming the efficient ion transport and low internal resistance.[25] Calculated from the GCD profiles, the specific capacitances for current densities from 0.2 - 20 A $g^{-1}$ are given in Figure 3.7c. NC700 delivered an impressive specific capacitance of 305 F $g^{-1}$ at 0.2 A $g^{-1}$, and retained 183 F $g^{-1}$ at a higher current density of 20 A $g^{-1}$, which are among the highest values of carbon-based materials, as compared in Table 3.2. 60% specific capacitance was retained when elevating the discharge rate 100 times, exhibiting decent rate capability. The voltage drop was 0.01 V at the start of a discharge curve at 0.2 A $g^{-1}$, indicating a very low resistance in the assembled supercapacitor. Nyquist plots of the device were shown in Figure 3.7d. The short x-intercept (0.16 Ω), small equivalent series resistance (0.33 Ω) assessed via the linear interpolation method (as depicted in the inset graph),[28] and the steep slope at low frequency region indicated that NC700 electrode possessed low internal and charge-transfer resistance, as well as superior pore accessibility to the electrolyte.[19]

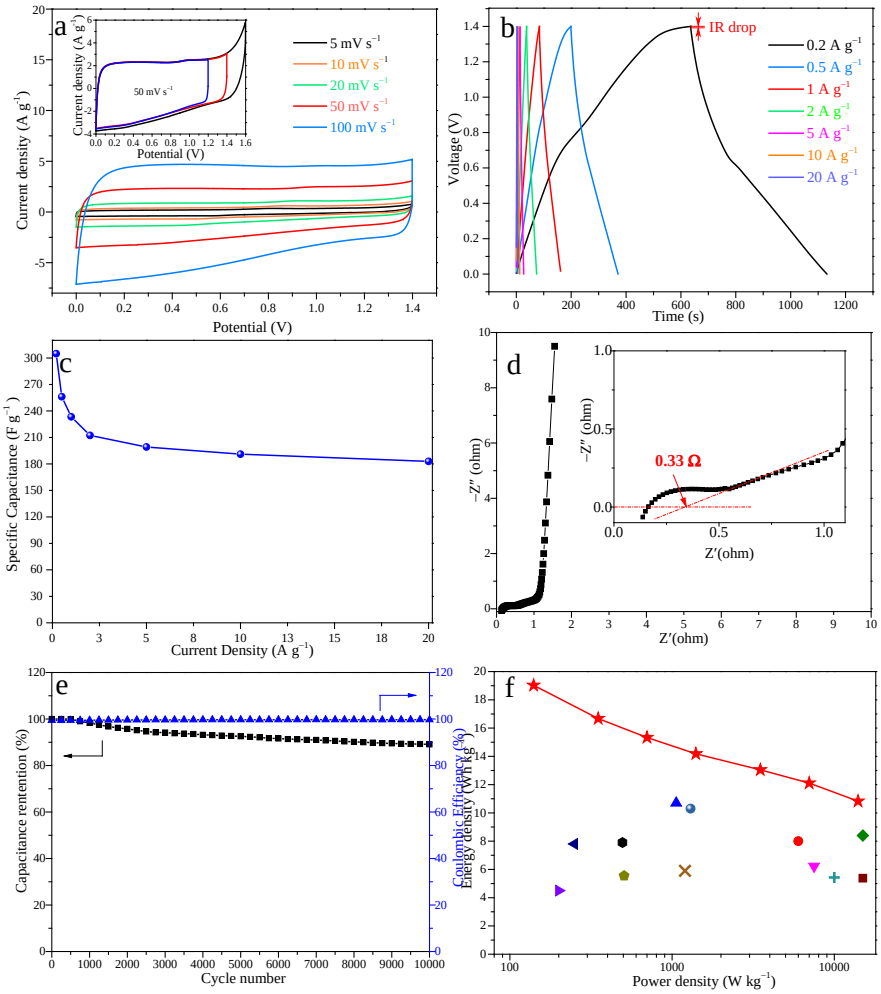


**Figure 3.7** Electrochemical capacitive behavior of NC700 symmetric supercapacitor in 6 M NaOH: a) CV curves in different voltage windows at a scan rate of 50 mV $s^{-1}$ (inset) and CV curves at different scan rates, b) GCD profiles, c) specific capacitance as a function of current density, d) Nyquist plot, e) cyclability and columbic efficiency over 10000 cycles at 5 A $g^{-1}$ and f) Ragone plot of our device in comparison of other reports. [29-39]

Figure 3.7e shows the cycling performance of this symmetric cell, which illustrated capacitance retention of about 89.1% after 10000 charge-discharge cycles at 5 A $g^{-1}$, with high columbic efficiency maintaining around 99.7%. More importantly, the assembled symmetric cell displayed a high energy density of 20.4 W h $kg^{-1}$ at a power density of 139 W $kg^{-1}$, while 9.6 W h/kg at the highest power density of 12213 W $kg^{-1}$. This performance is superior to those of previously reported symmetric carbon-based supercapacitors in aqueous electrolyte (Figure 3.7f).[29-39]

**Table 3.2** Comparison of specific capacitances with recently reported literature in a symmetric two-electrode system.

| Samples | $S_{BET}$ / $m^2 g^{-1}$ | Specific electrode capacitance (F $g^{-1}$) | Rate capability | Voltage windows (V) | Electrolyte | Test method |
|---|---|---|---|---|---|---|
| B/N-CS | 416 | 223 at 0.1 A $g^{-1}$ | 223 - 100 F $g^{-1}$ at 0.1 - 100 A $g^{-1}$ | -1 - -0.1 | 6 M KOH | 2-GCD [29] |
| THPC | 2870 | 200.8 at 5 A $g^{-1}$ | 236.3- 182.3 F $g^{-1}$ at 2 - 30 A $g^{-1}$ | 0 - 1 | 6 M KOH | 2-GCD [19] |
| A-HHPC | 2666 | 124 at 5 A $g^{-1}$ | 214 - 120 F $g^{-1}$ at 0.2 - 10 A $g^{-1}$ | -1 - 0 | 6 M KOH | 2-GCD [40] |
| UCM-1 | 1267.2 | 226.5 at 0.5 A $g^{-1}$ | - | 0 - 1 | 6 M KOH | 2-GCD [41] |
| A850-6-3 | 2294 | 225 at 0.5 A $g^{-1}$ | 225 - 192 F $g^{-1}$ at 0.5 - 10 A $g^{-1}$ | 0 - 1 | 6 M KOH | 2-GCD [32] |
| HPC | 353 | 204 at 0.5 A $g^{-1}$ | 204 - 152 F $g^{-1}$ at 0.5 - 32 A $g^{-1}$ | 0 - 0.8 | 6 M KOH | 2-GCD [33] |
| TC-1 | 2115 | 217.6 at 0.5 A $g^{-1}$ | 217.6 - 175.2 F $g^{-1}$ at 0.5 - 1 A $g^{-1}$ | 0 - 1 | 6 M KOH | 2-GCD [42] |
| FGH-150 | 1006 | 180 at 1 A $g^{-1}$ | - | 0 - 1 | 6 M KOH | 2-GCD [36] |
| HP-CF | 1175 | 237.6 at 0.5 A $g^{-1}$ | - | 0 - 1 | 3 M KOH | 2-GCD [43] |
| A-p-BC–N-x | 312.5 | 195.4 at 1 A $g^{-1}$ | - | 0 - 1 | 2 M $H_2SO_4$ | 2-GCD [44] |
| IMPC | 1327 | 254 at 0.5 A $g^{-1}$ | 254-140 F $g^{-1}$ at 0.5 - 30 A $g^{-1}$ | 0-1 | 1 M $H_2SO_4$ | 2-GCD [9] |
| NC 700 | 2118 | 256 at 0.5 A $g^{-1}$ | 305 - 183 F $g^{-1}$ at 0.2 - 20 A $g^{-1}$ | 0 - 1.4 | 6 M NaOH | 2-GCD, This work |

The above results suggest that the synthesized pillared-layered porous carbon is an excellent electrode material for supercapacitors. The well-defined supercapacitor performance can be ascribed to the following attributes: (i) oxygenated or N functionalities promote surface wettability while curved graphitic texture endows it with outstanding electrical conductivity and ultrafast charge-discharge ability;[19] (ii) high surface area as well as abundant micropores wetted by the electrolyte can serve as electrochemically active sites for ion adsorption and electrical-double-layer formation;[45] (iii) the cross-linked, pillared-layered mesopores can provide continuous channels for fast electrolyte ion transport to promote excellent power performance.[2]

*3.3.4 Environmental Application of NCs for Water Remediation*

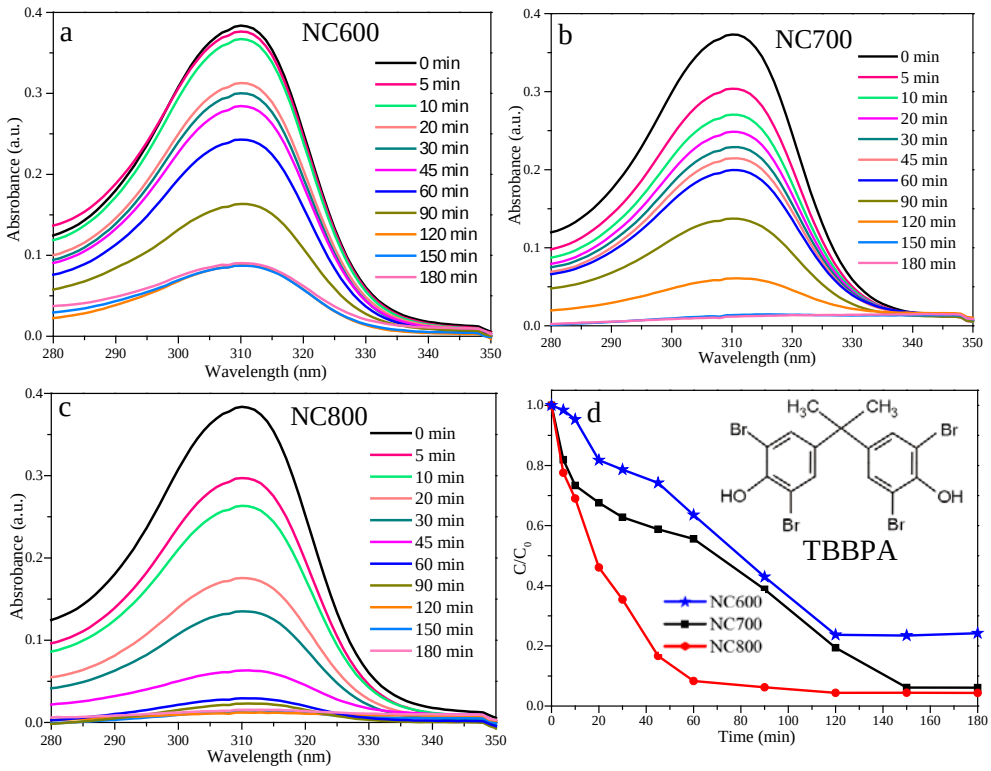


**Figure 3.8** Adsorption test on TBBPA using NCs. a-c) UV-vis absorption spectra of TBBPA solution after adding NCs at 25 °C at different time intervals. d) TBBPA removal by adsorption calculated from the peak value ratios of a-c. The insert image is the molecular structure of TBBPA. (Adsorbent: 0.05 g $L^{-1}$, TBBPA: 20 mg $L^{-1}$)

Adsorption experiment was performed on TBBPA, as presented in Figure 3.8. Although the BET surface area of NC800 is not the highest, NC800 adsorbed 94% of TBBPA (20 mg $L^{-1}$), acquiring the highest adsorption capacity of 372 mg $g^{-1}$, followed by NC700 (364 mg $g^{-1}$) and NC600 (287 mg $g^{-1}$). The adsorption capability of NC800 is more superior after normalized with BET surface area (Table 3.3). Similar adsorption experiment using NCs was conducted on SCP and provided in Figure 3.9. Also, NC800 exhibited the best adsorption performance and provided 77% of SCP removal, followed by NC700 (69%) and NC600 (40%). The calculated adsorption capacity of NC800 on SCP (288 mg $g^{-1}$) is 96, 9.6, and 3.6 times better than other common metal-free adsorbents including graphene oxide (GO), reduced graphene oxide (rGO) and single-walled carbon nanotube (SWCNT), as compared in Table 3.3. After normalizing with $S_{BET}$, the adsorption capabilities of NC600 and NC700 were similar to GO and rGO, while NC800

was much higher, approaching SWCNT. Generally, the adsorption ability involves several aspects, e.g. interaction with surface O-functional groups, van der Waals forces, π-π interaction.[46-48] It is deduced that the higher graphitic degree in NC800 (as confirmed by Raman results) makes for its elevated adsorption capability. It is widely agreed that the interaction between $sp^2$-bonded carbon atoms and delocalized π-bond of the organic aromatic compounds is a crucial adsorption driving force.[47, 48]

**Table 3.3** Comparison in adsorption with different carbon forms.

| | GO[11] | rGO[11] | SWCNT[11] | NC600 | NC700 | NC800 |
|---|---|---|---|---|---|---|
| Adsorption capacity for SCP ($q_m$, mg $g^{-1}$) | 3 | 30 | 80 | 148 | 260 | 288 |
| $S_{BET}$ ($m^2$ $g^{-1}$) | 30 | 255 | 366 | 1227 | 2118 | 1392 |
| $q_m/S_{BET}$ for SCP (mg $m^{-2}$) | 0.10 | 0.12 | 0.22 | 0.12 | 0.12 | 0.21 |
| Adsorption capacity for TBBPA ($q_m$, mg $g^{-1}$) | - | - | - | 287 | 364 | 372 |

As aforementioned, AOPs via PS activation is a more efficient approach compared to adsorption for removing organic pollutant completely in wastewater. PS is stable at room temperature, and it can be activated via different techniques like heating, UV light irradiation, carbon-based catalysts, transition metals, etc.[49] Highly reactive sulfate radicals ($SO_4^{\bullet-}$) will be formed through PS activation, as shown in Equation 3.8.

$$S_2O_8^{2-} + \text{activator} \rightarrow SO_4^{\bullet-} + (SO_4^{\bullet-} \text{ or } SO_4^{2-}) \quad (3.8)$$

Sulfate radicals will react with water and generate hydroxyl radicals (Equation 3.9). It is reported that sulfate and hydroxyl radicals (•OH) take part in the reactions of AOPs equally.

$$SO_4^{\bullet-} + H_2O \rightarrow SO_4^{2-} + \bullet OH + H^+ \quad (3.9)$$

Here this study also tested the catalytic ability of NCs for PS activation. For SCP removal by AOPs, PS alone could hardly affect SCP decomposition as shown in Figure 3.9a. Remarkably, after addition with NC600, NC700 and NC800, complete SCP removal was achieved in 30, 5 and 25 min. The following pseudo-first-order reaction was used to calculate the kinetic reaction rates during these PS-activated AOPs.

$$\ln(C/C_0) = -kt \qquad (4.0)$$

Here $C_0$ and C represent the initial concentration and that after different reaction time, while k refers to the reaction rate constant.

NC600, NC700 and NC800 delivered a reaction rate constant of 0.12, 0.51 and 0.21 $min^{-1}$, respectively. NC700 displayed a really powerful catalytic degradation capability with such a low concentration (0.05 g $L^{-1}$) in 20 mg $L^{-1}$ SCP solution. PS activation over NC700 was also conducted at 25, 35, and 45 $^oC$ (Figure 3.9b), suggesting that higher reaction rate could be achieved at a higher temperature. Although NC700 loading was halved, 100% SCP removal was still achieved in 30 min at 35 $^oC$ while 10 min at 45 $^oC$. Using the Arrhenius equation (4.1), the activation energy ($E_a$) of NC700 for SCP degradation was estimated to be 76.1 kJ $mol^{-1}$ (Figure 3.9c, $R^2 = 0.97$).

$$\ln(k) = -\frac{E_a}{RT} + \ln(A) \qquad (4.1)$$

Here k is the reaction rate constant, R is the gas constant, T is the reaction temperature, and A is a rate constant. Plot a straight line using ln(k) versus $T^{-1}$, whose gradient and intercept are adopted to evaluate $E_a$ and A.

To make clear which radical species dominate the powerful AOP process, in-situ electron paramagnetic resonance (EPR) was performed. 5, 5-dimethyl-1-pyrroline N-oxide (DMPO) was utilized as a spin trapping agent to capture the generated radicals. As shown in Figure 3.9d, apart from DMPOX which was denoted as the oxidized DMPO, strongly oxidizing sulfate radicals ($SO_4^{\bullet-}$) and strong signals of hydroxyl radicals (•OH) were detected after PS and NC700 addition. Therefore, as described in Scheme 3.1, NC 700 work effectively in catalyzing PS to produce $SO_4^{\bullet-}$ and •OH, which contributed collectively to the efficient oxidation and degradation of SCP.

Generally, the excellent catalytic ability of NC700 in activating PS can be analysed in several aspects. i) Effective N doping is widely considered to benefit the catalytic ability. It is reported that negatively charged N species will affect the charge density of adjacent carbon, inducing more positively charged C for better reactivity in catalysis.[50-52] ii) The high $S_{BET}$ and interconnected pore structure allow more exposure of catalytically active sites. iii) Excellent adsorption also promotes better catalytic activity, but these are

two process, and high adsorption capacity does not mean high catalytic ability. The final performance in AOPs is determined by the catalytic ability of NCs. As indicated in this work, NC700 possessed an inferior adsorption capacity but a better catalytic performance than NC800.

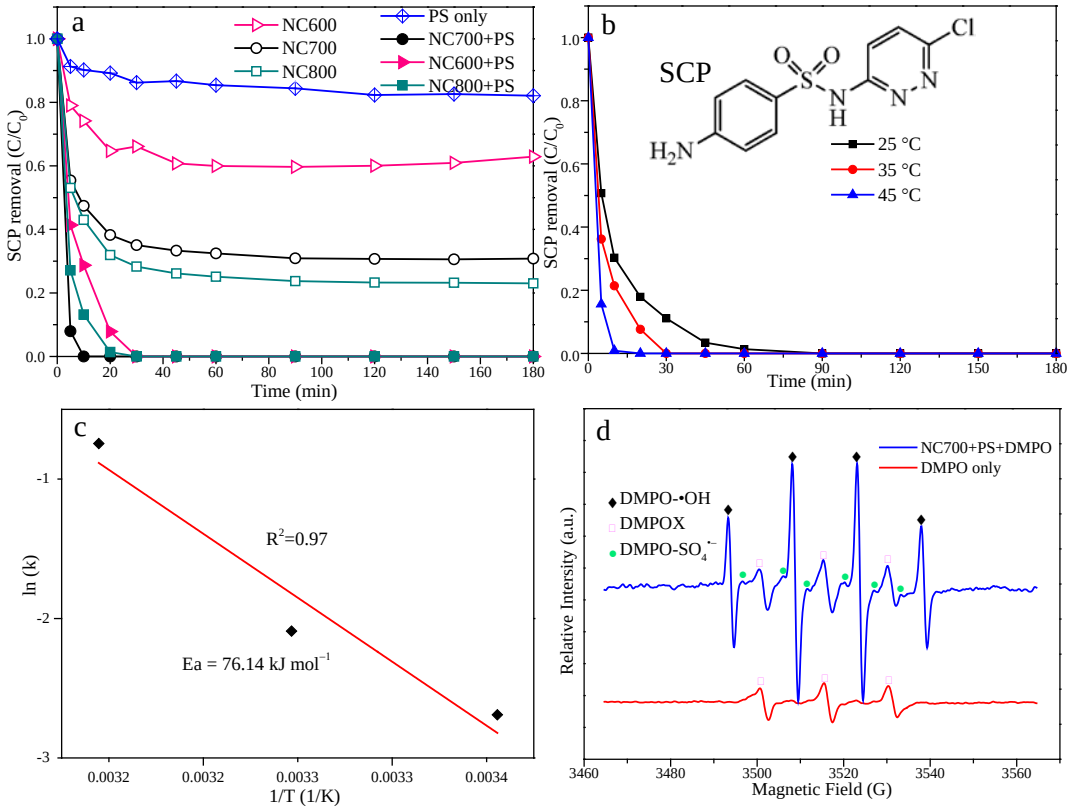


**Figure 3.9** a) SCP removal by adsorption and AOP degradation at 25 °C (Adsorbent or catalyst: 0.05 g $L^{-1}$, SCP: 20 mg $L^{-1}$, PS 6.5 mM); b) impact of solution temperature on the AOP process on SCP (Catalyst: NC700, 0.0025 g $L^{-1}$, PS 6.5 mM, SCP: 20 mg $L^{-1}$) and the insert is the molecular structure of SCP; c) estimation of the activation energy for NC700 and d) EPR test.

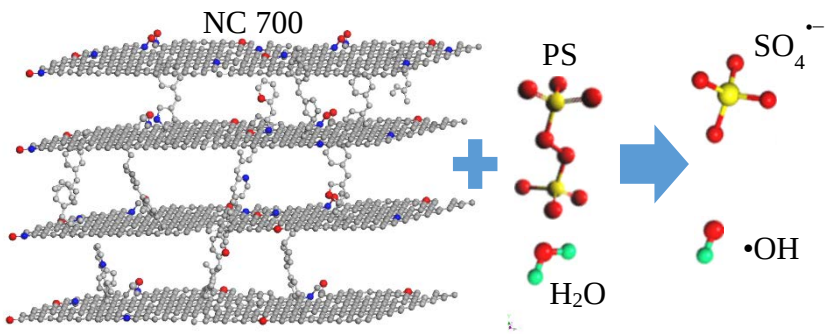


**Scheme 3.1** Schematic illustration of PS activation by N-doped porous carbon. (C: Grey; O: Red; N: Blue; S: Yellow; H: Green)

## 3.4 Conclusions

In conclusion, N-doped, pillared-layered porous carbons were prepared at 600, 700 and 800 ºC via a flexible and scalable pyrolysis process. Synthesis temperature induces a crucial impact on the physical, chemical properties as well as the corresponding supercapacitor, adsorption and AOP performance. The porous carbons were constructed of the 3D network with open pores consisting of graphitic domains and a narrow pore size distribution. NC700 exhibits a high specific capacitance, excellent power performance and attractive energy densities for supercapacitor application. NC800 shows a high adsorption capacity towards SCP and TBBPA, while NC700 is most effective to activate PS to generate sulfate and hydroxyl radicals for efficient SCP removal in AOPs. NCs show great potential for application in flexible energy storage system and can serve as a promising metal-free candidate for environmental pollution management.

## References

[1] E. Raymundo-Pinero, M. Cadek, F. Beguin, Tuning Carbon Materials for Supercapacitors by Direct Pyrolysis of Seaweeds, Advanced Functional Materials, 19 (2009) 1032.

[2] K.S. Xia, Q.M. Gao, J.H. Jiang, J. Hu, Hierarchical Porous Carbons with Controlled Micropores and Mesopores for Supercapacitor Electrode Materials, Carbon, 46 (2008) 1718.

[3] Y. Gao, Y.S. Zhou, M. Qian, X.N. He, J. Redepenning, P. Goodman, H.M. Li, L. Jiang, Y.F. Lu, Chemical Activation of Carbon Nano-Onions for High-Rate Supercapacitor Electrodes, Carbon, 51 (2013) 52.

[4] J.B. Zhang, L.J. Jin, J. Cheng, H.Q. Hu, Hierarchical Porous Carbons Prepared from Direct Coal Liquefaction Residue and Coal for Supercapacitor Electrodes, Carbon, 55 (2013) 221.

[5] G. Feng, P.T. Cummings, Supercapacitor Capacitance Exhibits Oscillatory Behavior as a Function of Nanopore Size, Journal of Physical Chemistry Letters, 2 (2011) 2859.

[6] J. Yan, J. Liu, Z. Fan, T. Wei, L. Zhang, High-Performance Supercapacitor Electrodes Based on Highly Corrugated Graphene Sheets, Carbon, 50 (2012) 2179.

[7] X. Li, B.Q. Wei, Supercapacitors Based on Nanostructured Carbon, Nano Energy, 2 (2013) 159.

[8] C.Z. Zhu, H. Li, S.F. Fu, D. Du, Y.H. Lin, Highly Efficient Nonprecious Metal Catalysts Towards Oxygen Reduction Reaction Based on Three-Dimensional Porous Carbon Nanostructures, Chemical Society Reviews, 45 (2016) 517.

[9] D. Puthusseri, V. Aravindan, S. Madhavi, S. Ogale, 3D Micro-Porous Conducting Carbon Beehive by Single Step Polymer Carbonization for High Performance Supercapacitors: The Magic of in Situ Porogen Formation, Energy & Environmental Science, 7 (2014) 728.

[10] X. Wang, X. Hu, H. Zhang, F. Chang, Y. Luo, Photolysis Kinetics, Mechanisms, and Pathways of Tetrabromobisphenol a in Water under Simulated Solar Light Irradiation, Environmental Science & Technology, 49 (2015) 6683.

[11] W.J. Tian, H.Y. Zhang, X.G. Duan, H.Q. Sun, M.O. Tade, H.M. Ang, S.B. Wang, Nitrogen- and Sulfur-Codoped Hierarchically Porous Carbon for Adsorptive and Oxidative Removal of Pharmaceutical Contaminants, ACS Applied Materials & Interfaces, 8 (2016) 7184.

[12] A. Dirany, I. Sires, N. Oturan, A. Ozcan, M.A. Oturan, Electrochemical Treatment of the Antibiotic Sulfachloropyridazine: Kinetics, Reaction Pathways, and Toxicity Evolution, Environmental Science & Technology, 46 (2012) 4074.

[13] W.H. Glaze, J.-W. Kang, D.H. Chapin, The Chemistry of Water Treatment Processes Involving Ozone, Hydrogen Peroxide and Ultraviolet Radiation, Ozone: Science & Engineering, 9 (1987) 335.

[14] K.E. O'Shea, D.D. Dionysiou, Advanced Oxidation Processes for Water Treatment, Journal of Physical Chemistry Letters, 3 (2012) 2112.

[15] Y. Li, G. Wang, T. Wei, Z. Fan, P. Yan, Nitrogen and Sulfur Co-Doped Porous Carbon Nanosheets Derived from Willow Catkin for Supercapacitors, Nano Energy, 19 (2016) 165.

[16] E. Vilaplana-Ortego, M.A. Lillo-Rodenas, J. Alcaniz-Monge, D. Cazorla-Amoros, A. Linares-Solano, Isotropic Petroleum Pitch as a Carbon Precursor for the Preparation of Activated Carbons by Koh Activation, Carbon, 47 (2009) 2141.

[17] M.A. Lillo-Rodenas, D. Cazorla-Amoros, A. Linares-Solano, Understanding Chemical Reactions between Carbons and Naoh and Koh - an Insight into the Chemical Activation Mechanism, Carbon, 41 (2003) 267.

[18] J. Wei, D.D. Zhou, Z.K. Sun, Y.H. Deng, Y.Y. Xia, D.Y. Zhao, A Controllable Synthesis of Rich Nitrogen-Doped Ordered Mesoporous Carbon for $CO_2$ Capture and Supercapacitors, Advanced Functional Materials, 23 (2013) 2322.

[19] L. Qie, W.M. Chen, H.H. Xu, X.Q. Xiong, Y. Jiang, F. Zou, X.L. Hu, Y. Xin, Z.L. Zhang, Y.H. Huang, Synthesis of Functionalized 3D Hierarchical Porous Carbon for High-Performance Supercapacitors, Energy & Environmental Science, 6 (2013) 2497.
[20] H. Wang, Z.W. Xu, A. Kohandehghan, Z. Li, K. Cui, X.H. Tan, T.J. Stephenson, C.K. King'ondu, C.M.B. Holt, B.C. Olsen, J.K. Tak, D. Harfield, A.O. Anyia, D. Mitlin, Interconnected Carbon Nanosheets Derived from Hemp for Ultrafast Supercapacitors with High Energy, Acs Nano, 7 (2013) 5131.
[21] D.Y. Chung, K.J. Lee, S.H. Yu, M. Kim, S.Y. Lee, O.H. Kim, H.J. Park, Y.E. Sung, Alveoli-Inspired Facile Transport Structure of N-Doped Porous Carbon for Electrochemical Energy Applications, Advanced Energy Materials, 5 (2015).
[22] J.F. Moulder, J. Chastain, R.C. King, Handbook of X-Ray Photoelectron Spectroscopy: A Reference Book of Standard Spectra for Identification and Interpretation of Xps Data, Perkin-Elmer Eden Prairie, MN1992.
[23] Q. Shi, R. Zhang, Y. Lv, Y. Deng, A.A. Elzatahrya, D. Zhao, Nitrogen-Doped Ordered Mesoporous Carbons Based on Cyanamide as the Dopant for Supercapacitor, Carbon, 84 (2015) 335.
[24] J. Lim, U.N. Maiti, N.Y. Kim, R. Narayan, W.J. Lee, D.S. Choi, Y. Oh, J.M. Lee, G.Y. Lee, S.H. Kang, H. Kim, Y.H. Kim, S.O. Kim, Dopant-Specific Unzipping of Carbon Nanotubes for Intact Crystalline Graphene Nanostructures, Nature Communications, 7 (2016).
[25] Y.J. Li, G.L. Wang, T. Wei, Z.J. Fan, P. Yan, Nitrogen and Sulfur Co-Doped Porous Carbon Nanosheets Derived from Willow Catkin for Supercapacitors, Nano Energy, 19 (2016) 165.
[26] P.L. Taberna, P. Simon, J.F. Fauvarque, Electrochemical Characteristics and Impedance Spectroscopy Studies of Carbon-Carbon Supercapacitors, Journal of the Electrochemical Society, 150 (2003) A292.
[27] R.Z. Li, Y.M. Wang, C. Zhou, C. Wang, X. Ba, Y.Y. Li, X.T. Huang, J.P. Liu, Carbon-Stabilized High-Capacity Ferroferric Oxide Nanorod Array for Flexible Solid-State Alkaline Battery-Supercapacitor Hybrid Device with High Environmental Suitability, Advanced Functional Materials, 25 (2015) 5384.
[28] S. Zhang, N. Pan, Supercapacitors Performance Evaluation, Advanced Energy Materials, 5 (2015) 1401401.
[29] Z. Ling, Z.Y. Wang, M.D. Zhang, C. Yu, G. Wang, Y.F. Dong, S.H. Liu, Y.W. Wang, J.S. Qiu, Sustainable Synthesis and Assembly of Biomass-Derived B/N Co-Doped Carbon

Nanosheets with Ultrahigh Aspect Ratio for High-Performance Supercapacitors, Advanced Functional Materials, 26 (2016) 111.
[30] Y.F. Zhao, Z. Zhang, Y.Q. Ren, W. Ran, X.Q. Chen, J.S. Wu, F.M. Gao, Vapor Deposition Polymerization of Aniline on 3D Hierarchical Porous Carbon with Enhanced Cycling Stability as Supercapacitor Electrode, Journal of Power Sources, 286 (2015) 1.
[31] W.J. Qian, J.Y. Zhu, Y. Zhang, X. Wu, F. Yan, Condiment-Derived 3d Architecture Porous Carbon for Electrochemical Supercapacitors, Small, 11 (2015) 4959.
[32] Y.X. Huang, L.L. Peng, Y. Liu, G.J. Zhao, J.Y. Chen, G.H. Yu, Biobased Nano Porous Active Carbon Fibers for High-Performance Supercapacitors, Acs Applied Materials & Interfaces, 8 (2016) 15205.
[33] F.J. Miao, C.L. Shao, X.H. Li, K.X. Wang, N. Lu, Y.C. Liu, Three-Dimensional Freestanding Hierarchically Porous Carbon Materials as Binder-Free Electrodes for Supercapacitors: High Capacitive Property and Long-Term Cycling Stability, Journal of Materials Chemistry A, 4 (2016) 5623.
[34] F.W. Ma, D. Ma, G. Wu, W.D. Geng, J.Q. Shao, S.J. Song, J.F. Wan, J.S. Qiu, Construction of 3d Nanostructure Hierarchical Porous Graphitic Carbons by Charge-Induced Self-Assembly and Nanocrystal-Assisted Catalytic Graphitization for Supercapacitors, Chemical Communications, 52 (2016) 6673.
[35] L.F. Chen, X.D. Zhang, H.W. Liang, M.G. Kong, Q.F. Guan, P. Chen, Z.Y. Wu, S.H. Yu, Synthesis of Nitrogen-Doped Porous Carbon Nanofibers as an Efficient Electrode Material for Supercapacitors, Acs Nano, 6 (2012) 7092.
[36] H.R. An, Y. Li, P. Long, Y. Gao, C.Q. Qin, C. Cao, Y.Y. Feng, W. Feng, Hydrothermal Preparation of Fluorinated Graphene Hydrogel for High-Performance Supercapacitors, Journal of Power Sources, 312 (2016) 146.
[37] L.M. Zhang, T.T. You, T. Zhou, X. Zhou, F. Xu, Interconnected Hierarchical Porous Carbon from Lignin-Derived Byproducts of Bioethanol Production for Ultra-High Performance Supercapacitors, ACS Applied Materials & Interfaces, 8 (2016) 13918.
[38] G.Q. Wang, J. Zhang, S. Kuang, J. Zhou, W. Xing, S.P. Zhuo, Nitrogen-Doped Hierarchical Porous Carbon as an Efficient Electrode Material for Supercapacitors, Electrochimica Acta, 153 (2015) 273.
[39] Y.L. Cheng, L. Huang, X. Xiao, B. Yao, L.Y. Yuan, T.Q. Li, Z.M. Hu, B. Wang, J. Wan, J. Zhou, Flexible and Cross-Linked N-Doped Carbon Nanofiber Network for High Performance Freestanding Supercapacitor Electrode, Nano Energy, 15 (2015) 66.

[40] B. You, F. Kang, P.Q. Yin, Q. Zhang, Hydrogel-Derived Heteroatom-Doped Porous Carbon Networks for Supercapacitor and Electrocatalytic Oxygen Reduction, Carbon, 103 (2016) 9.
[41] Y.S. Yun, S. Lee, N.R. Kim, M. Kang, C. Leal, K.Y. Park, K. Kang, H.J. Jin, High and Rapid Alkali Cation Storage in Ultramicroporous Carbonaceous Materials, Journal of Power Sources, 313 (2016) 142.
[42] Y.Q. Zhao, M. Lu, P.Y. Tao, Y.J. Zhang, X.T. Gong, Z. Yang, G.Q. Zhang, H.L. Li, Hierarchically Porous and Heteroatom Doped Carbon Derived from Tobacco Rods for Supercapacitors, Journal of Power Sources, 307 (2016) 391.
[43] J.Z. Chen, J.L. Xu, S. Zhou, N. Zhao, C.P. Wong, Nitrogen-Doped Hierarchically Porous Carbon Foam: A Free-Standing Electrode and Mechanical Support for High-Performance Supercapacitors, Nano Energy, 25 (2016) 193.
[44] L.F. Chen, Z.H. Huang, H.W. Liang, W.T. Yao, Z.Y. Yu, S.H. Yu, Flexible All-Solid-State High-Power Supercapacitor Fabricated with Nitrogen-Doped Carbon Nanofiber Electrode Material Derived from Bacterial Cellulose, Energy & Environmental Science, 6 (2013) 3331.
[45] Q. Wang, J. Yan, Y. Wang, T. Wei, M. Zhang, X. Jing, Z. Fan, Three-Dimensional Flower-Like and Hierarchical Porous Carbon Materials as High-Rate Performance Electrodes for Supercapacitors, Carbon, 67 (2014) 119.
[46] I. Efremenko, M. Sheintuch, Predicting Solute Adsorption on Activated Carbon: Phenol, Langmuir, 22 (2006) 3614.
[47] G.X. Zhao, L. Jiang, Y.D. He, J.X. Li, H.L. Dong, X.K. Wang, W.P. Hu, Sulfonated Graphene for Persistent Aromatic Pollutant Management, Advanced Materials, 23 (2011) 3959.
[48] L.L. Ji, W. Chen, L. Duan, D.Q. Zhu, Mechanisms for Strong Adsorption of Tetracycline to Carbon Nanotubes: A Comparative Study Using Activated Carbon and Graphite as Adsorbents, Environmental Science & Technology, 43 (2009) 2322.
[49] L.W. Matzek, K.E. Carter, Activated Persulfate for Organic Chemical Degradation: A Review, Chemosphere, 151 (2016) 178.
[50] J. Liang, Y. Jiao, M. Jaroniec, S.Z. Qiao, Sulfur and Nitrogen Dual-Doped Mesoporous Graphene Electrocatalyst for Oxygen Reduction with Synergistically Enhanced Performance, Angewandte Chemie-International Edition, 51 (2012) 11496.
[51] J.T. Zhang, Z.H. Xia, L.M. Dai, Carbon-Based Electrocatalysts for Advanced Energy Conversion and Storage, Science Advances, 1 (2015) e1500564.

[52] H. Zhang, W. Tian, Z. Qian, T. Ouyang, M. Saunders, J. Qin, S. Wang, M.O. Tadé, H. Sun, Co@C/$CoO_x$ Coupled with N-Doped Layer-Structured Carbons for Excellent $CO_2$ Capture and Oxygen Reduction Reaction, Carbon, 133 (2018) 306.

# Chapter 4. Synthesis of Nitrogen and Sulfur Co-Doped Porous Carbon for Adsorptive and Oxidative Removal of Pharmaceutical Contaminants

## Abstract

*In Chapter 3, N-doped porous carbons were prepared by one-step pyrolysis of glucose, sodium bicarbonate and urea. In this Chapter, N and S co-doped porous carbons with high surface areas and hierarchically porous structures are further synthesized via direct pyrolysis of a mixture containing glucose, sodium bicarbonate and thiourea. The resulting N-S co-doped porous carbons (N-S-PCs) exhibit excellent adsorption abilities and are highly efficient for potassium persulfate (PS) activation when employed as catalysts for oxidative degradation of sulfachloropyridazine (SCP) solutions. The adsorption capacities of N-S-PC-2 (which contains 4.51 at.% of N and 0.22 at.% of S, and exhibits $S_{BET}$ of 1608 $m^2$ $g^{-1}$) are 73, 7 and 3 times higher than graphene oxide (GO), reduced-graphene oxide (rGO) and commercial single-walled carbon nanotube (SWCNT), respectively. For oxidation, the reaction rate constant of N-S-PC-2 is 0.28 $min^{-1}$. This facile approach not only contributes to the large-scale production and application of high-quality catalysts in water remediation but also provides an innovative strategy for production of heteroatom-doped porous carbons for energy applications.*

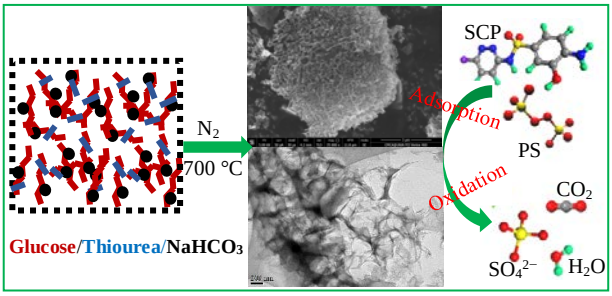

## 4.1 Introduction

The heavy pressure caused by the fresh water scarcity and increasing water consumption have urged rigorous pollution control and effective remediation technologies.[1] Particular attention should be paid to emerging contaminants. More recently, worldwide discharge of pharmaceuticals in municipal waste water has been recognized as one of the emerging environmental issues.[2-6] Among these pharmaceuticals, sulfonamide antibiotics have become one of the major contributors. Sulfonamides have been among the most extensively used antibiotics in aquaculture, animal husbandry and also in human medicine since they were discovered in 1930s.[7] Sulfonamides are polar amphoteric compounds that are water-soluble and are easy to migrate in the environment.[1, 2] Sulfonamides would not undergo biodegradation neither under aerobic nor anaerobic conditions.[8] In addition, due to their anionic character and antibacterial nature, they may bypass the depuration activity in municipal sewage treatment plants.[1, 9] As a result, sulphonamides are regularly detected in the environment such as hospital waste dumps, fish farming wastewaters, animal manure effluents, and manure waste lagoons from swine farms.[10] Continuous exposure to the sulphonamides contained in water supplies, even in trace amounts, could induce high levels of microbial resistance in wildlife and humans.[2-6] Moreover, the highly toxic effects of sulfadiazine on daphnia magna, green algae and lemna minor have already been observed.[11, 12] Also, more evidence have suggested the antibiotic resistance transfer between aquatic bacteria and human pathogens.[13]

It is therefore critical to develop and apply efficient water treatment method to remove sulfonamides from various effluents. So far, several trials have been reported in the removal of sulfonamides, such as adsorption,[7, 14, 15] membrane filtration,[16] chemical remediation and photocatalytic degradation.[8] As mentioned in Chapter 1 and 3, adsorption is feasible and economical to conduct, yet it has been limited by the capability for ultralow pollutant concentration because of the adsorption-desorption equilibrium. It also requires a proper post-treatment. In pursuit of complete decomposition of the target organic pollutants into harmless substances, AOPs have demonstrated competing capabilities.[9, 17] Carbon-based materials such as graphene, carbon nanotubes, porous carbon and activated carbons, have received much attention for water remediation recently, because of their high efficiencies in pollutant removal and prevention of potential

secondary contamination from toxic metal leaching.[25] Chemically reduced graphene oxide, graphene, and carbon nanotubes all showed high efficiency to activate PMS or PS for phenol degradation.[18-20] However, the preparation of graphene oxides and carbon nanotubes commonly involves multi-steps, high cost and harsh treatment (such as using sulphuric acid). For widespread applications, scalable, economical and simple synthesis would make such carbon-based catalysts more appealing.

Hierarchically porous carbon materials with a high surface area, well-defined porosity, tuneable surface chemistry, good electrical conductivity and excellent chemical stability are attracting great attention on account of their potentials in addressing energy and environmental issues.[26-28] Typical approaches include hard or soft templating processes, and the porosity can be generated by removing those hard or soft sacrificial constituents after carbonization.[26-28]

However, there exist some common drawbacks with the hard-templating method.[26] Although soft-templating methods are more facile, most of the already explored soft-templates are based on rather expensive and non-renewable surfactants or block-copolymers.[26, 28] Therefore, it is highly desirable to develop scalable, economical, efficient and feasible methods to fabricate hierarchically porous carbon structures. Since pristine carbons are very poor in their catalytic performance such as oxygen reduction reaction or the activation of oxidants in AOPs, heteroatom doping has been widely adopted to improve their catalytic abilities, and nitrogen is recognized as a preeminent dopant.[25, 29] Very recently, sulfur is receiving intensive attention as a complementing element to N.[29] As is known, N is able to tune electronic properties of the carbon materials, whereas S is able to induce high chemical reactivity.[29] More importantly, both experimental studies and quantum calculations have proven that catalysts dually doped with N and S exhibited better performances than that with solely N or S doping due to a synergistic effect.[29-32] Therefore, for efficient catalysis, the introduction of N, S atoms into the structure of porous carbons is promising.

The study in chapter 2 has demonstrated the facile synthesis of N-doped layered porous carbon for water treatment and supercapacitors. In this chapter, the author continues to describe a facile method for synthesis of N-S co-doped porous carbons with well-defined pore structures by a pyrolysis process of glucose, sodium bicarbonate and thiourea at 700

°C under nitrogen flow. Glucose was used as the carbon source, which is of great significance because of its low value, a huge amount, easy access, rapid regeneration and environmental friendliness. With similar attributes, sodium bicarbonate, one of the most widely used osteoporosis agent in the food industry, was applied as the pore-forming agents. Thiourea was also used to allow for dual doping of nitrogen and sulfur. Compared to the hard-templating method, the craft adopted in this thesis is more feasible, economical and involves no harsh treatment. On the other hand, sodium bicarbonate is also cost-effective compared with the expensive soft templates.[26, 28] The N, S co-doped porous carbons (N-S-PCs) were applied for adsorption and degradation of SCP, a broad spectrum of sulfonamide. It was observed that N-S-PC-2 (which contains 4.51 at.% of N and 0.22 at.% of S and exhibits $S_{BET}$ of 1608 $m^2$ $g^{-1}$) demonstrated not only excellent adsorption ability but also a remarkable catalytic oxidation capability for SCP removal, making it an attractive alternative for water remediation. The mechanism of adsorption and degradation was also discussed.

## 4.2 Experimental Section

### *4.2a .1 Chemical Reagents*

D-(+)-glucose (≥ 99.5%), sodium bicarbonate (≥ 99.7%), thiourea (≥ 99.0%), potassium persulfate (≥ 99.0 %), sodium nitrite (≥ 99.0 %), and 5, 5-dimethyl-1-pyrroline N-oxide (≥ 97.0%) were purchased from Sigma-Aldrich. Commercial single-walled carbon nanotube (SWCNT, ≥ 95.0%) was purchased from Chengdu Organic Chemicals, China. All chemicals were used without further purification.

### *4.2.2 Preparation of Carbon Materials*

For the synthesis of N-S-PCs, glucose, sodium bicarbonate and thiourea were firstly dissolved in pure water, followed by evaporation of the aqueous solution at 105 °C in the air. After that, the dried mixture was put into a tube furnace and calcined at 700 °C for 2 h with a heating rate of 5 °C/min under $N_2$ flow. The carbonized materials were grinded to powder and then washed by water and ethanol for several times. The final carbon samples were obtained after drying. In this process, the mass ratio between glucose and sodium bicarbonate was kept constant to be 1:1. The mass proportion of thiourea in the mixture varied from 5, 15 to 25% to manipulate the doping level so as to tune the functionality of the porous carbons. Accordingly, the samples were referred to as N-S-

PC-1, N-S-PC-2 and N-S-PC-3. For reference samples, blank porous carbon (PC) with no heteroatom doping was prepared by calcination of glucose and sodium bicarbonate, while non-porous carbon (NONPC) was obtained by calcining pure glucose only. GO was produced from a natural graphite powder by the modified Hummers' method,[18] while rGO was prepared according to our previous synthesis method.[19]

### *4.2.3 Characterization*

SEM, TEM, XPS, $N_2$ sorption, EPR measurements can refer to Chapter 3. X-ray diffraction (XRD) patterns were conducted on a Bruker D8-Advanced X-ray instrument. A thermogravimetric analysis instrument (TGA/DSC1 STAR$^e$ system, METTLER-TOLEDO) was also employed.

### *4.2.4 Adsorption and Catalytic Oxidation Procedures*

Typical adsorption experiments were carried out at 25 $^oC$ by dispersing the carbon samples (0.05 g $L^{-1}$) in SCP solutions (20 mg $L^{-1}$, pH 7). At certain time intervals, 1 mL of the solution was withdrawn using a syringe and filtered by filters with 0.45 μm millipore films. The concentrations of these samples were determined by an ultra-high performance liquid chromatography (UHPLC).

SCP oxidation tests were conducted in a 500 mL glass reactor at 25 $^oC$. The carbon samples (0.05 g $L^{-1}$) and PS (6.5 mM) were added to the SCP (20 mg $L^{-1}$, pH 7) solutions together to initiate the reaction. At each time interval, 1.0 mL solution of water samples were taken, filtered and quenched immediately by mixing with 0.5 mL of sodium nitrite solution (0.1 M). Each experiment was repeated, and the results were reproducible. For the reusability tests, the catalyst was collected by vacuum filtration after each of 3 h reaction, then washed with deionized water for several times and dried in an oven at 60 °C.

## 4.3 Results and Discussion

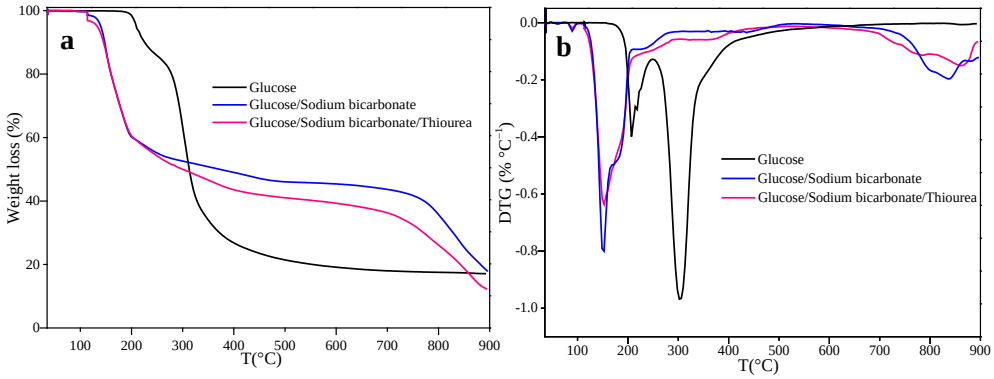


**Figure 4.1** a) TGA and b) DTG curves of the precursors heated under argon atmosphere.

TGA and DTG were conducted by heating the precursors to synthesize NONPC, PC and N-S-PC-2 under an argon atmosphere to gain insights into the formation mechanism of porous carbon during pyrolysis (Figure 4.1). As indicated by the curves of pure glucose, there was a mild weight loss between 180 and 250 °C, which could be ascribed to the dehydration of glucose. Following that, a further larger decomposition process was observed with an apparent weight loss occurred between 250 and 400 °C. After that, the curve was flat to 900 °C. However, in terms of glucose/sodium bicarbonate as well as glucose/sodium bicarbonate/thiourea systems, their TGA and DTG curves were distinct from those of pure glucose, with weight loss happening only at one temperature interval. Apart from that, the beginning temperature was decreased to 115 °C while ended earlier at 280 °C. This indicated that the addition of sodium bicarbonate might promote the self-assembly among the precursors before pyrolysis, which could facilitate the noncovalent interactions among them, such as hydrogen bonding, van der Waals forces and electrostatic interaction, thereby beneficial for the synthesis of high-quality carbons. The further mass loss above 700 °C could be attributed to the thermal decomposition of $Na_2CO_3$, removal of some heteroatoms or reduction of $Na_2CO_3$ at higher temperatures.[33] Therefore, to avoid such chemical loss, the fabrication temperature was set at 700 °C.

With the assistance from TGA results, the overall procedures for the synthesis of N-S-PCs can be illustrated in Scheme 4.1. In the evaporation process at 105 °C, the self-assembly process of glucose, sodium bicarbonate and thiourea occurred. Then during the heat-

treatment of the mixture at 700 °C under a nitrogen flow, well-defined hierarchically porous structures could be generated.

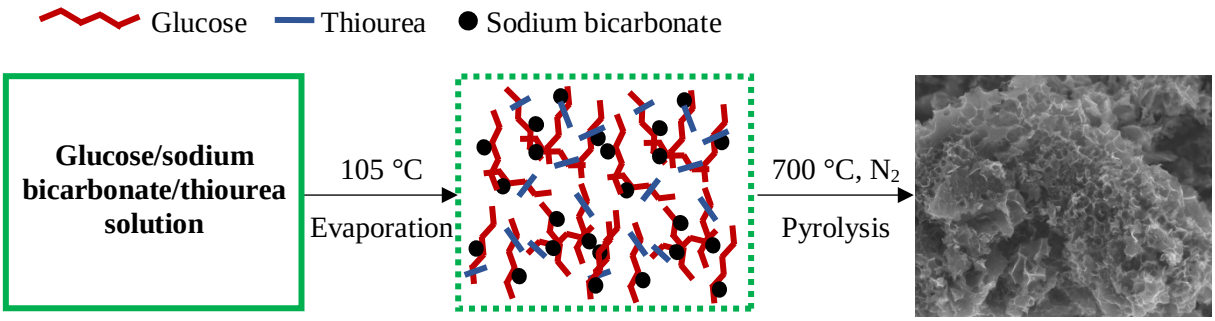


**Scheme 4.1** Synthesis of N, S co-doped porous carbons.

*4.3.1 Characterization of Materials*

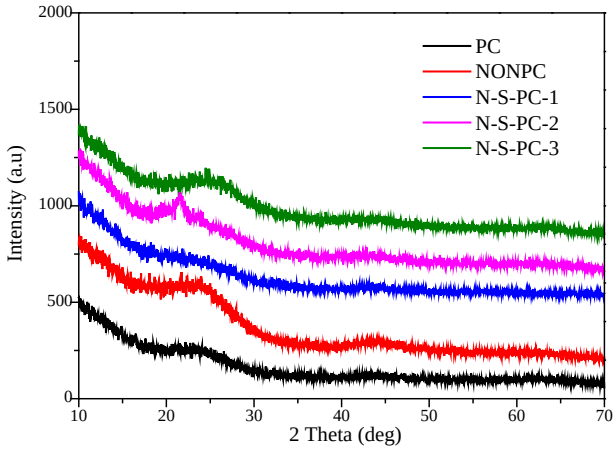


**Figure 4.2** Powder XRD patterns of synthesized carbons.

XRD patterns of the prepared carbons depict two weak broad peaks located at about 25 and 44°, typical for amorphous carbon (Figure 4.2). SEM images shown in Figure 4.3a confirm that NONPC from direct carbonization of glucose is nonporous, while porous carbon was successfully produced when sodium bicarbonate was applied (Figure 4.3b, PC) and N-S-PCs all possess highly porous structures (Figure 4.3 c-e). Representative TEM image (Figure 4.3f) demonstrates that N-S-PC-2 is composed of a three-dimensional interconnected pore system. There were evident macrospores on the surfaces of the porous carbons, and N-S-PC-3 possesses obviously wider pore walls than N-S-PC-1 and -2 (Figure 4.4).

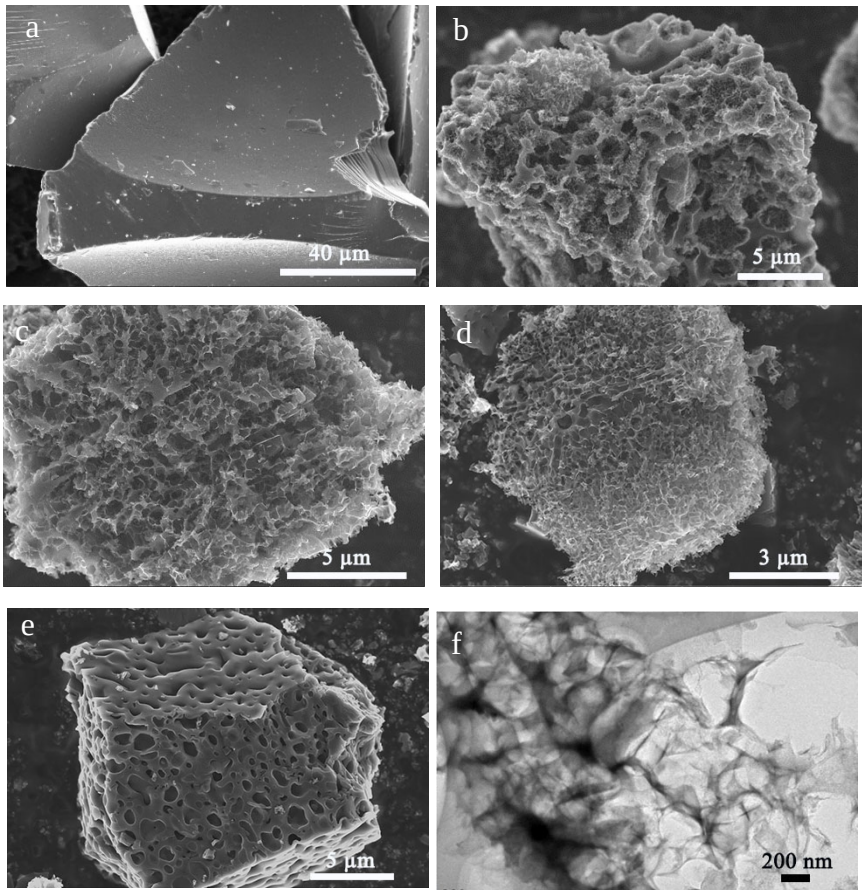


**Figure 4.3** SEM images of a) NONPC, b) PC, c) N-S-PC-1, d) N-S-PC-2, and e) N-S-PC-3. (f) Representative TEM image of N-S-PC-2.

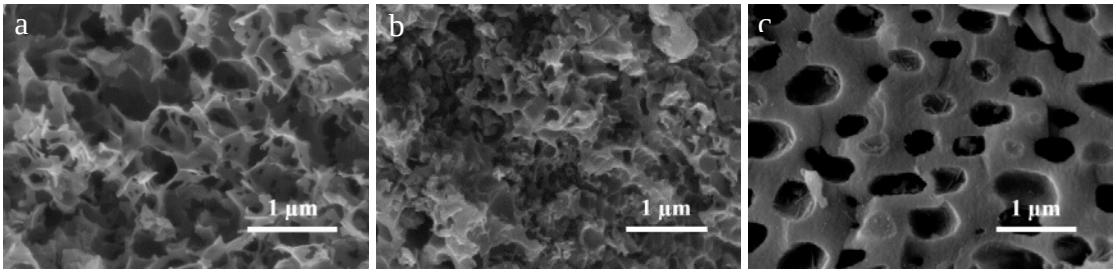


**Figure 4.4** Magnified SEM images of N-S-PCs: (a) N-S-PC-1, (b) N-S-PC-2, (c) N-S-PC-3.

To further examine their distinctions, the BET specific surface areas and pore structure details of these samples were measured by $N_2$ sorption, and corresponding results are summarized in Figure 4.5 and Table 4.1. The porous carbons show type-I isotherms with desorption hysteresis and a steep increase at relatively low pressures, followed by a moderate increase at intermediate relative pressures. This highlights the formation of a hierarchical pore architecture consisting of micro- (< 2 nm) and mesopores (2-50 nm).[27]

It is deduced that the macropores observed in SEM images only exist on the surface in low quantities. NONPC possesses an appreciable low BET surface area (2 $m^2 g^{-1}$) with virtually no pores. In contrast, a high BET surface area ($S_{BET}$, 459 $m^2 g^{-1}$) and an improved total pore volume ($V_t$, 0.46 $cm^3 g^{-1}$) are obtained in PC. $CO_2$ and $H_2O$ released from $NaHCO_3$ decomposition created mainly mesopores in PC. Then $Na_2CO_3$ left in the inner pore channels was removed by water washing, which produced further porosities. Thiourea decomposition created both mesopores and micropores in N-S-PCs. The BET surface areas were enhanced to 1044 $m^2 g^{-1}$ in N-S-PC-1, reaching 1608 $m^2 g^{-1}$ in N-S-PC-2, and then decreasing in N-S-PC-3 (1016 $m^2 g^{-1}$). The total pore volumes of N-S-PCs were also improved greatly compared to PC, with N-S-PC-2 having the highest total pore volume (1.0 $cm^3 g^{-1}$). As shown in Table 4.1, the micropore volume ($V_{mic}$) increases steadily with increasing N, S doping amount, while mesopore volume ($V_{meso}$) increases first, and then decreases in N-S-PC-3. This is because the decomposition of thiourea is conducive for pore generation on one hand while on the other hand, heteroatom doping can potentially block the pore channels of porous carbons, leading to higher $V_{mic}$ and lower $V_{meso}$. It is also noted that the mesopores in these porous carbons were dominated by ponysize mesopores, peaked near 2 nm (Figure 4.5b).

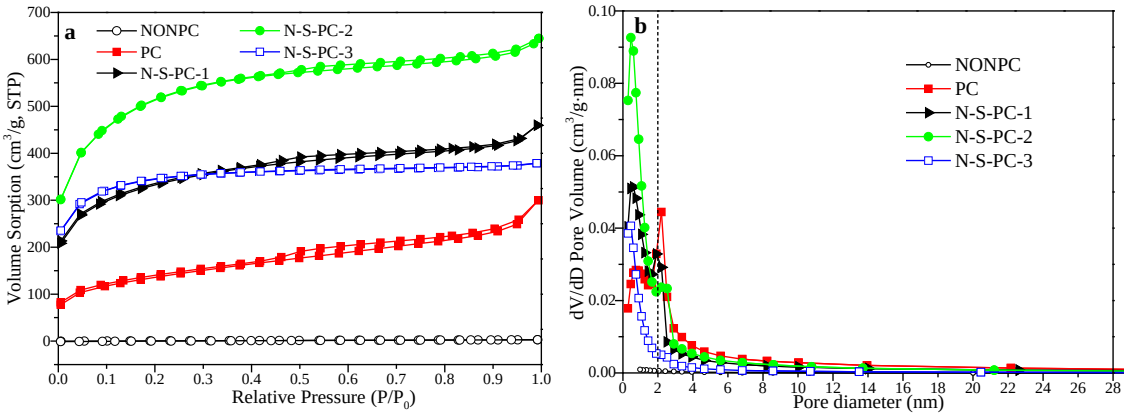


**Figure 4.5** a) Nitrogen sorption isotherms at –196 °C and b) BJH pore size distributions of the carbon samples.

**Table 4.1** Textural characteristics of the porous carbon samples.

| Samples | $S_{BET}$ [a] / $m^2 g^{-1}$ | $S_{mic}$ [b] / $m^2 g^{-1}$ | $V_t$ [c] / $cm^3 g^{-1}$ | $V_{mic}$ [b] / $cm^3 g^{-1}$ | $V_{meso}$ [d] / $cm^3 g^{-1}$ |
|---|---|---|---|---|---|
| NONPC | 2 | - | 0.0035 | - | - |
| PC | 459 | 79 | 0.46 | 0.04 | 0.42 |

| | | | | | |
|---|---|---|---|---|---|
| N-S-PC-1 | 1044 | 388 | 0.71 | 0.23 | 0.48 |
| N-S-PC-2 | 1608 | 550 | 1.00 | 0.33 | 0.67 |
| N-S-PC-3 | 1016 | 644 | 0.59 | 0.37 | 0.22 |

[a] Surface area calculated using the BET method.
[b] Evaluated by the t-plot method.
[c] Total pore volume calculated at $P/P_0 = 0.99$.
[d] Mesopore volume obtained through the difference between $V_t$ and $V_{mic}$.

It was known that the functionalities of carbons are closely linked to their surface chemical states, especially to N, S-containing functional groups.[30, 34] XPS analysis of N-S-PCs was then performed to investigate the compositional information of the materials. The surface chemical compositions and the resulting spectra are presented in Figure 4.6. Specifically, the atomic ratios of N in N-S-PCs were determined to be from 3.42, 4.51 to 9.61% for N-S-PC-1, -2 and -3, respectively. In the high-resolution N 1s spectra, the spectra were resolved to four peaks centred at around 398, 400, 401 and 405 eV, corresponding to pyridinic-N (N-1), pyrrolic-N (N-2), graphitic-N (N-3), and oxidized-N (N-4), respectively.[35, 36] With the increase of thiourea proportion, the contents of N-1 and N-3 increased notably (Figure 4.6d). This might be meaningful considering that pyridinic N and graphitic N are conducive for enhanced catalytic performance in oxygen reduction reaction (ORR).[37]

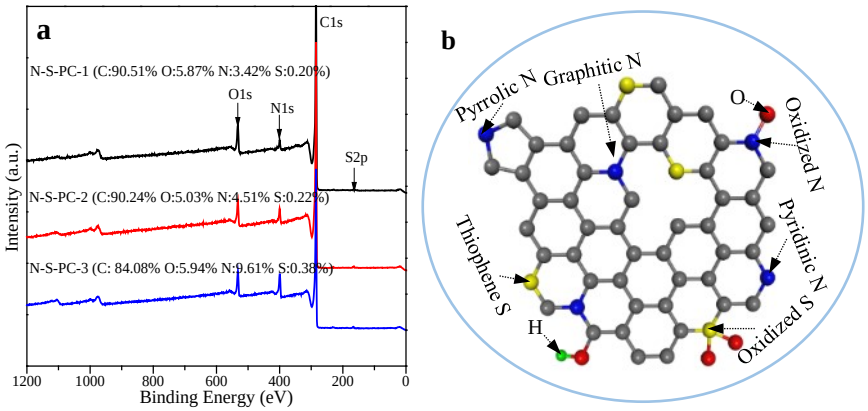

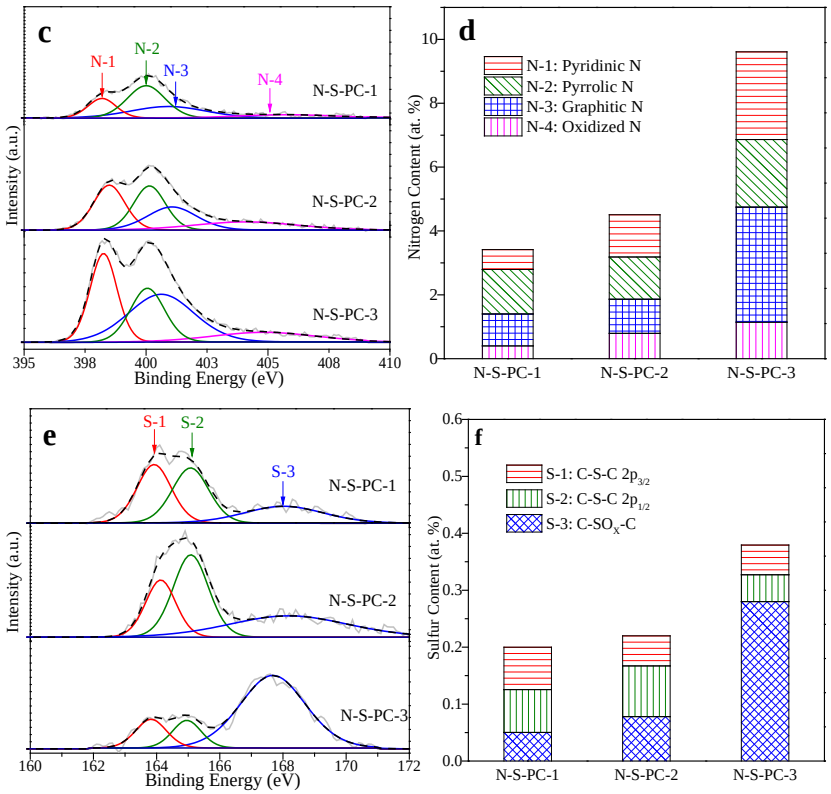


**Figure 4.6** a) Wide survey of XPS spectra of N-S-PCs, b) schematic illustration of doped N, S atoms, c) high resolution N 1s spectra of N-S-PCs, d) the content of four nitrogen species, e) S 2p spectra of N-S-PCs, and f) the content of sulfur species.

One the other hand, S contents did not change as much as N, merely in the scope of 0.20, 0.22 and 0.38 at. % for N-S-PC-1, -2 and -3, respectively. All the high resolution S 2p peaks of N-S-PCs were fitted to three components centred at around 164, 165, and 168 eV, respectively. The former two peaks correspond to S $2p_{3/2}$ (S-1) and S $2p_{1/2}$ (S-2) positions of thiophene-S, derived from the spin-orbit splitting of thiophenic sulfur atoms incorporated into the carbon framework.[38] The last peak possibly arose from some oxidized S (S-3).[29, 37, 39, 40] Compared with N-S-PC-1, the amount of S-3 was slightly higher in N-S-PC-2, while it was dominant in N-S-PC-3 and the amount of thiophene-S decreased accordingly (Figure 4.6f). This may be detrimental, as S-C bonds are presumed to play a more vital role in ORR catalytic activity compared with S-O bonds.[37] As shown in Figure 4.6b, several N binding configurations can exist. In contrast to N-doping modality, S atoms are prone to be doped at the edges or defects of the carbon network.[37] As a result, the overall sulfur contents were much lower than nitrogen in N-S-PCs.

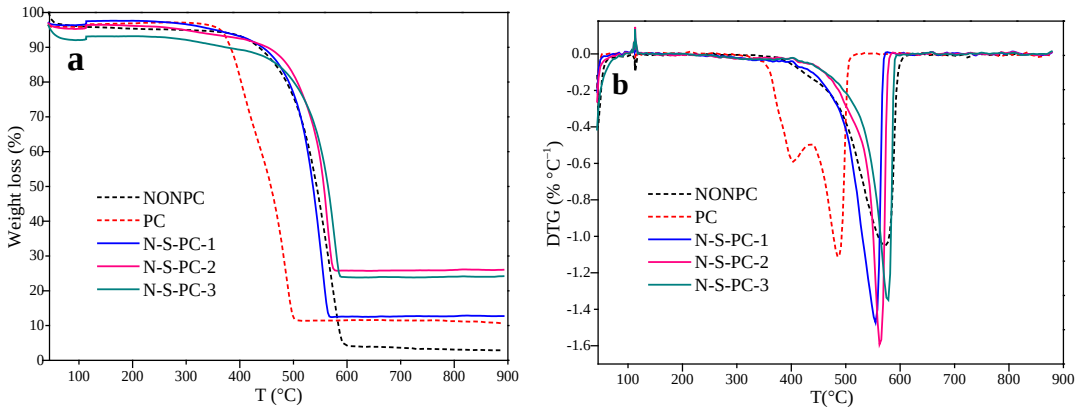


**Figure 4.7** a) TGA and b) DTG curves of the carbon samples heated under air.

TGA and DTG of NONPC and PC (Figure 4.7, under air) depict that the creation of pore structures lowered the thermal stability of carbon structure by approximately 100 °C. However, heteroatom doping successfully made the porous carbons more thermally stable. The onset of burning temperatures of N-S-PCs under air was comparable to that of NONPC. Even after water washing, trace levels of encapsulated Na-compounds might be left in the inner pores since they were hard to be removed completely and might be difficult to be detected by XPS surface analysis. This might lead to the residues left after combustion, as displayed in Figure 4.7a.

### *4.3.2 SCP Removal*

Comparative studies were performed on N-S-PC-2 and some reference carbons of GO, rGO and commercial SWCNT first, followed by a comparison among the carbons prepared under different conditions in this study. Figure 4.8 exhibits the adsorption and degradation of SCP on different carbon materials. It is shown in Figure 4.8a that GO could hardly adsorb SCP, whereas SWCNT and rGO provided about 21% and 7% of SCP adsorption, respectively. Remarkably, when N-S-PC-2 was introduced, the adsorptive removal of SCP reached 60%, far better than the reference carbons. Figure 4.8b indicates that N-S-PC-2 possessed the best adsorption performance among all the porous carbons prepared with different chemical contents. The detailed adsorption information of these carbon samples are summarized in Table 4.2. The calculated adsorption capacity of N-S-PC-2 can reach 220 mg $g^{-1}$, which was 73, 7 and 3 times higher than GO, rGO and commercial SWCNT, respectively. NONPC had few effects, yet PC could adsorb 16% of SCP in 30 min. The adsorption capacities ($q_m$) of SCP over N-S-PC-1 and N-S-PC-3 were

calculated to be 190 mg $g^{-1}$ and 126 mg $g^{-1}$, respectively. However, there were no obvious differences in their surface-area-normalized adsorption capacities ($q_m/S_{BET}$, Table 4.2), indicating that the adsorption performances of as-prepared porous carbons were basically consistent with their BET surface area. The $q_m/S_{BET}$ values of the porous carbons were also similar to GO and rGO, yet SWCNT was higher, indicating that SWCNT had decent adsorption ability. The adsorption capacity of N-S-PC-2 was also compared with some frequently-used activated carbon adsorbents on pharmaceutical compounds under similar conditions, as given in Table 4.3. It is shown that N-S-PC-2 was comparable or better than these activated carbons from the viewpoint of both adsorption capacity and surface-area-normalized adsorption capacities with a much lower dosage.

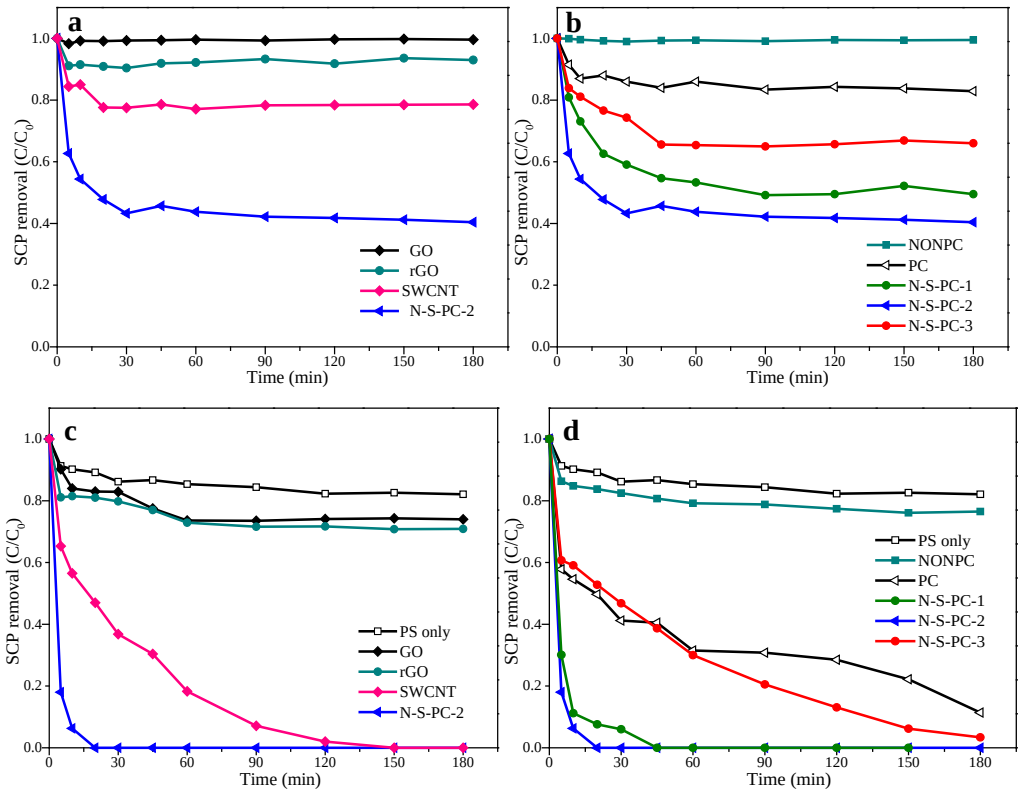


**Figure 4.8** a) and b) SCP removal by adsorption (Adsorbent 0.05 g $L^{-1}$, SCP 20 mg $L^{-1}$, and T 25 °C). c) and d) SCP oxidative degradation (Catalyst 0.05 g $L^{-1}$, PS 6.5 mM, SCP 20 mg $L^{-1}$, and T 25 °C).

**Table 4.2** Adsorption details of the various carbons.

| | GO | rGO | SWCNT | NONPC | PC | N-S-PC-1 | N-S-PC-2 | N-S-PC-3 |
|---|---|---|---|---|---|---|---|---|

| | | | | | | | | |
|---|---|---|---|---|---|---|---|---|
| Adsorption capacity ($q_m$,mg $g^{-1}$) | 3 | 30 | 80 | 2 | 60 | 190 | 220 | 126 |
| $S_{BET}$ ($m^2$ $g^{-1}$) | 30 [30] | 255 [30] | 366 [41] | 2 | 459 | 1044 | 1608 | 1016 |
| $q_m/S_{BET}$ (mg $m^{-2}$) | 0.10 | 0.12 | 0.22 | 1 | 0.13 | 0.13 | 0.14 | 0.12 |

**Table 4.3** Comparison of adsorption capacities with activated carbon for some pharmaceutical compounds removal reported in literature

| Adsorbent | Contaminant | Adsorption capacity ($q_m$, mg $g^{-1}$) | $S_{BET}$ ($m^2$ $g^{-1}$) | $q_m/S_{BET}$ (mg $m^{-2}$) | pH | Initial adsorbate concentration (mg $L^{-1}$) | Ref. |
|---|---|---|---|---|---|---|---|
| Commercial activated carbon | Ibuprofen | 22 | 1000 | 0.022 | 6.5 | 10 | [42] |
| Activated carbon | Tetracycline | 30 | 316 | 0.09 | - | 20 | [43] |
| Commercial granulated activated carbon | Ibuprofen | 50 | 800 | 0.063 | 7 | 20 | [44] |
| Artemisia vulgaris-derived activated carbon | Ibuprofen | 13 | 358 | 0.036 | 2 | 20 | [45] |
| Industrial pre-treated cork activated carbons | Ibuprofen | 130 | 948 | 0.14 | 5 | 20 | [46] |
| N-S-PC-2 | Sulfachloro-pyridazine | 220 | 1608 | 0.14 | 7 | 20 | This work |

The catalytic SCP oxidation with PS is depicted in Figure 4.8c and d. It is noted that PS alone could hardly degrade SCP (less than 15% removal in 180 min), and neither can GO and rGO for PS activation. Commercial SWCNT was better, which could achieve 100% SCP removal in 150 min, but still far lower if compared to N-S-PC-2. Rapid decomposition of SCP was observed on N-S-PC-2, with complete SCP removal in 20 min at only 0.05 g $L^{-1}$ catalyst loading. The rate constant ($k$) calculated from the first order kinetic model in N-S-PC-2/PS system was 0.28 $min^{-1}$ ($R^2$ = 0.994). As to the other carbon samples (Figure 4.8d), there was almost no effect on NONPC. PC showed a moderate ability in PS activation. N-S-PC-1 achieved 100% SCP removal in 45 min ($k$ = 0.22 $min^{-1}$, $R^2$ = 0.996), and N-S-PC-2 exhibited the best performance, whereas N-S-PC-3 only decomposed 97% SCP in 180 min ($k$ = 0.015 $min^{-1}$, $R^2$ = 0.962).

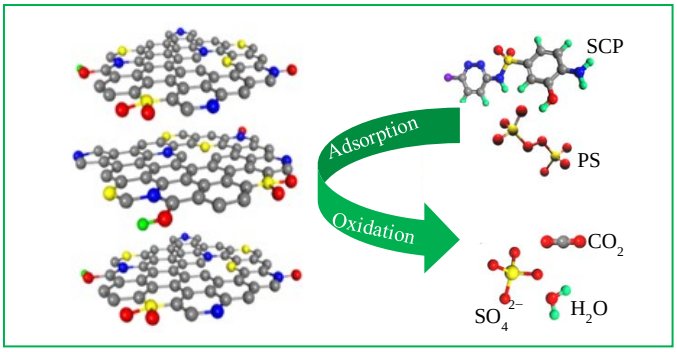


**Scheme 4.2** Catalytic process of SCP on N-S-PC-2. (The grey, blue, red, yellow and green atoms are C, N, O, S and H atoms, respectively.)

The excellent catalytic effect of N-S-PC-2 can be explained in several aspects. To begin with, its high BET surface area and well-defined pore structure enable more active sites to be exposed. It is also believed that the synergistic effect of adsorption and catalysis promote more efficient AOP process,[25] as illustrated in Scheme 4.2. The other factors are associated with N, S atom doping species and amounts, which can be investigated from the point of density functional theory.[30] Compared with carbon (2.55) atoms, N atoms are more electronegative (3.04). As a result, N atoms can create a net positive charge on the adjacent carbon atoms. On the other hand, the electronegativity of sulfur atoms (2.58) is close to carbon, which can reduce the energy difference among unoccupied carbon molecular orbitals.[29] It was thus suggested that appropriate amount of nitrogen and sulfur doping could break the chemical inertness of carbon and exert a synergistic effect on the improvement of catalytic activity owing to the redistribution of spin and charge densities and creation of more active sites.[29, 47] Therefore, N-S-PC-2 with a moderate doping amount exhibited the best promoting effect. However, as indicated in calculation results,[30] over-doping of N or S might break the charge balance of the covalent carbon electron system, disrupt the charge redistribution, and then weaken the synergistic effect. Figure 4.9 presents the activity of recycled N-S-PC-2 in SCP degradation. As seen, 80% removal was obtained in the second run and 44% removal in the third run, still much better than the performance of the first run testing of GO and rGO. According to the former study of our group, it is conjectured that surface chemistry changes and intermediate coverage on the catalyst surface are reasons for the deteriorating cycling performance.[18, 48] To recover the catalytic ability of the used carbon-based

catalysts, it is suggested that proper treatment can be adopted such as do the heteroatom doping again to recover the surface chemistry.

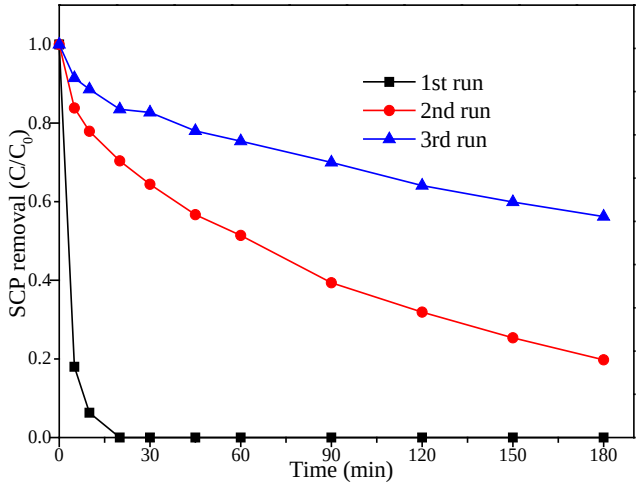


**Figure 4.9** Stability tests of PS/N-S-PC-2 (Catalyst 0.05 g $L^{-1}$, PS 6.5 mM, SCP 20 mg $L^{-1}$, T 25 °C).

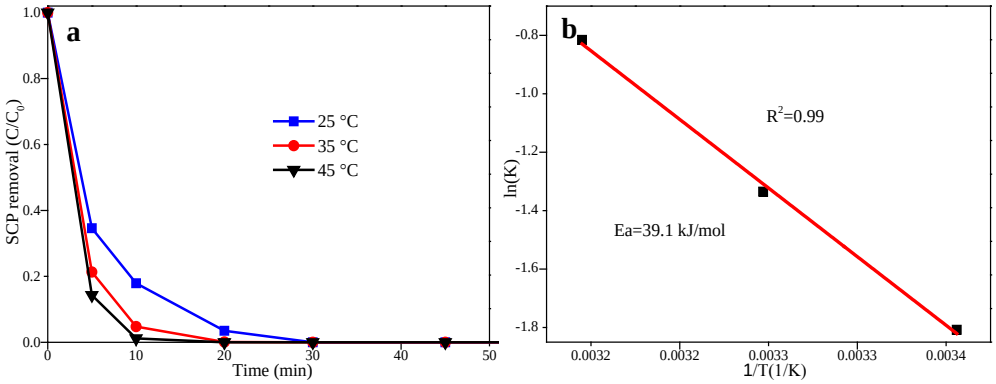


**Figure 4.10** a) Effect of solution temperature on catalytic activity (Catalyst 0.0025 g $L^{-1}$, PS 6.5 mM, SCP 20 mg $L^{-1}$), b) Estimation of the activation energy.

The influence of solution temperature on PS activation over N-S-PC-2 was conducted at 25, 35, and 45 °C. It is suggested that higher reaction rate was achieved by elevating the reaction temperature, as illustrated in Figure 4.10a. The concentration of catalyst was reduced to 0.0025 g $L^{-1}$, considering its excellent degradation performance. Specifically, complete SCP removal was obtained in 20 min at 35 °C ($k$ = 0.30 $min^{-1}$, $R^2$ = 0.98) and 15 min at 45 °C (0.44 $min^{-1}$, $R^2$ = 0.99). It is worth noting that although the catalyst concentration was very low, the SCP removal could still be achieved in 30 min by N-S-PC-2 ($k$ = 0.16 $min^{-1}$, $R^2$ = 0.99), which exhibited a powerful degradation capability. The SCP degradation curves of N-S-PC-2 can be fitted well by the first-order kinetics with high values of regressions coefficients ($R^2$ = 0.99). Based on the Arrhenius equation, the

activation energy ($E_a$) of N-S-PC-2 for catalytic SCP oxidative degradation was obtained to be 39.1 kJ $mol^{-1}$ (Figure 4.10b).

### *4.3.3 Catalytic Mechanism of PS Activation on N-S-PCs*

It is reported that, in most AOPs, the reactive radicals produced from the PS activation play a dominant role in attacking and degrading organics. Thus, in-situ electron paramagnetic resonance (EPR) was employed to obtain more insights into the radical generation and evolution. DMPO was adopted as a spin trapping agent to capture the free radicals. Figure 4.11 shows that N-S-PC-2 was able to effectively activate PS to generate reactive radicals of $SO_4^{\bullet-}$ and •OH. It is also noted that the signal of DMPO–$SO_4^{\bullet-}$ was much weaker than DMPO–•OH. This can be ascribed to the superior high adsorption capability of N-S-PC-2, which can adsorb not only SCP but also anionic $S_2O_8^{2-}$ and $SO_4^{\bullet-}$. Hence the generated $SO_4^{\bullet-}$ radicals might also be adsorbed on the surface of N-S-PC-2, which greatly accelerate the SCP oxidation process.

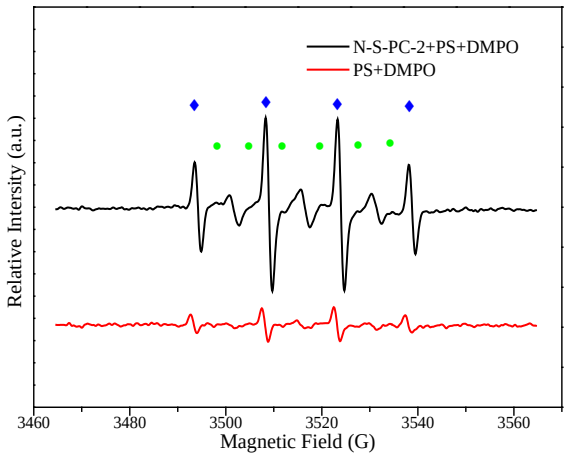


**Figure 4.11** EPR spectra of PS activation with N-S-PC-2 (Catalyst 0.05 g $L^{-1}$, PS 6.5 mM, SCP 20 mg $L^{-1}$, T 25 $^oC$, and DMPO 0.16 M. ♦ DMPO-OH, ● DMPO-$SO_4$).

## 4.4 Conclusions

In summary, this study firstly proposes an easily-handled $NaHCO_3$-based activation pyrolysis method for preparation of N-S co-doped porous carbon materials. N and S doping play a crucial role in determining the overall functionalities. The prepared N-S-PC-2 demonstrated a well-developed hierarchical porosity and high surface area. This work unambiguously shows the great potential of N-S co-doped porous carbon materials

for SCP removal. This facile, green, and economical protocol is highly promising for the large-scale production of high-quality catalysts for water remediation. This synthetic approach can also be extended to fabrication of functional carbon materials with applications in other fields such as separation, energy and medicine.

## References

[1] M. Haidar, A. Dirany, I. Sires, N. Oturan, M.A. Oturan, Electrochemical Degradation of the Antibiotic Sulfachloropyridazine by Hydroxyl Radicals Generated at a Bdd Anode, Chemosphere, 91 (2013) 1304.

[2] Y. Luo, L. Xu, M. Rysz, Y.Q. Wang, H. Zhang, P.J.J. Alvarez, Occurrence and Transport of Tetracycline, Sulfonamide, Quinolone, and Macrolide Antibiotics in the Haihe River Basin, China, Environmental Science & Technology, 45 (2011) 1827.

[3] R. Andreozzi, V. Caprio, C. Ciniglia, M. De Champdore, R. Lo Giudice, R. Marotta, E. Zuccato, Antibiotics in the Environment: Occurrence in Italian Stps, Fate, and Preliminary Assessment on Algal Toxicity of Amoxicillin, Environmental Science & Technology, 38 (2004) 6832.

[4] D.W. Kolpin, E.T. Furlong, M.T. Meyer, E.M. Thurman, S.D. Zaugg, L.B. Barber, H.T. Buxton, Pharmaceuticals, Hormones, and Other Organic Wastewater Contaminants in Us Streams, 1999-2000: A National Reconnaissance, Environmental Science & Technology, 36 (2002) 1202.

[5] D. Bendz, N.A. Paxeus, T.R. Ginn, F.J. Loge, Occurrence and Fate of Pharmaceutically Active Compounds in the Environment, a Case Study: Hoje River in Sweden, Journal of Hazardous Materials, 122 (2005) 195.

[6] W.J. Sim, J.W. Lee, J.E. Oh, Occurrence and Fate of Pharmaceuticals in Wastewater Treatment Plants and Rivers in Korea, Environmental Pollution, 158 (2010) 1938.

[7] A. Martucci, M.A. Cremonini, S. Blasioli, L. Gigli, G. Gatti, L. Marchese, I. Braschi, Adsorption and Reaction of Sulfachloropyridazine Sulfonamide Antibiotic on a High Silica Mordenite: A Structural and Spectroscopic Combined Study, Microporous and Mesoporous Materials, 170 (2013) 274.

[8] K. Zessel, S. Mohring, G. Hamscher, M. Kietzmann, J. Stahl, Biocompatibility and Antibacterial Activity of Photolytic Products of Sulfonamides, Chemosphere, 100 (2014) 167.

[9] A. Dirany, I. Sires, N. Oturan, A. Ozcan, M.A. Oturan, Electrochemical Treatment of the Antibiotic Sulfachloropyridazine: Kinetics, Reaction Pathways, and Toxicity Evolution, Environmental Science & Technology, 46 (2012) 4074.
[10] W. Baran, E. Adamek, J. Ziemianska, A. Sobczak, Effects of the Presence of Sulfonamides in the Environment and Their Influence on Human Health, Journal of Hazardous Materials, 196 (2011) 1.
[11] R.A. Brain, A.J. Ramirez, B.A. Fulton, C.K. Chambliss, B.W. Brooks, Herbicidal Effects of Sulfamethoxazole in Lemna Gibba: Using P-Aminobenzoic Acid as a Biomarker of Effect, Environmental Science & Technology, 42 (2008) 8965.
[12] A. Fabianska, A. Bialk-Bielinska, P. Stepnowski, S. Stolte, E.M. Siedlecka, Electrochemical Degradation of Sulfonamides at Bdd Electrode: Kinetics, Reaction Pathway and Eco-Toxicity Evaluation, Journal of Hazardous Materials, 280 (2014) 579.
[13] F.C. Cabello, Heavy Use of Prophylactic Antibiotics in Aquaculture: A Growing Problem for Human and Animal Health and for the Environment, Environmental Microbiology, 8 (2006) 1137.
[14] I. Braschi, S. Blasioli, L. Gigli, C.E. Gessa, A. Alberti, A. Martucci, Removal of Sulfonamide Antibiotics from Water: Evidence of Adsorption into an Organophilic Zeolite Y by Its Structural Modifications, Journal of Hazardous Materials, 178 (2010) 218.
[15] M. Kahle, C. Stamm, Sorption of the Veterinary Antimicrobial Sulfathiazole to Organic Materials of Different Origin, Environmental Science & Technology, 41 (2007) 132.
[16] I. Koyuncu, O.A. Arikan, M.R. Wiesner, C. Rice, Removal of Hormones and Antibiotics by Nanofiltration Membranes, Journal of Membrane Science, 309 (2008) 94.
[17] M. Klavarioti, D. Mantzavinos, D. Kassinos, Removal of Residual Pharmaceuticals from Aqueous Systems by Advanced Oxidation Processes, Environment International, 35 (2009) 402.
[18] H.Q. Sun, Y.X. Wang, S.Z. Liu, L. Ge, L. Wang, Z.H. Zhu, S.B. Wang, Facile Synthesis of Nitrogen Doped Reduced Graphene Oxide as a Superior Metal-Free Catalyst for Oxidation, Chemical Communications, 49 (2013) 9914.
[19] H.Q. Sun, S.Z. Liu, G.L. Zhou, H.M. Ang, M.O. Tade, S.B. Wang, Reduced Graphene Oxide for Catalytic Oxidation of Aqueous Organic Pollutants, ACS Applied Materials & Interfaces, 4 (2012) 5466.

[20] X.G. Duan, H.Q. Sun, Y.X. Wang, J. Kang, S.B. Wang, N-Doping-Induced Nonradical Reaction on Single-Walled Carbon Nanotubes for Catalytic Phenol Oxidation, ACS Catalysis, 5 (2015) 553.
[21] R.H. Waldemer, P.G. Tratnyek, R.L. Johnson, J.T. Nurmi, Oxidation of Chlorinated Ethenes by Heat-Activated Persulfate: Kinetics and Products, Environmental Science & Technology, 41 (2007) 1010.
[22] T.K. Lau, W. Chu, N.J.D. Graham, The Aqueous Degradation of Butylated Hydroxyanisole by Uv/S2o82-: Study of Reaction Mechanisms Via Dimerization and Mineralization, Environmental Science & Technology, 41 (2007) 613.
[23] J.C. Yan, M. Lei, L.H. Zhu, M.N. Anjum, J. Zou, H.Q. Tang, Degradation of Sulfamonomethoxine with $Fe_3O_4$ Magnetic Nanoparticles as Heterogeneous Activator of Persulfate, Journal of Hazardous Materials, 186 (2011) 1398.
[24] Y.C. Lee, S.L. Lo, J. Kuo, C.P. Huang, Promoted Degradation of Perfluorooctanic Acid by Persulfate When Adding Activated Carbon, Journal of Hazardous Materials, 261 (2013) 463.
[25] X.B. Wang, Y.L. Qin, L.H. Zhu, H.Q. Tang, Nitrogen-Doped Reduced Graphene Oxide as a Bifunctional Material for Removing Bisphenols: Synergistic Effect between Adsorption and Catalysis, Environmental Science & Technology, 49 (2015) 6855.
[26] S. Dutta, A. Bhaumik, K.C.W. Wu, Hierarchically Porous Carbon Derived from Polymers and Biomass: Effect of Interconnected Pores on Energy Applications, Energy & Environmental Science, 7 (2014) 3574.
[27] J. Lee, J. Kim, T. Hyeon, Recent Progress in the Synthesis of Porous Carbon Materials, Advanced Materials, 18 (2006) 2073.
[28] D.C. Wu, Z.H. Li, M.J. Zhong, T. Kowalewski, K. Matyjaszewski, Templated Synthesis of Nitrogen- Enriched Nanoporous Carbon Materials from Porogenic Organic Precursors Prepared by Atrp, Angewandte Chemie-International Edition, 53 (2014) 3957.
[29] J. Liang, Y. Jiao, M. Jaroniec, S.Z. Qiao, Sulfur and Nitrogen Dual-Doped Mesoporous Graphene Electrocatalyst for Oxygen Reduction with Synergistically Enhanced Performance, Angewandte Chemie-International Edition, 51 (2012) 11496.
[30] X.G. Duan, K. O'Donnell, H.Q. Sun, Y.X. Wang, S.B. Wang, Sulfur and Nitrogen Co-Doped Graphene for Metal-Free Catalytic Oxidation Reactions, Small, 11 (2015) 3036.
[31] Y. Zheng, Y. Jiao, L. Ge, M. Jaroniec, S.Z. Qiao, Two-Step Boron and Nitrogen Doping in Graphene for Enhanced Synergistic Catalysis, Angewandte Chemie-International Edition, 52 (2013) 3110.

[32] Z.S. Wu, A. Winter, L. Chen, Y. Sun, A. Turchanin, X.L. Feng, K. Mullen, Three-Dimensional Nitrogen and Boron Co-Doped Graphene for High-Performance All-Solid-State Supercapacitors, Advanced Materials, 24 (2012) 5130.
[33] J.W. Kim, H.G. Lee, Thermal and Carbothermic Decomposition of $Na_2CO_3$ and Li(2)CO3, Metallurgical and Materials Transactions B-Process Metallurgy and Materials Processing Science, 32 (2001) 17.
[34] W. Xing, C. Liu, Z.Y. Zhou, L. Zhang, J. Zhou, S.P. Zhuo, Z.F. Yan, H. Gao, G.Q. Wang, S.Z. Qiao, Superior $CO_2$ Uptake of N-Doped Activated Carbon through Hydrogen-Bonding Interaction, Energy & Environmental Science, 5 (2012) 7323.
[35] L.T. Qu, Y. Liu, J.B. Baek, L.M. Dai, Nitrogen-Doped Graphene as Efficient Metal-Free Electrocatalyst for Oxygen Reduction in Fuel Cells, ACS Nano, 4 (2010) 1321.
[36] Y. Wang, Y.Y. Shao, D.W. Matson, J.H. Li, Y.H. Lin, Nitrogen-Doped Graphene and Its Application in Electrochemical Biosensing, ACS Nano, 4 (2010) 1790.
[37] S.B. Yang, L.J. Zhi, K. Tang, X.L. Feng, J. Maier, K. Mullen, Efficient Synthesis of Heteroatom (N or S)-Doped Graphene Based on Ultrathin Graphene Oxide-Porous Silica Sheets for Oxygen Reduction Reactions, Advanced Functional Materials, 22 (2012) 3634.
[38] F. Buckel, F. Effenberger, C. Yan, A. Golzhauser, M. Grunze, Influence of Aromatic Groups Incorporated in Long-Chain Alkanethiol Self-Assembled Monolayers on Gold, Advanced Materials, 12 (2000) 901.
[39] J.X. Xu, Y. Zhao, C. Shen, L.H. Guan, Sulfur- and Nitrogen-Doped, Ferrocene-Derived Mesoporous Carbons with Efficient Electrochemical Reduction of Oxygen, ACS Applied Materials & Interfaces, 5 (2013) 12594.
[40] L. Roldan, I. Santos, S. Armenise, J.M. Fraile, E. Garcia-Bordeje, The Formation of a Hydrothermal Carbon Coating on Graphite Microfiber Felts for Using as Structured Acid Catalyst, Carbon, 50 (2012) 1363.
[41] S. Indrawirawan, H.Q. Sun, X.G. Duan, S.B. Wang, Nanocarbons in Different Structural Dimensions (0-3D) for Phenol Adsorption and Metal-Free Catalytic Oxidation, Applied Catalysis B-Environmental, 179 (2015) 352.
[42] P. Iovino, S. Canzano, S. Capasso, A. Erto, D. Musmarra, A Modeling Analysis for the Assessment of Ibuprofen Adsorption Mechanism onto Activated Carbons, Chemical Engineering Journal, 277 (2015) 360.
[43] X.D. Zhu, Y.C. Liu, C. Zhou, G. Luo, S.C. Zhang, J.M. Chen, A Novel Porous Carbon Derived from Hydrothermal Carbon for Efficient Adsorption of Tetracycline, Carbon, 77 (2014) 627.

[44] H. Guedidi, L. Reinert, J.M. Leveque, Y. Soneda, N. Bellakhal, L. Duclaux, The Effects of the Surface Oxidation of Activated Carbon, the Solution PH and the Temperature on Adsorption of Ibuprofen, Carbon, 54 (2013) 432.
[45] S.P. Dubey, A.D. Dwivedi, M. Sillanpaa, K. Gopal, Artemisia Vulgaris-Derived Mesoporous Honeycomb-Shaped Activated Carbon for Ibuprofen Adsorption, Chemical Engineering Journal, 165 (2010) 537.
[46] A.S. Mestre, R.A. Pires, I. Aroso, E.M. Fernandes, M.L. Pinto, R.L. Reis, M.A. Andrade, J. Pires, S.P. Silva, A.P. Carvalho, Activated Carbons Prepared from Industrial Pre-Treated Cork: Sustainable Adsorbents for Pharmaceutical Compounds Removal, Chemical Engineering Journal, 253 (2014) 408.
[47] S.A. Wohlgemuth, R.J. White, M.G. Willinger, M.M. Titirici, M. Antonietti, A One-Pot Hydrothermal Synthesis of Sulfur and Nitrogen Doped Carbon Aerogels with Enhanced Electrocatalytic Activity in the Oxygen Reduction Reaction, Green Chemistry, 14 (2012) 1515.
[48] H. Sun, S. Liu, G. Zhou, H.M. Ang, M.O. Tadé, S. Wang, Reduced Graphene Oxide for Catalytic Oxidation of Aqueous Organic Pollutants, ACS Applied Materials & Interfaces, 4 (2012) 5466.

# Chapter 5. Heteroatom (N or N-S)-Doping Induced Layered and Honeycomb Microstructures of Porous Carbons for $CO_2$ Capture and Energy Applications

## Abstract

*In chapter 3, N-doped layered porous carbon (NCs) at different temperatures have been prepared through a one-pot pyrolysis process of the mixture containing glucose, sodium bicarbonate, and urea, which proves 700 ºC to be the optimum synthesis temperature. In chapter 4, N-S co-doped honeycomb porous carbons (NSC) were prepared at 700 ºC by pyrolysis of glucose, sodium bicarbonate, and thiourea and the doping level can be adjusted by tuning the amount of thiourea. In this chapter, the effect of urea content on the microstructure of NCs is studied. The formation mechanism of the varying pore frameworks in NCs and NSC induced by heteroatom (N or N, S) doping is analyzed. In addition, NCs and NSC are investigated for other applications including $CO_2$ uptake and oxygen reduction reaction (ORR). Specifically, NSC displays a similar $CO_2$ adsorption capacity (4.7 mmol $g^{-1}$ at 0 °C), a better $CO_2/N_2$ selectivity and higher activity in ORR as compared with NC-3 (the NC sample with the highest N content of 7.3%). NSC favors an efficient four-electron reduction pathway and presents better methanol tolerance than Pt/C in alkaline media. The porous carbons also exhibit excellent rate performance as supercapacitors.*

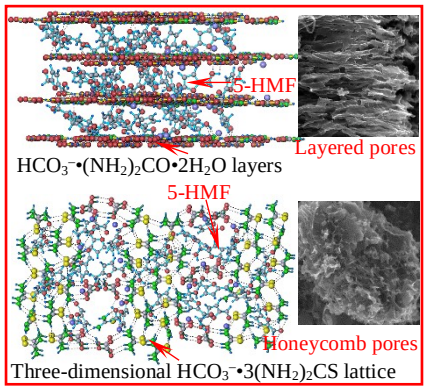

## 5.1 Introduction

Efficient $CO_2$ capture and sequestration become more and more critical for climate change mitigation, atmospheric pollution control in enclosed spaces, mining safety, and production processes of synthetic fuels and high valued chemicals.[1-3] Conventional $CO_2$ removal employs amine-based solvents to absorb $CO_2$ from the exhaust gas,[4] yet the technique suffers from inherent drawbacks, for examples, intensive energy input, the low thermal stability of solvents, equipment corrosion and inefficiency, volatility of the amines and toxicity.[4, 5] Thus, novel materials with a high $CO_2$ uptake capacity but featuring a lower energy penalty for regeneration would be crucial for improving commercial viability. Recently, the development of porous solid adsorbents has attracted considerable attention. A variety of solid materials such as metal organic frameworks (MOFs),[6] zeolites,[7] porous carbons,[2, 8] and coordination organic polymers (COPs)[9] have been developed for $CO_2$ uptake. Among them, porous carbons have been demonstrated to be of low cost and have excellent thermal and chemical stability, a hydrophobic surface, high surface area, absence of toxicity and cost-effective regeneration for $CO_2$ uptake.

On the other hand, in order to mitigate $CO_2$ emissions from fossil fuel combustion, the deployment of renewable and clean energy sources such as $H_2$ can be a promising alternative. Therefore, suitable energy conversion and storage technologies are highly in demand. Among these approaches, fuel cells have been recognized to possess the cleanest and most efficient energy conversion. In the processes the fuels react with $O_2$ through benign electrochemical processes at a high fuel-conversion efficiency, avoiding direct combustion.[10, 11] Oxygen reduction reaction (ORR) is the cornerstone of cathode reactions in fuel cells in which an oxygen molecule receives electrons to form products.[11-13] Pt and Pt-based alloys are the most efficient ORR catalysts to date, yet the scarcity, high price, poor stability and poor tolerance of Pt catalysts to methanol severely hinder their wide-spread implementation.[13] Rational design of highly efficient non-precious catalysts with a comparable ORR activity to Pt-based alloys but superior stability and alcohol-tolerance is a hot topic of research in this field. In this regard, carbon materials become fantastic candidates, considering their high electronic conductivity, tunable porosity, excellent stability and unique electrocatalytic selectivity. Therefore,

tremendous efforts have been devoted to developing porous carbons to address various issues such as structure-dependent mass-diffusion limitations.[14]

For $CO_2$ uptake and ORR applications, the performance of porous carbon materials can be affected by both the intrinsic nature and the porous structure. The intrinsic activity can be improved by introducing heteroatoms.[14, 15] Typically, nitrogen doping is most attractive since it can induce some basicity for enhanced interactions with acidic gas $CO_2$. Recent studies also indicated that polar sulfur-containing groups could facilitate $CO_2$ adsorption on carbon materials,[16] yet few investigations have been performed in $CO_2$ capture by porous carbons with nitrogen and sulfur doping. For ORR, N incorporation can disrupt the electro-neutrality of adjacent C atoms, creating charges and spin redistribution to favor oxygen adsorption and reduction.[14] Besides, N and S co-doping has been adopted in ORR to obtain enhanced activities compared with mono-atom doping, evidenced in experiment and simulation.[17] Despite extensive studies having been carried out, the available catalyst materials are still far from satisfactory from economical, technical and environmental viewpoints.[14, 15]

Hierarchically porous carbons with both mesopores and micropores are believed to be favored for both $CO_2$ uptake and ORR. Specifically, mesopores enable fast gas diffusion, while micropores induce high surface area for a high $CO_2$ adsorption capacity.[18] With regard to ORR, micropores can expose large amounts of potential active sites whereas mesopores are conducive for mass transfer during electrochemical reactions.[19] Soft- and hard-templating approaches have been applied to fabricate the desired porous structures.[20] In the former synthesis, soft-templates can be easily removed by heating. The interaction between surfactant molecules and guest species is crucial for the formation of porous structures.[20, 21] Since slight fluctuation of synthesis condition can affect the co-assembly process, the hydrolysis and condensation of guest species and their assembly with the surfactants should be carefully controlled to generate the desired porosity.[22, 23] The hard-templating route is able to fabricate a wide variety of materials. However, it has the limitations associated with the complex and time-consuming template-removing procedures.[19, 24] To date, it still remains a challenge to rationally design and prepare hierarchically porous structures by a green and feasible protocol.[18]

Based on previous work in chapter 3 and 4, N-doped porous carbon (NC) and N, S co-doped carbon (NSC) were fabricated through a one-pot pyrolysis process of the mixture containing glucose, sodium bicarbonate, and urea or thiourea. Compared with soft-templating methods, this protocol is easy to handle since the self-assembly among the precursors is effortless to happen by evaporation due to the strong hydrogen-bond interactions. In comparison with the hard-templating craft, our process based on the pore-foaming of sodium bicarbonate is evidently more green and scalable, because the decomposition product (sodium carbonate) can be easily removed by water washing.

NCs exhibit pillaring-layered microstructure while NSC has a honeycomb-porous morphology. By tailoring urea addition, the N functionalities and hierarchical porosities can be designed and optimized. The content of NSC was decided according to Chapter 4. Apart from applications in water treatment and supercapacitors studied in chapter 3 and 4, NCs and NSC are further explored for $CO_2$ capture and ORR tests in this chapter. Based on hydrogen-bond interactions, the formation mechanism of the different pore frameworks is revealed, which is of significance for designing various porous carbon materials. Non-doped porous carbon (PC) was also prepared from glucose and sodium bicarbonate. It is indicated that all the synthesized porous carbons have a high $sp^2$-C ratio. With a combination of high surface areas and interconnected pore networks, they show a great potential to serve as both effective $CO_2$ adsorbents and metal-free electrocatalysts for ORR. In addition, to elucidate the transport issues in the ORR activity, supercapacitor measurements were also conducted. This study opens a route for the large-scale production of highly-active porous carbons.

## 5.2. Experimental Section

### *5.2.1 Chemical Reagents*

D-(+)-glucose (≥ 99.5%), urea (≥ 99.5%), sodium bicarbonate (≥ 99.7%), thiourea (≥ 99.0%), Nafion® 117 solution (5wt.%, Aldrich), potassium hydroxide (≥ 70%, 30% water), isopropanol alcohol (≥ 99.7%), methanol (≥ 99.9%), commercial Pt/C (20 wt.%, Vulcan) were purchased from Sigma-Aldrich and used directly without further purification.

*5.2.2 Preparation of Porous Carbon Materials*

(1) Dissolve glucose (0.9 g), sodium bicarbonate (0.9 g) and urea (the mass changed from 0.3, 0.9 to 1.2 g to synthesize NC-1, NC-2 and NC-3, respectively) in pure water and then evaporate the water at 105 $^{o}$C; (2) heat treatment of the mixture at 700 $^{o}$C for 2 h with a heating rate of 5 $^{o}$C/min under $N_2$ flow to form NCs. PC and NSC were prepared according to chaper 4. Briefly, pyrolysis of the mixture of 0.9 g glucose and 0.9g sodium bicarbonate (PC) as well as these two chemicals with 0.3 g thiourea (NSC) at 700 $^{o}$C. Finally, the carbonized materials were grinded and washed with water and ethanol for several times, then dried in an oven.

*5.2.3 Characterizations*

The details on $N_2$ sorption, SEM, TEM, HRTEM, HAADF-STEM, XPS, Roman spectroscopy and EDX elemental mapping analysis can refer to chapter 3. The carbon electron energy-loss spectroscopy (EELS) spectra were obtained by FEI Titan G2 80-200 TEM/STEM.

*5.2.4 $CO_2$ Adsorption at 0 and 25 °C*

The adsorption isotherms of each sample over pure $CO_2$ (99.999%) were recorded by a Micromeritics instrument (Gemini I-2360) at 0 and 25 $^{o}$C under low pressure up to 760 mmHg. All samples were degassed at 110 °C overnight before the tests. $N_2$ adsorption isotherm at 0 °C was also measured on this instrument to view the relative $CO_2$ selective adsorption.

*5.2.5 Electrode Preparation for Electrochemical Measurements*

2 mg of the as-prepared porous carbons were grinded firstly and then blended with 500 µL isopropanol and 25 µL of Nafion® 117 solution to form a 3.6 mg $mL^{-1}$ suspension by sonication. Then, 9 µL of the catalyst ink (containing 32.4 µg of catalyst) was dipped onto the surface of a pre-polished glassy carbon electrode (5.0 mm in diameter) and dried in air. For comparison, commercial Pt/C (20 wt.%, Vulcan) was also prepared by a similar procedure with the same loading on the surface of the working electrode.

Electrochemical measurements were conducted using an MSR-RDE rotating disk (Pine Instrument Company, USA) controlled with a Zennium electrochemical workstation (Zahner, Germany) under ambient conditions. A three-electrode system was used with Ag/AgCl (KCl sat.) electrode and platinum wire as the counter electrode and the reference electrode, respectively, and a rotating disk electrode (RDE) with a glassy carbon as the working electrode. The potential differences between Ag/AgCl and reversible hydrogen electrode (RHE) were calibrated through equation (5.1):

$$E_{RHE} = E_{Ag/Agcl} + 0.059\,pH + 0.197 \qquad (5.1)$$

All potential data in this study refer to RHE.

*5.2.6 ORR Measurements*

Cyclic voltammetry (CV) experiments of different catalysts were performed in $N_2/O_2$-saturated KOH (0.1 M) solution at a scan rate of 50 mV $s^{-1}$. All electrochemical data were recorded until stable curves were obtained. For the RDE tests, the working electrode was conducted at a sweep rate of 10 $mVs^{-1}$ with varying rotating speeds from 225 to 2500 rpm. All sample tests were repeated at least 3 times to avoid any incidental errors.

The Koutecky-Levich (K-L) plots ($J^{-1}$ vs $\omega^{-1/2}$) were obtained according to the linear fitting of the reciprocal rotating speed versus reciprocal current density at various electrode potentials. The overall electron transfer numbers (n) per oxygen molecule during a typical ORR process were calculated according to the slopes of linear fit lines in the K-L plots, on the basis of the Koutecky-Levich equations:[11]

$$1/J = 1/J_K + 1/B\,\omega^{1/2} \qquad (5.2)$$

$$B = 0.2nFC_0(D_0)^{2/3}\nu^{-1/6} \qquad (5.3)$$

where $J$ is the measured current density, $J_K$ the kinetic current density, $\omega$ the electrode rotating speed in rpm, B the reciprocal slopes of the K-L plots, n transferred electron number per oxygen molecule and the constant 0.2 is used when the rotating speed is in rpm. For the Tafel plots, $J_K$ was determined from the mass-transport correction of RDE at 1600 rpm by equation (5.4):

$$J_K = (J * J_L)/(J_L - J) \qquad (5.4)$$

where $J_L$ is the diffusion-limiting current density.

*5.2.7 Supercapacitor and Electrochemical Impedance Spectroscopy (EIS) Test*

Supercapacitor performance was evaluated by measuring CVs in 1 M KOH with $N_2$ purging using the same electrical devices and procedures as described above. EIS was measured from 10 mHz to 100 KHz.

## 5.3. Results and Discussion

*5.3.1 Properties of Porous Carbons and Their $CO_2$ Capture*

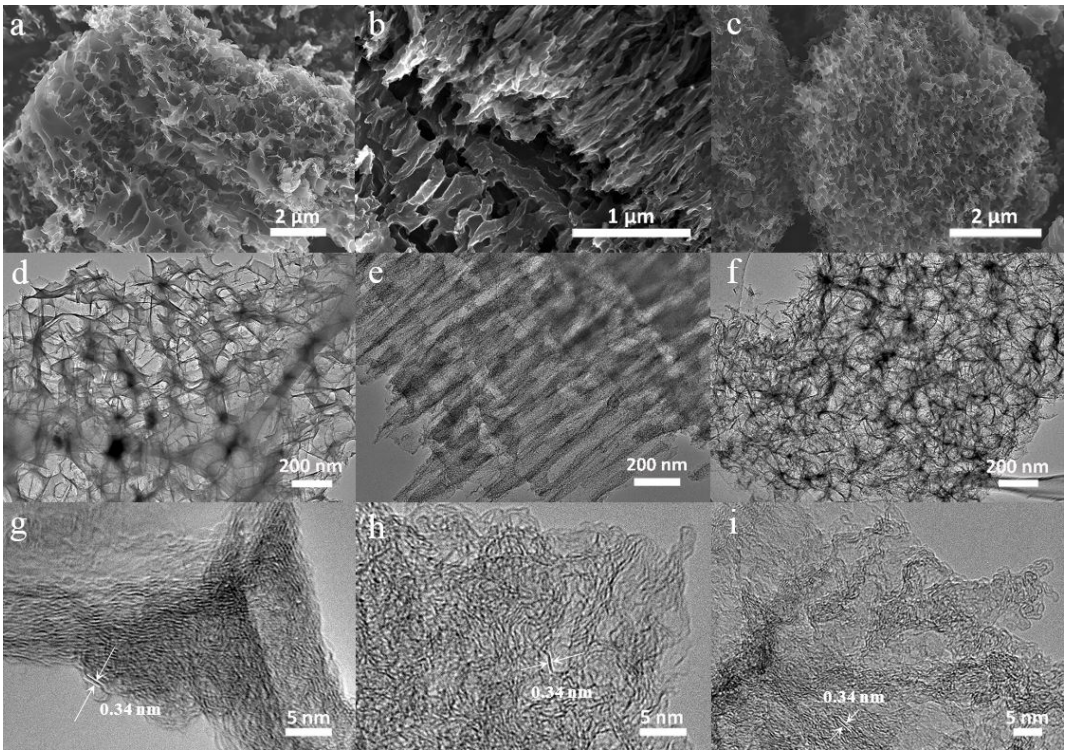


**Figure 5.1** EM images of the three porous carbons. (a-c) SEM images, (d-f) TEM images, (g-i) HRTEM images. Wherein, a, d, g) PC; b, e, h) NC-2; c, f, i) NSC.

SEM images (Figure 5.1a) of PC confirm that it is highly porous. TEM further reveals that uniform, honeycomb-like pores in PC form a three-dimensionally interconnected network (Figure 5.1d). NCs (nitrogen-doped carbons derived from urea, sodium bicarbonate and glucose) with increasing N loadings are referred to as NC-1, NC-2 and NC-3, respectively. Interestingly, NCs not only possess numerous pores but also exhibit a pillaring layered structure, which are different from PC (Figure 5.1b, e). Moreover, small rounded pores in NCs exist along the layered pore channels. However, the involvement of thiourea did not change the pore frameworks and the pore shapes in NSC (Figure 5.1c,

f), compared to PC. As shown in the HRTEM images, multiple randomly oriented graphitic layers can be clearly seen in the pore frameworks of all porous carbon samples, with an identified interlayer spacing of 0.34 nm, which can be assigned to the (002) of graphite. This result suggests the high ratio of $sp^2$-C, which can also be verified by carbon EELS analysis (Figure 5.2a-d).

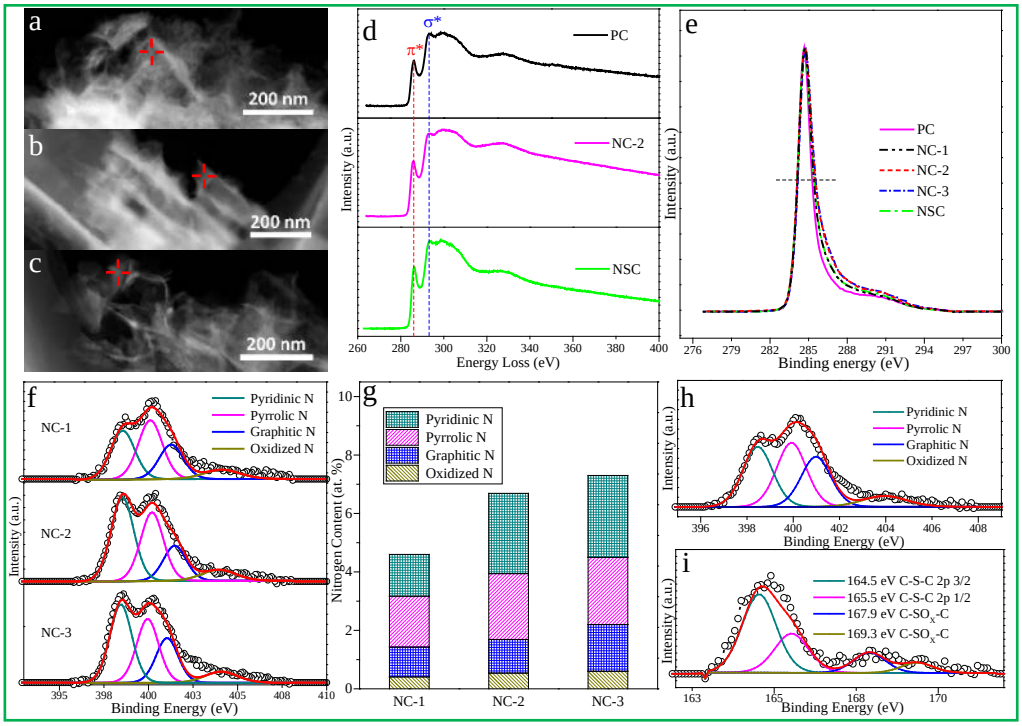


**Figure 5.2** Dark field STEM images of a) PC, b) NC-2 and c) NSC; d) EELS spectra obtained at the marked points in a-c; e) High resolution N 1s spectra of all the porous carbons; f) High resolution N 1s spectra of NCs; g) The contents of four nitrogen species in NCs; h) High resolution N 1s spectra of NSC; i) S 2p spectra of NSC.

The carbon K-edge spectra of the PC, NC-2 and NSC exhibit sharply-defined peaks at around 285.8 eV due to transitions from the 1s to the π* states, followed by the peaks at about 293.1 eV due mainly to transitions from 1s to σ* states, corresponding to the $sp^2$-hybridization states.[25-28] The strong and sharp π* peaks prove the high $sp^2$-C ratios in the porous carbons,[26, 29] consistent with the HRTEM observation. Since $sp^2$ bonding is correlated to the electrical conductivity, the synthesized porous carbons are of high quality with an interconnected open-pore system, which can easily activate the electron transfer for electrochemical energy applications.

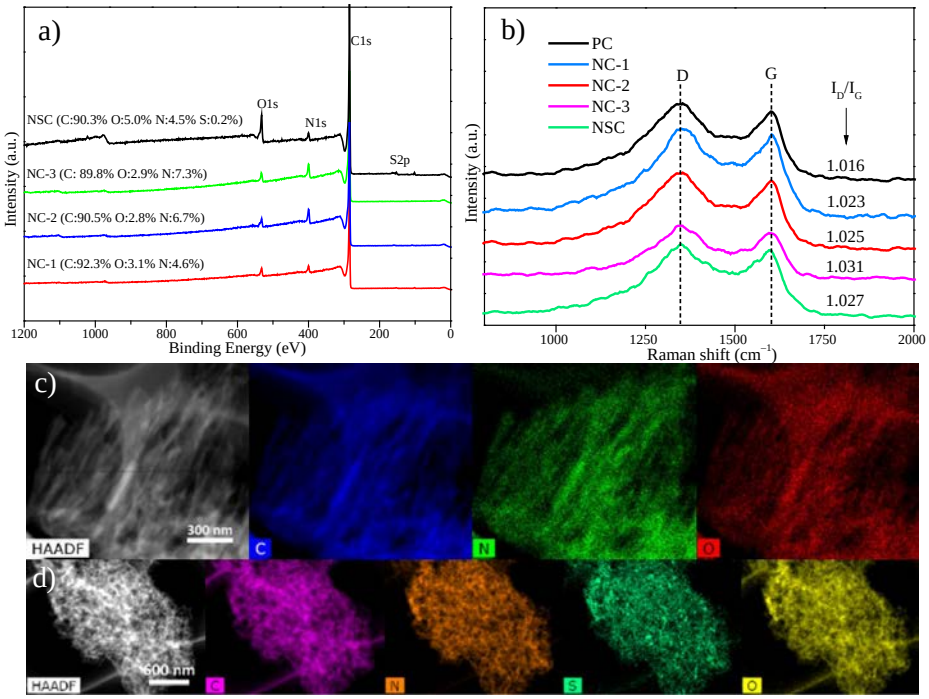


**Figure 5.3** a) Wide survey of XPS spectra of the samples and b) Raman spectra of various samples. HAADF-STEM with EDX elemental mapping images of c) NC-2 and d) NSC.

XPS was employed to analyze the surface chemical states and the composition of the samples. As urea acts as N-donor agent, with increasing urea amount in the precursors, N content increases steadily in the resulting NCs. Specifically, the N contents were found to be 4.5 at.% in NC-1, 6.7 at.% in NC-2 and 7.3 at.% in NC-3 (Figure 5.3a). NSC possesses a similar surface N content to NC-1 (4.6 at.%). In addition, the elemental mapping analysis of NC-2 and NSC shows that the chemical distributions of these elements along the pore frameworks are uniform (Figure 5.3c and d).According to previous studies, the introduction of heteroatoms into pristine carbon tends to produce more structural defects, reflected by the broadened FWHM (full width at half maximum) of C 1s peaks.[27, 28] Accordingly, NCs and NSC show slightly wider FWHMs than PC (Figure 5.2e). The tails between 286 and 292 eV can be ascribed to the surface carbon-oxygen, carbon-nitrogen or carbon-sulfur-containing groups and energy loss “shake-up” features.[27, 29, 30] However, changes in the overall degree of graphitization of the porous carbons induced by heteroatom-doping were tiny, because the differences in $I_D/I_G$ ratios obtained by their Raman spectra were minor (Figure 5.3b). For NCs and NSC, the XPS N1s spectra (Figure 5.2f and h) can be fitted into four peaks with the binding energies at around 398, 400, 401 and 405 eV, corresponding to pyridinic-N, pyrrolic-N, graphitic-N, and oxidized-N,

respectively.[31-33] Except for the almost unchanged oxidized-N, the other N species show an increasing trend in NCs with increasing total N content (Figure 5.2g). It was documented that pyrrolic-N generally has a greater contribution to $CO_2$ capture than other species,[2, 34, 35] whereas graphitic-N and pyridinic-N are the most active sites in ORR.[33, 36, 37] The high resolution S 2p peaks can be fitted into four peaks centred at around 164.5, 165.5, 167.9 and 169.3 eV, respectively (Figure 5.2i). The former two peaks correspond to S $2p_{3/2}$ and S $2p_{1/2}$ positions of thiophene-S (-C-S-C-), while the peaks at 167.9 and 169.3 eV can be assigned to oxidized-S groups (-C-$SO_x$-C-).[30, 33, 38] The oxidized-S plays a significant role in $CO_2$ adsorption,[39] yet it is chemically inactive for ORR where thiophene-S is believed to be more effective.[40] The chemical compositions of the prepared samples suggested the functional groups potentially active for both $CO_2$ uptake and ORR.

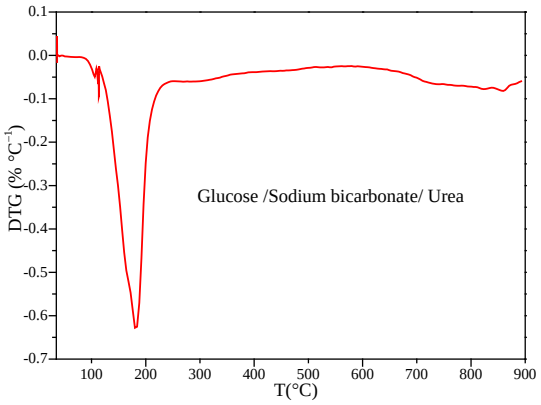


**Figure 5.4**. DTG curve of the pristine mixture of glucose (0.9 g), sodium bicarbonate (0.9 g) and urea (0.9 g) heated under argon atmosphere.

According to our previous finding in chapter 4, pure glucose decomposition has two peaks at 209 and 305 °C in DTG curve while glucose/sodium bicarbonate and glucose/bicarbonate/thiourea only have one peak at about 150 °C. Consistent with that, the DTG curve of the glucose/sodium bicarbonate/urea mixture (Figure 5.4) suggested the occurrence of the evaporated-induced self-assembly process among the precursors before pyrolysis, as it has only one decomposition peak at around 180 °C.

The dependence of the pore formation mechanism on hydrogen-bond interaction during the evaporation process of different precursor materials has been discussed. Based on reference,[41] the hydrogen-bonding interactions of urea, water and bicarbonate ions are

described in Scheme 5.1a. Specifically, urea, water molecules and hydrogen carbonate anions are linked side by side alternately via N-H···O and O-H···O hydrogen bonds to form a ribbon. Cross-linkage between adjacent ribbons generates a puckered urea-anion-water ($HCO_3^-$•$(NH_2)_2CO$•$2H_2O$) layer, and the two-dimensional network is built as a result. Scheme 5.1b describes several layers of such a network. On the other hand, preliminary findings showed that glucose solutions could be thermally decomposed under excessive heat, causing the formation of 5-hydroxymethylfurfural (5-HMF) during evaporation at 105 ºC.[42] It is proposed that the formed 5-HMF might be alternately arranged and sandwiched between the adjacent $HCO_3^-$•$(NH_2)_2CO$•$2H_2O$ layers, bridged by O-H···O, H-O···H and O···H-N hydrogen bonds, as shown in Scheme 5.1c. Finally, during the pyrolysis of the mixture, 5-HMF is dehydrated and then carbonized to form the wall of pillaring-layered pores. Urea and sodium bicarbonate transformation, together with water molecules escaping, lead to the formation of the pillared-layered pore channels, which may also generate the cross-sectional pores in the channel walls (Scheme 5.1d). Since urea decomposition will leave a small amount of carbon residues, some pores could also be observed on the channels of NCs.

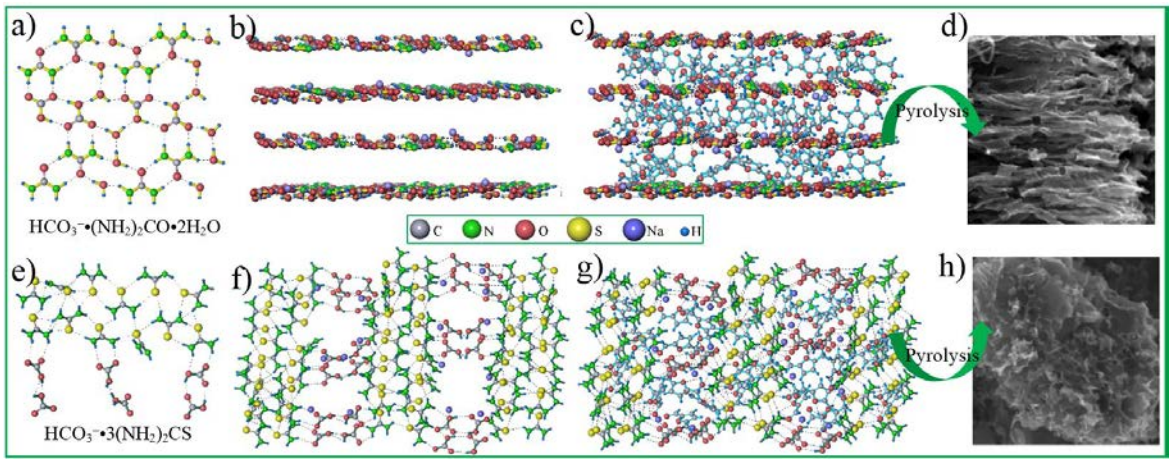


**Scheme 5.1** Stereo drawing of the formation mechanism of (a-d) N-doped pillared-layered porous carbon and (e-h) N-S co-doped honeycomb-porous carbon.

Scheme 5.1e illustrates the hydrogen-bonding interactions among the thiourea molecules and bicarbonate ions.[43] Thiourea molecules are connected in turn by the pairs of N-H···S hydrogen bonds to form a zigzag ribbon. Unlike Scheme 1a, there is a highly twisted shape in this process. Twisted thiourea ribbons are jointed by lateral N-H···S to produce puckered double-ribbons, which are further cross-linked by $(HCO_3^-)_2$ units in an $HCO_3^-$

•3$(NH_2)_2CS$ manner, resulting in a three-dimensional host-lattice with open channels (Scheme 5.1f). 5-HMF is closely involved in the host lattice by O-H···O, H-O···H, O-H···S and O···H-N hydrogen-bond-interactions, as shown in Scheme 5.1g. During the heating process, 5-HMF, thiourea and sodium bicarbonate decomposed, and a large number of pores are generated, resulting in a three-dimensional honeycomb pore network (Scheme 5.1h).

For the non-doped porous carbon without the involvement of urea or thiourea, it can be speculated that the pore structure in PC is formed following a similar principle, in which 5-HMF and $HCO_3^-$ are cross-connected by O-H···O and H-O···H hydrogen bonds. The $CO_2$ formation and escaping lead to the highly-porous structures.

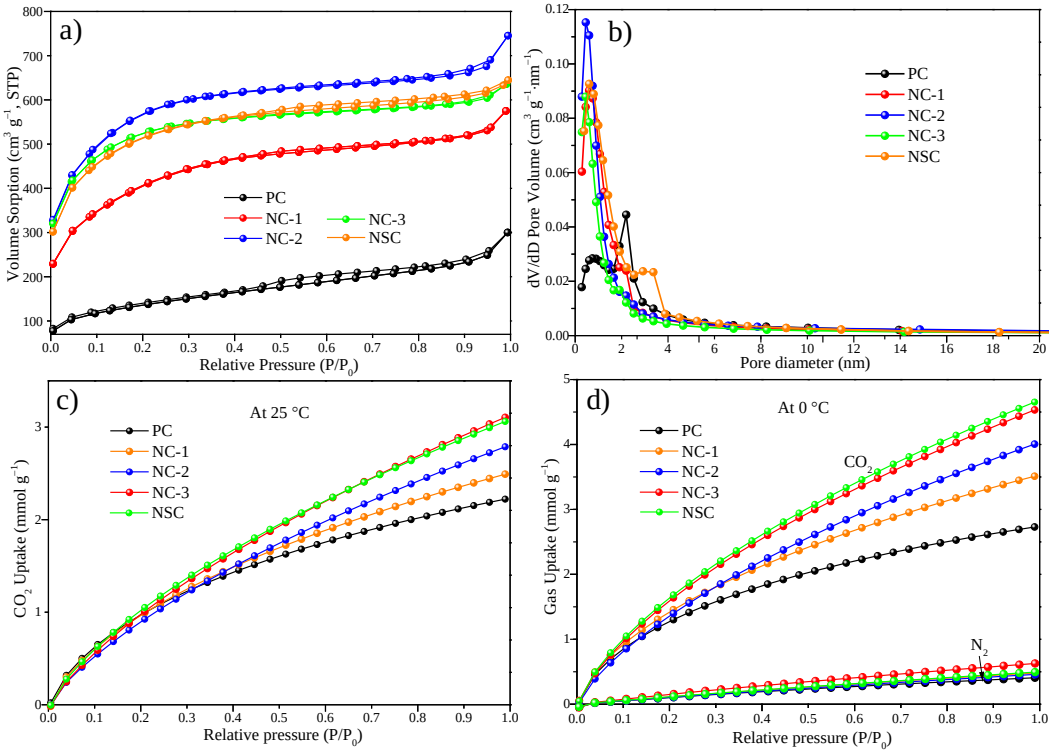


**Figure 5.5** a) $N_2$ adsorption-desorption isotherms of the carbon samples, b) Pore size distributions calculated by BJH desorption, c) $CO_2$ adsorption isotherms on the as-prepared carbon samples at 25 °C and d) $CO_2$ and $N_2$ uptake isotherms at 0 °C under ambient pressure (1.0 atm).

To assess the textural properties of these carbons, $N_2$ adsorption-desorption isotherms were acquired and summarized in Figure 5.5 and Table 5.1. The average pore sizes of all porous carbons are less than 50.6 nm, with hierarchical porosities of mesopores and

micropores. Notably, after N or N, S doping, the BET surface areas of NCs (1344-1840 $m^2 g^{-1}$) and NSC (1608 $m^2 g^{-1}$) are much larger than PC and are accompanied by enlarged pore volumes. The results proved that urea or thiourea might have triple functions in the pore formation processes: as an extra pore-generating agent, second carbon source and a dopant precursor. The comparisons among NCs indicate that increasing N content leads to a higher micropore volume ($V_{mic}$). However, the mesopore volume ($V_{meso}$) increases first, then decreases with further increasing N content due to the potential blocking of pore channels by adventitious species. Considering that micropores are usually favored for $CO_2$ adsorption, raising the N doping content might be a good way to obtain high $CO_2$ uptake capacities. On the other hand, increasing $V_{mic}$ may increase the contact resistance from isolated carbon particles and limit the conductivity, which should be considered when designing electrode materials for ORR. Therefore, a suitable mesopore and micropore ratio needs to be carefully controlled according to different applications.

**Table 5.1** Textural characteristics of the carbon samples.

| Samples | $S_{BET}$ [a] / $m^2 g^{-1}$ | $V_t$ [c]/ $cm^3 g^{-1}$ | $V_{mic}$ [b]/ $cm^3 g^{-1}$ | $V_{meso}$ [d] / $cm^3 g^{-1}$ | $CO_2$ uptake at 0 °C (mmol $g^{-1}$) | $CO_2$ uptake at 25 °C (mmol $g^{-1}$) |
|---|---|---|---|---|---|---|
| PC | 459 | 0.46 | 0.04 | 0.42 | 2.7 | 2.2 |
| NC-1 | 1344 | 0.89 | 0.12 | 0.77 | 3.5 | 2.5 |
| NC-2 | 1840 | 1.15 | 0.35 | 0.8 | 4.0 | 2.8 |
| NC-3 | 1666 | 0.98 | 0.42 | 0.56 | 4.5 | 3.1 |
| NSC | 1608 | 1.00 | 0.33 | 0.67 | 4.7 | 3.1 |

[a] Surface area calculated by the BET method; [b] Micropore volume calculated by the t-plot method; [c] Total pore volume calculated at a $P/P_0 = 0.99$; [d] Mesopore volume obtained by the difference between $V_t$ and $V_{mic}$

$CO_2$ sorption measurements were performed at 25 and 0 °C under an atmospheric pressure range (0 - 1 atm) to evaluate the gas sorption properties of the prepared porous carbons. Figure 5.5c and d show $CO_2$ uptake isotherms for the porous carbons and the capacity values are summarized in Table 5.1. PC shows a moderate $CO_2$ uptake capacity. With increasing N doping level, the adsorption capacity increased gradually for NCs. According to recent studies on N-decorated carbons, apart from the BET surface area and microporosity, N doping level and hydrogen bonding are two other factors closely governing the $CO_2$ capture performance.[44] Specifically, the presence of N atoms in the

carbon, with the most active pyrrolic-N,[2, 34] will increase the basicity by offering electron donor groups and facilitate their interactions with acidic $CO_2$. In addition, the introduction of N into a carbon surface will improve the hydrogen-bonding interactions between the C-H groups and $CO_2$ molecules, leading to greater $CO_2$ uptake.[3] It is thus deduced that higher micropore volume and pyrrolic N content are generally responsible for the highest capacity of NC-3 among the NCs (3.1 mmol $g^{-1}$ at 25 °C and 4.5 mmol $g^{-1}$ at 0 °C), better than NC-2 with the highest $S_{BET}$. NSC displays a similar $CO_2$ uptake to NC-3 at 25 °C, yet slightly higher adsorption at 0 °C (4.8 mmol $g^{-1}$). This performance is among the best porous carbons and superior to most MOFs (Table 5.2). It is also worth noting that the selectivity of $CO_2/N_2$ of NSC outperforms NC-3 at 0 °C with lower $N_2$ adsorption while demonstrating a slightly higher $CO_2$ capture (Figure 5.5d). Previous studies indicated that the selective $CO_2$ uptakes are mainly ascribed to the functional groups.[45] Given that NSC possesses a comparable surface area, a lower micropore volume and lower N content than NC-3, the higher $CO_2$ capture capacity and better selectivity can be attributed to the trace amount of doping S atoms, mainly as oxidized-S.[39] According to the calculations based on natural bonding orbitals, O in thiophene (–0.94) possesses a more negative charge than N in pyrrole (–0.59) affected by the highly positive charge of S in thiophene.[39] Thus, the attraction energy between $O_{thiophene}$ and $C_{CO2}$ (+1.07) is higher than that of $N_{pyrrole}$ with $C_{CO2}$. As a result, NSC exhibited a better selectivity and a comparative $CO_2$ capture capacity with NC-3.

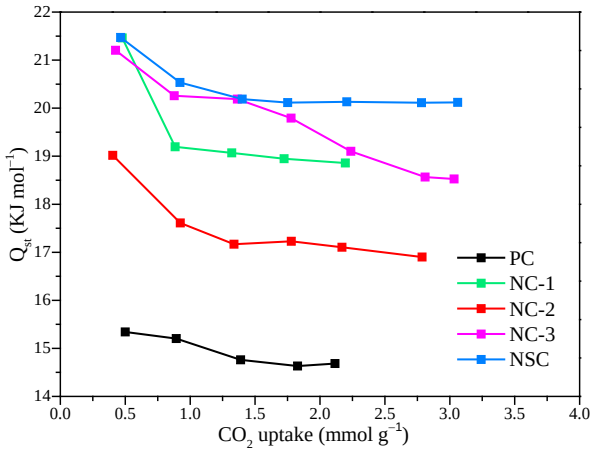


**Figure 5.6** Isosteric heats of adsorption of the various samples.

To determine the interaction strengths between the carbon samples and adsorbed $CO_2$, isosteric heats of adsorption ($Q_{st}$) for all the porous carbons were obtained from $CO_2$

capture isotherms at 0 and 25 °C based on the Clausius-Clapeyron equation (Figure 5.6). The $Q_{st}$ values of all samples are in the range of 14.7-21.5 kJ $mol^{-1}$, which show an increasing trend after N doping compared to PC. Furthermore, NSC exhibits the highest $Q_{st}$ values among all porous carbons, which also helps explain for its better selectivity for $CO_2$ over $N_2$.[46]

**Table 5.2** $CO_2$ uptakes on the synthesized carbon samples at 1.0 bar.

| | BET surface area | Total pore volume | Activation | $CO_2$ uptake at 0 °C (mmol $g^{-1}$) | $CO_2$ uptake at 25 °C (mmol $g^{-1}$) | References |
|---|---|---|---|---|---|---|
| d-MCN | 463 | 0.25 | no | 1.77 | 1.16 | [47] Carbon 2016 |
| NMC600-330-1h | 907 | 0.77 | no | 3.97 | 2.74 | [48] Chem Commun 2015 |
| HTC-K1-T8 | 1013 | 0.56 | yes (KOH) | 4.9 | 3.0 | [49] Carbon 2015 |
| H-NMC-2.5 | 537 | 0.47 | yes (KOH) | - | 3.2 | [24] Adv Funct Mater 2013 |
| NC900 | 2747 | 1.58 | yes (NH4OH) | 5.1 | 3.9 | [46] J Am Chem Soc 2014 |
| nZDC-700 | 950 | 0.35 | no | - | 3.51 | [50] Chemsuschem 2015 |
| RFL-500 | 467 | 0.23 | no | - | 3.13 | [51] Adv Mater 2010 |
| HCM-DAH-1-900-1 | 670 | 0.46 | no | 4.9 | 3.3 | [52] J Am Chem Soc 2011 |
| ZIF-8 (24h@500 °C, MOF) | 942 | - | no | 3.0 | 1.79 | [53] Energ Environ Sci 2014 |
| IFMC-69 (MOF) | 581 | 0.25 | no | 2.5 | 1.6 | [54] Chem Sci 2014 |
| NENU-520 (MOF) | 387 | 0.27 | no | 3.56 | 2.72 | [55] J Mater Chem A 2015 |
| MOF-5 (6h@380 °C) (MOF) | 988 | 1.23 | no | - | 2 | [56] Chem Mater 2014 |
| Bio-MOF-14 (MOF) | - | - | no | 4.1 | - | [57] J Am Chem Soc 2013 |
| MONT 7 (MOF) | - | - | no | - | 1.51 | [58] J Am Chem Soc 2014 |
| Ln–MOF (MOF) | 1074 | - | no | 3.43 | 1.54 | [59] Chem-Eur J 2015 |
| NC-3 | 1666 | 0.98 | no | 4.5 | 3.1 | This work |
| NSC | 1608 | 1.0 | no | 4.8 | 3.1 | This work |

*5.3.2 Electrocatalytic Performance*

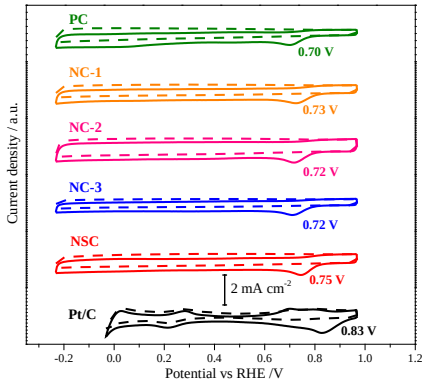


**Figure 5.7** CV curves of the as-prepared carbon samples and Pt/C at a scan rate of 50 mV $s^{-1}$ in $N_2$-saturated (dash line) and $O_2$-saturated (solid-line) 0.1 M KOH solutions.

**Table 5.3** Electrocatalytic performance of the catalysts.

| | Onset potential (V vs. RHE) | Half-wave potential (V vs. RHE) | Current density at 1600 rpm (mA $cm^{-2}$) | Electron transfer numbers (n) [a)] |
|---|---|---|---|---|
| PC | 0.81 | 0.66 | 5.0 | 2.7-3.2 |
| NC-1 | 0.84 | 0.69 | 4.7 | 2.7-3.3 |
| NC-2 | 0.84 | 0.70 | 4.8 | 2.9-3.5 |
| NC-3 | 0.84 | 0.71 | 4.8 | 3.2-3.8 |
| NSC | 0.87 | 0.74 | 5.1 | 3.8-4.0 |
| Pt/C (Vulcan) | 0.94 | 0.83 | 5.0 | 3.8-4.0 |

a) Calculated at potentials of 0.3 - 0.7 V

To evaluate the catalytic ORR performance, cyclic voltammetry (CV) tests were conducted on the as-prepared carbons and commercial Pt/C **(**20 wt.% Pt, Vulcan) reference catalyst in $N_2$- and $O_2$-saturated 0.1 M KOH aqueous solutions (Figure 5.7). In $N_2$ environment, the CV curves showed nearly rectangular shapes, as a result of the typical capacitive effect.[60] When $O_2$ was introduced, well-defined ORR peaks centred at around 0.72 V were observed on NCs, which are positive than that of PC. After N, S co-doping, the peak potential of NSC shifted to a more positive 0.75 V, suggesting a better ORR activity.[14] Similar trends were observed with linear sweep voltammetry (LSV) tests on a rotating-disk electrode (RDE), recorded at different rotating speeds from 225 to 2500 rpm (Figures 5.8a and 5.9). Due to the combined effects of N functionalities and mesopore/micropore ratio, NCs exhibited similar onset-potentials (0.84 V) and half-wave

potentials ($E_{1/2}$, 0.69 - 0.71 V), positive than PC (Table 5.3). Remarkably, compared with the mono-atom doped NCs, NSC displayed a higher ORR activity, as evidenced by the onset-potential of 0.87 V and $E_{1/2}$ of 0.74 V, comparable to 0.94 and 0.83 V on reference Pt/C. In addition, the ORR reaction current of NSC was similar to Pt/C.

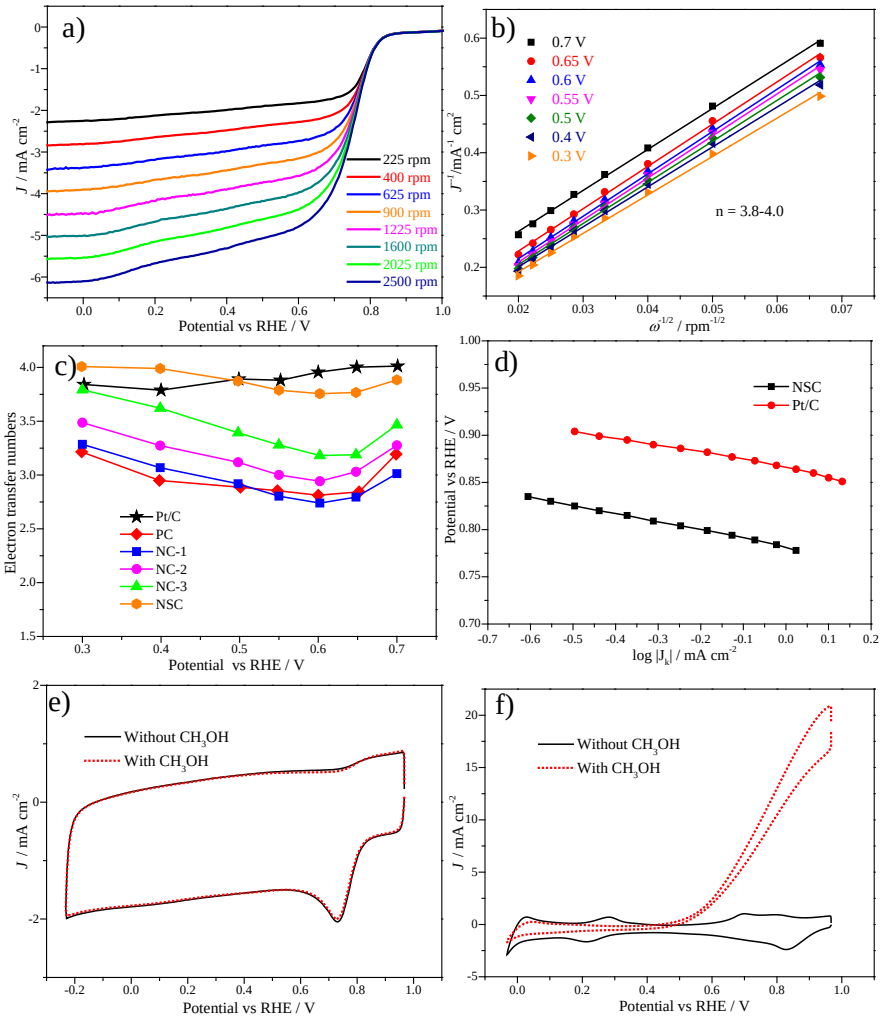


**Figure 5.8** a) LSV curves (scan rate = 10 mV $s^{-1}$) for NSC in an $O_2$- saturated 0.1 M KOH electrolyte; b) K-L plots ($J^{-1}$ versus $\omega^{-0.5}$) for NSC at different potentials; c) Electron-transfer numbers (n) of different samples calculated by their K-L plots; d) Tafel plots of NSC and Pt/C derived from their LSVs at 1600 rpm. CV curves of e) NSC and f) Pt/C in $O_2$- saturated 0.1 M KOH without and with 1.0 M $CH_3OH$ (scan rate = 50 mV $s^{-1}$).

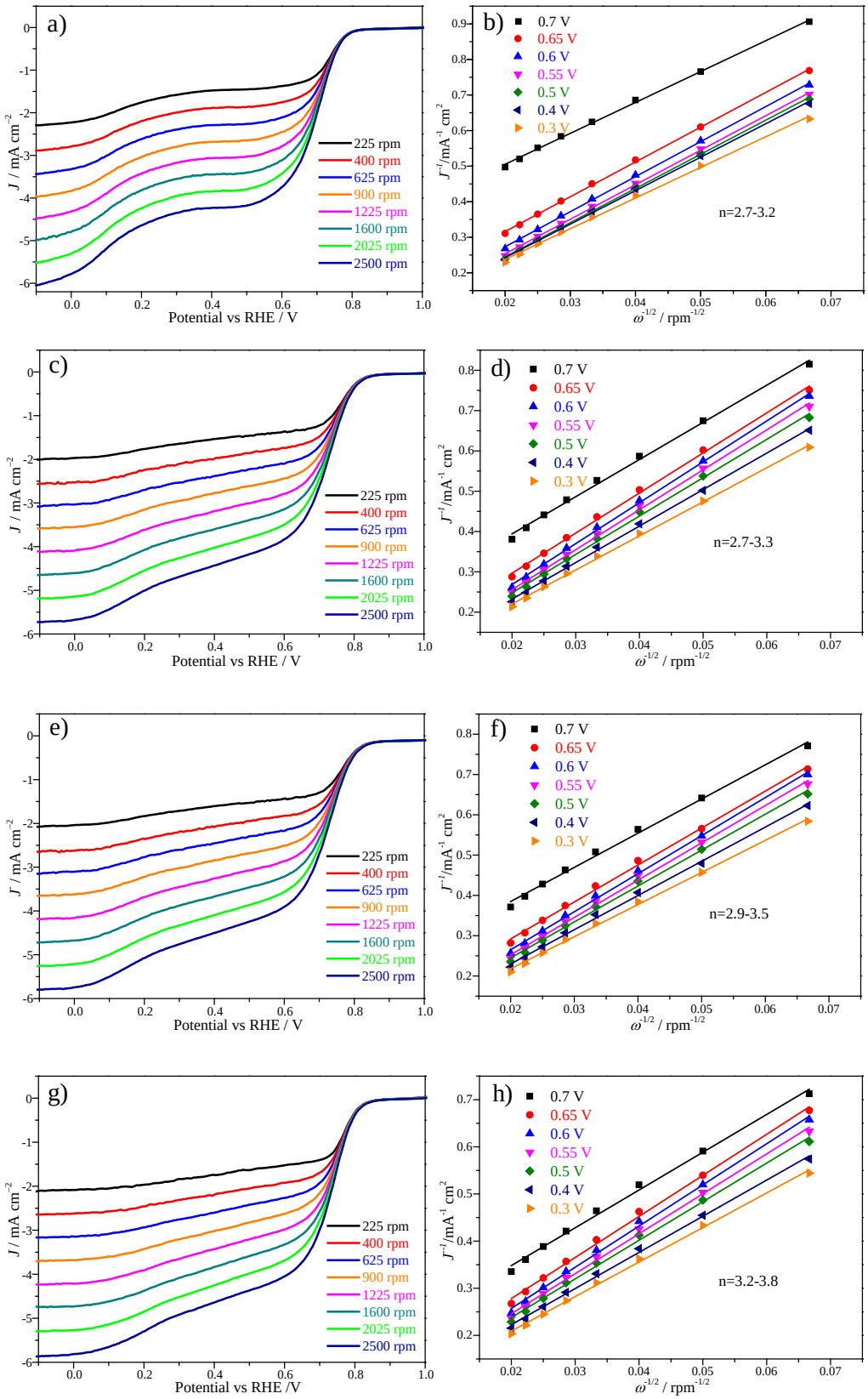
a)
J / mA cm-2
Potential vs RHE / V
225 rpm
400 rpm
625 rpm
900 rpm
1225 rpm
1600 rpm
2025 rpm
2500 rpm
b)
0.7 V
0.65 V
0.6 V
0.55 V
0.5 V
0.4 V
0.3 V
J-1/mA-1 cm2
ω-1/2 / rpm-1/2
n=2.7-3.2
c)
J / mA cm-2
Potential vs RHE / V
225 rpm
400 rpm
625 rpm
900 rpm
1225 rpm
1600 rpm
2025 rpm
2500 rpm
d)
0.7 V
0.65 V
0.6 V
0.55 V
0.5 V
0.4 V
0.3 V
J-1/mA-1 cm2
ω-1/2 / rpm-1/2
n=2.7-3.3
e)
J / mA cm-2
Potential vs RHE / V
225 rpm
400 rpm
625 rpm
900 rpm
1225 rpm
1600 rpm
2025 rpm
2500 rpm
f)
0.7 V
0.65 V
0.6 V
0.55 V
0.5 V
0.4 V
0.3 V
J-1/mA-1 cm2
ω-1/2 / rpm-1/2
n=2.9-3.5
g)
J / mA cm-2
Potential vs RHE /V
225 rpm
400 rpm
625 rpm
900 rpm
1225 rpm
1600 rpm
2025 rpm
2500 rpm
h)
0.7 V
0.65 V
0.6 V
0.55 V
0.5 V
0.4 V
0.3 V
J-1/mA-1 cm2
ω-1/2 / rpm-1/2
n=3.2-3.8

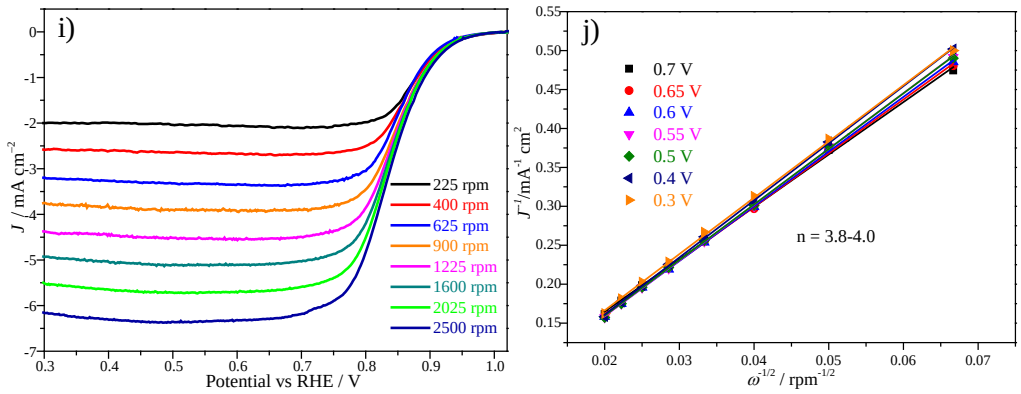


**Figure 5.9** LSVs of a) PC, c) NC-1, e) NC-2, g) NC-3 and i) Pt/C at a sweep rate of 10 mV $s^{-1}$. The corresponding K-L plots ($J^{-1}$ versus $\omega^{-1/2}$) of b) PC, d) NC-1, f) NC-2, h) NC-3 and j) Pt/C at different potentials.

The electrocatalytic $O_2$ reduction in alkaline medium proceeds via the following recognized pathways.

$$O_2 + 2H_2O + 4e \rightarrow 4OH^- \quad \text{(i)}$$

$$O_2 + H_2O + 2e \rightarrow HO_2^- + OH^- \quad \text{(ii)}$$

$$HO_2^- + H_2O + 2e \rightarrow 3OH^- \quad \text{(iii)}$$

$$HO_2^- \rightarrow OH^- + 1/2O_2 \quad \text{(iv)}$$

Among these pathways, the four-electron reduction pathway (i) is more favourable and energy efficient for fuel cell applications.

To qualify the ORR processes, Koutecky-Levich (K-L) plots ($J^{-1}$ vs, $\omega^{-1/2}$) were obtained for each sample using the RDE at various rotating speeds. With increasing rotating speeds, the cathodic current was enlarged due to the improved mass transport at the electrode surface. Figure 5.8b shows K-L plots of NSC. The electron transfer numbers (n) were calculated by the slopes of the linear fitted K-L plots on the basis of the K-L equation. The n values of NSC were 3.8-4.0 at the potentials of 0.3-0.7 V, suggesting an electrochemically stable ORR process favored by a four-electron reduction pathway which directly reduces $O_2$ into $OH^-$. This is promising for the construction of fuel cells with high efficiency. The electron transfer numbers of other samples were also calculated by the correspondingly fitted K-L plots (Figure 5.9), which are summarized in Figure 5.8c. With increasing N-doping levels in NCs, n increased, yet was still lower than NSC. Figure 5.8d shows the Tafel plots of NSC and commercial Pt/C, derived from Figures 5.8a and 5.9i. NSC has a Tafel slope of 87.0 mV/decade in 0.1 M KOH, close to the 81.1 mV/decade of Pt/C, indicating that NSC has an excellent kinetic process for ORR.[61]

The tolerance of NSC and Pt/C toward methanol (MeOH) was determined by introducing 1.0 M MeOH into $O_2$ saturated 0.1 M KOH electrolyte.[61] Figure 5.8e shows almost no variation in the ORR peak current for NSC after adding MeOH, whereas significant oxidation current was observed in the CV of Pt/C catalyst (Figure 5.8f). This result suggests that NSC has a much better catalytic selectivity for ORR than Pt/C along with strong tolerance to the crossover effect.[61]

**Table 5.4** Summary of reported ORR performance of heteroatom-doped carbon catalysts in 0.1 M KOH.

| Sample | Pt/C | Catalyst loading (mg $cm^{-2}$) | Medium | $J^{carbon}$/ $J^{Pt/C}$ (mA $cm^{-2}$) [a] | $E_{1/2}{}^{carbon}$/ $E_{1/2}{}^{Pt/C}$ (V) [b] | $E_{on}{}^{carbon}$/ $E_{on}{}^{Pt/C}$ (V) [c] | Reference electrode | References |
|---|---|---|---|---|---|---|---|---|
| NC900 | HiSPEC 2000, 10 wt. % | 0.034 | 0.1 M KOH | 4.9/5.8 (2500 rpm) | - | 0.83/0.95 | RHE | [46] J. Am. Chem. Soc. 2014 |
| NC-A | E-TEK, 20 wt. % | 0.128 | 0.1 M KOH | 4.54/4.66 (1600) | –0.133/–0.128 | - | Ag/AgCl | [14] Angew. Chem. Int. Ed. 2014 |
| N, S-CN | Vulcan, 20 wt % | 0.2 | 0.1 M KOH | 4.4/4.6 (1600 rpm) | –0.2/–0.15 | –0.06/–0.03 | Ag/AgCl | [62] Nano Energy 2016 |
| Carbon-L | Johnson Matthey, 20 wt. % | 0.102 | 0.1 M KOH | 4.59/4.86 (1600 rpm) | 0.68/0.80 | 0.86/0.92 | RHE | [63] Energ. Environ. Sci. 2014 |
| MOF CN900 | 40 wt. % | 0.254 | 0.1 M KOH | 4.2/5.6 (1600 rpm) | - | 0.035/0.1 | Hg/HgO | [64] Chem. Commun. 2014 |
| $^{A}$N-C/CNT$^{N15.3}$ | Vulcan, 20 wt. % | 0.421 | 0.1 M KOH | 5.5/5.5 (1600 rpm) | 0.83/0.86 | 0.97/0.98 | RHE | [65] ACS Catalysis 2016 |
| NSC | Vulcan, 20 wt. % | 0.165 | 0.1 M KOH | 5.1/5.0 (1600 rpm) | 0.74/0.83 | 0.87/0.94 | RHE | This work |

[a] Current density comparisons between carbon materials and commercial Pt/C; [b] Half-wave potential comparisons between carbon materials and commercial Pt/C; [c] Onset potential comparisons between carbon materials and commercial Pt/C.

Similar to most referenced carbon materials (Table 5.4), the onset potential and activity of NSC are still not as good as the commercial Pt/C, yet its high electrocatalytic efficiency and better selectivity over methanol make it a promising candidate for the next generation of cost-effective ORR electrocatalysts.

*5.3.3 Supercapacitor and Transport Characterization*

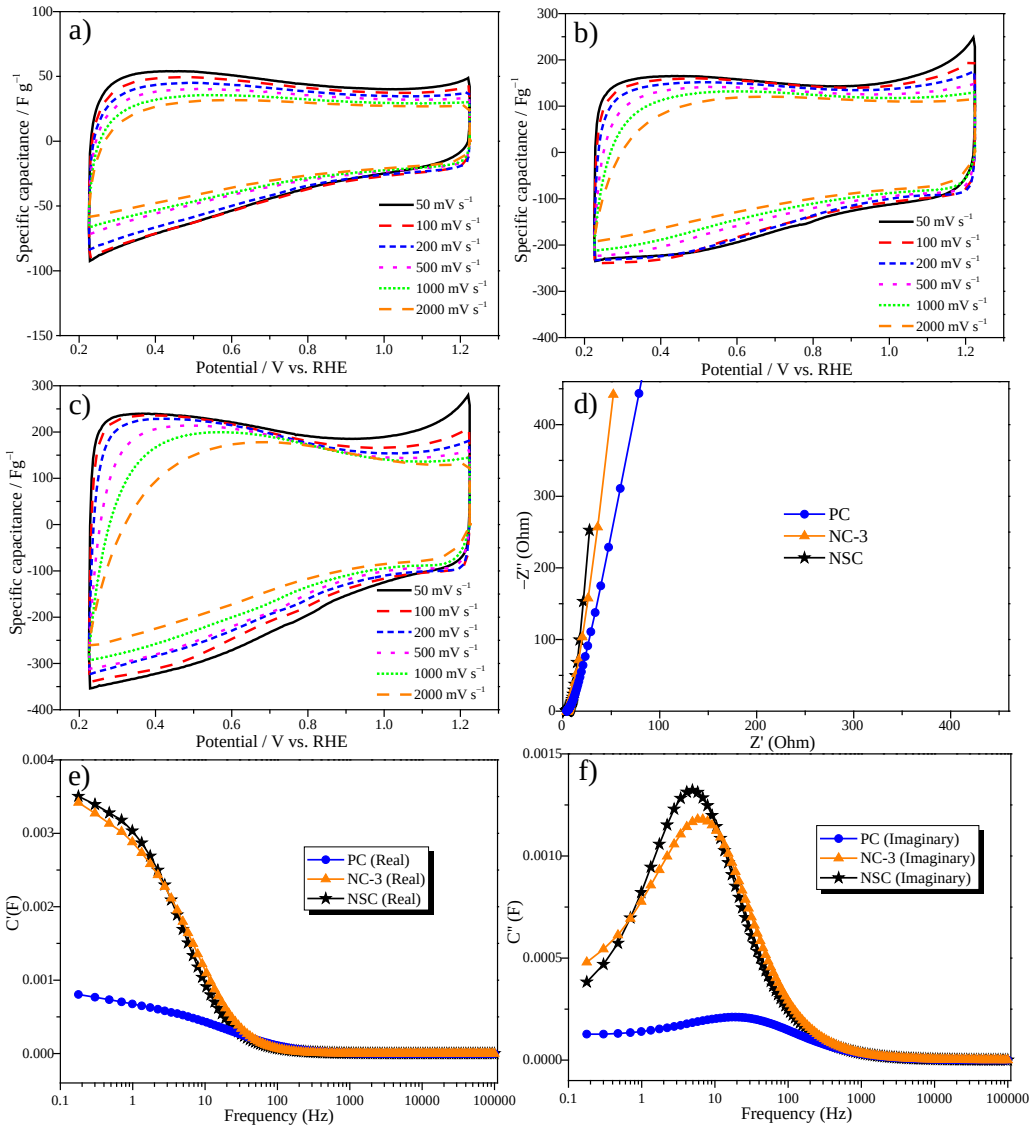


**Figure 5.10** CV curves in 1 M KOH with different scan rates of a) PC, b) NC-3 and c) NSC; d) Nyquist plots of EIS measurements; e) Real and f) Imaginary capacitance plots for the complex capacitance analysis.

To investigate the transport issues in ORR activity, supercapacitor measurements were conducted. According to CVs measured in 1 M KOH at different scan rates, PC, NC-3 and NSC showed similar quasi-rectangular shapes (Figure 5.10a-c). It is noteworthy that the specific capacitances of these samples showed minor deactivation even up to an extremely high rate of 2000 mV $s^{-1}$, which was comparable to or better than previous results with superior rate performance.[26, 66, 67] The rate performance is closely related to transport issues, which indicate the porous carbons synthesized in this work have excellent mass transport properties. Electrochemical impedance spectroscopy (EIS)

(Figure 5.10d) further confirmed this point, because the three samples featured small arcs in the high frequency region, reflecting the low charge transfer resistance and well-defined electrical conductivity contributed by the interconnected pore framework and high $sp^2$-C ratio.[14, 26] As the three samples possess outstanding mass transport properties, the better ORR activities of NC-3 and NSC than pristine PC highlight the importance of heteroatom functionality.

As an alternative approach to analyzing the supercapacitor frequency behavior, the real and imaginary parts of the capacitance were analyzed using the impedance data based on the following equations:[68]

$$Z(\omega) = \frac{1}{j\omega C(\omega)} \qquad (5.5)$$

$$Z(\omega) = Z'(\omega) + jZ''(\omega) \qquad (5.6)$$

$$C(\omega) = C'(\omega) - jC'''(\omega) \qquad (5.7)$$

$$C'(\omega) = \frac{-Z''(\omega)}{\omega|Z(\omega)|^2} \qquad (5.8)$$

$$C''(\omega) = \frac{Z''(\omega)}{\omega|Z(\omega)|^2} \qquad (5.9)$$

where $Z'(\omega)$ and $Z''(\omega)$ are the real and imaginary parts of the impedance, respectively; $C'(\omega)$ and $C''(\omega)$ represent the real and imaginary parts of the accessible capacitance, respectively. As shown in Figure 5.10e, $C'(\omega)$ sharply increases when the frequency decreases; then it is less dependent on frequencies. This is the feature of conversion from the electrode structure to electrode/electrolyte interface.[68] $C''(\omega)$ is related to the energy loss due to the irreversible process of the electrode, such as IR drop and Faradaic charge transfer. As shown in Figure 5.10f, $C''(\omega)$ goes through a maximum at peak frequency ($f_0$), defining a relaxation time constant ($\tau_0 = (2\pi f_0)^{-1}$), which reflects the kinetic performance of the supercapacitor.[69] Interestingly, PC, NC-3, and NSC show peaks at 22.0, 6.4 and 5.0 Hz, indicating the relaxation time of ~0.045, 0.16 and 0.20 s, respectively. In other words, PC is able to discharge its stored energy with high efficiency, 3.6 and 4.4 times faster than NC-3 and NSC. The electron and ion transport can be correlated to $O_2$ transport issues in ORR. Considering that NSC and NC-3 possess similar surface area, adjacent electrical conductivity properties deduced from their close relaxation time, whereas NSC has a lower N content, better ORR performance of NSC emphasizes the excellent synergistic effect of N, S co-doping than solely N-doping for ORR catalysis. Therefore,

compared to transport issues and BET surface areas, it is spectulated that surface functionality plays a more important role in our synthesized porous carbons, which needs to be enhanced to achieve the best ORR performance. In future research endeavours, more efforts will be made to further improve the overall properties, such as adopting KOH or $NH_3$ activation,[14, 15] or decoration with non-precious metallic compounds.[70, 71]

## 5.4 Conclusions

In summary, this study demonstrates a facile and scalable strategy to prepare heteroatom-doped, pillared-layered and/or honeycomb-like, porous carbons with high graphitic degrees, interconnected networks and high surface areas. The pore framework shapes, heteroatom functionalities, mesopore/micropore ratio and surface areas can be feasibly and rationally tailored. The as-prepared porous carbons show excellent $CO_2$ uptake capacities, high-rate performance and outstanding ORR activities as Pt-free catalysts in alkaline media. It is believed that this work is important for the design and large-scale production of porous carbons via a benign route, which implies promising applications in gas separation and energy storage/conversion.

## References

[1] N.L. Bindoff, P.A. Stott, K.M. AchutaRao, M.R. Allen, N. Gillett, D. Gutzler, K. Hansingo, G. Hegerl, Y. Hu, S. Jain, I.I. Mokhov, J. Overland, J. Perlwitz, R. Sebbari, X. Zhang, Detection and Attribution of Climate Change: From Global to Regional, in: T.F. Stocker, D. Qin, G.-K. Plattner, M. Tignor, S.K. Allen, J. Boschung, A. Nauels, Y. Xia, V. Bex, P.M. Midgley (Eds.) Climate Change 2013: The Physical Science Basis. Contribution of Working Group I to the Fifth Assessment Report of the Intergovernmental Panel on Climate Change, Cambridge University Press, Cambridge, United Kingdom and New York, NY, USA, 2013, pp. 867.

[2] M. Sevilla, P. Valle-Vigon, A.B. Fuertes, N-Doped Polypyrrole-Based Porous Carbons for $CO_2$ Capture, Advanced Functional Materials, 21 (2011) 2781.

[3] W. Xing, C. Liu, Z.Y. Zhou, L. Zhang, J. Zhou, S.P. Zhuo, Z.F. Yan, H. Gao, G.Q. Wang, S.Z. Qiao, Superior $CO_2$ Uptake of N-Doped Activated Carbon through Hydrogen-Bonding Interaction, Energy & Environmental Science, 5 (2012) 7323.

[4] G.T. Rochelle, Amine Scrubbing for $CO_2$ Capture, Science, 325 (2009) 1652.

[5] P. Markewitz, W. Kuckshinrichs, W. Leitner, J. Linssen, P. Zapp, R. Bongartz, A. Schreiber, T.E. Muller, Worldwide Innovations in the Development of Carbon Capture Technologies and the Utilization of $CO_2$, Energy & Environmental Science, 5 (2012) 7281.
[6] R. Vaidhyanathan, S.S. Iremonger, G.K.H. Shimizu, P.G. Boyd, S. Alavi, T.K. Woo, Direct Observation and Quantification of $CO_2$ Binding within an Amine-Functionalized Nanoporous Solid, Science, 330 (2010) 650.
[7] W. Morris, B. Leung, H. Furukawa, O.K. Yaghi, N. He, H. Hayashi, Y. Houndonougbo, M. Asta, B.B. Laird, O.M. Yaghi, A Combined Experimental-Computational Investigation of Carbon Dioxide Capture in a Series of Isoreticular Zeolitic Imidazolate Frameworks, Journal of the American Chemical Society, 132 (2010) 11006.
[8] M. Sevilla, A.B. Fuertes, Sustainable Porous Carbons with a Superior Performance for $CO_2$ Capture, Energy & Environmental Science, 4 (2011) 1765.
[9] H. Furukawa, O.M. Yaghi, Storage of Hydrogen, Methane, and Carbon Dioxide in Highly Porous Covalent Organic Frameworks for Clean Energy Applications, Journal of the American Chemical Society, 131 (2009) 8875.
[10] W. Xia, A. Mahmood, Z.B. Liang, R.Q. Zou, S.J. Guo, Earth-Abundant Nanomaterials for Oxygen Reduction, Angewandte Chemie-International Edition, 55 (2016) 2650.
[11] Y.Y. Liang, Y.G. Li, H.L. Wang, J.G. Zhou, J. Wang, T. Regier, H.J. Dai, $Co_3O_4$ Nanocrystals on Graphene as a Synergistic Catalyst for Oxygen Reduction Reaction, Nature Materials, 10 (2011) 780.
[12] G. Wu, K.L. More, C.M. Johnston, P. Zelenay, High-Performance Electrocatalysts for Oxygen Reduction Derived from Polyaniline, Iron, and Cobalt, Science, 332 (2011) 443.
[13] M.K. Debe, Electrocatalyst Approaches and Challenges for Automotive Fuel Cells, Nature, 486 (2012) 43.
[14] W.H. He, C.H. Jiang, J.B. Wang, L.H. Lu, High-Rate Oxygen Electroreduction over Graphitic-N Species Exposed on 3D Hierarchically Porous Nitrogen-Doped Carbons, Angewandte Chemie-International Edition, 53 (2014) 9503.
[15] H.-W. Liang, X. Zhuang, S. Brüller, X. Feng, K. Müllen, Hierarchically Porous Carbons with Optimized Nitrogen Doping as Highly Active Electrocatalysts for Oxygen Reduction, Nature Communications, 5 (2014) 4973.
[16] M. Kwiatkowski, A. Policicchio, M. Seredych, T.J. Bandosz, Evaluation of $CO_2$ Interactions with S-Doped Nanoporous Carbon and Its Composites with a Reduced GO:

Effect of Surface Features on an Apparent Physical Adsorption Mechanism, Carbon, 98 (2016) 250.
[17] J. Liang, Y. Jiao, M. Jaroniec, S.Z. Qiao, Sulfur and Nitrogen Dual-Doped Mesoporous Graphene Electrocatalyst for Oxygen Reduction with Synergistically Enhanced Performance, Angewandte Chemie-International Edition, 51 (2012) 11496.
[18] J.W.F. To, J.J. He, J.G. Mei, R. Haghpanah, Z. Chen, T. Kurosawa, S.C. Chen, W.G. Bae, L.J. Pan, J.B.H. Tok, J. Wilcox, Z.N. Bao, Hierarchical N-Doped Carbon as $CO_2$ Adsorbent with High $CO_2$ Selectivity from Rationally Designed Polypyrrole Precursor, Journal of the American Chemical Society, 138 (2016) 1001.
[19] E. Proietti, F. Jaouen, M. Lefevre, N. Larouche, J. Tian, J. Herranz, J.P. Dodelet, Iron-Based Cathode Catalyst with Enhanced Power Density in Polymer Electrolyte Membrane Fuel Cells, Nature Communications, 2 (2011) 416.
[20] Q. Shi, R.Y. Zhang, Y.Y. Lu, Y.H. Deng, A.A. Elzatahrya, D.Y. Zhao, Nitrogen-Doped Ordered Mesoporous Carbons Based on Cyanamide as the Dopant for Supercapacitor, Carbon, 84 (2015) 335.
[21] W. Luo, Y. Wang, S. Chou, Y. Xu, W. Li, B. Kong, S.X. Dou, H.K. Liu, J. Yang, Critical Thickness of Phenolic Resin-Based Carbon Interfacial Layer for Improving Long Cycling Stability of Silicon Nanoparticle Anodes, Nano Energy, 27 (2016) 255.
[22] W. Li, J. Liu, D. Zhao, Mesoporous Materials for Energy Conversion and Storage Devices, Nature Reviews Materials, (2016) 16023.
[23] W. Luo, Y.H. Li, J.P. Dong, J. Wei, J.Q. Xu, Y.H. Deng, D.Y. Zhao, A Resol-Assisted Co-Assembly Approach to Crystalline Mesoporous Niobia Spheres for Electrochemical Biosensing, Angewandte Chemie-International Edition, 52 (2013) 10505.
[24] J. Wei, D.D. Zhou, Z.K. Sun, Y.H. Deng, Y.Y. Xia, D.Y. Zhao, A Controllable Synthesis of Rich Nitrogen-Doped Ordered Mesoporous Carbon for $CO_2$ Capture and Supercapacitors, Advanced Functional Materials, 23 (2013) 2322.
[25] S.D. Berger, D.R. Mckenzie, P.J. Martin, Eels Analysis of Vacuum Arc-Deposited Diamond-Like Films, Philosophical Magazine Letters, 57 (1988) 285.
[26] D.Y. Chung, K.J. Lee, S.H. Yu, M. Kim, S.Y. Lee, O.H. Kim, H.J. Park, Y.E. Sung, Alveoli-Inspired Facile Transport Structure of N-Doped Porous Carbon for Electrochemical Energy Applications, Advanced Energy Materials, 5 (2015).
[27] Y.M. Lin, X.L. Pan, W. Qi, B.S. Zhang, D.S. Su, Nitrogen-Doped Onion-Like Carbon: A Novel and Efficient Metal-Free Catalyst for Epoxidation Reaction, Journal of Materials Chemistry A, 2 (2014) 12475.

[28] Y.J. Cho, H.S. Kim, S.Y. Baik, Y. Myung, C.S. Jung, C.H. Kim, J. Park, H.S. Kang, Selective Nitrogen-Doping Structure of Nanosize Graphitic Layers, Journal of Physical Chemistry C, 115 (2011) 3737.
[29] Y.W. Zhu, S. Murali, M.D. Stoller, K.J. Ganesh, W.W. Cai, P.J. Ferreira, A. Pirkle, R.M. Wallace, K.A. Cychosz, M. Thommes, D. Su, E.A. Stach, R.S. Ruoff, Carbon-Based Supercapacitors Produced by Activation of Graphene, Science, 332 (2011) 1537.
[30] W.T. Gu, M. Sevilla, A. Magasinski, A.B. Fuertes, G. Yushin, Sulfur-Containing Activated Carbons with Greatly Reduced Content of Bottle Neck Pores for Double-Layer Capacitors: A Case Study for Pseudocapacitance Detection, Energy & Environmental Science, 6 (2013) 2465.
[31] L.T. Qu, Y. Liu, J.B. Baek, L.M. Dai, Nitrogen-Doped Graphene as Efficient Metal-Free Electrocatalyst for Oxygen Reduction in Fuel Cells, ACS Nano, 4 (2010) 1321.
[32] Y. Wang, Y.Y. Shao, D.W. Matson, J.H. Li, Y.H. Lin, Nitrogen-Doped Graphene and Its Application in Electrochemical Biosensing, ACS Nano, 4 (2010) 1790.
[33] C. Han, X.J. Bo, Y.F. Zhang, M.A. Li, L.P. Guo, One-Pot Synthesis of Nitrogen and Sulfur Co-Doped Onion-Like Mesoporous Carbon Vesicle as an Efficient Metal-Free Catalyst for Oxygen Reduction Reaction in Alkaline Solution, Journal of Power Sources, 272 (2014) 267.
[34] J.R. Pels, F. Kapteijn, J.A. Moulijn, Q. Zhu, K.M. Thomas, Evolution of Nitrogen Functionalities in Carbonaceous Materials During Pyrolysis, Carbon, 33 (1995) 1641.
[35] R.Z. Bai, M.L. Yang, G.S. Hu, L.Q. Xu, X. Hu, Z.M. Li, S.L. Wang, W. Dai, M.H. Fan, A New Nanoporous Nitrogen-Doped Highly-Efficient Carbonaceous $CO_2$ Sorbent Synthesized with Inexpensive Urea and Petroleum Coke, Carbon, 81 (2015) 465.
[36] L.F. Lai, J.R. Potts, D. Zhan, L. Wang, C.K. Poh, C.H. Tang, H. Gong, Z.X. Shen, L.Y. Jianyi, R.S. Ruoff, Exploration of the Active Center Structure of Nitrogen-Doped Graphene-Based Catalysts for Oxygen Reduction Reaction, Energy & Environmental Science, 5 (2012) 7936.
[37] D. Guo, R. Shibuya, C. Akiba, S. Saji, T. Kondo, J. Nakamura, Active Sites of Nitrogen-Doped Carbon Materials for Oxygen Reduction Reaction Clarified Using Model Catalysts, Science, 351 (2016) 361.
[38] J.F. Moulder, J. Chastain, R.C. King, Handbook of X-Ray Photoelectron Spectroscopy: A Reference Book of Standard Spectra for Identification and Interpretation of XPS Data, Perkin-Elmer Eden Prairie, MN1992.

[39] H. Seema, K.C. Kemp, N.H. Le, S.W. Park, V. Chandra, J.W. Lee, K.S. Kim, Highly Selective $CO_2$ Capture by S-Doped Microporous Carbon Materials, Carbon, 66 (2014) 320.

[40] S.B. Yang, L.J. Zhi, K. Tang, X.L. Feng, J. Maier, K. Mullen, Efficient Synthesis of Heteroatom (N or S)-Doped Graphene Based on Ultrathin Graphene Oxide-Porous Silica Sheets for Oxygen Reduction Reactions, Advanced Functional Materials, 22 (2012) 3634.

[41] C.K. Lam, T.C. Mak, A New Layer Type Anionic Host Lattice Constructed from Urea, Squarate, Bicarbonate, and Water Molecules, Journal of Structural Chemistry, 40 (1999) 714.

[42] N.E. Webb, G.J. Sperandio, A.N. Martin, A Study of the Decomposition of Glucose Solutions, Journal of the American Pharmaceutical Association, 47 (1958) 101.

[43] Q. Li, T.C.W. Mak, Inclusion-Compounds of Thiourea and Peralkylated Ammonium-Salts .2. Hydrogen-Bonded Host Lattices Built of Thiourea and Cyclic Dimeric Bicarbonate Moieties, Journal of Inclusion Phenomena and Molecular Recognition in Chemistry, 20 (1994) 73.

[44] G. Sethia, A. Sayari, Comprehensive Study of Ultra-Microporous Nitrogen-Doped Activated Carbon for CO2 Capture, Carbon, 93 (2015) 68.

[45] Q.G. Zhai, N. Bai, S.N. Li, X.H. Bu, P.Y. Feng, Design of Pore Size and Functionality in Pillar-Layered Zn-Triazolate-Dicarboxylate Frameworks and Their High $CO_2/CH_4$ and $C_2$ Hydrocarbons/$CH_4$ Selectivity, Inorganic Chemistry, 54 (2015) 9862.

[46] S.E. Bae, K.J. Kim, I.H. Choi, S. Huh, Preparation of N-Doped Microporous Carbon Nanospheres by Direct Carbonization of as-Prepared Mesoporous Silica Nanospheres Containing Cetylpyridinium Bromide Template, Carbon, 99 (2016) 8.

[47] K. Huang, S.H. Chai, R.T. Mayes, G.M. Veith, K.L. Browning, M.A. Sakwa-Novak, M.E. Potter, C.W. Jones, Y.T. Wu, S. Dai, An Efficient Low-Temperature Route to Nitrogen-Doping and Activation of Mesoporous Carbons for $CO_2$ Capture, Chemical Communications, 51 (2015) 17261.

[48] F.J. Martin-Jimeno, F. Suarez-Garcia, J.I. Paredes, A. Martinez-Alonso, J.M.D. Tascon, Activated Carbon Xerogels with a Cellular Morphology Derived from Hydrothermally Carbonized Glucose-Graphene Oxide Hybrids and Their Performance Towards $CO_2$ and Dye Adsorption, Carbon, 81 (2015) 137.

[49] A. Aijaz, N. Fujiwara, Q. Xu, From Metal-Organic Framework to Nitrogen-Decorated Nanoporous Carbons: High CO2 Uptake and Efficient Catalytic Oxygen Reduction, Journal of the American Chemical Society, 136 (2014) 6790.

[50] S. Gadipelli, Z.X. Guo, Tuning of ZIF-Derived Carbon with High Activity, Nitrogen Functionality, and Yield - a Case for Superior $CO_2$ Capture, Chemsuschem, 8 (2015) 2123.
[51] G.P. Hao, W.C. Li, D. Qian, A.H. Lu, Rapid Synthesis of Nitrogen-Doped Porous Carbon Monolith for CO2 Capture, Advanced Materials, 22 (2010) 853.
[52] G.P. Hao, W.C. Li, D. Qian, G.H. Wang, W.P. Zhang, T. Zhang, A.Q. Wang, F. Schuth, H.J. Bongard, A.H. Lu, Structurally Designed Synthesis of Mechanically Stable Poly(Benzoxazine-Co-Resol)-Based Porous Carbon Monoliths and Their Application as High-Performance $CO_2$ Capture Sorbents, Journal of the American Chemical Society, 133 (2011) 11378.
[53] S. Gadipelli, W. Travis, W. Zhou, Z.X. Guo, A Thermally Derived and Optimized Structure from ZIF-8 with Giant Enhancement in $CO_2$ Uptake, Energy & Environmental Science, 7 (2014) 2232.
[54] P. Shen, W.W. He, D.Y. Du, H.L. Jiang, S.L. Li, Z.L. Lang, Z.M. Su, Q. Fu, Y.Q. Lan, Solid-State Structural Transformation Doubly Triggered by Reaction Temperature and Time in 3D Metal-Organic Frameworks: Great Enhancement of Stability and Gas Adsorption, Chemical Science, 5 (2014) 1368.
[55] S.J. Bao, R. Krishna, Y.B. He, J.S. Qin, Z.M. Su, S.L. Li, W. Xie, D.Y. Du, W.W. He, S.R. Zhang, Y.Q. Lan, A Stable Metal-Organic Framework with Suitable Pore Sizes and Rich Uncoordinated Nitrogen Atoms on the Internal Surface of Micropores for Highly Efficient $CO_2$ Capture, Journal of Materials Chemistry A, 3 (2015) 7361.
[56] S. Gadipelli, Z.X. Guo, Postsynthesis Annealing of MOF-5 Remarkably Enhances the Framework Structural Stability and $CO_2$ Uptake, Chemistry of Materials, 26 (2014) 6333.
[57] T. Li, J.E. Sullivan, N.L. Rosi, Design and Preparation of a Core-Shell Metal-Organic Framework for Selective $CO_2$ Capture, Journal of the American Chemical Society, 135 (2013) 9984.
[58] C.R. Murdock, D.M. Jenkins, Isostructural Synthesis of Porous Metal-Organic Nanotubes, Journal of the American Chemical Society, 136 (2014) 10983.
[59] S. Pal, A. Bhunia, P.P. Jana, S. Dey, J. Mollmer, C. Janiak, H.P. Nayek, Microporous La-Metal-Organic Framework (MOF) with Large Surface Area, Chemistry-a European Journal, 21 (2015) 2789.
[60] W. Yang, T.P. Fellinger, M. Antonietti, Efficient Metal-Free Oxygen Reduction in Alkaline Medium on High-Surface-Area Mesoporous Nitrogen-Doped Carbons Made

from Ionic Liquids and Nucleobases, Journal of the American Chemical Society, 133 (2011) 206.

[61] W.X. Yang, X.J. Liu, X.Y. Yue, J.B. Jia, S.J. Guo, Bamboo-Like Carbon Nanotube/$Fe_3C$ Nanoparticle Hybrids and Their Highly Efficient Catalysis for Oxygen Reduction, Journal of the American Chemical Society, 137 (2015) 1436.

[62] K.G. Qu, Y. Zheng, S. Dai, S.Z. Qiao, Graphene Oxide-Polydopamine Derived N, S-Codoped Carbon Nanosheets as Superior Bifunctional Electrocatalysts for Oxygen Reduction and Evolution, Nano Energy, 19 (2016) 373.

[63] P. Zhang, F. Sun, Z.H. Xiang, Z.G. Shen, J. Yun, D.P. Cao, ZIF-Derived in Situ Nitrogen-Doped Porous Carbons as Efficient Metal-Free Electrocatalysts for Oxygen Reduction Reaction, Energy & Environmental Science, 7 (2014) 442.

[64] S. Pandiaraj, H.B. Aiyappa, R. Banerjee, S. Kurungot, Post Modification of MOF Derived Carbon Via G-$C_3N_4$ Entrapment for an Efficient Metal-Free Oxygen Reduction Reaction, Chemical Communications, 50 (2014) 3363.

[65] H. Ba, Y. Liu, L. Truong-Phuoc, C. Duong-Viet, J.-M. Nhut, D.L. Nguyen, O. Ersen, G. Tuci, G. Giambastiani, C. Pham-Huu, N-Doped Food-Grade-Derived 3D Mesoporous Foams as Metal-Free Systems for Catalysis, ACS Catalysis, 6 (2016) 1408.

[66] L. Qie, W.M. Chen, H.H. Xu, X.Q. Xiong, Y. Jiang, F. Zou, X.L. Hu, Y. Xin, Z.L. Zhang, Y.H. Huang, Synthesis of Functionalized 3D Hierarchical Porous Carbon for High-Performance Supercapacitors, Energy & Environmental Science, 6 (2013) 2497.

[67] Y.L. Cheng, L. Huang, X. Xiao, B. Yao, L.Y. Yuan, T.Q. Li, Z.M. Hu, B. Wang, J. Wan, J. Zhou, Flexible and Cross-Linked N-Doped Carbon Nanofiber Network for High Performance Freestanding Supercapacitor Electrode, Nano Energy, 15 (2015) 66.

[68] P.L. Taberna, P. Simon, J.F. Fauvarque, Electrochemical Characteristics and Impedance Spectroscopy Studies of Carbon-Carbon Supercapacitors, Journal of the Electrochemical Society, 150 (2003) A292.

[69] J. Lim, U.N. Maiti, N.Y. Kim, R. Narayan, W.J. Lee, D.S. Choi, Y. Oh, J.M. Lee, G.Y. Lee, S.H. Kang, H. Kim, Y.H. Kim, S.O. Kim, Dopant-Specific Unzipping of Carbon Nanotubes for Intact Crystalline Graphene Nanostructures, Nature Communications, 7 (2016).

[70] J. Masa, W. Xia, M. Muhler, W. Schuhmann, On the Role of Metals in Nitrogen-Doped Carbon Electrocatalysts for Oxygen Reduction, Angewandte Chemie-International Edition, 54 (2015) 10102.

[71] J.X. Zhao, Z.F. Chen, Carbon-Doped Boron Nitride Nanosheet: An Efficient Metal-Free Electrocatalyst for the Oxygen Reduction Reaction, Journal of Physical Chemistry C, 119 (2015) 26348.

# Chapter 6. One-Step Synthesis of Flour-Derived Functional Nanocarbons with Hierarchical Pores for Versatile Environmental Applications


## Abstract

*Chapter 3-5 have described glucose-derived porous carbons. In this chapter, wheat flour is adopted as the carbon source which is more cost-effective for scalable production of functional carbons with tuneable hierarchical porous structure and tailored surface chemistry for environmental applications in $CO_2$ adsorption and carbocatalysis to remove emerging water contaminants. By pyrolyzing a mixture of wheat flour and $NaHCO_3$/$Na_2CO_3$/$K_2CO_3$ at 700 °C, honeycomb structured carbons (700-PC) with dominant micropores can be formed and exhibit an excellent $CO_2$ storage capacity of 6.8 mmol $g^{-1}$ at 0 °C and ambient pressure. By including dicyandiamide in the precursors, coralloid carbon skeletons in micro- and meso-porous texture are selectively formed in the N-doped hierarchical porous carbons (N-PCs). 800-N-PC (N-PCs prepared at 800 °C) with a high surface area of 3041 $m^2$ $g^{-1}$ shows an enhanced capacity of 19.4 mmol $g^{-1}$ at 0 °C, 10 bar. For water remediation, 800-N-PC exhibits the most efficient degradation of p-hydroxybenzoic acid (HBA) by AOPs with a high reaction rate constant of 0.39 $min^{-1}$ at 25 °C. In addition, 800-N-PC shows selective adsorption of HBA in a mixed solution of HBA and phenol, while both of them can be effectively degraded by the AOPs. The mechanism of adsorption and catalysis of the newly developed porous carbon is discussed.*


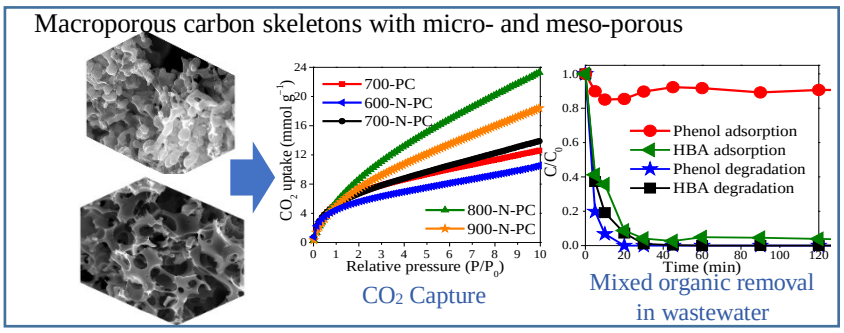

## 6.1 Introduction

The growing atmospheric concentration of carbon dioxide ($CO_2$) that is mostly emitted from fossil fuel combustion has raised intensive concerns on its grave consequences such as ocean acidification and climate change. Due to the delay in the systematic use of clean energy sources such as wind power, solar energy and hydrogen, fossil fuels are still the main source of energy and $CO_2$ concentration is forecasted to continue to grow in the foreseeable future.[1] Efficient $CO_2$ uptake sorbents for both pre- and post-combustion have received continuous attention over the past few decades.[2-4] Compared to conventional $CO_2$ capture media like amine solution scrubbing,[5] which suffers from drawbacks in the volatility, toxicity, instability and high regeneration energy, porous sorbents are more promising alternatives.[5] Accordingly, quite a number of porous materials such as porous organic polymers, zeolites, porous carbons, and metal-organic frameworks (MOFs) have been tailor-made and investigated extensively.[3, 6-8] Especially, light-weight porous carbons are suggested as more advantageous candidates, given their low costs, remarkable stability, structural flexibility, sustainability and excellent recycling performance.[3, 9]

Apart from $CO_2$ capture, the unique attributes of porous carbons also make them applicable in the adsorptive and catalytic removal of water pollutants.[10, 11] It is known that fresh water contaminated by persistent organic pollutants (POPs) is a serious issue brought by human activities.[12, 13] Emerging toxic water contaminants such as 4-hydroxybenzoic acid (HBA) and phenolics have posed serious threats to the well-being of human health and aquatic life.[14-16] Porous carbons with high specific surface areas (SSAs) can act as effective adsorbents for feasible adsorptive removal of these pollutants.[11, 17, 18] More importantly, they can function as efficient metal-free catalysts to activate peroxymonosulfate ($HSO_5^-$, PMS) in advanced oxidation processes (AOPs) for complete decomposition of these organics.[19-21]

Similar to persulfate (PS), PMS as an oxidant can be activated by carbon-based (C) materials to generate sulfate and hydroxyl radicals (Equation 6.1-6.3),[22] which has broad application in removal of various pollutants in aqueous solution.

$$HSO_5^- + C \rightarrow OH^- + SO_4^{\bullet -} + C^+ \qquad (6.1)$$

$$HSO_5^- + C \rightarrow \bullet OH + SO_4^{2-} + C^+ \qquad (6.2)$$

$$HSO_5^- + C^+ \rightarrow H^+ + SO_5^{\bullet -} + C \qquad (6.3)$$

With the aim to improve the performances of $CO_2$ capture and water treatment, enhancing SSAs and porous properties seems to be the most effective and straight-forward approach.[23] In addition, incorporation of heteroatoms, for instance, nitrogen, into nanocarbons has been demonstrated to be a super effective approach in improving their efficiency in both $CO_2$ capture and AOPs.[11, 18, 24] To prepare porous carbons, some investigators adopted toxic and expensive chemicals such as resorcinol, p-nitrophenol, 4-hexylresorcinol, and polypyrrole as precursors.[6, 17, 25, 26] Compared with them, biomass materials are more desirable as carbon sources as they are readily available, renewable and cheap. To the best of our knowledge, it is still challenging to design high-surface-area porous carbons using biomass by a feasible and green protocol.[27]

Many reported methods for synthesis of high-surface-area porous carbons use sacrificial templates such as zeolites[17] and MOFs,[3] and utilize hydrothermal carbonization process.[28-30] However, the complex synthesis, high material costs and time consumption add difficulties for large-scale production and control. In this regard, chemical activation by direct pyrolysis is more feasible to handle. Common chemical activating agents include KOH, $ZnCl_2$, $Na_2CO_3$, $K_2CO_3$, $NaHCO_3$, NaOH, $H_3PO_4$, and $H_2SO_4$.[11, 31-33] KOH is most frequently used in previous literature and the porous carbons with high $CO_2$ capture capacities were almost all involved with KOH activation.[28, 30, 34-36] However, the corrosive behavior of KOH and pollution problems during residue removal impede the implementation in industrial application.[33] Among all the candidates, frequently-used food additives like $K_2CO_3$, $Na_2CO_3$ and $NaHCO_3$ are good choices as environmentally benign activators and can mitigate the corrosion of KOH to the equipment at high temperatures.

In this chapter, employing wheat flour as a biomass carbon source, dicyandiamide (DICY) as the nitrogen source, and $NaHCO_3$/$Na_2CO_3$/$K_2CO_3$ as the activation agents, the authors successfully acquire porous nanocarbons with super high SSAs by a one-pot mild pyrolysis process. These carbons demonstrate to be excellent adsorbents for $CO_2$ capture and water contaminant adsorption, as well as catalysts for organic removals in wastewater. The facile preparation approach endows these functionalized porous nanocarbons with scalable production and versatile opportunities in environmental application.

## 6.2 Experimental Section

### *6.2.1 Chemical Reagents*

Wheat flour obtained from a supermarket contains mainly starch (with both amylose and amylopectin). About 11 wt.% proteins are also included and other ingredients with low contents have little effect on the preparation process. Sodium bicarbonate (≥ 99.7%), dicyandiamide (DICY, 99%), potassium hydroxide (≥ 85.0%), peroxymonosulfate (≥ 99.0%), methanol (≥ 99.9%), *p*-hydroxybenzoic acid (HBA, ≥ 97.0%), phenol (≥ 99.0%) and 5, 5-dimethyl-1-pyrroline N-oxide (≥ 97.0%, DMPO) were received from Sigma-Aldrich.

### *6.2.2 Carbon Sample Synthesis*

For the synthesis of N-PCs, 2 g of wheat flour was added into 40 mL deionized water under magnetic stirring. Then, 2 g sodium bicarbonate and 1.2 g potassium hydroxide were dissolved in 50 mL water to generate a solution containing 0.5 g $NaHCO_3$, 0.9 g $Na_2CO_3$ and 1.2 g $K_2CO_3$, which was then mixed with a 30 mL water solution containing 2.0 g dicyandiamide (DICY). The mixture was then added to the above flour solution. After magnetic stirring and drying at 90 $^oC$, the mixture was put in a tube furnace and pyrolyzed under an $N_2$ flow at 600, 700, 800 and 900 $^oC$ for 2 h. The heating ramp rate was 5 °C/min. The carbonized materials were pestled to powders and washed with water and ethanol. Finally, the powders were dried in an oven. The as-obtained samples were denoted as 600-N-PC, 700-N-PC, 800-N-PC and 900-N-PC, respectively. For comparison, 700-PC was fabricated with the similar procedure by carbonization of the precursors without DICY at 700 $^oC$. Blank carbon was obtained as the reference material by carbonization of wheat flour powder only.

It is noted that $NaHCO_3$ and KOH were used to generate a mixture solution of $NaHCO_3/Na_2CO_3/K_2CO_3$ due to their comparatively lower cost as compared to using three chemicals, $NaHCO_3$, $Na_2CO_3$, and $K_2CO_3$ (prices from Sigma-Aldrich). In the solution, KOH was instantly consumed and would produce little corrosion to the equipment during high-temperature pyrolysis.

### *6.2.3. Sample Characterizations*

Details of SEM, TEM, XPS, EPR, $N_2$ sorption measurements can refer to chapter 3.

### *6.2.4 $CO_2$ Adsorption*

$CO_2$ adsorption (at 0 and 25 °C) at pressures from 0 to 1 bar was conducted on a Micromeritics Tristar 3000 since it is good at analyzing $CO_2$ capture in this pressure range. The $CO_2$ capture isotherms under high pressures ranging from 0 to 10 bar were investigated at 0 and 25 °C using a Micromeritics ASAP 2050. All the samples were degassed at 130 °C under high vacuum for 6 h prior to each sorption experiment.

### *6.2.5 Aqueous Adsorption and AOP Procedures*

HBA and phenol solutions (20 mg $L^{-1}$) were prepared by directly dissolving the chemicals in deionized water. Adsorption experiments on HBA were performed by dispersing 15 mg adsorbent in 150 mL 20 mg $L^{-1}$ HBA solutions at 25 $^{o}$C under constant stirring (adsorbent concentration: 0.1 g $L^{-1}$). At certain time intervals, 1 mL of the solution was withdrawn and filtered. The concentrations of HBA were determined by an ultra-high performance liquid chromatography (UHPLC).

Typical HBA oxidation experiments were conducted at 25 $^{o}$C unless otherwise illustrated. Peroxymonosulfate ($HSO_5^-$, PMS, 6.5 mM) and the carbon sample (0.1 g $L^{-1}$) were added simultaneously in HBA solution (20 mg $L^{-1}$) to start the catalytic process. At a certain time, 1.0 mL mixed solution was withdrawn, filtered and mixed instantly with 0.5 mL methanol to stop the reaction.

Selective adsorptive and catalytic oxidation tests by 800-N-PC were carried out in a mixed solution of 100 mL 20 mg $L^{-1}$ HBA and 100 mL 20 mg $L^{-1}$ phenol solution. As a result, the concentrations of HBA and phenol in the mixed solution were both 10 mg $L^{-1}$. The loading concentration of 800-N-PC was 0.066 g $L^{-1}$. Still, PMS concentration was 6.5 mM in AOP.

## 6.3 Results and Discussion

*6.3.1 Material Characterizations*

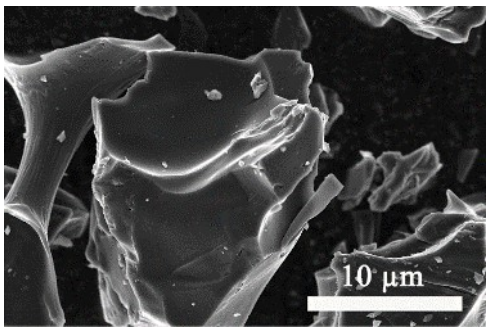


**Figure 6.1** SEM image of flour-carbonized blank carbon.

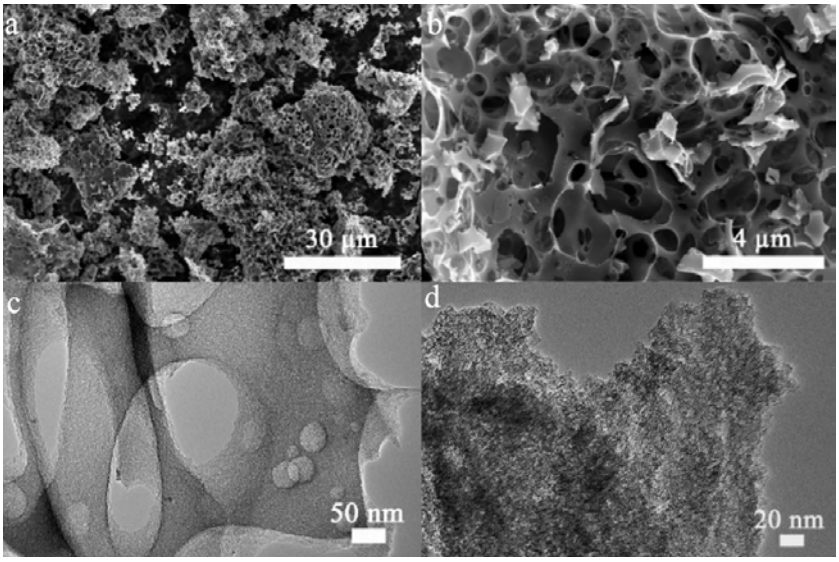


**Figure 6.2** a, b) SEM and c,d) TEM images of 700-PC.

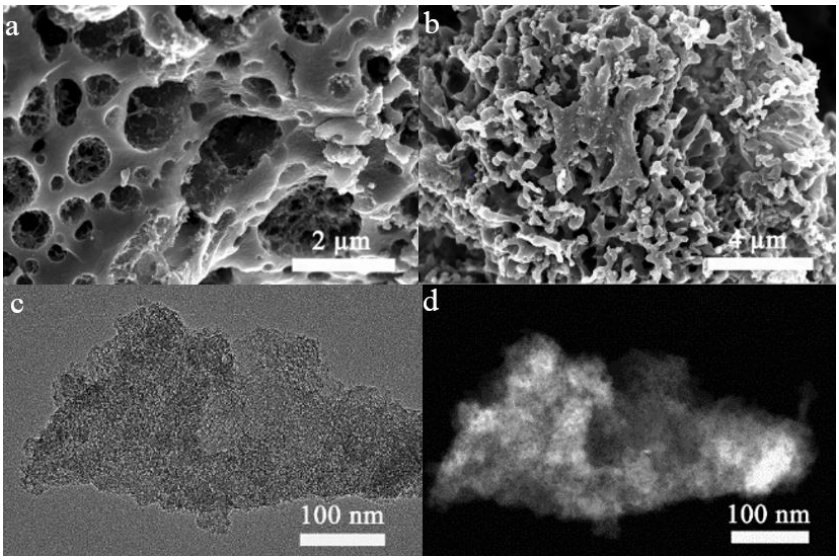


**Figure 6.3** a, b) SEM, c) TEM and d) HAADF-STEM images of 600-N-PC.

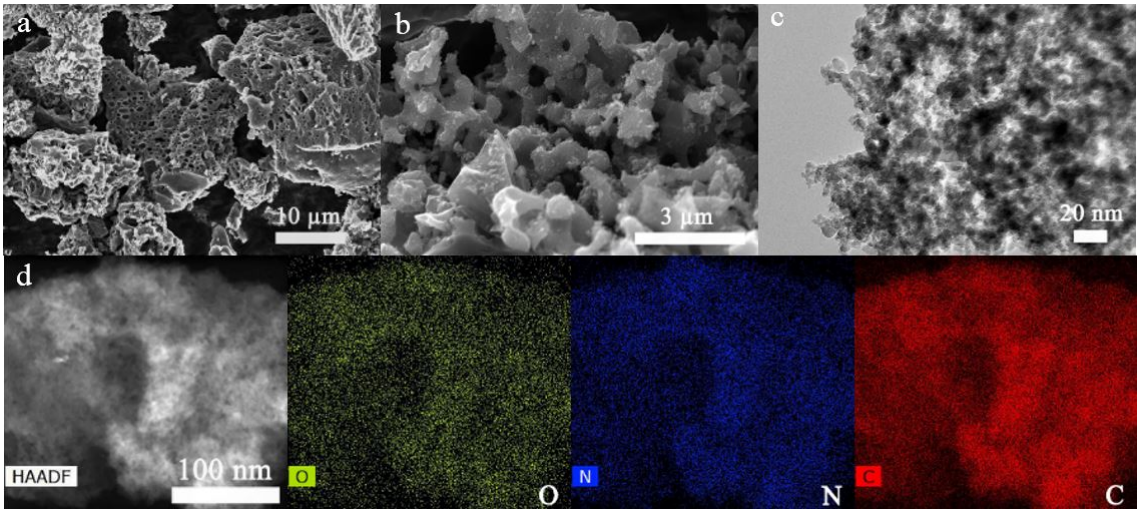


**Figure 6.4** a, b) SEM c) TEM and d) HAADF-STEM and corresponding EDX elemental mapping images of 700-N-PC.

SEM image of blank carbon obtained by the carbonization of flour only indicates a nonporous solid structure (Figure 6.1). SEM and TEM images reveal that 700-PC exhibits a honeycomb-like porous structure (Figure 6.2). Although visible surface pores are macropores or mesopores, magnified TEM image suggests the microporous texture of the carbon skeletons (Figure 6.2d). Interestingly, N-PCs exhibit porous structure with both honeycomb- and coralloid-like shapes after DICY involvement in the synthesis (Figures 6.3-6.6). Similar to 700-PC, the magnified SEM (Figures 6.5c and 6.6d), TEM (Figures 6.3c, 6.4c, 6.5f and 6.6e) and HAADF-STEM images (Figures 6.3d, 6.4d and 6.6f) of N-PCs indicate the mesoporous or microporous texture in the macroporous structures.

Representative EDX elemental mapping analysis of 700-N-PC (Figure 6.4d) and 800-N-PC (Figure 6.5g) show the uniform distributions of C, N, and O elements within the carbon frameworks.

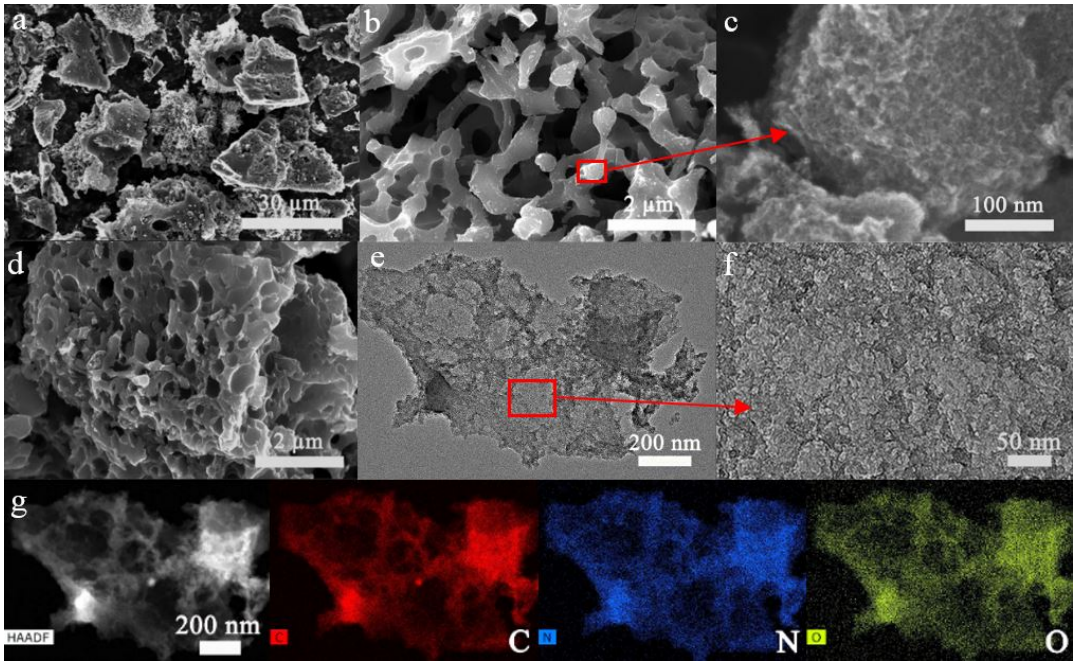


**Figure 6.5** a-d) SEM images; e,f) TEM images; g) HAADF-STEM image with EDX elemental mapping images of 800-N-PC.

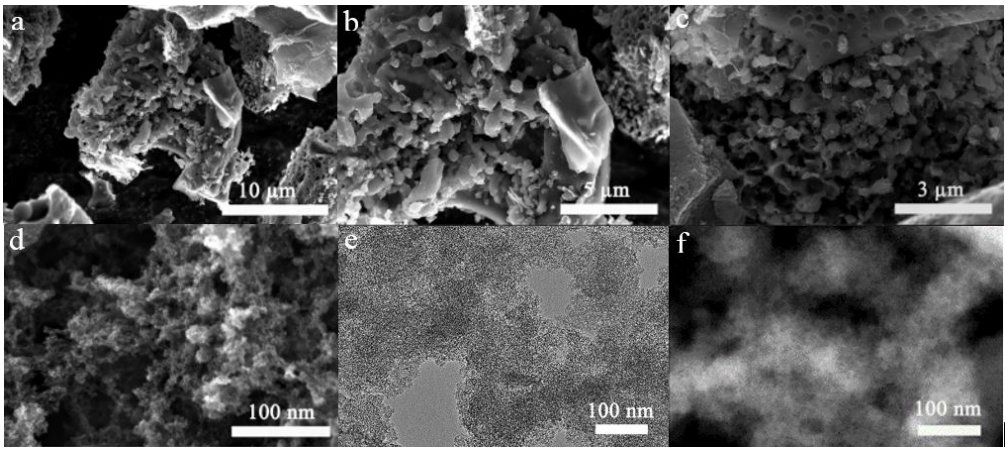


**Figure 6.6** a-d) SEM, e) TEM and f) HAADF-STEM images of 900-N-PC.

The production of carbons with high porosities in this system can be analyzed from the collaborative effect of physical and chemical activations. The physical activation takes place through the release of gas during the pyrolysis of all the precursors and Na or K intercalation to expand carbon lattices and create high microporosity.[32, 37] The

chemical activation occurs through the redox reaction between $K_2CO_3$ or $Na_2CO_3$ with carbon, which starts to proceed at above 600 °C, as shown in Equation 6.4.[31, 32]

$$M_2CO_3 + 2C \rightarrow 2M + 3CO \qquad (6.4)$$

Here *M* is either Na or K.

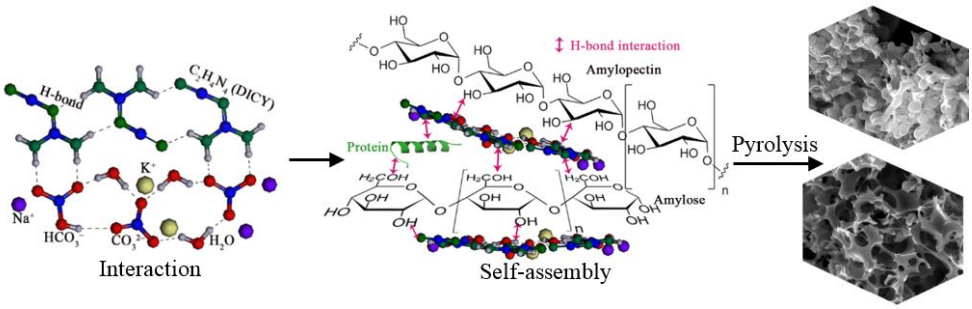


**Scheme 6.1** Illustrative formation for preparation of porous carbons.

Scheme 6.1 shows the possible H-bond and electrostatic interactions among $Na^+$, $HCO_3^-$, $CO_3^{2-}$, $K^+$ and DICY in water solution. The evaporation of the mixture induces self-assembly, where $Na^+$, $HCO_3^-$, $CO_3^{2-}$, $K^+$ and DICY are closely linked with protein, amylose and amylopectin in wheat flour. The closely interconnected precursors promote efficient chemical and physical activations that occur simultaneously with the carbonation, producing abundant porosities. Finally, any inorganic salts and residues were readily removed by simple water washing, which further released some porosity in the resultant carbon samples.

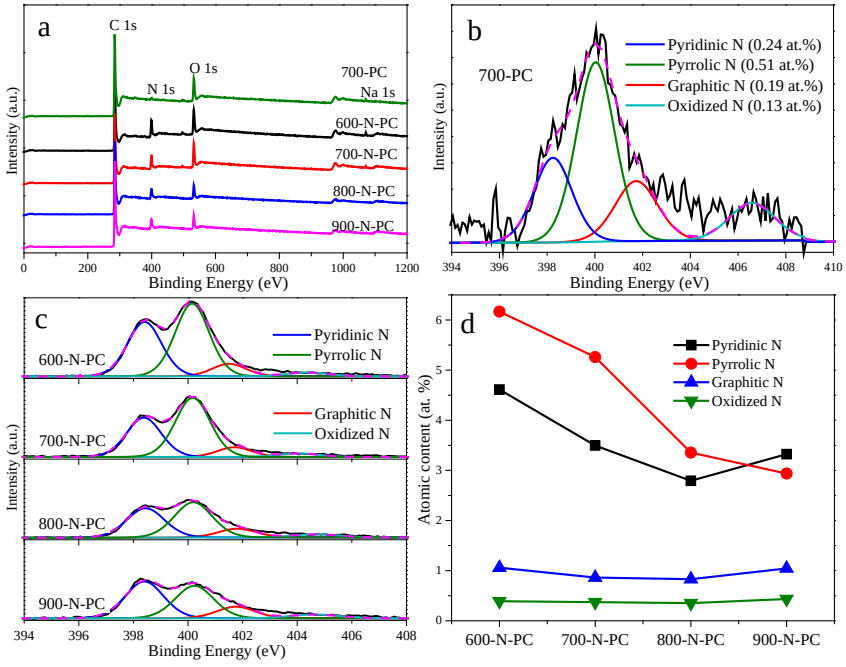

**Figure 6.7** a) XPS survey of the samples; b, c) high resolution N 1s and d) the atomic content evolution of different N species in N-PCs.

XPS was performed to analyze the surface chemical states, as summarized in Figure 6.7 and Table 6.1. 700-PC has 1.1 at.% of N, arising from the pyrolysis of proteins in wheat flour. The content of nitrogen declines from 12.23 at.% in 600-N-PC, 10.00 at.% in 700-N-PC to around 7.33 at.% and 7.74 at.% in 800-N-PC and 900-N-PC, respectively. Oxygen content descends steadily with elevated synthesis temperatures (12.20 - 5.61 at.%). These results suggest the partial decomposition of O- or N-containing functional groups at higher temperatures. A trace amount of Na was detected in several samples, which were not fully removed during washing. Figure 6.7b and c display the deconvoluted peaks of N 1s spectra. There are predominantly four types of N-containing groups in the form of pyridinic-, pyrrolic-, graphitic- and oxidized-N groups, centering at about 398, 400, 401 and 405 (or 407) eV, respectively.[11, 38, 39] It is further noted from Figure 6.7d that pyridinic-N and pyrrolic-N constitute the main N functional groups in the four samples, which decrease gradually with the increasing temperature, while the minority graphitic- and oxidized-N groups do not change much.

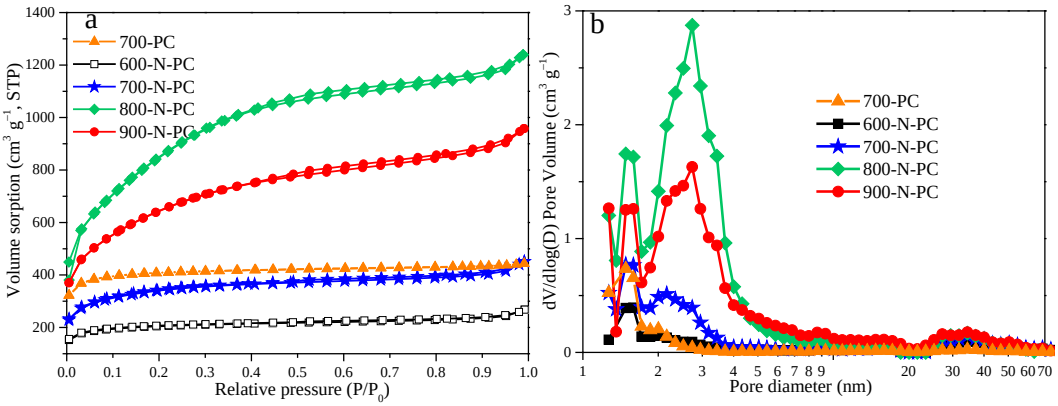


**Figure 6.8** a) $N_2$ adsorption-desorption isotherms achieved at −196 °C, and b) pore size distributions obtained from the DFT method.

The porous structural properties of the resulting samples were characterized by $N_2$ sorption isotherms, and are listed in Figure 6.8 and Table 6.1. 700-PC displays a type-I isotherm, typical for microporous materials (Figure 6.8a). The pore size distribution obtained by the DFT method (Figure 6.8b) further verifies that 700-PC possesses a structure with dominant micropores. The 700-PC has the highest micropore volume ($V_{mic}$,

0.58 $cm^3$ $g^{-1}$) of all the samples. By comparison, N-PCs show type-IV isotherms, and there are hysteresis loops at medium-to-high relative pressure region. N-PCs have hierarchically porous structures with abundant mesopores and micropores as well as a trace amount of macropores. Comparing 700-PC with 700-N-PC, increased mesopore volume ($V_{meso}$) is found in 700-N-PC, possibly arising from the enlargement of pore size by released gases during DICY decomposition. The best activation temperature is 800 °C for N-PCs, producing the highest SSA (3041 $m^2$ $g^{-1}$) and largest total pore volume ($V_t$, 1.90 $cm^3$ $g^{-1}$).

**Table 6.1** Textural and compositional properties of the synthesized samples.

| | SSA[a]/ $m^2$ $g^{-1}$ | $V_t$[b]/ $cm^3$ $g^{-1}$ | $V_{mic}$[c]/ $cm^3$ $g^{-1}$ | $V_{meso}$[d]/ $cm^3$ $g^{-1}$ | C/ at.% | N/ at.% | O/ at.% | Na/ at.% |
|---|---|---|---|---|---|---|---|---|
| 700-PC | 1278 | 0.68 | 0.58 | 0.10 | 88.14 | 1.07 | 10.57 | 0.22 |
| 600-N-PC | 646 | 0.41 | 0.27 | 0.14 | 75.18 | 12.23 | 12.20 | 0.39 |
| 700-N-PC | 1110 | 0.70 | 0.40 | 0.30 | 78.52 | 10.00 | 11.31 | 0.16 |
| 800-N-PC | 3041 | 1.90 | 0.41 | 1.49 | 86.23 | 7.33 | 6.44 | - |
| 900-N-PC | 2229 | 1.48 | 0.42 | 1.06 | 86.65 | 7.74 | 5.61 | - |

[a] Specific surface area based on the BET method. [b] Total pore volume at $P/P_0$ = 0.99. [c] Micropore volume calculated using the t-plot method. [d] Mesopore volume obtained by the difference between $V_t$ and $V_{mic}$.

### *6.3.2 $CO_2$ Uptake Analysis at Atmospheric and High Pressures*

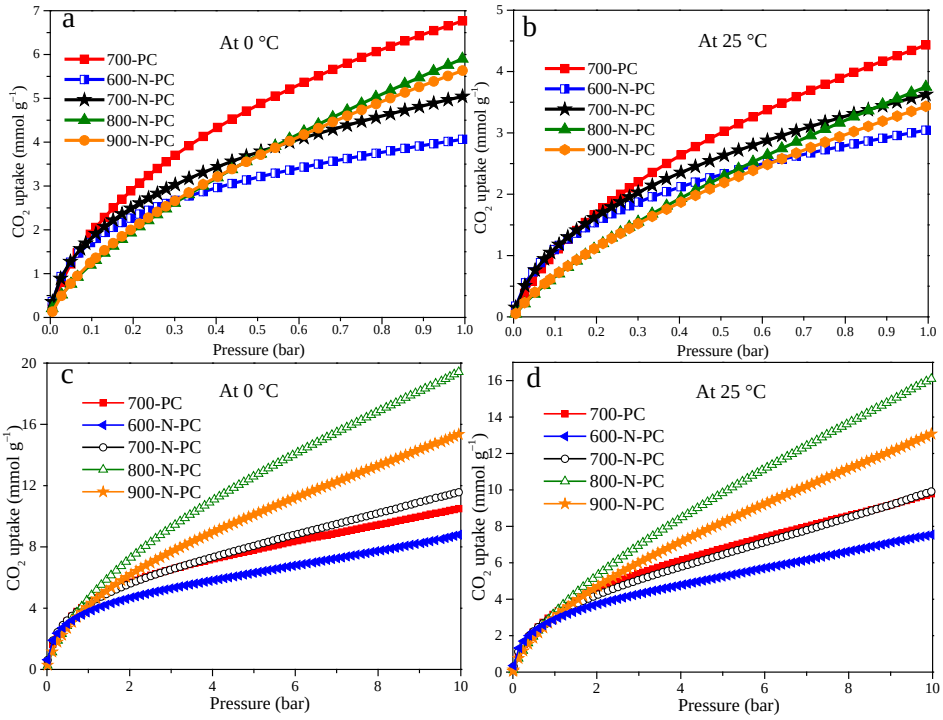

**Figure 6.9** $CO_2$ uptake isotherms at a) 0 ºC, b) 25 ºC up to 1 bar and c) 0 ºC, d) 25 ºC up to 10 bar.

$CO_2$ capture isotherms obtained at 0 - 1 bar mimic the post-combustion condition while that at pressures up to 10 bar imitate the pressure condition of pre-combustion. $CO_2$ capture at low and high pressures were tested separately on two different instruments which are specialized in ambient pressure and high pressure, respectively. The corresponding results are provided in Figure 6.9 and Table 6.2.

**Table 6.2** Summary of $CO_2$ capture performance of the synthesized materials.

| Samples | 0 ºC, 1 bar (mmol $g^{-1}$) | 25 ºC, 1 bar (mmol $g^{-1}$) | 0 ºC, 10 bar (mmol $g^{-1}$) | 25 ºC, 10 bar (mmol $g^{-1}$) |
|---|---|---|---|---|
| **700-PC** | **6.8** | **4.4** | 10.5 | 9.8 |
| **600-N-PC** | 4.0 | 3.0 | 8.8 | 7.5 |
| **700-N-PC** | 5.0 | 3.6 | 11.6 | 9.9 |
| **800-N-PC** | 5.9 | 3.8 | **19.4** | **16.1** |
| **900-N-PC** | 5.6 | 3.4 | 15.3 | 13.1 |

**Table 6.3** $CO_2$ capture capacities of 700-PC at 1 bar in comparison to the best performance of porous carbons, porous organic polymers and MOF materials reported in literature.

| | $CO_2$ uptake at 0 °C (mmol $g^{-1}$) | $CO_2$ uptake at 25 °C (mmol $g^{-1}$) | References |
|---|---|---|---|
| **d-MCN (Carbon)** | 1.77 | 1.16 | [40] Carbon 2016 |
| **NSC (Carbon)** | 4.8 | 3.1 | [41] Adv. Funct. Mater. 2016 |
| **HTC-K1-T8 (Carbon)** | 4.9 | 3.0 | [42] Carbon 2015 |
| **H-NMC-2.5 (Carbon)** | - | 3.2 | [43] Adv. Funct. Mater. 2013 |
| **NC900 (Carbon)** | 5.1 | 3.9 | [23] J. Am. Chem. Soc. 2014 |
| **HCM-DAH-1-900-1 (Carbon)** | 4.9 | 3.3 | [44] J. Am. Chem. Soc. 2011 |
| **SPC (Carbon)** | | 4.3 | [45] Nat. Commun. 2014 |
| **C@MF-700 (Carbon)** | 5.4 | 4.3 | [46] J. Mater. Chem. A 2017 |
| **CNF-1 (Carbon)** | 5.74 | 3.35 | [24] Adv. Funct. Mater. 2017 |
| **BTLP-4 (Polymer)** | 4.3 | 2.7 | [47] J. Mater. Chem. A 2017 |
| **CB-PCP-1 (Polymer)** | 2.05 | 1.2 | [48] J. Mater. Chem. A 2017 |
| **MM2 (Polymer)** | 4.76 | 3.13 | [49] J. Mater. Chem. A 2017 |
| **ZIF-8 (24h@500 °C, MOF)** | 3.0 | 1.79 | [50] Energy Environ. Sci. 2014 |
| **SIFSIX-30-Cu-I (MOF)_** | 6.5 | 5.4 | [2] Nature, 2013 |
| **IFMC-69 (MOF)** | 2.5 | 1.6 | [51] Chem. Sci. 2014 |
| **NENU-520 (MOF)** | 3.56 | 2.72 | [52] J. Mater. Chem. A 2015 |
| **MOF-5 (6h@380 °C) (MOF)** | - | 2 | [53] Chem. Mater. 2014 |
| **Bio-MOF-14 (MOF)** | 4.1 | - | [54] J. Am. Chem. Soc. 2013 |
| **MONT 7 (MOF)** | - | 1.51 | [55] J. Am. Chem. Soc. 2014 |

| | | | |
|---|---|---|---|
| **700-PC** | **6.8** | **4.4** | **This work** |

It is generally believed that $CO_2$ uptake in ambient condition is determined by microporosity because of a large caging effect.[3, 56] Besides, the presence of N atoms especially pyrrolic-N can serve as Lewis bases, thereby facilitating the adsorption of Lewis acidic $CO_2$.[36] Among N-PCs, 800-N-PC with the highest SSA, $V_t$, and medium N content displays the highest $CO_2$ capture capacity at ambient pressure (5.9 mmol $g^{-1}$ at 0 ºC). Interestingly, 700-PC, which has much lower SSA, $V_t$ and N content yet a higher $V_{mic}$, exhibits a higher $CO_2$ uptake capacity than 800-N-PC (6.8 mmol $g^{-1}$ at 0 ºC). This result proved the critical role of microporosity for post-combustion $CO_2$ capture. As compared in Table 6.3, this performance is among the best of reported porous carbons and superior to many porous organic polymers and MOF materials. It is noteworthy that here the preparation process is more feasible and cost-effective than most of the materials mentioned above.

**Table 6.4** High-pressure $CO_2$ capacities at around 25 ºC of 800-N-PC in comparison to literature reported porous carbons, porous organic polymers and MOF materials.

| **Samples** | **$CO_2$ adsorption (mmol $g^{-1}$)** | **Reference** |
|---|---|---|
| **800-N-PC** | **16.1, 10 bar** | **This work** |
| **KLB2 (Carbon)** | - | [57] Carbon 2017 |
| **Glc-Cs (Carbon)** | 14.2, 10 bar | [58] Chem. Eng. J. 2017 |
| **GODC4-600 (Carbon)** | 8.9, 20 bar | [59] Energy Environ. Sci. 2012 |
| **SCS-700 (Carbon)** | 10.66, 8 bar | [60] J. Phys. Chem. C 2017 |
| **SPC (Carbon)** | 12.0, 10 bar | [45] Nat. Commun. 2014 |
| **L2600P (Carbon)** | 12.8, 20 bar | [61] Adv. Energy Mater 2015 |
| **ACGR4700 (Carbon)** | 20, 20 bar | [34] J. Mater. Chem. A 2016 |
| **$CO_2$ treated CNHs (Carbon)** | 6.9, 30 bar | [62] J. Mater. Chem. A 2016 |
| **PAF1 (Polymer)** | 11.9, 10 bar | [63] J. Mater. Chem. A 2017 |
| **FMOF-1 (MOF)** | 0.00616, 55 bar | [64] Chem. Sci. 2017 |
| **Porous organic polymers** | 15, 35 bar | [65] J. Mater. Chem. A 2017 |
| **uGil-900 (Carbon)** | 13.6, 10 bar | [66] Adv. Energy Mater. 2017 |
| **MOF5b2-1100 (MOF)** | 14.2, 10 bar | [3] Energy Environ. Sci. 2014 |
| **HPC5b2-1100 (Carbon)** | 14.0, 10 bar | [3] Energy Environ. Sci. 2014 |

| | | |
|---|---|---|
| **MOF-205 (MOF)** | 11.4, 10 bar | [67] Science 2010 |

Although $CO_2$ uptake of the samples at low pressures has no clear correlation with SSAs, the $CO_2$ uptake at 10 bar is more or less positively proportional to their SSAs. Specifically, 800-N-PC exhibits the best $CO_2$ capture performance at 10 bar (19.4 mmol $g^{-1}$ at 0 ºC), which is amongst the highest values reported so far on porous carbons, porous organic polymers and MOF materials, as shown in Table 6.4. This is presumably attributable to the highest $V_{meso}$, as $CO_2$ adsorption at high-pressures also proceeds in the wider micropores and narrow mesopores.[3, 9] Moreover, the absolute $CO_2$ sorption isotherms of all the samples are almost linear with pressure at 10 bar, which is far from saturation, suggesting the exceedingly high adsorption.

Clearly, both SSA and N content are critical in determining the $CO_2$ uptake capacity. To clarify the impact of N-decoration, $CO_2$ adsorption isotherms at 0 ºC of different pressures were normalized with respect to the SSAs of different samples, as provided in Figure 6.10a and b. N-PCs display enhancement of $CO_2$ capture with higher N contents both at low and high pressure range. With the lowest N content, 700-PC shows moderate $CO_2$ uptake performance in both conditions, which can be attributed to its highest $V_{mic}$.

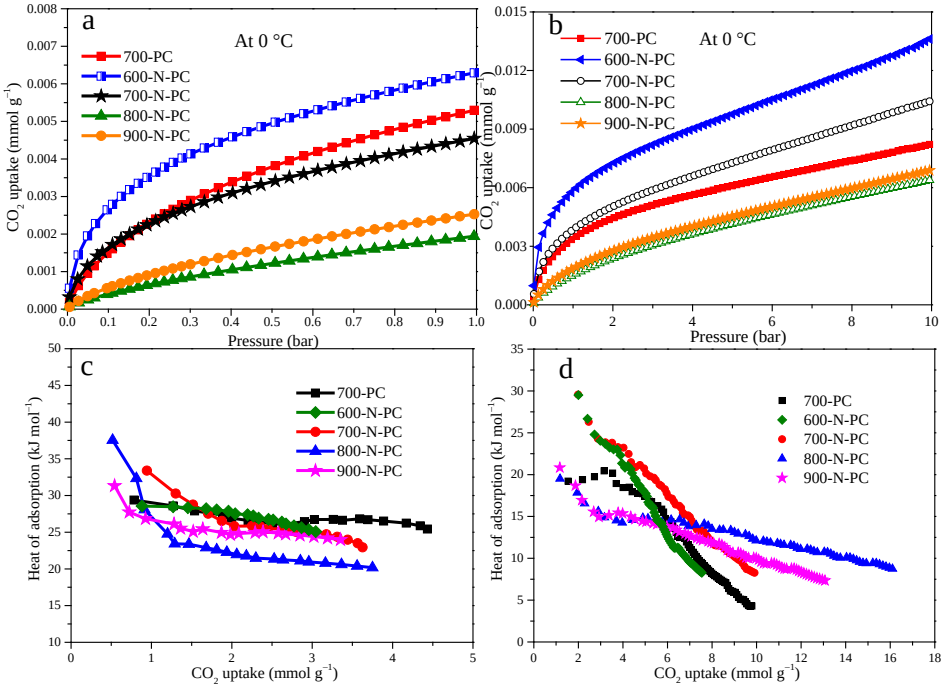

**Figure 6.10** $CO_2$ uptake isotherms at a) low pressure and b) high pressures of the samples at 0 ºC normalized by SSAs. Isosteric heats of adsorption ($Q_{st}$) of the samples at c) low pressures and d) high pressure range.

$CO_2$ adsorption at lower surface coverage (≤ 1 bar) is expected to be a better illustration of the sorbate-sorbent interaction.[45] Therefore, $CO_2$ sorption isotherms collected at 0 and 25 °C up to 1 bar (Figure 6.9a and b) were used in the Clausius-Clapeyron equation[26] to calculate the isosteric heat of $CO_2$ adsorption ($Q_{st}$, Figure 6.10c). $Q_{st}$ indicates the interaction between the sorbent and sorbate and can be used to evaluate the energy for regeneration.[68] Since the stronger affinity of $CO_2$ with the most active sites such as the surface basic functional N groups and narrow micropores generates the highest adsorption heat,[6, 23] the initial values of $Q_{st}$ are high for all the samples. Then, $Q_{st}$ declines gradually and becomes relatively constant, suggesting the homogeneous binding over higher $CO_2$ coverage.[2] $Q_{st}$ values were also calculated using high pressure $CO_2$ capture isotherms at 0 and 25 °C (Figure 6.10d). The considerable declined $Q_{st}$ with increasing $CO_2$ loading reveals that $CO_2$-$CO_2$ interactions become more crucial while the surface binding sites are less accessible at higher pressures.[9] On account of this, a super high BET surface area is greatly desirable for achieving excellent $CO_2$ uptake performance at high pressures. All the $Q_{st}$ values are within the physisorption range, favorable for reversible adsorption-desorption.[2, 69]

*6.3.3 HBA and Phenol Removals*

With N doping, large SSAs and pore volumes, the developed porous carbons are very appealing for adsorption and AOP catalysis in water treatment. Figure 6.11a shows the adsorptive performance of the as-synthesized porous carbons on HBA. It is shown that 600-N-PC, 700-N-PC, 700-PC, 800-N-PC, and 900-N-PC provide about 15%, 20%, 37%, 39% and 45% of HBA adsorptive removal efficiencies, respectively. 900-N-PC exhibits the highest adsorption capacity. For AOPs (Figure 6.11b), PMS alone has little effect on HBA removal. HBA degradation reaches 78% in 150 min with 700-PC/PMS, while 100% in 60 min is obtained in 700-N-PC/PMS. This result signifies the enhanced catalytic ability of porous carbon by N doping. As is known, the charge states of N is more negative than C, and thus N doping can induce charge transfer from adjacent carbon and produce more positively charged C, which is widely agreed to improve the catalytic ability of

carbon materials.[10, 70-72] Besides, high BET surface area and the hierarchical porous structure promote the penetration of PMS into the pore channels to access more active sites, further improving the catalytic performance. Facilitated by the effect of suitable nitrogen functionality and large SSA, 800-N-PC shows the most efficient catalytic ability in AOP and HBA is completely removed in 20 min.

The influence of solution temperature (15, 25, and 35 $^{o}$C) on the catalytic reaction of 800-N-PC/PMS was also investigated (Figure 6.11c). The reaction rate constant (k) can be calculated using the following equation:

$$\ln(C/C_0) = -kt \qquad (6.5)$$

where $C_0$ is the initial HBA concentration; C is the concentration of HBA dependent on reaction time (t). The reaction rate increases steadily with elevated temperatures from 15 $^{o}$C (k = 0.26 min$^{-1}$, $R^2$ = 0.98), 25 $^{o}$C (k = 0.39 min$^{-1}$, $R^2$ = 0.97) to 35 $^{o}$C (k = 0.52 min$^{-1}$, $R^2$ = 0.99). Calculated from the Arrhenius equation, the activation energy ($E_a$) of 800-N-PC for the catalytic HBA oxidation is obtained to be 26.3 kJ mol$^{-1}$.

It is reported that efficient AOPs rely on producing strong oxidizing radicals, which can readily oxidize the target organic pollutants.[19, 73] To detect the produced radicals, EPR was conducted on 800-N-PC. As shown in Figure 6.11d, after adding 800-N-PC/PMS to HBA solution, evident signals of hydroxyl ($^{\bullet}$OH) and sulfate ($SO_4^{\bullet-}$) radicals were captured by DMPO, which are responsible for the efficient degradation of the organics in AOPs.

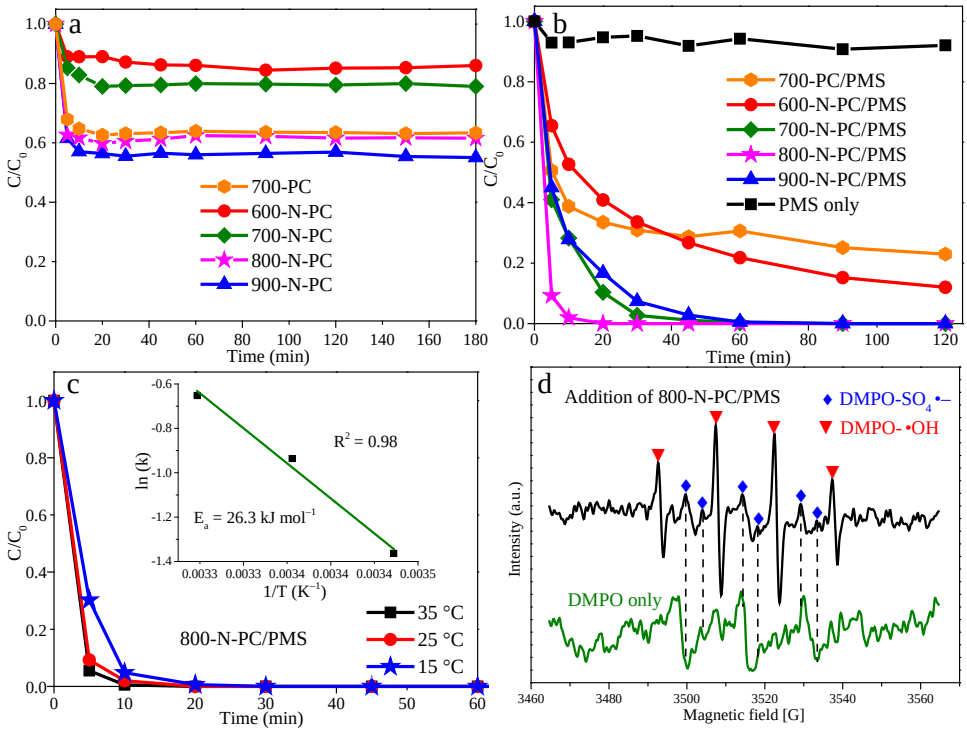


**Figure 6.11** HBA removal by a) adsorption and b) AOP degradation at 25 °C (Adsorbent or catalyst: 0.1 g $L^{-1}$, HBA: 20 mg $L^{-1}$, PMS 6.5 mM). c) Effect of solution temperature on HBA removal by 800-N-PC/PMS. d) EPR test during HBA degradation by 800-N-PC/PMS.

Considering that wastewater usually contains several kinds of organic pollutants, this thesis also studied the adsorption and AOP performance of 800-N-PC on the removal of mixed HBA and phenol solution (Figure 6.12). Interestingly, 800-N-PC shows selective adsorption to HBA while negligible adsorption of phenol. This can be explained mainly from the perspective of intermolecular Lewis acid-base interaction.[74] There are more acidic functional groups attached to a benzene ring in HBA (–COOH and –OH) than phenol (–OH), and the polarity of –COOH is much stronger than –OH. On account of this, the acid-base interaction between basic N-containing functional groups in 800-N-PC and the acid groups in HBA tends to be stronger than that in phenol. Therefore, 800-N-PC shows selective adsorption of HBA over phenol. This unique property makes 800-N-PC applicable in phase separation or purification. With PMS and a low loading amount of 800-N-PC (0.066 g $L^{-1}$), both phenol and HBA in the mixed solution can be decomposed completely in a short time. 800-N-PC is more efficient in the oxidation of phenol (k = 0.27 $min^{-1}$, $R^2$ = 0.97) than HBA (k = 0.13 $min^{-1}$, $R^2$ = 0.98). This result verifies that

adsorption and AOPs are two independent processes and the two performances are not directly correlated.

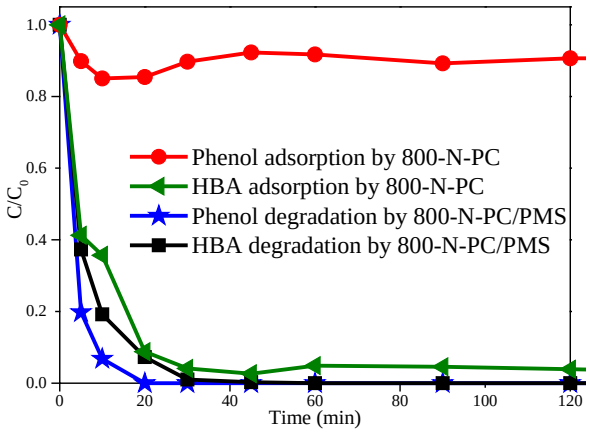


**Figure 6.12** Selective removal of HBA and phenol at 25 °C in a mixed solution of HBA (10 mg $L^{-1}$) and phenol (10 mg $L^{-1}$) (Adsorbent or catalyst: 0.066 g $L^{-1}$ 800-N-PC, PMS 6.5 mM).

## 6.4 Conclusions

This study reported a potentially scalable preparation using readily available and renewable raw materials to construct micropore-dominant nanocarbon or N-doped hierarchical porous nanocarbon with macroporous skeletons of meso- or microporous texture. $CO_2$ adsorption at the ambient pressure largely depends on the micropore volume and N content while $CO_2$ uptake capacity at a high pressure range has a direct relationship with SSA and N content. 700-PC displays an excellent $CO_2$ adsorption capacity of 6.8 mmol $g^{-1}$ at ambient pressure and 0 °C. 800-N-PC, with its SSA of 3041 $m^2$ $g^{-1}$ and pore volume of 1.9 $cm^3$ $g^{-1}$, has attained the position among the highest $CO_2$ capture capacities on porous sorbents at 10 bar (19.4 mmol $g^{-1}$ at 0 °C). N-PCs possess a powerful capability for water remediation with 800-N-PC being super-efficient for HBA degradation. In a mixed solution of HBA and phenol, 800-N-PC exhibits an adsorption superiority of HBA while both HBA and phenol can be catalytically decomposed with high efficiency. This work demonstrates a novel and economical designing opportunities of porous nanocarbons with promising versatile applications in environmental cleaning.

## References

[1] L.F. Zou, Y.J. Sun, S. Che, X.Y. Yang, X. Wang, M. Bosch, Q. Wang, H. Li, M. Smith, S. Yuan, Z. Perry, H.C. Zhou, Porous Organic Polymers for Post-Combustion Carbon Capture, Advanced Materials, 29 (2017) 1700229.

[2] P. Nugent, Y. Belmabkhout, S.D. Burd, A.J. Cairns, R. Luebke, K. Forrest, T. Pham, S. Ma, B. Space, L. Wojtas, M. Eddaoudi, M.J. Zaworotko, Porous Materials with Optimal Adsorption Thermodynamics and Kinetics for $CO_2$ Separation, Nature, 495 (2013) 80.

[3] G. Srinivas, V. Krungleviciute, Z.-X. Guo, T. Yildirim, Exceptional $CO_2$ Capture in a Hierarchically Porous Carbon with Simultaneous High Surface Area and Pore Volume, Energy & Environmental Science, 7 (2014) 335.

[4] X. Wang, B. Yuan, X. Zhou, Q. Xia, Y. Li, D. An, Z. Li, Novel Glucose-Based Adsorbents (Glc-Cs) with High $CO_2$ Capacity and Excellent $CO_2/CH_4/N_2$ Adsorption Selectivity, Chemical Engineering Journal, 327 (2017) 51.

[5] G.T. Rochelle, Amine Scrubbing for $CO_2$ Capture, Science, 325 (2009) 1652.

[6] M. Sevilla, P. Valle-Vigon, A.B. Fuertes, N-Doped Polypyrrole-Based Porous Carbons for $CO_2$ Capture, Advanced Functional Materials, 21 (2011) 2781.

[7] R. Vaidhyanathan, S.S. Iremonger, G.K.H. Shimizu, P.G. Boyd, S. Alavi, T.K. Woo, Direct Observation and Quantification of $CO_2$ Binding within an Amine-Functionalized Nanoporous Solid, Science, 330 (2010) 650.

[8] W.J. Tian, H.Y. Zhang, H.Q. Sun, A. Suvorova, M. Saunders, M. Tade, S.B. Wang, Heteroatom (N or N-S)-Doping Induced Layered and Honeycomb Microstructures of Porous Carbons for $CO_2$ Capture and Energy Applications, Advanced Functional Materials, 26 (2016) 8651.

[9] J. He, J.W.F. To, P.C. Psarras, H. Yan, T. Atkinson, R.T. Holmes, D. Nordlund, Z. Bao, J. Wilcox, Tunable Polyaniline-Based Porous Carbon with Ultrahigh Surface Area for $CO_2$ Capture at Elevated Pressure, Advanced Energy Materials, 6 (2016) 1502491.

[10] W. Tian, H. Zhang, Z. Qian, T. Ouyang, H. Sun, J. Qin, M.O. Tadé, S. Wang, Bread-Making Synthesis of Hierarchically Co@C Nanoarchitecture in Heteroatom Doped Porous Carbons for Oxidative Degradation of Emerging Contaminants, Applied Catalysis B: Environmental, 225 (2018) 76.

[11] W.J. Tian, H.Y. Zhang, X.G. Duan, H.Q. Sun, M.O. Tade, H.M. Ang, S.B. Wang, Nitrogen- and Sulfur-Codoped Hierarchically Porous Carbon for Adsorptive and

Oxidative Removal of Pharmaceutical Contaminants, ACS Applied Materials & Interfaces, 8 (2016) 7184.
[12] F.C. Moreira, R.A.R. Boaventura, E. Brillas, V.J.P. Vilar, Electrochemical Advanced Oxidation Processes: A Review on Their Application to Synthetic and Real Wastewaters, Applied Catalysis B-Environmental, 202 (2017) 217.
[13] C. Santhosh, V. Velmurugan, G. Jacob, S.K. Jeong, A.N. Grace, A. Bhatnagar, Role of Nanomaterials in Water Treatment Applications: A Review, Chemical Engineering Journal, 306 (2016) 1116.
[14] X. Wang, X. Hu, H. Zhang, F. Chang, Y. Luo, Photolysis Kinetics, Mechanisms, and Pathways of Tetrabromobisphenol a in Water under Simulated Solar Light Irradiation, Environmental Science & Technology, 49 (2015) 6683.
[15] F.J. Rivas, F.J. Beltrán, J. Frades, P. Buxeda, Oxidation of P-Hydroxybenzoic Acid by Fenton's Reagent, Water Research, 35 (2001) 387.
[16] J. Beltran-Heredia, J. Torregrosa, J.R. Dominguez, J.A. Peres, Comparison of the Degradation of P-Hydroxybenzoic Acid in Aqueous Solution by Several Oxidation Processes, Chemosphere, 42 (2001) 351.
[17] Y. Xia, R. Mokaya, G.S. Walker, Y. Zhu, Superior CO2 Adsorption Capacity on N-Doped, High-Surface-Area, Microporous Carbons Templated from Zeolite, Advanced Energy Materials, 1 (2011) 678.
[18] W.J. Tian, H.Y. Zhang, H.Q. Sun, M.O. Tade, S.B. Wang, Template-Free Synthesis of N-Doped Carbon with Pillared-Layered Pores as Bifunctional Materials for Supercapacitor and Environmental Applications, Carbon, 118 (2017) 98.
[19] K.E. O'Shea, D.D. Dionysiou, Advanced Oxidation Processes for Water Treatment, Journal of Physical Chemistry Letters, 3 (2012) 2112.
[20] P.D. Hu, M.C. Long, Cobalt-Catalyzed Sulfate Radical-Based Advanced Oxidation: A Review on Heterogeneous Catalysts and Applications, Applied Catalysis B-Environmental, 181 (2016) 103.
[21] O.M. Rodriguez-Narvaez, J.M. Peralta-Hernandez, A. Goonetilleke, E.R. Bandala, Treatment Technologies for Emerging Contaminants in Water: A Review, Chemical Engineering Journal, 323 (2017) 361.
[22] F. Ghanbari, M. Moradi, Application of Peroxymonosulfate and Its Activation Methods for Degradation of Environmental Organic Pollutants: Review, Chemical Engineering Journal, 310 (2017) 41.

[23] A. Aijaz, N. Fujiwara, Q. Xu, From Metal-Organic Framework to Nitrogen-Decorated Nanoporous Carbons: High $CO_2$ Uptake and Efficient Catalytic Oxygen Reduction, Journal of the American Chemical Society, 136 (2014) 6790.

[24] S.N. Talapaneni, J.H. Lee, S.H. Je, O. Buyukcakir, T.-w. Kwon, K. Polychronopoulou, J.W. Choi, A. Coskun, Chemical Blowing Approach for Ultramicroporous Carbon Nitride Frameworks and Their Applications in Gas and Energy Storage, Advanced Functional Materials, 27 (2017) 1604658.

[25] N. Lopez-Salas, M.C. Gutierrez, C.O. Ania, J.L.G. Fierro, M. Luisa Ferrer, F.d. Monte, Efficient Nitrogen-Doping and Structural Control of Hierarchical Carbons Using Unconventional Precursors in the Form of Deep Eutectic Solvents, Journal of Materials Chemistry A, 2 (2014) 17387.

[26] X.Y. Ma, Y. Li, M.H. Cao, C.W. Hu, A Novel Activating Strategy to Achieve Highly Porous Carbon Monoliths for $CO_2$ Capture, Journal of Materials Chemistry A, 2 (2014) 4819.

[27] J.W.F. To, J.J. He, J.G. Mei, R. Haghpanah, Z. Chen, T. Kurosawa, S.C. Chen, W.G. Bae, L.J. Pan, J.B.H. Tok, J. Wilcox, Z.N. Bao, Hierarchical N-Doped Carbon as $CO_2$ Adsorbent with High $CO_2$ Selectivity from Rationally Designed Polypyrrole Precursor, Journal of the American Chemical Society, 138 (2016) 1001.

[28] M. Sevilla, A.B. Fuertes, Sustainable Porous Carbons with a Superior Performance for $CO_2$ Capture, Energy & Environmental Science, 4 (2011) 1765.

[29] A.S. Mestre, C. Freire, J. Pires, A.P. Carvalho, M.L. Pinto, High Performance Microspherical Activated Carbons for Methane Storage and Landfill Gas or Biogas Upgrade, Journal of Materials Chemistry A, 2 (2014) 15337.

[30] N. Balahmar, A.C. Mitchell, R. Mokaya, Generalized Mechanochemical Synthesis of Biomass-Derived Sustainable Carbons for High Performance $CO_2$ Storage, Advanced Energy Materials, 5 (2015) 1500867.

[31] J. Hayashi, A. Kazehaya, K. Muroyama, A.P. Watkinson, Preparation of Activated Carbon from Lignin by Chemical Activation, Carbon, 38 (2000) 1873.

[32] S. Ucar, M. Erdem, T. Tay, S. Karagoz, Removal of Lead (II) and Nickel (II) Ions from Aqueous Solution Using Activated Carbon Prepared from Rapeseed Oil Cake by $Na_2CO_3$ Activation, Clean Technologies and Environmental Policy, 17 (2015) 747.

[33] L.M. Yue, Q.Z. Xia, L.W. Wang, L.L. Wang, H. DaCosta, J. Yang, X. Hu, $CO_2$ Adsorption at Nitrogen-Doped Carbons Prepared by $K_2CO_3$ Activation of Urea-Modified Coconut Shell, Journal of Colloid and Interface Science, 511 (2018) 259.

[34] H.M. Coromina, D.A. Walsh, R. Mokaya, Biomass-Derived Activated Carbon with Simultaneously Enhanced CO2 Uptake for Both Pre and Post Combustion Capture Applications, Journal of Materials Chemistry A, 4 (2016) 280.

[35] B. Adeniran, R. Mokaya, Compactivation: A Mechanochemical Approach to Carbons with Superior Porosity and Exceptional Performance for Hydrogen and $CO_2$ Storage, Nano Energy, 16 (2015) 173.

[36] G. Sethia, A. Sayari, Comprehensive Study of Ultra-Microporous Nitrogen-Doped Activated Carbon for $CO_2$ Capture, Carbon, 93 (2015) 68.

[37] J.C. Wang, S. Kaskel, KOH Activation of Carbon-Based Materials for Energy Storage, Journal of Materials Chemistry, 22 (2012) 23710.

[38] J.F. Moulder, J. Chastain, R.C. King, Handbook of X-Ray Photoelectron Spectroscopy: A Reference Book of Standard Spectra for Identification and Interpretation of XPS Data, Perkin-Elmer Eden Prairie, MN1992.

[39] Q. Shi, R. Zhang, Y. Lv, Y. Deng, A.A. Elzatahrya, D. Zhao, Nitrogen-Doped Ordered Mesoporous Carbons Based on Cyanamide as the Dopant for Supercapacitor, Carbon, 84 (2015) 335.

[40] N. Balahmar, A.M. Lowbridge, R. Mokaya, Templating of Carbon in Zeolites under Pressure: Synthesis of Pelletized Zeolite Templated Carbons with Improved Porosity and Packing Density for Superior Gas ($CO_2$ and $H_2$) Uptake Properties, Journal of Materials Chemistry A, 4 (2016) 14254.

[41] S.-E. Bae, K.-J. Kim, I.-H. Choi, S. Huh, Preparation of N-Doped Microporous Carbon Nanospheres by Direct Carbonization of as-Prepared Mesoporous Silica Nanospheres Containing Cetylpyridinium Bromide Template, Carbon, 99 (2016) 8.

[42] W. Tian, H. Zhang, H. Sun, A. Suvorova, M. Saunders, M. Tade, S. Wang, Heteroatom (N or N-S)-Doping Induced Layered and Honeycomb Microstructures of Porous Carbons for $CO_2$ Capture and Energy Applications, Advanced Functional Materials, 26 (2016) 8651.

[43] F.J. Martin-Jimeno, F. Suarez-Garcia, J.I. Paredes, A. Martinez-Alonso, J.M.D. Tascon, Activated Carbon Xerogels with a Cellular Morphology Derived from Hydrothermally Carbonized Glucose-Graphene Oxide Hybrids and Their Performance Towards $CO_2$ and Dye Adsorption, Carbon, 81 (2015) 137.

[44] J. Wei, D. Zhou, Z. Sun, Y. Deng, Y. Xia, D. Zhao, A Controllable Synthesis of Rich Nitrogen-Doped Ordered Mesoporous Carbon for $CO_2$ Capture and Supercapacitors, Advanced Functional Materials, 23 (2013) 2322.

[45] G.P. Hao, W.C. Li, D. Qian, G.H. Wang, W.P. Zhang, T. Zhang, A.Q. Wang, F. Schuth, H.J. Bongard, A.H. Lu, Structurally Designed Synthesis of Mechanically Stable Poly(Benzoxazine-Co-Resol)-Based Porous Carbon Monoliths and Their Application as High-Performance $CO_2$ Capture Sorbents, Journal of the American Chemical Society, 133 (2011) 11378.

[46] C.-C. Hwang, J.J. Tour, C. Kittrell, L. Espinal, L.B. Alemany, J.M. Tour, Capturing Carbon Dioxide as a Polymer from Natural Gas, 5 (2014) 3961.

[47] L. Liu, Z.-H. Xie, Q.-F. Deng, X.-X. Hou, Z.-Y. Yuan, One-Pot Carbonization Enrichment of Nitrogen in Microporous Carbon Spheres for Efficient $CO_2$ Capture, Journal of Materials Chemistry A, 5 (2017) 418.

[48] M.G. Rabbani, T. Islamoglu, H.M. El-Kaderi, Benzothiazole- and Benzoxazole-Linked Porous Polymers for Carbon Dioxide Storage and Separation, Journal of Materials Chemistry A, 5 (2017) 258.

[49] A. Dani, V. Crocella, C. Magistris, V. Santoro, J. Yuan, S. Bordiga, Click-Based Porous Cationic Polymers for Enhanced Carbon Dioxide Capture, Journal of Materials Chemistry A, 5 (2017) 372.

[50] S. Dey, A. Bhunia, H. Breitzke, P.B. Groszewicz, G. Buntkowsky, C. Janiak, Two Linkers Are Better Than One: Enhancing $CO_2$ Capture and Separation with Porous Covalent Triazine-Based Frameworks from Mixed Nitrile Linkers, Journal of Materials Chemistry A, 5 (2017) 3609.

[51] S. Gadipelli, W. Travis, W. Zhou, Z.X. Guo, A Thermally Derived and Optimized Structure from ZIF-8 with Giant Enhancement in $CO_2$ Uptake, Energy & Environmental Science, 7 (2014) 2232.

[52] P. Shen, W.W. He, D.Y. Du, H.L. Jiang, S.L. Li, Z.L. Lang, Z.M. Su, Q. Fu, Y.Q. Lan, Solid-State Structural Transformation Doubly Triggered by Reaction Temperature and Time in 3D Metal-Organic Frameworks: Great Enhancement of Stability and Gas Adsorption, Chemical Science, 5 (2014) 1368.

[53] S.J. Bao, R. Krishna, Y.B. He, J.S. Qin, Z.M. Su, S.L. Li, W. Xie, D.Y. Du, W.W. He, S.R. Zhang, Y.Q. Lan, A Stable Metal-Organic Framework with Suitable Pore Sizes and Rich Uncoordinated Nitrogen Atoms on the Internal Surface of Micropores for Highly Efficient $CO_2$ Capture, Journal of Materials Chemistry A, 3 (2015) 7361.

[54] S. Gadipelli, Z.X. Guo, Postsynthesis Annealing of Mof-5 Remarkably Enhances the Framework Structural Stability and $CO_2$ Uptake, Chemistry of Materials, 26 (2014) 6333.

[55] T. Li, J.E. Sullivan, N.L. Rosi, Design and Preparation of a Core-Shell Metal-Organic Framework for Selective $CO_2$ Capture, Journal of the American Chemical Society, 135 (2013) 9984.

[56] C.R. Murdock, D.M. Jenkins, Isostructural Synthesis of Porous Metal-Organic Nanotubes, Journal of the American Chemical Society, 136 (2014) 10983.

[57] G. Singh, I.Y. Kim, K.S. Lakhi, P. Srivastava, R. Naidu, A. Vinu, Single Step Synthesis of Activated Bio-Carbons with a High Surface Area and Their Excellent $CO_2$ Adsorption Capacity, Carbon, 116 (2017) 448.

[58] X. Wang, B. Yuan, X. Zhou, Q. Xia, Y. Li, D. An, Z. Li, Novel Glucose-Based Adsorbents (Glc-Cs) with High $CO_2$ Capacity and Excellent $CO_2/CH_4/N_2$ Adsorption Selectivity, Chemical Engineering Journal, 327 (2017) 51.

[59] G. Srinivas, J. Burress, T. Yildirim, Graphene Oxide Derived Carbons (Godcs): Synthesis and Gas Adsorption Properties, Energy & Environmental Science, 5 (2012) 6453.

[60] Y. Sun, J. Zhao, J. Wang, N. Tang, R. Zhao, D. Zhang, T. Guan, K. Li, Sulfur-Doped Millimeter-Sized Microporous Activated Carbon Spheres Derived from Sulfonated Poly(Styrene-Divinylbenzene) for $CO_2$ Capture, Journal of Physical Chemistry C, (2017).

[61] N. Balahmar, A.C. Mitchell, R. Mokaya, Generalized Mechanochemical Synthesis of Biomass-Derived Sustainable Carbons for High Performance $CO_2$ Storage, Advanced Energy Materials, 5 (2016).

[62] D.J. Babu, T. Herdt, S. Okeil, M. Bruns, R. Staudt, J.J. Schneider, Bud Type Carbon Nanohorns: Materials for High Pressure $CO_2$ Capture and Li-Ion Storage, Journal of Materials Chemistry A, (2016).

[63] P. Sozzani, A. Comotti, I. Bassanetti, D. Piga, J. Perego, S. Bracco, Porous 3D Polymers for High Pressure Methane Storage and Carbon Dioxide Capture, Journal of Materials Chemistry A, (2017).

[64] P.Z. Moghadam, J.F. Ivy, R.K. Arvapally, A.M. Dos Santos, J.C. Pearson, L. Zhang, E. Tylianakis, P. Ghosh, O. Iwh, U. Kaipa, Adsorption and Molecular Siting of $CO_2$, Water, and Other Gases in the Superhydrophobic, Flexible Pores of Fmof-1 from Experiment and Simulation, Chemical Science, 8 (2017) 3989.

[65] S. Nandi, J. Rother, D. Chakraborty, R. Maity, U. Wernerzwanziger, V. Ramanathan, Exceptionally Stable Bakelite-Type Polymers for Efficient Pre-Combustion $CO_2$ Capture and $H_2$ Purification, Journal of Materials Chemistry A, 5 (2017) 8431.

[66] A.S. Jalilov, Y. Li, J. Tian, J.M. Tour, Ultra-High Surface Area Activated Porous Asphalt for $CO_2$ Capture through Competitive Adsorption at High Pressures, Advanced Energy Materials, 7 (2017) 1600693.
[67] H. Furukawa, N. Ko, Y.B. Go, N. Aratani, S.B. Choi, E. Choi, A.Ö. Yazaydin, R.Q. Snurr, M. O'Keeffe, J. Kim, O.M. Yaghi, Ultrahigh Porosity in Metal-Organic Frameworks, Science, 329 (2010) 424.
[68] K. Li, S. Tian, J. Jianguo, J. Wang, X. Chen, F. Yan, Pine Cone Shell-Based Activated Carbon Used for $CO_2$ Adsorption, 2016.
[69] P. Tamilarasan, S. Ramaprabhu, Integration of Polymerized Ionic Liquid with Graphene for Enhanced $CO_2$ Adsorption, Journal of Materials Chemistry A, 3 (2015) 101.
[70] J. Liang, Y. Jiao, M. Jaroniec, S.Z. Qiao, Sulfur and Nitrogen Dual-Doped Mesoporous Graphene Electrocatalyst for Oxygen Reduction with Synergistically Enhanced Performance, Angewandte Chemie-International Edition, 51 (2012) 11496.
[71] J.T. Zhang, Z.H. Xia, L.M. Dai, Carbon-Based Electrocatalysts for Advanced Energy Conversion and Storage, Science Advances, 1 (2015) e1500564.
[72] H. Zhang, W. Tian, Z. Qian, T. Ouyang, M. Saunders, J. Qin, S. Wang, M.O. Tadé, H. Sun, Co@C/CoOx Coupled with N-Doped Layer-Structured Carbons for Excellent $CO_2$ Capture and Oxygen Reduction Reaction, Carbon, 133 (2018) 306.
[73] W.H. Glaze, J.-W. Kang, D.H. Chapin, The Chemistry of Water Treatment Processes Involving Ozone, Hydrogen Peroxide and Ultraviolet Radiation, Ozone: Science & Engineering, 9 (1987) 335.
[74] G.X. Zhao, L. Jiang, Y.D. He, J.X. Li, H.L. Dong, X.K. Wang, W.P. Hu, Sulfonated Graphene for Persistent Aromatic Pollutant Management, Advanced Materials, 23 (2011) 3959.

# Chapter 7. Bread-Making Synthesis of Hierarchical Co@C Nanoarchitecture in Heteroatom Doped Porous Carbons for Oxidative Degradation of Emerging Contaminants


## Abstract

*In chapter 6, N-doped functional porous carbons have been synthesized by pyrolyzing a mixture of wheat flour and $NaHCO_3$/$Na_2CO_3$/$K_2CO_3$/DICY at 700 °C. In this chapter, still employing low-cost and abundant wheat flour as carbon source while sodium bicarbonate, cysteine and cobalt nitrate as other precursors, the authors for the first time present a facile one-pot pyrolysis strategy for homogeneous assembly of core-shell Co@C nanoparticles with nitrogen and sulfur into hierarchically porous carbons (Co-N-S-PCs). The samples were highly efficient for oxidative decomposition of HBA and phenol. It was found that Co@C nanoparticles are crucial for the generation of singlet oxygen in continuous AOPs, which works together with hydroxyl and sulfate radicals in efficient decomposition of HBA. Density functional theory (DFT) calculations disclose that electron transfer from Co to C shells greatly improves the Fermi level and chemical activity of the C atoms. The combination of Co-C interaction with dual N, S doping further bring about active catalytic sites in the graphitic shells where the charge states of C atoms are increased. This template-free strategy is scalable to prepare highly efficient catalysts, including functional carbon materials modified with non-precious metal species or pure well-dispersed porous core-shell nanoparticles for environmental or energy applications.*


## 7.1 Introduction

The increasing demands for fresh drinking water supply have heightened a worldwide concern for growing water contamination by persistent organic pollutants (POPs) from agricultural, industrial and urban human activities.[1] For instance, non-biodegradable 4-hydroxybenzoic acid (HBA) and phenol have been widely detected in the wastewater,[2, 3] which can hardly decompose using conventional methods. Given that water quality is closely tied to the health of humankind and the well-being of the planet Earth, sustainable treatment techniques are urgently required.[1] Among several available technologies,

advanced oxidation processes (AOPs) are especially suitable for complete removal of organics and have attracted growing attention.[4, 5] In essence, AOPs are based on generating strong oxidizing radicals such as hydroxyl ($^{\bullet}OH$), sulfate ($SO_4^{\bullet-}$), and singlet oxygen ($^1O_2$),[4] that are able to oxidize or react with most organic pollutants into low toxic compounds or final products of water and carbon dioxide.[6] Compared with single $^{\bullet}OH$-generating AOPs by traditional Fenton reaction, $^{\bullet}OH$, $SO_4^{\bullet-}$, and $^1O_2$ can be simultaneously produced by the chemical activation of peroxymonosulfate ($HSO_5^-$, PMS), making the process more efficient, non-selective and stable.[7-9]

PMS can be activated via multifarious metal ions like $Fe^{2+}$, $Co^{2+}$, $Ni^{2+}$, $Mn^{2+}$, $Ce^{3+}$, and $Ru^{3+}$, among which $Co^{2+}$/PMS homogeneous system proves the best performance.[10] However, the excessive metal ions in solution are toxic and may have hazardous impacts on both the environment and public health.[11] Therefore, numerous approaches have been explored in the development of heterogeneous catalysts such as metal oxides and particularly carbon-based materials as green alternatives for PMS activation.[12-19] Recently, three-dimensional (3D) porous carbons have brought out new possibilities for efficient removal of organic pollutants in effluents, because of their fascinating advantages such as a large specific surface area (SSA), acceptable cost and desirable environmental benignity.[20, 21] However, pristine carbons show limited catalytic efficiencies. In the last decades, various routes by introducing heteroatoms or metal species to the carbon system have been attempted for synthesizing functional catalysts with tailored features and enhanced properties.[22, 23] N, B, S, and P are the commonly used heteroatoms.[24] It has been pointed out that, compared with single N or S doping, dual N, S doping into plain carbons can induce a synergistic effect for more efficient catalysis.[24, 25] Besides, the earth-abundant element of cobalt can catalyze the formation of more ordered $sp^2$-hybridized carbon, which works more effectively for PMS activation compared with the inactive $sp^3$-C.[9, 26]

In this chapter, the authors first demonstrate one-pot pyrolysis of wheat flour, sodium bicarbonate, and cysteine into nitrogen and sulfur co-doped three-dimensional (3D) porous carbons. With a cobalt precursor, Co core@N-S codoped C shell nanoparticles embedded uniformly in hierarchically porous structures (Co-N-S-PCs) can be fabricated. Wheat flour is chosen as the carbon source because it is cheap, abundant and reproducible. Using sodium bicarbonate as a porogen is originally inspired by the fact that it can act as

a swelling agent in bread-making processes. Cysteine, a flour dough improver, can supply N, S atoms and there is a complexation between cobalt (II) and cysteine,[27, 28] which is beneficial for self-assembly and homogenous distribution of cobalt (II) in a molecular dimension. The resulting Co-N-S-PCs are proven to be excellent catalysts in PMS activation for complete and efficient HBA and phenol decomposition. More importantly, density functional theory (DFT) calculations were carried out to gain an insight into the active sites introduced by Co@C structure and N, S dual doping in the graphitic shells. The scalable and economic synthesis route endows these materials with numerous opportunities for large-scale production and promising application in environmental and energy catalysis.

## 7.2 Experimental Section

### *7.2.1 Chemical Reagents*

Wheat flour was provided by a local supermarket, Coles in Australia, containing starch, protein (11 wt.%) and trace sodium. Sodium bicarbonate (≥ 99.7%), L-cysteine (≥ 98.0%), cobalt nitrate hexahydrate (99.9%), peroxymonosulfate (≥ 99.0%), hydrochloric acid (36.5%), methanol (≥ 99.9%), *p*-hydroxybenzoic acid (HBA, ≥ 97.0%), phenol (99.9%), 2, 2, 6, 6-tetramethyl-4-piperidinol (TMP, 98%) and 5, 5-dimethyl-1-pyrroline N-oxide (DMPO, ≥ 97.0%) were received from Sigma-Aldrich. All the chemicals were used directly without further purification.

### *7.2.2 Sample Synthesis*

For a typical fabrication of Co-N-S-PCs, 2 g wheat flour was first added in 50 mL deionized water by magnetic stirring at 25 ºC. Then, 3 g sodium bicarbonate, and 0.3 g cysteine were fully dissolved in 80 mL of deionized water, which was mixed with the flour solution. Subsequently, 0.15 g cobalt nitrate hexahydrate dissolved in 10 mL deionized water was added to the above solution dropwisely. After drying at 80 ºC under constant stirring, the as-obtained homogeneous mixture was subjected to pyrolysis at 700, 800 and 850 ºC for 2 h, respectively, with a ramp rate of 5 °C/min under an $N_2$ flow in a tube furnace. The carbonized materials were ground to powders, followed by washing with water and ethanol, and then dried in an oven. Accordingly, the samples obtained at different temperatures were denoted as Co-N-S-PC 700, Co-N-S-PC 800 and Co-N-S-PC

850, respectively. For comparison, blank carbon was prepared by carbonization of wheat flour at 700 °C, while N-S co-doped porous carbon was obtained by the pyrolysis of flour, sodium bicarbonate and L-cysteine at 700 °C without cobalt nitrate hexahydrate (N-S-PC 700). Co-N-S-PC 700 (Acid washing) was acquired by etching Co-N-S-PC 700 with 5 wt.% HCl solution for 10 h. After that, the sample was washed alternately with water and ethanol, and finally dried in an oven.

### *7.2.3 Characterizations*

Details on XRD, $N_2$ sorption, SEM, TEM, XPS, HAADF-STEM with EDX elemental mapping measurements can refer to chapter 3 and 4. Thermogravimetric analysis (TGA) and differential thermogravimetry analysis (DTG) were conducted on a thermogravimetric analysis instrument (TGA/DSC1 STAR$^e$ system, METTLER-TOLEDO). Electron paramagnetic resonance (EPR) was performed during HBA oxidation on a Bruker EMS-plus instrument to detect the free radicals, with DMPO or TMP as a spin-trapping agent and the results were analyzed by Xeon software (Bruker).

### *7.2.4 Adsorption and AOP Procedures*

Adsorption tests were conducted at 25 °C by dispersing 10 mg of the resulting samples in 150 mL HBA or phenol solutions (20 mg $L^{-1}$), which means the loading amount of the adsorbent is 0.066 g $L^{-1}$. At certain time intervals, 1 mL of the solution was withdrawn and filtered. The concentrations of HBA or phenol were determined by an ultra-high performance liquid chromatography (UHPLC).

Typical HBA or phenol oxidation tests were also carried out at 25 °C unless otherwise mentioned. The catalyst samples (0.066 g $L^{-1}$) and peroxymonosulfate ($HSO_5^-$, PMS, 6.5 mM) were added together in HBA or phenol (20 mg $L^{-1}$) solution to initiate the reaction. After certain reaction time, 1.0 mL filtered solution was mixed instantly with 0.5 mL methanol to stop the reaction. All the experiments were repeated with reproducible results.

### *7.2.5 DFT Calculations*

Ab initio calculations have been accomplished with density functional theory (DFT) using the projected augmented wave method[29] that is implemented in the Vienna Ab initio

Simulation Package (VASP).[30-32] The exchange-correlation interaction was represented by a generalized gradient approximation in the level of the Perdew-Burke-Ernzerhof (PEB) exchange correlation function.[33] The wave functions were expressed in plane-wave basis set with an energy cutoff of 520 eV. The structural optimization was done by relaxing all atomic positions using the conjugate gradient algorithm until all forces were smaller than 0.02 eV/Å. Only the gamma point was used for sampling the Brillouin zone in the stage of geometry optimization, electron density and density of states (DOS) calculations. The vacuum box of 25Å×25Å×20Å was set to avoid the interaction between the periodic images of the graphene patch. The carbon atoms at the open ends of the graphene patch were saturated by hydrogen atoms to avoid the dangling bonds effect. To describe the long-range bonding energies, the van der Waals (vdW) corrections were introduced in this work based on the DFT-D2 Grimme's method as implemented in VASP.[34] The quantity of the charge states of C, N, S atoms in the graphene patches were calculated using the Bader charge analysis method.[35]

## 7.3 Results and Discussion

### *7.3.1 Material Characterizations*

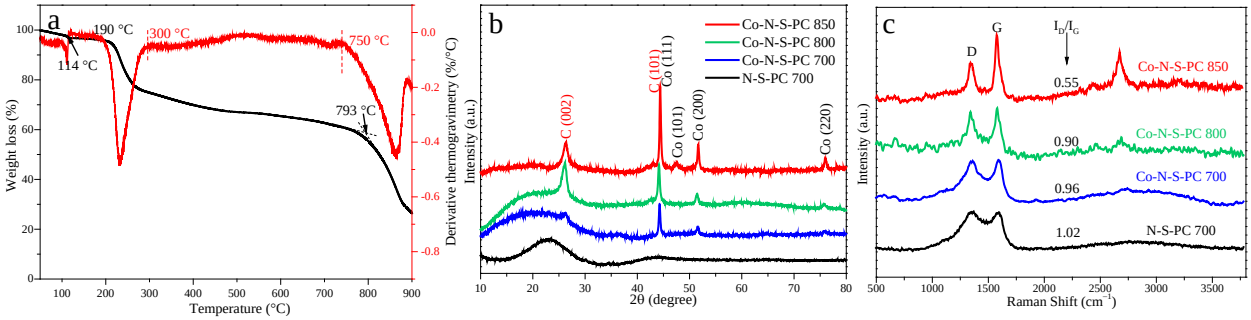


**Figure 7.1** a) TGA and DTG curves of the precursor mixture conducted in an argon atmosphere, b) XRD patterns and c) Raman spectra of the synthesized materials.

TGA and DTG curves provided in Figure 7.1a reveal the thermal decomposition of the precursor mixture to the synthesis of Co-N-S-PCs in Ar environment. The initial weight loss below 110 ºC is due to water evaporation.[36] The carbonization and decomposition of the precursors proceed in a temperature range between 190 and 300 ºC as reflected by a sharp weight loss in the curves. The thermal degradation is mild between 300 to 750 ºC.

Notably, there is a dramatic weight loss over 800 ºC, which also means the sharp reduction of sample yield.

Based on the TGA results, typical pyrolysis temperatures of 700, 800 and 850 ºC were selected to prepare Co-N-S-PC 700, Co-N-S-PC 800 and Co-N-S-PC 850, accordingly. For comparison, N-S-PC 700 was fabricated without a cobalt precursor. XRD pattern of N-S-PC 700 (Figure 7.1b) shows two broad peaks at 23º and 43º, respectively, which imply the formation of nanoscale graphitic units assembled in topological disorder.[37, 38] Superimposed upon the two broad peaks, sharp narrow peaks located at 26.2º and 44.3º start to appear in Co-N-S-PC 700, and the intensities of which increase in Co-N-S-PC 800. The two sharp peaks are assigned to the (002) and (101) planes of graphite (PDF#41-1487), respectively, indicating the development of graphitic domains on an amorphous C matrix. The broad peaks nearly disappear in Co-N-S-PC 850, which suggests the removal of amorphous carbon over 850 ºC. The cobalt species in Co-N-S-PCs accord well with the (111), (101), (200) and (220) planes of cubic cobalt (PDF#15-0806). D/G intensity ratio ($I_D/I_G$ in the Raman spectra in Figure 7.1c) of the samples decreases continuously from N-S-PC 700, Co-N-S-PC 700 to Co-N-S-PC 800, declaring increasing graphitized carbon ratio induced by cobalt catalysis at rising synthesis temperatures. Consistent with XRD results, Co-N-S-PC 850 demonstrates a significantly enhanced graphitic degree with a much lower $I_D/I_G$ ratio compared to the other samples.

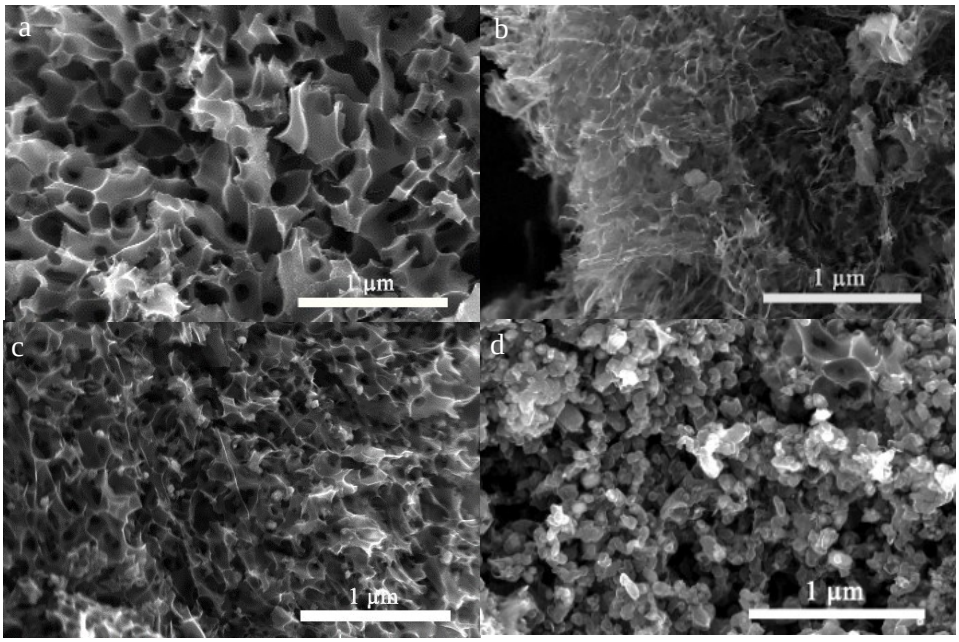

**Figure 7.2** SEM images of a) N-S-PC 700, b) Co-N-S-PC 700, c) Co-N-S-PC 800 and d) Co-N-S-PC 850.

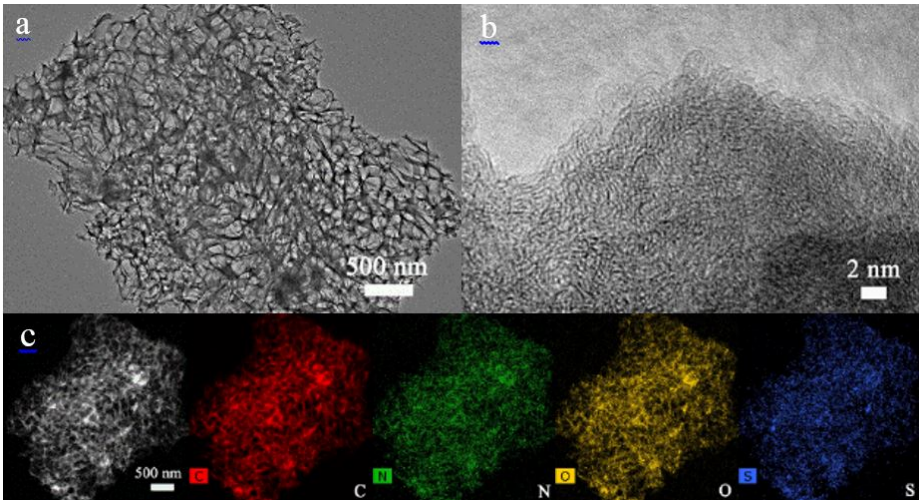


**Figure 7.3** a) TEM, b) HRTEM and c) HAADF-STEM with EDX elemental mapping images of N-S-PC 700.

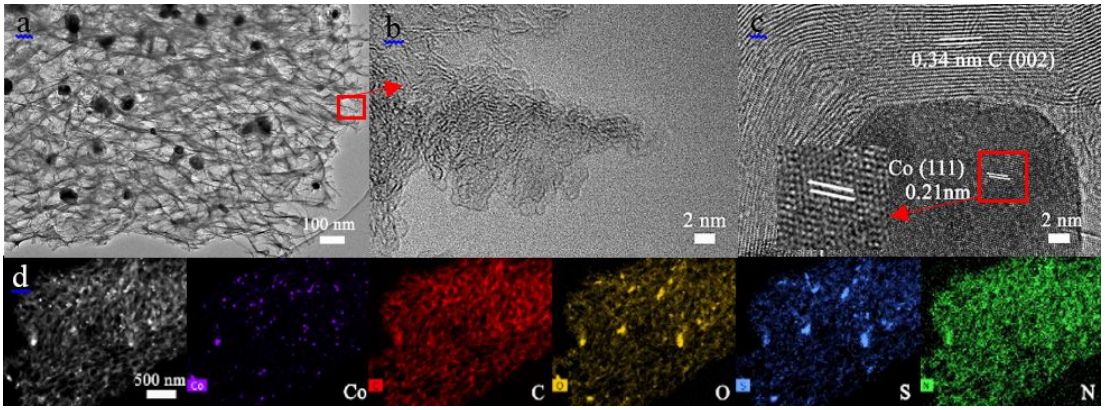


**Figure 7.4** a) TEM; b, c) HRTEM and d) HAADF-STEM with EDX elemental mapping images of Co-N-S-PC 700.

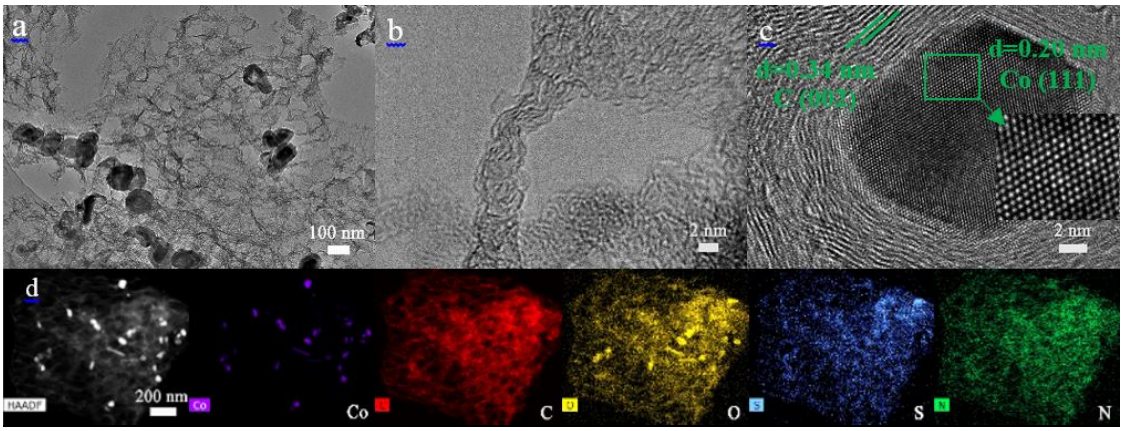

**Figure 7.5** a) TEM; b, c) HRTEM and d) HAADF-STEM with EDX elemental mapping images of Co-N-S-PC 800.

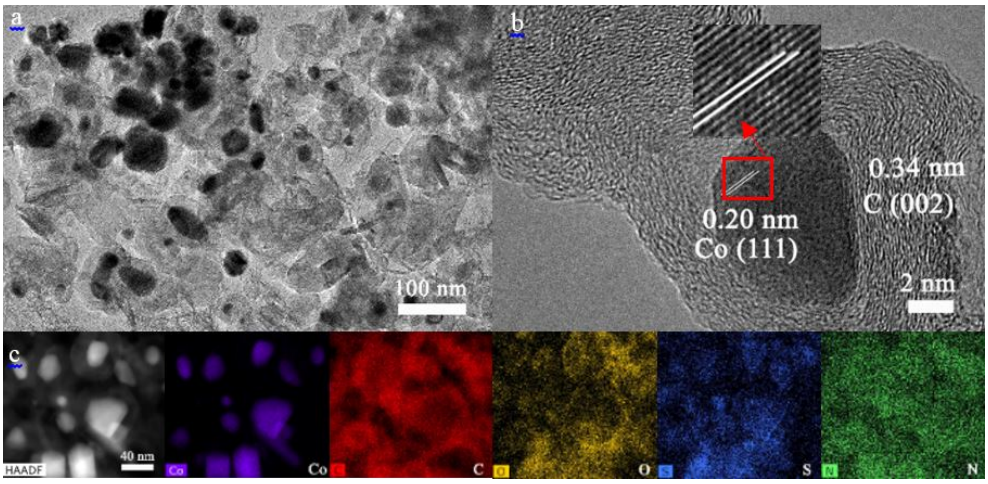


**Figure 7.6** a) TEM, b) HRTEM and c) HAADF-STEM with EDX elemental mapping images of Co-N-S-PC 850.

As indicated in chapter 6, blank carbon derived from carbonization of flour displays a nonporous morphology. In contrast, SEM and TEM images show that a hierarchically porous structure is developed on N-S-PC 700 (Figures 7.2a and 7.3a), which can be primarily attributed to the gas and water vapor released from the decomposition of cysteine and sodium bicarbonate during the pyrolysis process. SEM and TEM images of Co-N-S-PC 700 and 800 (Figures 7.2b and c, 7.4a, 7.5a) reveal 3D porous networks in which granular nanoparticles are homogenously embedded in the pores. HRTEM images of the porous carbon skeletons in N-S-PC 700, Co-N-S-PC 700 and Co-N-S-PC 800, disclose the nature of amorphous carbon constructed of scrambled graphitic layers (Figures 7.3b, 7.4b and 7.5b). HRTEM analysis indicates that the granular cobalt nanoparticles are composed of outer continuous graphitic layers with interspacing of 0.34 nm ((002) plane) and cubic Co core ((111) plane), generating a Co@C core-shell structure (Figures 7.4c, 7.5c and 7.6b). It is noticed that the 3D porous carbon matrix of Co-N-S-PC 800 is thinner than that of Co-N-S-PC 700. Figures 7.2d and 7.6a further display that Co-N-S-PC 850 mainly consists of Co@C nanoparticles. This means that the porous carbon skeletons can be gradually decomposed until completely removed at high temperatures, and thus this facile approach can be used to obtain well-dispersed Co@C nanoarchitecture. This helps explain the highest graphitization degree in Co-N-S-PC 850 as suggested by XRD and Raman data. Figure 7.3c display that C, N, O, S distribute

uniformly in N-S-PC 700. For other carbons, Co-N-S-PC 700, 800 and 850, HAADF-STEM analysis with EDX mapping images (Figures 7.4c, 7.5c and 7.6c) show the presence of C, N, O, S in both the 3D porous structure and the carbon shells in Co@C nanoparticles.

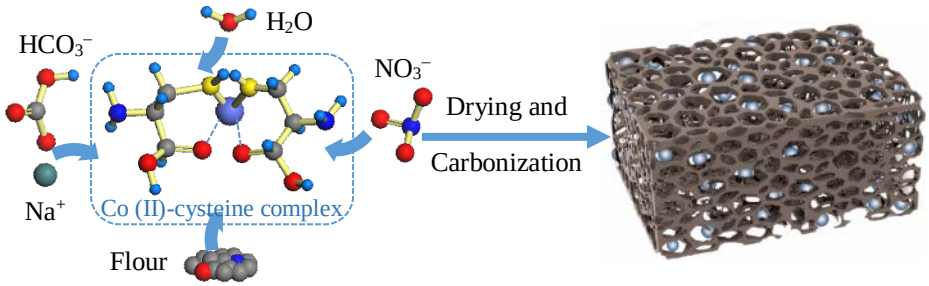


**Scheme 7.1** Formation process of Co-N-S-PCs.

The formation mechanism of the unique structure of Co-N-S-PCs is proposed in Scheme 7.1. After all the precursors are dissolved in water, the interactions of cobalt cations (II) with sulfur and carboxylate groups in cysteine will first lead to Co(II)-cysteine complexes, as evidenced by numerous studies.[27, 28] The strong hydrogen-bond or electrostatic interactions among the precursors ($Na^+$, $HCO_3^-$, flour, $NO_3^-$ and Co(II)-cysteine complexes) then facilitate uniform self-assembly during the water evaporation process. After drying and carbonization of the mixture, Co@C nanoparticles are in-situ generated in the pores of 3D porous carbon. With higher synthesis temperatures over 850 ºC, the amorphous porous carbon matrix can be removed, resulting in dispersive Co@C nanoparticles.

XPS results are summarized in Figure 7.7 and Table 7.1. The nitrogen in blank carbon originates from carbonization of proteins in the wheat flour. N-S-PC 700 and Co-N-S-PC 700 possess similar N and S doping levels. There are slight decreases of N, O and S contents from Co-N-S-PC 700 to Co-N-S-PC 850 by elevating pyrolysis temperatures. Since wheat flour contains a trace amount of sodium compounds and sodium bicarbonate was used as the porogen, all the samples have sodium residuals. Surface cobalt contents were measured to be 0.55-1.5 at.% in Co-N-S-PCs. To evaluate the weight ratio of cobalt, TGA tests of the samples were performed under air (Figure 7.7a). The thermal decomposition completed at above 650 ºC. The residual weight in N-S-PC 700 (15 wt.%) originates from sodium residuals, which was utilized to estimate cobalt content in Co-N-

S-PCs. After compensating sodium compound weight percentage, Co-N-S-PC 700, Co-N-S-PC 800 and Co-N-S-PC 850 present about 7, 11 and 33 wt.% cobalt compound contents, respectively. The residual cobalt form should be $Co_3O_4$ oxidized from Co calcinated under air. Therefore, the weight ratios of Co were further calculated to be 1.72, 2.70 and 8.09 wt.%, respectively in Co-N-S-PCs. High resolution Co 2p spectra in Co-N-S-PCs feature Co $2p_{3/2}$ at 778.1 eV and Co $2p_{1/2}$ at 793.1 eV with an energy separation of 15.0 eV, typical as metallic Co (Figure 7.7b).[39, 40] Figure 7.7c confirms that doping N atoms exist in the form of pyridinic (398 eV), pyrrolic (400 eV), quaternary (401 eV) and oxidized nitrogen (405 eV).[20, 41, 42] For S atoms (Figure 7.7d), typical thiophene-S peaks arising from the S $2p_{3/2}$ (164 eV) and S $2p_{1/2}$ (165 eV) multiplets are observed, in together with oxidizing $SO_x$ centered at around 168 and 170 eV.[20, 40]

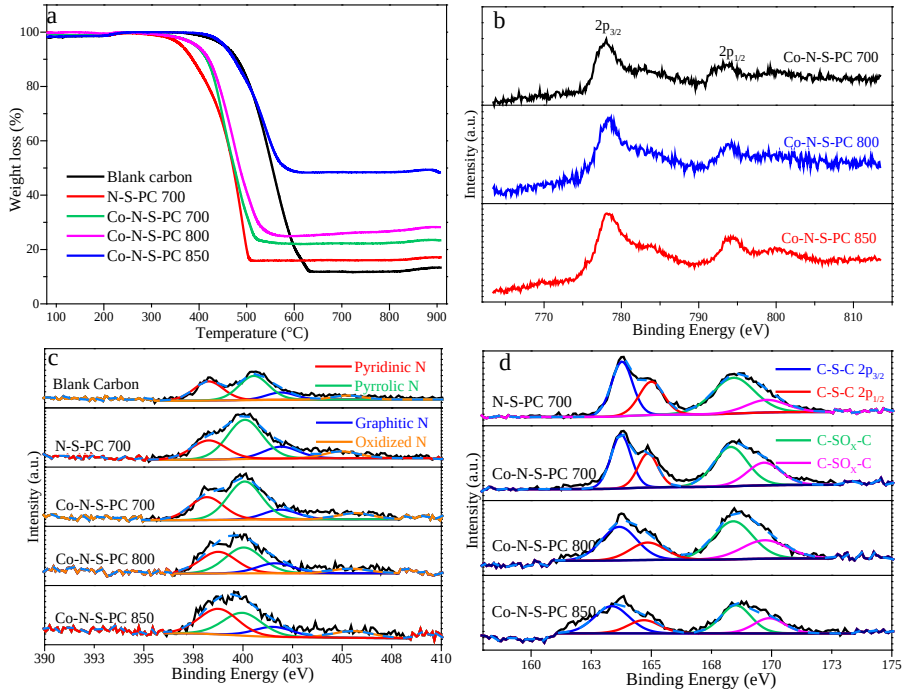


**Figure 7.7** a) TGA tests of the samples conducted in air. XPS core level spectra of b) Co 2p, c) N 1s and d) S 2p.

It is noticeable that $N_2$ sorption behaviors on samples vary due to different precursors and synthesis temperatures (See Table 7.1 and Figure 7.8). The type I isotherm of N-S-PC 700 with saturation in high-pressure range reveals that the material contains a large fraction of micropores.[38] Co-N-S-PCs display type IV isotherms with the capillary condensation steps, suggesting the well-developed mesoporosity after cobalt introduction. The pore size

distribution curve indicates that N-S-PC 700 has a hierarchically porous structure with micropores and mesopores. Apart from micropores and mesopores, a small amount of macropores were also developed in Co-N-S-PCs.

**Table 7.1** Chemical compositions and textural properties of the samples.

| | C/ at.% | N/ at.% | O/ at.% | S/ at.% | Na/ at.% | Co/ at.% | Co/ wt.% | SSA[a] / $m^2 g^{-1}$ | $V_t$ [b] / $cm^3 g^{-1}$ | $V_{mic}$ [c] / $cm^3 g^{-1}$ |
|---|---|---|---|---|---|---|---|---|---|---|
| **Blank carbon** | 90.05 | 1.99 | 7.78 | - | 0.18 | - | - | 5 | 0.005 | - |
| **N-S-PC 700** | 88.80 | 1.60 | 8.46 | 0.42 | 0.72 | - | - | 332 | 0.25 | 0.12 |
| **Co-N-S-PC 700** | 87.39 | 1.89 | 9.03 | 0.52 | 0.43 | 0.74 | 1.72 | 505 | 0.42 | 0.20 |
| **Co-N-S-PC 800** | 92.29 | 1.17 | 5.51 | 0.34 | 0.14 | 0.55 | 2.70 | 734 | 0.58 | 0.21 |
| **Co-N-S-PC 850** | 91.64 | 0.91 | 5.39 | 0.29 | 0.27 | 1.50 | 8.09 | 379 | 0.50 | 0.049 |

[a] Specific surface area calculated by the BET method.
[b] Total pore volume at $P/P_0 = 0.99$.
[c] Micropore volume calculated using the t-plot method.

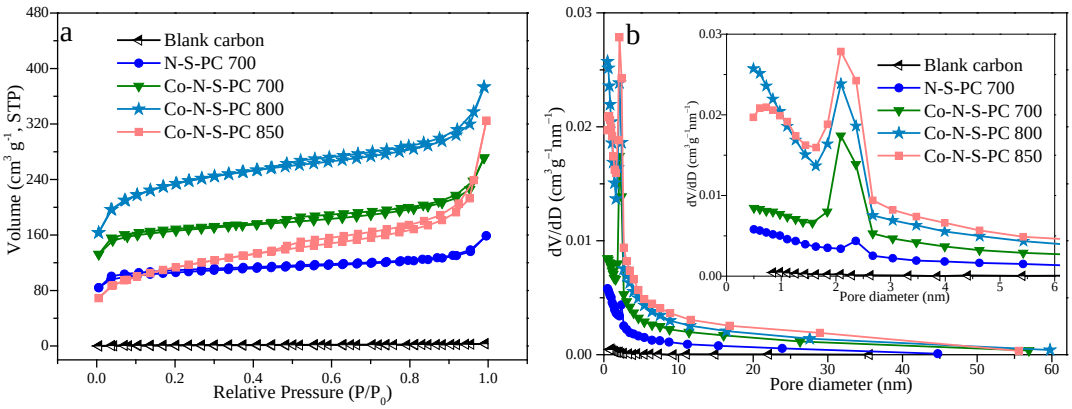


**Figure 7.8** a) $N_2$ sorption isotherms and b) BJH pore size distributions of the as-synthesized catalysts.

N-S-PC has an SSA of 332 $m^2 g^{-1}$, in contrast to blank carbon (5 $m^2 g^{-1}$). This result proves that sodium bicarbonate and cysteine are crucial in forming the large porosity in these systems. Co-N-S-PC 700 has a 1.5-time-larger SSA than N-S-PC 700, which seems to be originated from a better cooperative interaction among all precursors promoted by cobalt ions in the self-assembly process, as described in Scheme 7.1. The maximal SSA and pore volume are recorded on Co-N-S-PC 800, while there is a drastic decline of micropore volume and SSA in Co-N-S-PC 850.

*7.3.2 Environmental Application of the Synthesized Materials for HBA and Phenol Removal*

With N, S co-doping and Co@C nanoparticles in hierarchical porous structure, the developed Co-N-S-PCs are very appealing for adsorption and catalysis. As an example, they were used as catalysts for PMS activation in AOPs at a low catalyst loading of 0.066 g $L^{-1}$. Since adsorption is usually occurring along with AOPs, the adsorptive ability was also evaluated (Figure 7.9a). Co-N-S-PC 800 showed the highest HBA adsorption (17%) due to the highest SSA, whereas the adsorption on other materials was less than 10%. For AOPs, PMS alone generated trace degradation of HBA. With N-S-PC 700/PMS in the solution, HBA removal reached 60% degradation in 150 min. In contrast, complete HBA removal was achieved in 60 min for Co-N-S-PC 700/PMS, while 45 min for both Co-N-S-PC 800/PMS and Co-N-S-PC 850/PMS. It is therefore concluded that Co@C nanoparticles play a key role in efficient HBA removal. Ascribed to incremental proportion of Co@C structure in the samples, the reaction rate constants (k) of N-S-PC 700, Co-N-S-PC 700, Co-N-S-PC 800 and Co-N-S-PC 850 show an increasing trend, which were estimated to be 0.0047, 0.058, 0.068 and 0.11 $min^{-1}$, respectively, by the first-order kinetic model, as presented in Chapter 3.[43] The reaction efficiency in Co-N-S-PC 700/PMS system was elevated by about 12 times compared with N-S-PC 700/PMS in HBA oxidation.

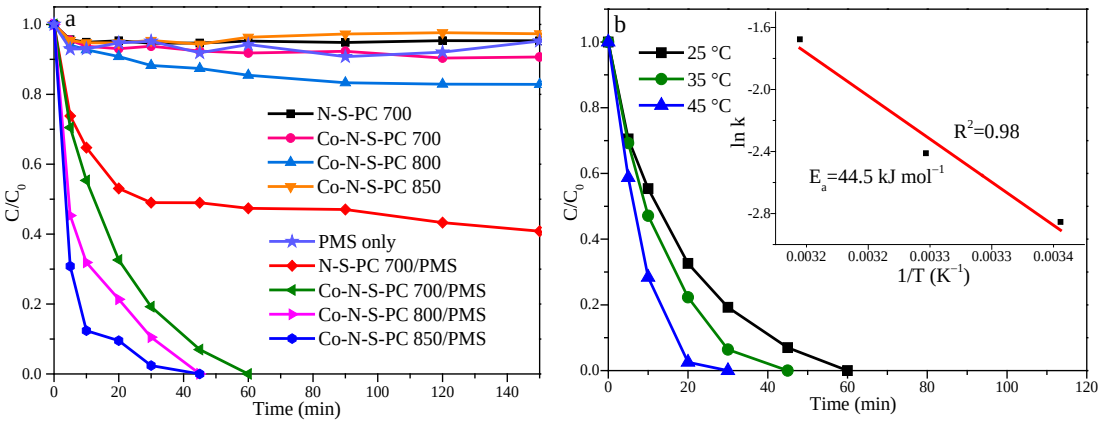


**Figure 7.9** a) HBA removal by adsorption and AOPs, b) the influence of different reaction temperatures on HBA degradation for Co-N-S-PC 700/PMS.

Given that the production yield of Co-N-S-PCs decreases with rising temperatures especially at 850 ºC as perceived from Figure 7.1a, Co-N-S-PC 700 is more suitable for large-scale production with comparable catalytic performance to Co-N-S-PC 800 and Co-N-S-PC 850. Figure 7.9b exhibits that a higher reaction solution temperature leads to a higher HBA oxidation efficiency. Compared to 60 min degradation time at 25 ºC, HBA removal completed in 45 min at 35 ºC while 30 min at 45 ºC by Co-N-S-PC 700/PMS. With rising temperatures, the rate constants increase steadily from 0.058, 0.090 to 0.19 $min^{-1}$. Based on the Arrhenius correlation, the activation energy ($E_a$) of Co-N-S-PC 700 for the catalytic HBA degradation is calculated to be 44.5 kJ $mol^{-1}$. Figure 7.10a shows the performance of recycled Co-N-S-PC 700 in HBA degradation. A deactivation occurred in the catalytic performance in the second run, yet 98% of HBA could still be removed in 120 min by the catalyst and about 76% of HBA was degraded in the third use. No obvious changes in the structure of Co-N-S-PC 700 were observed in SEM images before and after the third use (Figure 7.11a, b). However, STEM analysis (Figure 7.11c) indicated that the contents of N and S elements decreased obviously in the sample after the third run. XPS was conducted on Co-N-S-PC 700 after third-run, which proved an increased O content and decreased N and S contents (Figure 7.12). This is understandable considering the strong oxidation environment in AOPs. Combined with our previous study, it is deduced that the changes in surface chemistry and coverage of intermediates on the catalyst surface are accountable for the deteriorating performance in recycling tests.[26, 44] Stability tests were also carried out on Co-N-S-PC 800/PMS and Co-N-S-PC 850/PMS (Figure 7.10b and c), which provided 100% degradation on HBA in the second run, while 58% and 52% HBA removal in 120 min in the third run, respectively.

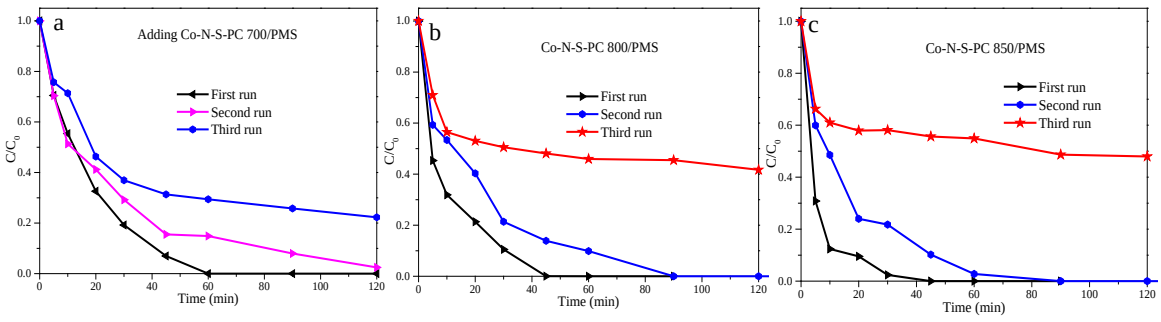


**Figure 7.10** Stability tests of Co-N-S-PCs (catalyst 0.066 g $L^{-1}$, PMS 6.5 mM, T 25 ºC).

Not only effective for HBA removal, but Co-N-S-PCs also displayed a highly efficient catalytic activity in degradation of other organic pollutants such as phenol solution. Figure 7.13 shows that Co-N-S-PCs provided about 40% of phenol adsorption. Co-N-S-PC 700 and 800 achieved 100% phenol degradation in 1 h, compared to complete degradation in 10 min by Co-N-S-PC 850/PMS.

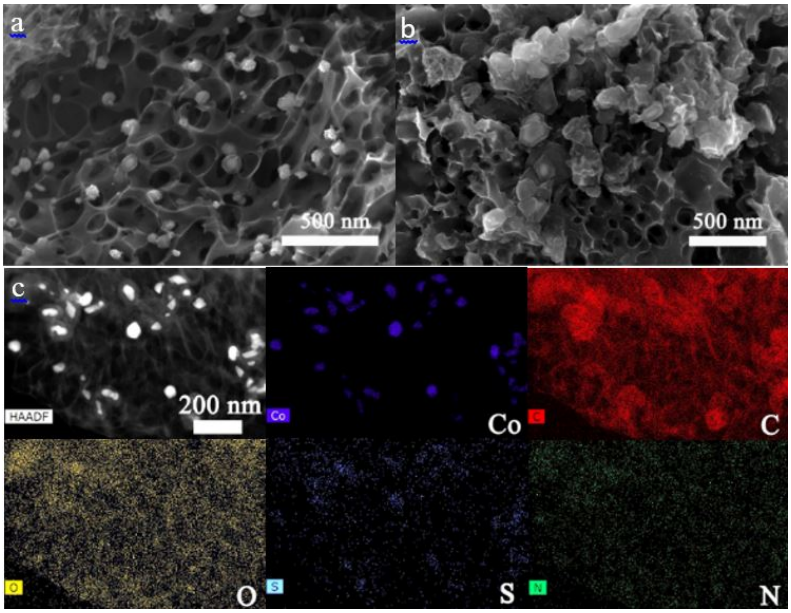


**Figure 7.11** SEM images of Co-N-S-PC 700: a) before and b) after third-run cycling test. c) HAADF-STEM with EDX elemental mapping images of Co-N-S-PC 700 after third-run cycling test.

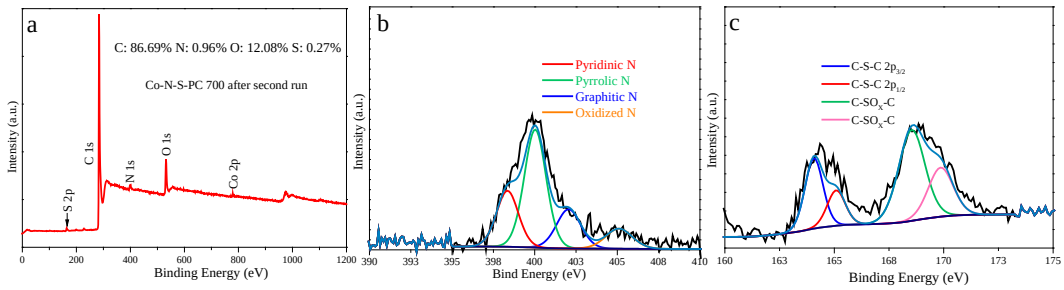


**Figure 7.12** a) XPS survey and high resolution spectra of b) N 1s, c) S 2p for Co-N-S-PC 700 after third-run.

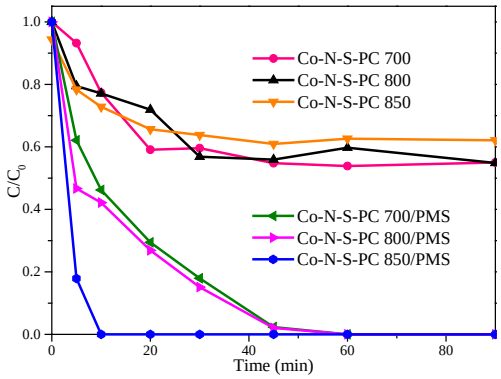


**Figure 7.13** Adsorption and AOPs of phenol solution (20 mg $L^{-1}$) by adding Co-N-S-PCs (catalyst 0.066 g $L^{-1}$, PMS 6.5 mM, T 25 ºC).

*7.3.3 Mechanism Study in AOPs*

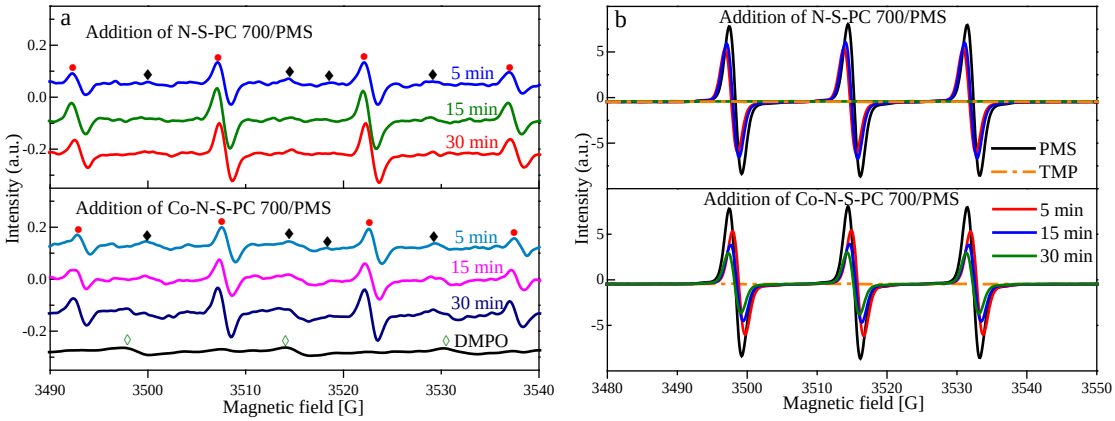


**Figure 7.14** a) EPR tests on ˙OH and $SO_4^{\bullet-}$ during HBA degradation (DMPO-˙OH-●; DMPO-$SO_4^{\bullet-}$-♦; DMPOX-◊), and b) EPR measurements for $^1O_2$ during HBA degradation.

As discussed before, AOPs are based on the generation of highly reactive radicals. As a strong oxidant, hydroxyl (˙OH) radical is able to react almost non-selectively with most organic pollutants.[45] Compared to ˙OH, sulfate ($SO_4^{\bullet-}$) radical reacts more efficiently and selectively with organic compounds with a longer half-life period.[5] In addition, our group recently proved that $^1O_2$ contributed significantly to the catalytic degradation of phenolic compounds.[7, 43] To elucidate the various catalytic processes in N-S-PC 700/PMS and Co-N-S-PC 700/PMS, EPR technique was adopted to inspect the radical generation and evolution during HBA degradation. DMPO is effective to capture signals of ˙OH and $SO_4^{\bullet-}$ and the results are provided in Figure 7.14a. Both N-S-PC 700/PMS and Co-N-S-PC 700/PMS produced a mass of ˙OH throughout 30 min reaction time. $SO_4^{\bullet-}$

signals were also detected in both systems and the intensities slightly dropped from 5 to 30 min reaction time due to the potential consumption by AOPs. Despite little difference in terms of $^{\bullet}OH$ and $SO_4^{\bullet-}$, a clear distinction in singlet oxygen ($^1O_2$) activation was observed between the two systems (Figure 7.14b). Utilizing TMP as the trapping agent, three typical lines with equal intensities can be detected for $^1O_2$. It was reported that $^1O_2$ could be produced by the self-decomposition of PMS at a low rate.[46] In N-S-PC 700/PMS system, the intensity of $^1O_2$ declined and went to zero in 30 min consumed by the reactive degradation of HBA, implying that N-S-PC 700 is inactive to activate PMS in continuous $^1O_2$ production. In contrast, there were strong $^1O_2$ signals after adding Co-N-S-PC 700/PMS into HBA solution even after 30 min reaction. Therefore, it is reasonable to assert that Co@C nanoparticles in Co-N-S-PCs promote PMS activation to produce $^1O_2$ radicals, which work together with $^{\bullet}OH$ and $SO_4^{\bullet-}$ for the efficient decomposition of HBA.

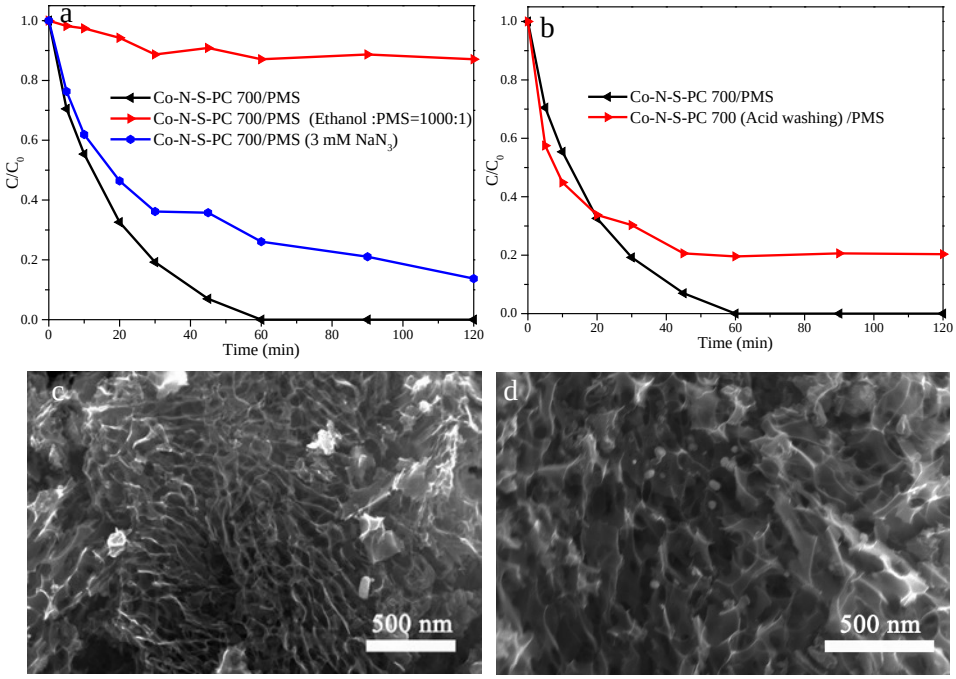


**Figure 7.15** a) Influence of various quenching agents on HBA degradation by Co-N-S-PC 700/PMS. b) HBA degradation comparison of Co-N-S-PC 700 before and after acid washing. (Catalyst 0.066 g $L^{-1}$, PMS 6.5 mM, T 25 $^{o}$C) c, d) SEM images of Co-N-S-PC 700 after 5 wt.% HCl washing.

To probe the roles of $^{\bullet}OH$, $SO_4^{\bullet-}$ and $^1O_2$ in HBA degradation by Co-N-S-PC 700/PMS, quenching experiments were further carried out (Figure 7.15a). Ethanol (Ethanol: PMS =

1000 : 1) was chosen to quench $^{\bullet}OH$ and $SO_4^{\bullet-}$ while $NaN_3$ (3 mM) was adopted as the scavengers for $^1O_2$. The concentration of quenching agents was determined according to our recent study.[7] Both ethanol and $NaN_3$ quenching affected the degradation efficiency obviously, proving that $^{\bullet}OH$, $SO_4^{\bullet-}$ and $^1O_2$ work together for effective HBA decomposition.

The better catalytic activity of Co-N-S-PC 700 promoted by Co@C nanoparticles may originate from three characteristics: (i) the graphitic carbon shell contains a high ratio of $sp^2$-C, which is more active than $sp^3$-C for PMS activation;[9, 26] (ii) N and S co-doping can exert a synergistic effect and make a further enhancement in the catalytic activity of the carbon shells. This is owing to the more active sites after N and S codoping and the redistribution of spin and charge densities of C;[24, 47] (iii) encapsulated cobalt nanoparticles might facilitate the catalysis by altering the electron densities of C in the external carbon shells. To inspect the role of cobalt in catalysis, Co-N-S-PC 700 (Acid washing) was prepared and tested for HBA degradation (Figure 7.15b). Although SEM characterization (Figure 7.15c, d) indicates that Co was not fully removed by acid washing due to the protection of the outer carbon shells, the catalytic performance in HBA removal was impaired obviously. Only 80% of HBA was removed in 120 min. This result suggests that the Co cores in Co@C nanoparticles are essential for efficient AOPs.

### *7.3.4 DFT Calculations*

DFT calculations were adopted to better understand the nature of active sites induced by N, S codoped Co@C nanoparticles. Since the carbon layers covering cobalt cores have been proven to be graphitic layers, three models were constructed in Figure 7.16 including graphene patch (designated as G), $Co_4$ cluster on graphene patch ($Co_4$@G) and $Co_4$ cluster on N, S codoped graphene patch ($Co_4$@N-S-G).

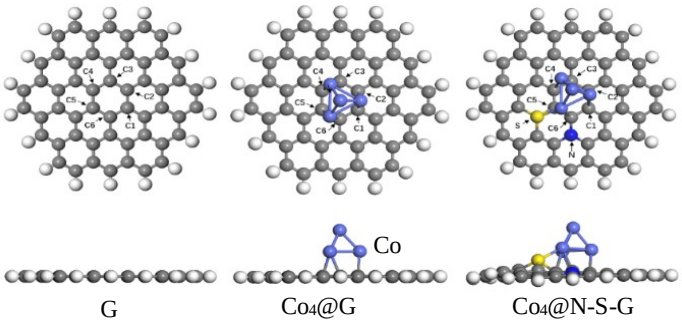

**Figure 7.16** Optimized structure model of G, $Co_4$@G and $Co_4$@N-S-G in DFT calculations.

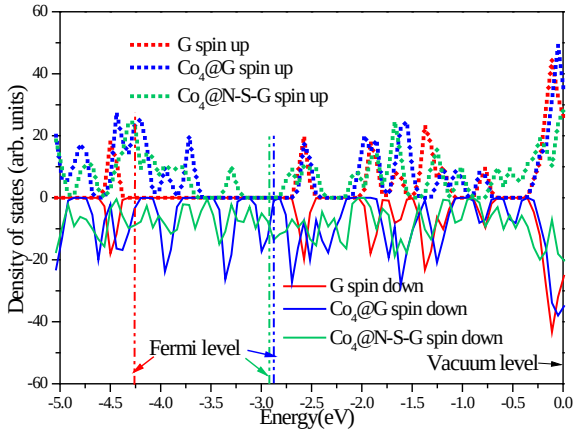


**Figure 7.17** The calculated total density of states (TDOS) in three models with the vacuum level aligned at 0 eV.

**Table 7.2** The calculated charge states of C, N and S atoms in different systems.

| Atom number | G | $Co_4$@G | $Co_4$@N-S-G |
|---|---|---|---|
| **C1** | -0.03 | -0.08 | -0.20 |
| **C2** | +0.04 | -0.04 | +0.05 |
| **C3** | -0.01 | -0.08 | -0.14 |
| **C4** | -0.02 | -0.03 | -0.09 |
| **C5** | 0.00 | -0.07 | -0.21 |
| **C6** | +0.01 | -0.06 | +0.25 |
| **N** | -- | -- | -1.13 |
| **S** | -- | -- | -1.66 |

The total density of states (TDOS) of C atoms in three models are presented in Figure 7.17. Co-C interaction and the dual doping of N and S introduce asymmetrical TDOS in the spin up and down modes. Apparently, the density of states increase significantly in the energy range of 4.3 to 2.0 eV, suggesting an elevated catalytic activity.[24] Promoted by electron transfer from $Co_4$ cluster to C as verified by C1-C6 atoms in Table 7.2, the Fermi level of the system advances by 1.39 eV towards the vacuum level in $Co_4$@G, while 1.36 eV in $Co_4$@N-S-G compared with G. This change decreases the local work function and increases chemical activity of the functionalized region in graphene.[23] After N, S doping, the spin down TDOS near the Fermi level in $Co_4$@N-S-G is higher than that in

$Co_4$@G system, which is expected to further elevate the catalytic reactivity of carbon in the doped area. Figure 7.18a illustrates the charge redistribution caused by Co-C interaction and N, S atom co-doping. The charge accumulates between C and Co atoms in $Co_4$@G model, which means the strong interaction between them. After N, S doping, charge accumulation between S and Co atoms turns stronger. Table 7.2 provides the charge states of several typical atoms in the three systems. Single Co-C interaction leads to the decreased charge states in C1-C6 atoms while after N, S dual-doping, the charge states in the adjacent C2 and C6 atoms are positively increased, which can serve as catalytic active sites.[24] It is believed that the positively charged C atoms and the modified chemical reactivity by introducing Co@N, S codoped C promote the adsorption and activation of PMS to generate effective radicals including $^1O_2$, $^{\bullet}OH$, and $SO_4^{\bullet-}$, leading to considerably enhanced HBA degradation, as depicted in Figure 7.18b.

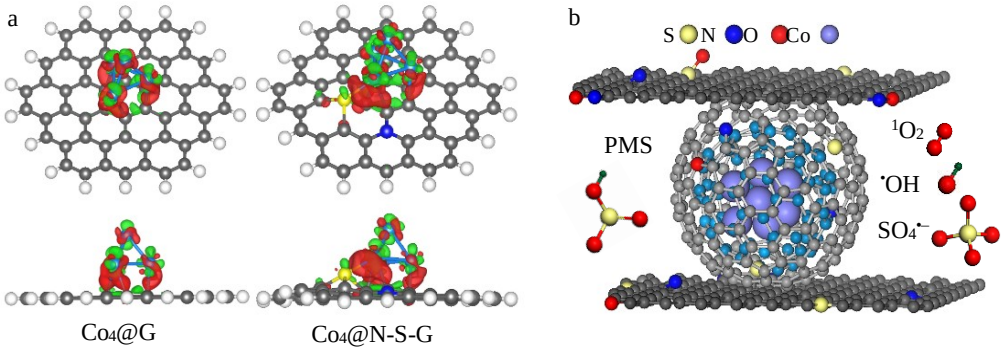


**Figure 7.18** a) The different charge densities in $Co_4$@G and $Co_4$@N-S-G. The green regions illustrate charge depletion while red regions indicate charge accumulation. The isovalue = 0.006 e/Å$^3$. b) A schematic illustration for the AOPs in Co-N-S-PCs/PMS system.

## 7.4 Conclusions

A template-free, bread-making inspired strategy was applied to assemble N, S co-doped core-shell Co@C nanoparticles into hierarchical porous carbons. The porous carbon matrix can be removed to obtain evenly-distributed porous Co@C nanostructure in Co-N-S-PC 850. The Co-N-S-PCs exhibit an excellent activity in PMS activation for HBA and phenol oxidation. Compared with N-S-PC 700/PMS, the reaction rate in HBA degradation by Co-N-S-PC 700/PMS is enhanced by about 12 times. Co@C nanoparticles facilitate generation of $^1O_2$ in AOPs, which works together with $^{\bullet}OH$ and $SO_4^{\bullet-}$ in efficient decomposition of HBA by Co-N-S-PCs. DFT calculations prove that Co-C interaction

improves the Fermi level and chemical activity of the functionalized C atoms. With the synergistic effect of Co-C interaction and N, S co-doping, the charge states of some C atoms are positively elevated to act as active sites for catalysis. Considering the diversity of carbon sources and non-precious metal species, the proposed method may offer a facile method to design hierarchical nanostructures with enhanced performance in environment and energy related catalysis.

## References


[1] M.A. Shannon, P.W. Bohn, M. Elimelech, J.G. Georgiadis, B.J. Marinas, A.M. Mayes, Science and Technology for Water Purification in the Coming Decades, Nature, 452 (2008) 301.

[2] F.J. Rivas, F.J. Beltrán, J. Frades, P. Buxeda, Oxidation of P-Hydroxybenzoic Acid by Fenton's Reagent, Water Research, 35 (2001) 387.

[3] J. Beltran-Heredia, J. Torregrosa, J.R. Dominguez, J.A. Peres, Comparison of the Degradation of P-Hydroxybenzoic Acid in Aqueous Solution by Several Oxidation Processes, Chemosphere, 42 (2001) 351.

[4] K.E. O'Shea, D.D. Dionysiou, Advanced Oxidation Processes for Water Treatment, Journal of Physical Chemistry Letters, 3 (2012) 2112.

[5] P.D. Hu, M.C. Long, Cobalt-Catalyzed Sulfate Radical-Based Advanced Oxidation: A Review on Heterogeneous Catalysts and Applications, Applied Catalysis B-Environmental, 181 (2016) 103.

[6] W.H. Glaze, J.-W. Kang, D.H. Chapin, The Chemistry of Water Treatment Processes Involving Ozone, Hydrogen Peroxide and Ultraviolet Radiation, Ozone: Science & Engineering, 9 (1987) 335.

[7] P. Liang, C. Zhang, X. Duan, H. Sun, S. Liu, M.O. Tade, S. Wang, An Insight into Metal Organic Framework Derived N-Doped Graphene for the Oxidative Degradation of Persistent Contaminants: Formation Mechanism and Generation of Singlet Oxygen from Peroxymonosulfate, Environmental Science: Nano, 4 (2017) 315.

[8] E. Saputra, S. Muhammad, H. Sun, H.-M. Ang, M.O. Tadé, S. Wang, Shape-Controlled Activation of Peroxymonosulfate by Single Crystal A-$Mn_2O_3$ for Catalytic Phenol Degradation in Aqueous Solution, Applied Catalysis B: Environmental, 154–155 (2014) 246.

[9] H.Q. Sun, S.Z. Liu, G.L. Zhou, H.M. Ang, M.O. Tade, S.B. Wang, Reduced Graphene Oxide for Catalytic Oxidation of Aqueous Organic Pollutants, ACS Applied Materials & Interfaces, 4 (2012) 5466.

[10] G.P. Anipsitakis, D.D. Dionysiou, Radical Generation by the Interaction of Transition Metals with Common Oxidants, Environmental Science & Technology, 38 (2004) 3705.

[11] X.B. Wang, Y.L. Qin, L.H. Zhu, H.Q. Tang, Nitrogen-Doped Reduced Graphene Oxide as a Bifunctional Material for Removing Bisphenols: Synergistic Effect between Adsorption and Catalysis, Environmental Science & Technology, 49 (2015) 6855.

[12] T.K. Lau, W. Chu, N.J.D. Graham, The Aqueous Degradation of Butylated Hydroxyanisole by Uv/S2o82-: Study of Reaction Mechanisms Via Dimerization and Mineralization, Environmental Science & Technology, 41 (2007) 613.

[13] R.H. Waldemer, P.G. Tratnyek, R.L. Johnson, J.T. Nurmi, Oxidation of Chlorinated Ethenes by Heat-Activated Persulfate: Kinetics and Products, Environmental Science & Technology, 41 (2007) 1010.

[14] S. Indrawirawan, H. Sun, X. Duan, S. Wang, Nanocarbons in Different Structural Dimensions (0-3D) for Phenol Adsorption and Metal-Free Catalytic Oxidation, Applied Catalysis B: Environmental, 179 (2015) 352.

[15] S. Indrawirawan, H. Sun, X. Duan, S. Wang, Low Temperature Combustion Synthesis of Nitrogen-Doped Graphene for Metal-Free Catalytic Oxidation, Journal of Materials Chemistry A, 3 (2015) 3432.

[16] G. Li, Y. Lu, C. Lu, M. Zhu, C. Zhai, Y. Du, P. Yang, Efficient Catalytic Ozonation of Bisphenol-A over Reduced Graphene Oxide Modified Sea Urchin-Like α-$MnO_2$ Architectures, Journal of Hazardous Materials, 294 (2015) 201.

[17] L. Duan, X. Zhou, S. Liu, P. Shi, W. Yao, 3D-Hierarchically Structured $Co_3O_4$/Graphene Hydrogel for Catalytic Oxidation of Orange II Solutions by Activation of Peroxymonosulfate, Journal of the Taiwan Institute of Chemical Engineers, 76 (2017) 101.

[18] G. Li, K. Li, A. Liu, P. Yang, Y. Du, M. Zhu, 3D Flower-Like β-$MnO_2$/Reduced Graphene Oxide Nanocomposites for Catalytic Ozonation of Dichloroacetic Acid, 7 (2017) 43643.

[19] Y. Liu, X. Liu, Y. Zhao, D.D. Dionysiou, Aligned A-Feooh Nanorods Anchored on a Graphene Oxide-Carbon Nanotubes Aerogel Can Serve as an Effective Fenton-Like Oxidation Catalyst, Applied Catalysis B: Environmental, 213 (2017) 74.

[20] W.J. Tian, H.Y. Zhang, X.G. Duan, H.Q. Sun, M.O. Tade, H.M. Ang, S.B. Wang, Nitrogen- and Sulfur-Codoped Hierarchically Porous Carbon for Adsorptive and Oxidative Removal of Pharmaceutical Contaminants, ACS Applied Materials & Interfaces, 8 (2016) 7184.

[21] C.Z. Zhu, H. Li, S.F. Fu, D. Du, Y.H. Lin, Highly Efficient Nonprecious Metal Catalysts Towards Oxygen Reduction Reaction Based on Three-Dimensional Porous Carbon Nanostructures, Chemical Society Reviews, 45 (2016) 517.

[22] W. Xia, R.Q. Zou, L. An, D.G. Xia, S.J. Guo, A Metal-Organic Framework Route to in Situ Encapsulation of Co@$Co_3O_4$@C Core@Bishell Nanoparticles into a Highly Ordered Porous Carbon Matrix for Oxygen Reduction, Energy & Environmental Science, 8 (2015) 568.

[23] D.H. Deng, L. Yu, X.Q. Chen, G.X. Wang, L. Jin, X.L. Pan, J. Deng, G.Q. Sun, X.H. Bao, Iron Encapsulated within Pod-Like Carbon Nanotubes for Oxygen Reduction Reaction, Angewandte Chemie-International Edition, 52 (2013) 371.

[24] J. Liang, Y. Jiao, M. Jaroniec, S.Z. Qiao, Sulfur and Nitrogen Dual-Doped Mesoporous Graphene Electrocatalyst for Oxygen Reduction with Synergistically Enhanced Performance, Angewandte Chemie-International Edition, 51 (2012) 11496.

[25] Z.S. Wu, A. Winter, L. Chen, Y. Sun, A. Turchanin, X.L. Feng, K. Mullen, Three-Dimensional Nitrogen and Boron Co-Doped Graphene for High-Performance All-Solid-State Supercapacitors, Advanced Materials, 24 (2012) 5130.

[26] H.Q. Sun, Y.X. Wang, S.Z. Liu, L. Ge, L. Wang, Z.H. Zhu, S.B. Wang, Facile Synthesis of Nitrogen Doped Reduced Graphene Oxide as a Superior Metal-Free Catalyst for Oxidation, Chemical Communications, 49 (2013) 9914.

[27] C. Bresson, C. Colin, F. Chartier, C. Moulin, Cobalt Speciation Study in the Cobalt-Cysteine System by Electrospray Ionization Mass Spectrometry and Anion-Exchange Chromatography Inductively Coupled Plasma Atomic Emission Spectrometry, Applied Spectroscopy, 59 (2005) 696.

[28] W. Buchmann, R. Spezia, G. Tournois, T. Cartailler, J. Tortajada, Structures and Fragmentations of Cobalt(II)-Cysteine Complexes in the Gas Phase, Journal of Mass Spectrometry, 42 (2007) 517.

[29] P.E. Blochl, Projector Augmented-Wave Method, Physical Review B, 50 (1994) 17953.

[30] G. Kresse, J. Hafner, Ab-Initio Molecular-Dynamics Simulation of the Liquid-Metal Amorphous-Semiconductor Transition in Germanium, Physical Review B, 49 (1994) 14251.
[31] G. Kresse, Ab-Initio Molecular-Dynamics for Liquid-Metals, Journal of Non-Crystalline Solids, 193 (1995) 222.
[32] G. Kresse, J. Furthmuller, Efficient Iterative Schemes for Ab Initio Total-Energy Calculations Using a Plane-Wave Basis Set, Physical Review B, 54 (1996) 11169.
[33] J.P. Perdew, K. Burke, M. Ernzerhof, Generalized Gradient Approximation Made Simple, Physical Review Letters, 77 (1996) 3865.
[34] S. Grimme, Semiempirical Gga-Type Density Functional Constructed with a Long-Range Dispersion Correction, Journal of Computational Chemistry, 27 (2006) 1787.
[35] R.F.W. Bader, Atoms in Molecules: A Quantum Theory, Clarendon Press1994.
[36] R. Sharma, K.K. Kar, Effects of Structural Disorder and Nitrogen Content on the Oxygen Reduction Activity of Polyvinylpyrrolidone-Derived Multi-Doped Carbon, Journal of Materials Chemistry A, 3 (2015) 11948.
[37] G.A. Ferrero, A.B. Fuertes, M. Sevilla, N-Doped Porous Carbon Capsules with Tunable Porosity for High-Performance Supercapacitors, Journal of Materials Chemistry A, 3 (2015) 2914.
[38] D. Puthusseri, V. Aravindan, S. Madhavi, S. Ogale, 3D Micro-Porous Conducting Carbon Beehive by Single Step Polymer Carbonization for High Performance Supercapacitors: The Magic of in Situ Porogen Formation, Energy & Environmental Science, 7 (2014) 728.
[39] Y.Y. Li, F.Y. Cheng, J.N. Zhang, Z.M. Chen, Q. Xu, S.J. Guo, Cobalt-Carbon Core-Shell Nanoparticles Aligned on Wrinkle of N-Doped Carbon Nanosheets with Pt-Like Activity for Oxygen Reduction, Small, 12 (2016) 2839.
[40] J.F. Moulder, J. Chastain, Handbook of X-Ray Photoelectron Spectroscopy: A Reference Book of Standard Spectra for Identification and Interpretation of XPS Data, Physical Electronics Division, Perkin-Elmer Corporation 1992.
[41] W. Tian, H. Zhang, H. Sun, M.O. Tadé, S. Wang, Template-Free Synthesis of N-Doped Carbon with Pillared-Layered Pores as Bifunctional Materials for Supercapacitor and Environmental Applications, Carbon, 118 (2017) 98.
[42] W. Tian, H. Zhang, H. Sun, A. Suvorova, M. Saunders, M. Tade, S. Wang, Heteroatom (N or N-S)-Doping Induced Layered and Honeycomb Microstructures of

Porous Carbons for $CO_2$ Capture and Energy Applications, Advanced Functional Materials, 26 (2016) 8651.
[43] C. Wang, J. Kang, P. Liang, H. Zhang, H. Sun, M.O. Tade, S. Wang, Ferric Carbide Nanocrystals Encapsulated in Nitrogen-Doped Carbon Nanotubes as an Outstanding Environmental Catalyst, Environmental Science: Nano, 4 (2017) 170.
[44] H. Sun, S. Liu, G. Zhou, H.M. Ang, M.O. Tadé, S. Wang, Reduced Graphene Oxide for Catalytic Oxidation of Aqueous Organic Pollutants, ACS Applied Materials & Interfaces, 4 (2012) 5466.
[45] F.C. Moreira, R.A.R. Boaventura, E. Brillas, V.J.P. Vilar, Electrochemical Advanced Oxidation Processes: A Review on Their Application to Synthetic and Real Wastewaters, Applied Catalysis B-Environmental, 202 (2017) 217.
[46] D.F. Evans, M.W. Upton, Studies on Singlet Oxygen in Aqueous-Solution. Part 3. The Decomposition of Peroxy-Acids, Journal of the Chemical Society-Dalton Transactions, (1985) 1151.
[47] S.A. Wohlgemuth, R.J. White, M.G. Willinger, M.M. Titirici, M. Antonietti, A One-Pot Hydrothermal Synthesis of Sulfur and Nitrogen Doped Carbon Aerogels with Enhanced Electrocatalytic Activity in the Oxygen Reduction Reaction, Green Chemistry, 14 (2012) 1515.

# Chapter 8 Conclusions and Perspectives

## 8.1 Conclusions

In this thesis, a scalable, template-free and easily-handled one-step pyrolysis approach is presented to synthesize hierarchically porous carbons with high surface areas and suitable surface chemistry (N or N, S doping, or Co modification), using cost-effective sodium bicarbonate as the porogen, abundant glucose or wheat flour as carbon sources and some other doping agents (urea, thiourea, dicyandiamide, or cysteine) or metal species (cobalt nitrate). The main objectives proposed in Chapter 1 have been comprehensively realized. Various techniques were adopted to fully reveal the structural features of the samples which are ideal for water remediation. The as-synthesized functional porous carbons demonstrated excellent adsorptive performance on several representative organic pollutants in wastewater including SCP, TBBPA, HBA and phenol. In addition, they were highly efficient for complete removal of these contaminants by effective activation of PS or PMS in AOPs, the mechanisms of which were illustrated to be related with producing active oxidizing radicals (hydroxyl, sulfate or singlet oxygen). Benefited from the unique properties of the functional porous carbons, they also acted as excellent adsorbents for $CO_2$ uptake, active catalysts for ORR and superior supercapacitor electrode materials.

### *8.1.1 Template-Free Synthesis of N-doped Carbon with Pillared-Layered Pores as Bifunctional Materials for Supercapacitor and Environmental Applications*

- N-doped, pillared-layered porous carbons (NCs) were prepared via a template-free pyrolysis of glucose, sodium bicarbonate and urea at 600 (NC600), 700 (NC700) and 800 °C (NC800), which had bifunctional applications in supercapacitors and environmental remediation.
- NC700 displayed a high surface area (2118 $m^2\ g^{-1}$) and a specific capacitance of 305 F $g^{-1}$ at 0.2 A $g^{-1}$ in a two-electrode setup.
- For water remediation, NC800 displayed high adsorption capacities towards flame retardant TBBPA (372 mg $g^{-1}$) and antibiotic SCP (288 mg $g^{-1}$) solution, while NC700 showed the most efficient SCP oxidation removal by activating PS to produce hydroxyl and sulfate radicals.

*8.1.2 Nitrogen- and Sulfur-Codoped Hierarchically Porous Carbon for Adsorptive and Oxidative Removal of Pharmaceutical Contaminants*

- N and S co-doped porous carbons (N-S-PCs) with high surface areas (up to 1608 $m^2 g^{-1}$) and hierarchically porous structures were synthesized via a direct pyrolysis of a mixture of glucose, sodium bicarbonate and thiourea.
- N-S-PCs were highly efficient for PS activation to generate hydroxyl and sulfate radicals when employed as catalysts for oxidative degradation of SCP solutions, with a reaction rate constant up to 0.28 $min^{-1}$.
- The adsorption capacities of N-S-PC-2 (which contains 4.51 at. % of N and 0.22 at. % of S) on SCP were 73, 7 and 3 times higher than GO, rGO and commercial SWCNT, respectively.

*8.1.3 Heteroatom (N or N-S)-Doping Induced Layered and Honeycomb Microstructures of Porous Carbons for $CO_2$ Capture and Energy Applications*

- N-doped layered porous carbons (NCs) with different N doping contents were synthesized.
- The formation mechanism of the varying pore frameworks in N-doped layered porous carbons (NCs) and N, S codoped honeycomb porous carbon (NSC) was analyzed to arise from different hydrogen-bond interactions.
- NCs and NSC were investigated for other applications including $CO_2$ uptake and ORR.
- NSC displayed a similar $CO_2$ adsorption capacity (4.7 mmol $g^{-1}$ at 0 °C), a better $CO_2/N_2$ selectivity and higher activity in ORR as compared with NC-3 (the NC sample with the highest N content of 7.3%).
- NSC favored an efficient four-electron reduction pathway and presented better methanol tolerance than Pt/C in alkaline media.
- The porous carbons exhibited excellent rate performance as supercapacitors.

*8.1.4 One-Step Synthesis of Flour-Derived Functional Nanocarbons with Hierarchical Pores for Versatile Environmental Applications*

- Honeycomb structured carbon (700-PC) with dominant micropores was synthesized by pyrolyzing a mixture of wheat flour and $NaHCO_3/Na_2CO_3/K_2CO_3$

at 700 °C, which exhibited an excellent $CO_2$ storage capacity of 6.8 mmol $g^{-1}$ at 0 °C and ambient pressure.

- By including dicyandiamide in the precursors and adjusting synthesis temperatures, N-doped hierarchical porous carbons (N-PCs) in a micro- and meso-porous texture were selectively generated with high surface areas up to 3041 $m^2$ $g^{-1}$ and excellent high-pressure $CO_2$ uptake capacities up to 19.4 mmol $g^{-1}$ at 0 °C, 10 bar.
- For water remediation, 800-N-PC (N-PCs prepared at 800 °C) exhibited the most efficient degradation of HBA with a high reaction rate constant of 0.39 $min^{-1}$ at 25 °C, by activating PMS to create abundant hydroxyl and sulfate radicals.
- 800-N-PC showed selective adsorption of HBA in a mixed solution of HBA and phenol, while could be effectively degraded by the AOPs.

*8.1.5 Bread-Making Synthesis of Hierarchical Co@C Nanoarchitecture in Heteroatom Doped Porous Carbons for Oxidative Degradation of Emerging Contaminants*

- A facile one-pot pyrolysis strategy was proposed for homogeneous assembly of core-shell Co@C nanoparticles with nitrogen and sulfur into hierarchically porous carbon (Co-N-S-PCs).
- Co-N-S-PCs were highly efficient for oxidative decomposition of HBA and phenol.
- Co@C nanoparticles are crucial for the generation of singlet oxygen in continuous AOPs, which works together with hydroxyl and sulfate radicals in efficient decomposition of HBA.
- DFT calculations disclose that electron transfer from Co to C shells greatly improves the Fermi level and chemical activity of the C atoms. The combination of Co-C interaction with dual N, S doping further bring about catalytic active sites in the graphitic shells where the charge states of C atoms are increased.

Overall, all the porous carbon-based samples are produced by a one-step pyrolysis process in this thesis. As the carbon source, glucose is more soluble in water than wheat flour which is a mixture mainly of starch and protein. Therefore, the hydrogen-bonding or other interactions between glucose and other precursors in aqueous solution tends to be stronger during the self-assembly process, which are critical to generate pores and achieve high-performance porous carbons in the following pyrolysis process. As a result, glucose-

derived porous carbons all show excellent textural properties after mild activation of sodium bicarbonate with suitable atom doping, and have decent performance in versatile applications. However, glucose is still expensive for practical production of porous carbons, while wheat flour is much cheaper. Since wheat flour is partially soluble, the self-assembly with other precursors is not that adequate and it is not easy to derive high SSA porous carbon by mild $NaHCO_3$ activation only, which will have an impact on their final performance. Therefore, cobalt modification is introduced to enhance the catalytic ability of porous carbons in PMS activation. In addition, multiple porogens ($NaHCO_3$/$Na_2CO_3$/$K_2CO_3$) can be used with wheat flour and doping agent to enhance the activation effect and achieve porous carbons with super high SSAs for $CO_2$ capture, organic adsorption and degradation in wastewater.

## 8.2 Perspectives and Suggestions for Future Research

In the future study, some efforts can be given on porous carbons with different structures (e.g. different pore shapes, graphitic degree) in the adsorption and catalysis of AOPs for deeper understanding of the active sites and the adsorptive and catalytic nature. Controlled experiment in combination with simulations will be conducted.

For practical applications, continual attention should focus on further reducing the cost of production of high-surface-area functional porous carbons in the premise that the performance will not be impaired. Some attentions should be paid on improving the reusability of porous carbon-based catalysts in AOPs.

Considering the complex composition of wastewater, more work needs to be done on studying the activity of functional porous carbons in adsorption or degradation of several kinds of organic pollutants. Meanwhile, the reaction condition, dosage of porous carbon or/and PMS/PS should also be optimized for real wastewater applications. Intermediate products from degradation of these harmful organic pollutants should be inspected to make sure the byproducts of AOPs are harmless.

In addition, the relation of porous carbon microstructures in PS/PMS activation and the producing radical species need further understanding. Apart from singlet oxygen, hydroxyl and sulfate radicals, there may exist other reactive radical species which may

contribute to organic degradation. Combined EPR, quenching experiments will be demanded in the future.

# Appendix

## Copyright Permissions

Permissions from the copyright owners have been obtained to reproduce copyright materials in this thesis and the details are shown as follows:

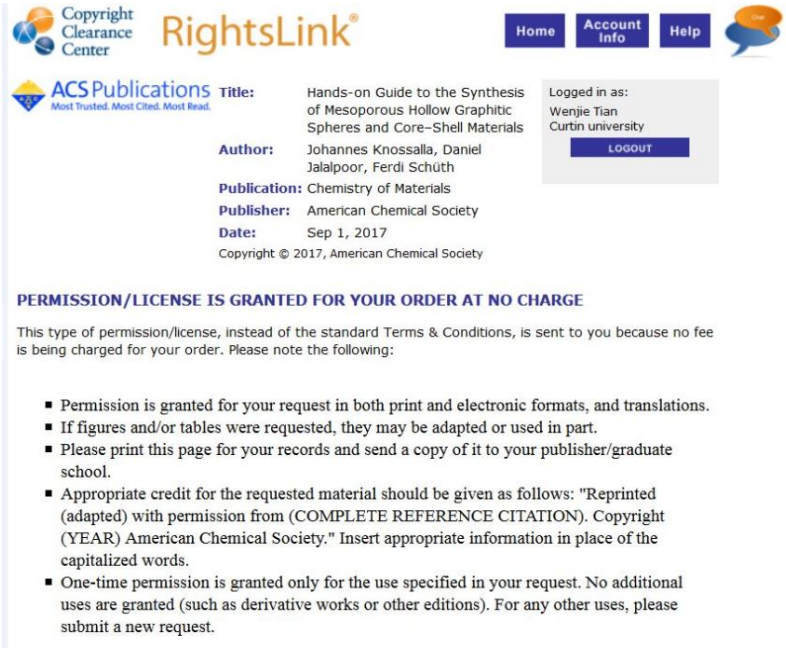

Copyright Clearance Center RightsLink®

Home | Account Info | Help

ACS Publications Most Trusted. Most Cited. Most Read.

Title: Hands-on Guide to the Synthesis of Mesoporous Hollow Graphitic Spheres and Core–Shell Materials

Author: Johannes Knossalla, Daniel Jalalpoor, Ferdi Schüth

Publication: Chemistry of Materials

Publisher: American Chemical Society

Date: Sep 1, 2017

Copyright © 2017, American Chemical Society

Logged in as: Wenjie Tian Curtin university

LOGOUT

**PERMISSION/LICENSE IS GRANTED FOR YOUR ORDER AT NO CHARGE**

This type of permission/license, instead of the standard Terms & Conditions, is sent to you because no fee is being charged for your order. Please note the following:

- Permission is granted for your request in both print and electronic formats, and translations.
- If figures and/or tables were requested, they may be adapted or used in part.
- Please print this page for your records and send a copy of it to your publisher/graduate school.
- Appropriate credit for the requested material should be given as follows: "Reprinted (adapted) with permission from (COMPLETE REFERENCE CITATION). Copyright (YEAR) American Chemical Society." Insert appropriate information in place of the capitalized words.
- One-time permission is granted only for the use specified in your request. No additional uses are granted (such as derivative works or other editions). For any other uses, please submit a new request.

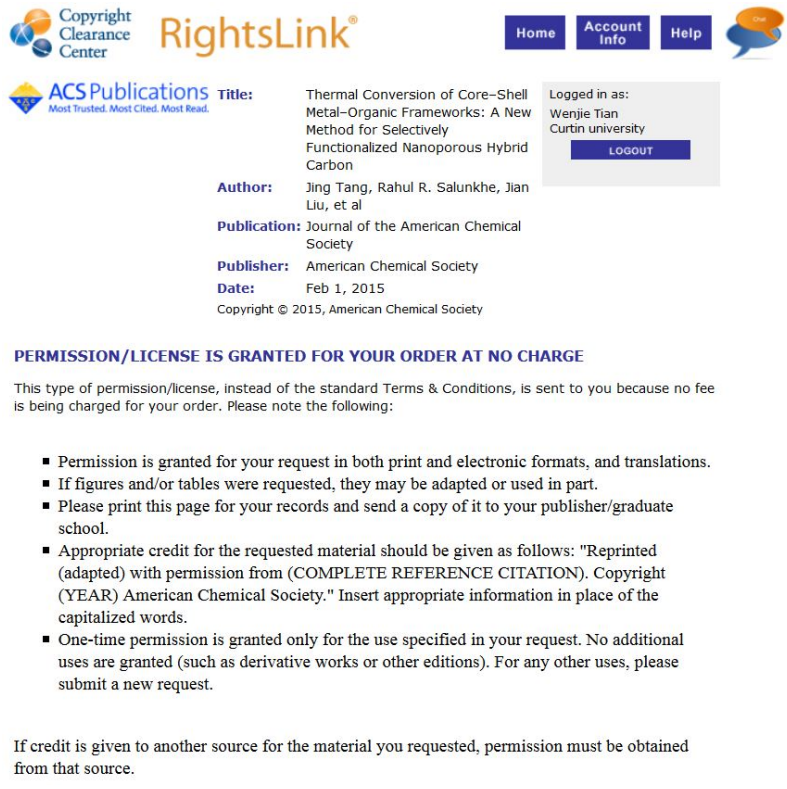

Copyright Clearance Center RightsLink®

Home | Account Info | Help

ACS Publications Most Trusted. Most Cited. Most Read.

Title: Thermal Conversion of Core–Shell Metal–Organic Frameworks: A New Method for Selectively Functionalized Nanoporous Hybrid Carbon

Author: Jing Tang, Rahul R. Salunkhe, Jian Liu, et al

Publication: Journal of the American Chemical Society

Publisher: American Chemical Society

Date: Feb 1, 2015

Copyright © 2015, American Chemical Society

Logged in as: Wenjie Tian Curtin university

LOGOUT

**PERMISSION/LICENSE IS GRANTED FOR YOUR ORDER AT NO CHARGE**

This type of permission/license, instead of the standard Terms & Conditions, is sent to you because no fee is being charged for your order. Please note the following:

- Permission is granted for your request in both print and electronic formats, and translations.
- If figures and/or tables were requested, they may be adapted or used in part.
- Please print this page for your records and send a copy of it to your publisher/graduate school.
- Appropriate credit for the requested material should be given as follows: "Reprinted (adapted) with permission from (COMPLETE REFERENCE CITATION). Copyright (YEAR) American Chemical Society." Insert appropriate information in place of the capitalized words.
- One-time permission is granted only for the use specified in your request. No additional uses are granted (such as derivative works or other editions). For any other uses, please submit a new request.

If credit is given to another source for the material you requested, permission must be obtained from that source.

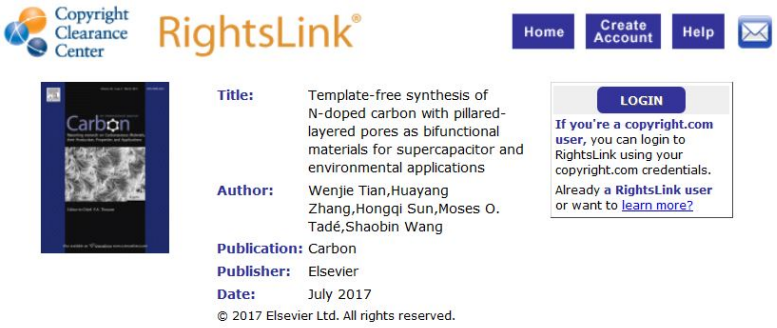


Please note that, as the author of this Elsevier article, you retain the right to include it in a thesis or dissertation, provided it is not published commercially. Permission is not required, but please ensure that you reference the journal as the original source. For more information on this and on your other retained rights, please visit: https://www.elsevier.com/about/our-business/policies/copyright#Author-rights


Please note that, as the author of this Elsevier article, you retain the right to include it in a thesis or dissertation, provided it is not published commercially. Permission is not required, but please ensure that you reference the journal as the original source. For more information on this and on your other retained rights, please visit: https://www.elsevier.com/about/our-business/policies/copyright#Author-rights

| Order Date | Article Title | Publication | Type Of Use | Order Status | Licence Number |
|---|---|---|---|---|---|
| 15-May-2018 | Heteroatom (N or N-S)-Doping Induced Layered and Honeycomb Microstructures of Porous Carbons for $CO_2$ Capture and Energy Applications | Advanced Functional Materials | Dissertation/Thesis | Completed | 4350211424555 |
| 15-May-2018 | Biological cell derived N-doped hollow porous carbon microspheres for lithium–sulfur batteries | Journal of Materials Chemistry A | Thesis/Dissertation | Completed | 4350211284014 |
| 15-May-2018 | A 3D bi-functional porous N-doped carbon microtube sponge electrocatalyst for oxygen reduction and oxygen evolution reactions | Energy & Environmental Science | Thesis/Dissertation | Completed | 4350211152729 |
| 15-May-2018 | Enabling high-volumetric-energy-density supercapacitors: designing open, low-tortuosity heteroatom-doped porous carbon-tube bundle electrodes | Journal of Materials Chemistry A | Thesis/Dissertation | Completed | 4350211017896 |
| 15-May-2018 | Surface-coating synthesis of nitrogen-doped inverse opal carbon materials with ultrathin micro/mesoporous | Journal of Materials Chemistry A | Thesis/Dissertation | Completed | 4350210860646 |

| Order Date | Article Title | Publication | Type Of Use | Order Status | Licence Number |
|---|---|---|---|---|---|
| | graphene-like walls for oxygen reduction and supercapacitors | | | | |
| 15-May-2018 | Ordered Hierarchical Mesoporous/Macroporous Carbon: A High-Performance Catalyst for Rechargeable Li–$O_2$ Batteries | Advanced Materials | Dissertation/Thesis | Completed | 4350210702735 |
| 15-May-2018 | Nitrogen-Doped Porous Carbon Superstructures Derived from Hierarchical Assembly of Polyimide Nanosheets | Advanced Materials | Dissertation/Thesis | Completed | 4350210572431 |
| 15-May-2018 | Controllable synthesis of highly uniform flower-like hierarchical carbon nanospheres and their application in high performance lithium–sulfur batteries | Journal of Materials Chemistry A | Thesis/Dissertation | Completed | 4350201152512 |
| 15-May-2018 | Twin Polymerization at Spherical Hard Templates: An Approach to Size-Adjustable Carbon Hollow Spheres with Micro- or Mesoporous Shells | Angewandte Chemie International Edition | Dissertation/Thesis | Completed | 4350200997562 |
| 15-May-2018 | A facile way to fabricate double-shell pomegranate-like porous carbon microspheres for high-performance Li-ion batteries | Journal of Materials Chemistry A | Thesis/Dissertation | Completed | 4350200829472 |
| 15-May-2018 | Hollow Mesoporous Carbon Nanocubes: Rigid-Interface-Induced Outward Contraction of Metal-Organic Frameworks | Advanced Functional Materials | Dissertation/Thesis | Completed | 4350200711569 |
| 15-May-2018 | Metal–Organic-Framework-Derived Hybrid Carbon Nanocages as a Bifunctional Electrocatalyst for Oxygen Reduction and Evolution | Advanced Materials | Dissertation/Thesis | Completed | 4350200514568 |
| 15-May-2018 | Fabrication of carbon nanorods and graphene nanoribbons from a metal–organic framework | Nature Chemistry | Thesis/Dissertation | Completed | 4350200063231 |
| 15-May-2018 | Variable texture few-layer ordered macroporous carbon for high-performance electrochemical capacitors | Journal of Materials Chemistry A | Thesis/Dissertation | Completed | 4350191349655 |
| 15-May-2018 | Metal-Free Nitrogen-Doped Mesoporous Carbon for Electroreduction of $CO_2$ to Ethanol | Angewandte Chemie International Edition | Dissertation/Thesis | Completed | 4350190906966 |
| 15-May-2018 | Preparation of N-doped microporous carbon nanospheres by direct carbonization of as-prepared mesoporous silica nanospheres containing cetylpyridinium bromide template | Carbon | reuse in a thesis/dissertation | Completed | 4350190676665 |

| Order Date | Article Title | Publication | Type Of Use | Order Status | Licence Number |
|---|---|---|---|---|---|
| 15-May-2018 | Lanthanum-catalysed synthesis of microporous 3D graphene-like carbons in a zeolite template | Nature | Thesis/Dissertation | Completed | 4350190407311 |
| 15-May-2018 | Controlling macro- and mesostructures with hierarchical porosity through combined hard and soft templating | Chemical Society Reviews | Thesis/Dissertation | Completed | 4350180488946 |
| 15-May-2018 | Mesoporous materials for energy conversion and storage devices | Nature Reviews Materials | Thesis/Dissertation | Completed | 4350171212746 |